FAKULTÄT FÜR MEDIZIN

DER TECHNISCHE UNIVERSITÄT MÜNCHEN

Ph. D. Thesis

Incorporating Sensor Properties in Optoacoustic Imaging

Author: Miguel Ángel Araque Caballero

Referees: Prof. Dr. Vasilis Ntziachristos (TUM)

               Prof. Dr. Rudolf Gross (TUM)

               Prof. Dr. Daniel Razansky (TUM)

TECHNISCHE UNIVERSITÄT MÜNCHEN

Lehrstuhl für Biologische Bildgebung

Incorporating Sensor Properties in Optoacoustic Imaging

Miguel Ángel Araque Caballero

Vollständiger Abdruck der von der Fakultät für Medizin der Technischen Universität München zur Erlangung des akademischen Grades eines

Doktors der Naturwissenschaften (Dr. rer. nat.)

genehmigten Dissertation.

Vorsitzender: Univ.-Prof. Dr. Gabriele Multhoff

Prüfer der Dissertation:

1. Univ.- Prof. Vasilis Ntziachristos, Ph. D.

2. Univ.- Prof. Dr. Rudolf Gross

Die Dissertation wurde am 07.03.2013 bei der Technischen Universität München eingereicht und durch die Fakultät für Medizin am 10.04.2013 angenommen.

For my family and friends

Contents

1. INTRODUCTION

Optical imaging has proved a versatile and powerful tool for scientific investigation throughout modern history. In the biological sciences, it has been fundamental in the discovery of a number of microscopic entities and processes: from the first images of bacteria by A. van Leeuwenhoek in the 1600s [1], through the depiction of neuronal structure by S. Ramón y Cajal in the late 1800s , to the current swath of cellular and sub-cellular imaging of both function and structure. These applications have relied mainly on the use of microscopy, not only due to the desire to understand biological tissue at the sub-micrometer scale, but also due to the fundamental limitations of optical imaging at millimeter scales or larger [2]. In recent years, optoacoustic imaging is overcoming these limitations by offering a distinct approach to optical imaging [3]. This work aims to provide an understanding of the underlying physical processes that take place during optoacoustic imaging, and how this understanding can be used to provide accurate images of biological tissue at scales traditionally outside the optical domain.

In the following paragraphs, the previous concepts are described in more detail. First, the limitations of conventional optical imaging are explained, followed by a description of optoacoustic imaging and how it is able to go beyond the optical depths. Afterwards, the exposition will delve deeper into the general features of optoacoustic imaging, its applications, and the specific motivation and aim of this work within that context. At the end of the introduction, the outline of the dissertation is provided.

Optical microscopy techniques are limited to the investigation of relatively thin or transparent samples. This is due to the interaction of light with tissue, which may scatter or absorb the propagating photons, up to the point where no structural information of the sample can be obtained. These diffusive interactions become significant after light has propagated a few tens to hundreds of micrometers in the tissue, depending on the wavelength of the light and the tissue properties. As a result, microscopy is limited to samples in which diffusion can be mostly neglected, either because they are very transparent or because they are few tens of micrometers thick [2]. Purely optical tomographic techniques have been developed in the past decades to cope with this limitation [4]. They rely on the measurement of the diffused light at several positions relative to the sample and the posterior reconstruction of the initial photon distribution. Combined with other imaging modalities and through the use of novel fluorescence agents, they have successfully provided quantitative molecular imaging at depths of a few centimeters in small animals (commonly mice) [3]. However, tomography in diffusive media

is in general a complex imaging problem, which has limited the resolution of these techniques to a few millimeters.

Optoacoustic imaging, conversely, is a hybrid modality that avoids the use of diffused light for image formation. Instead, the tissue is excited with pulsed laser light, which generates broadband ultrasonic waves due to the thermoelastic effect [5]. The waves propagate outwards from the sample and can be measured with conventional ultrasound sensors. The amplitude and spectrum of the optoacoustic waves depend on the size of the absorbing structures and the locally deposited energy, which is in turn proportional to the tissue absorption [6]. In macroscopic applications, acoustic scattering and attenuation in tissue are in general weaker than their optical counterparts, and as a consequence optoacoustic waves propagate for longer distances than light does [7]. In this manner, optoacoustic imaging may be used for the visualization of optical tissue properties at greater depths than purely optical imaging. Additionally, the ultrasonic nature of the optoacoustic waves results in resolutions that range from 100 μm in whole-body small-animal imaging to sub-micrometer resolution in superficial applications [8].

Optoacoustic imaging has seen a rapid development in the last two decades, where it has gone from simple investigations of the phenomenon in tissue-like media [5], to the application of the modality in a broad range of biological studies [9]. In particular, when combined with illumination at multiple wavelengths such in the Multispectral Optoacoustic Tomography (MSOT) technique, it has seen applications to the imaging of pharmacokinetics [10], in-vivo physiology [11], and cardiovascular dynamics [12]. In this manner, optoacoustic imaging has not only overcome the limitations of optical imaging, but has also inherited and enhanced its powerful features for molecular imaging applications.

There exist several implementations of optoacoustic imaging, which are suited for different applications. Whole-body imagers work at ultrasonic frequencies up to 10 MHz and are typically arranged in a tomographic fashion, providing a cross-sectional or a three-dimensional view of the animal [11, 13-15]. On the other hand, meso- and microscopic setups are in general based on the scanning of high-frequency (>20 MHz) sensors and are well suited for superficial vasculature imaging [16-19]. After measurement, image reconstruction methods aim to recover the initial distribution of optoacoustic pressure, which is proportional to the absorbed optical energy within the tissue [20, 21].

Ultimately, it is the interplay between illumination, measurement geometry, sensor properties and reconstruction algorithm which determines the performance of an optoacoustic system. In a tomographic setup, for example, excitation and detection on the

same plane results in a better delimitation of the imaged cross-section of the sample [22]. In a scanning modality, confocal excitation and detection may be utilized to achieve optical resolution [18]. In both cases, it is important that the image reconstruction algorithm accurately describes the optoacoustic generation, propagation and detection processes in order to obtain an accurate image of the energy deposited in the sample.

In particular, it has been shown both in theory and in experiment, that the properties of ultrasound transducers may distort the optoacoustic waves in a non-trivial manner, which in turn may result in image artifacts or degraded resolution [23, 24]. In spite of this, most image reconstruction algorithms work under the assumption that the ultrasound sensors are isotropic and have an infinite acoustic bandwidth, which are not valid assumptions in most cases. Only in recent years have there been attempts to take into account the properties of the detector during image formation, either in 2D [24] or 3D [25] detection geometries. However, these have been performed as proof-of-principle studies in simple phantoms –the application of these methods to biological tissue is yet to be demonstrated.

The aim of this work is to provide optoacoustic image formation algorithms that take into account the properties of the ultrasound detectors and result in accurate image reconstructions of biological samples.

A previous necessary step, of course, is to gain knowledge on the properties of ultrasound sensors and develop accurate descriptions of those properties. Due to conceptual and practical similarities between optoacoustic and ultrasound imaging, there exists a well-researched body of knowledge on the properties of ultrasound sensors that can be used as a starting point for this task [26, 27]. However, the differences between the two modalities make it necessary to review the calibration techniques and rethink the relevant properties of ultrasound sensors when used in an optoacoustic environment.

The dissertation is structured along these lines, as follows. In the following chapter (Chapter 2), a detailed background of optoacoustic imaging and the relevant physical processes is provided. The chapter includes a general description of ultrasound sensors and a definition of their properties, as well as a section describing existing image reconstruction algorithms. In Chapter 3, the proposed optoacoustic methods for the characterization of ultrasound transducers are described, and different theoretical models for their description are assessed experimentally. In Chapter 4, the knowledge acquired in the previous chapter is applied to an optoacoustic scanning modality, microscanning. Reconstruction methods for point-like, large unfocused and focused transducers are reported and their performance

assessed with simulations and experiment. In Chapter 5, preliminary results on 3D reconstruction algorithms that include the properties of the detector are demonstrated numerically and experimentally. Finally, in Chapter 6 the results of the dissertation are reviewed and the consequences for future optoacoustic imaging applications are discussed.

2.   THEORETICAL AND TECHNICAL BACKGROUND

In this chapter, a theoretical overview of the fundamental principles behind optoacoustic imaging is provided. The aim is to present key concepts about the nature of the optoacoustic signal, the properties of ultrasound transducers and the features of image reconstruction algorithms. The concepts presented herein are intended to provide the background needed to understand the theoretical discussions, experiments and numerical results presented in the following chapters. For a more thorough derivation of the subjects here discussed, the reader is invited to refer to the cited literature.

The chapter is divided into four major parts. In Section 2.1, the general concept of optoacoustic imaging is presented, with an overview of the relevant physical processes in soft, tissue-like media: light propagation; the optoacoustic effect itself; ultrasound propagation and related phenomena, such as absorption, refraction and diffraction. In Section 2.2, the general properties of optoacoustic sources are presented, both in the time and the frequency domain. Section 2.3 deals with the measurement of optoacoustic waves and the properties of ultrasound sensors. Finally, in Section 2.4 the basics of optoacoustic image reconstruction are presented.

2.1   Optoacoustic principles

An optoacoustic imaging system is schematically represented in Fig. 1. The sample to be imaged is illuminated with a high-power light source, typically a laser at near infrared to visible wavelengths. The light is absorbed by the tissue, which results in transient localized heating followed by a pressure rise due to the thermoelastic effect [6]. Then, the tissue relaxes by emitting broadband ultrasonic waves that propagate outwards from the sample and are detected by sensors at different locations. Afterwards, image reconstruction algorithms aim to recover the initial distribution of optical energy deposited within the tissue from the detected signals. Such a distribution is therefore dependent on the optical properties of the object and the illumination. In this section, the different physical processes from illumination to wave propagation are detailed, in the order they take place during an optoacoustic measurement.

2.1.1 Illumination and light propagation in tissue

When light propagates inside tissue, it is absorbed and scattered as it delves deeper into the medium. Absorption occurs when light is taken up by the tissue and subsequently transformed into other forms of energy, such as heat, optoacoustic waves or fluorescence. Scattering represents the deflection of light from its original direction of propagation, but may occur without energy transfer. Light transport in tissue can be divided into two
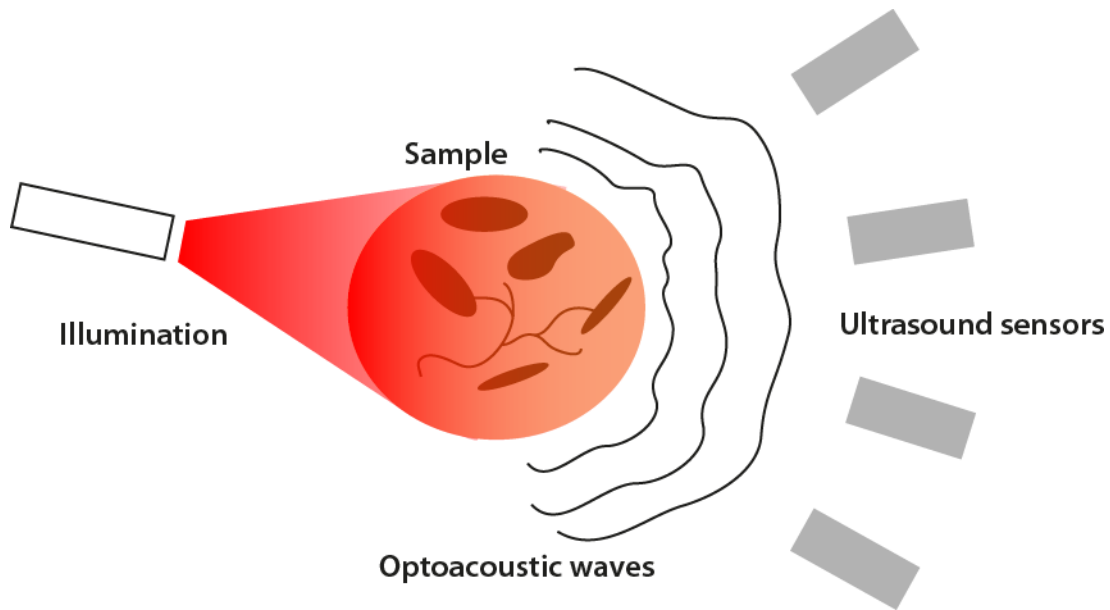
Figure 1: Sketch of a prototypic optoacoustic setup. The laser illuminates the sample, and the absorbing structures within emit optoacoustic waves. These are detected by ultrasound sensors placed at several locations with respect to the sample.

propagation regimes, dependent on the optical properties of the tissue, the optical wavelength, and the distance over which the light propagates [2]. Ballistic transport of photons takes place over short distances (1 to 10 mm) or in low-scattering tissue. Light transport can be then described by the laws of geometrical optics. At greater depths or in highly scattering media, photons may undergo several scattering events as and information on the original direction of propagation is completely lost. At such depths, light transport is best described as a diffusion process.

Light propagation is therefore important in optoacoustics as it ultimately determines the imaging depth to scales ranging from several millimeter to a few centimeters depending on the light wavelength [3]. Moreover, light propagation models may be employed in optoacoustic imaging to discriminate between the features in the image that represent intrinsic tissue properties, extrinsic contrast agents, or light diffusion [8, 28]. However, such models typically require an initial estimate of the shape and optical properties of the sample, or operate as a post-processing step after preliminary image formation. Since the aim of the present work is to provide image reconstruction algorithms that incorporate detector properties, without prior knowledge of the sample, throughout this work light diffusion in tissue was not corrected during image formation, unless stated otherwise.

2.1.2 Optoacoustic signal generation

Upon illumination, the absorption of light by the tissue results in a slight temperature rise (in the order of millikelvin). The tissue then relaxes by heat diffusion and

14

through the generation of optoacoustic waves. The relative importance of both phenomena depends on the duration of the laser excitation. If the excitation is shorter than the time it takes for the heat to diffuse to neighboring tissue, the heating is localized and optoacoustic waves are generated. This condition is referred to as "heat confinement". Additionally, if the pulse duration is much shorter than the time it takes for the optoacoustic waves to propagate, the illumination can be assumed instantaneous and the optoacoustic emission is localized in time. The excitation is then said to be under "stress confinement". In order to achieve high signal amplitudes and good spatial resolution both confinement conditions should be fulfilled, and nanosecond pulsed lasers are therefore used for optoacoustic signal generation[*].

Under stress and heat confinement, the relationship between the initial induced pressure p_0 at a given point $\vec{r}$ within tissue and the absorbed optical energy can be expressed as:

$$p_0(\vec{r}) = \Gamma H_r(\vec{r}) = \Gamma \mu_a(\vec{r})\Phi(\vec{r}) \,, \tag{2.1}$$

where $\mu_a(\vec{r})$ represents the absorption coefficient of the tissue (with units of reciprocal length, typically cm^{-1}) and $\Phi(\vec{r})$ represents the local optical fluence (energy per surface, typically J/cm^2). Γ is the Grüneisen parameter (dimensionless) [5], which represents the amount of temperature converted to pressure and can be thus understood as the optoacoustic generation efficiency of the tissue. Once the optoacoustic effect has taken place, the extra pressure propagates then as a wave at ultrasonic frequencies. This takes us to the next section.

2.1.3 Optoacoustic wave propagation in the time-domain

The advantage of using the time-domain representation to describe wave propagation is that it relates directly to the actual measurement process of the optoacoustic wave, (presented in Section 2.3). Such representation arises from the optoacoustic wave equation, which describes the relationship between the laser excitation and the ultrasound propagation in a medium:

$$\frac{\partial^2 p(\vec{r},t)}{\partial t^2} - c^2 \nabla^2 p(\vec{r},t) = \Gamma \, \frac{\partial H(\vec{r},t)}{\partial t} \,, \tag{2.2}$$

---

[*] Using chirp-modulated or continuous wave lasers violates these conditions, but gives rise to the so-called frequency-domain optoacoustic effect, which also can be used for imaging applications 29.　Fan, Y., et al., *Development of a laser photothermoacoustic frequency-swept system for subsurface imaging: theory and experiment.* J Acoust Soc Am, 2004. **116**(6): p. 3523-33.. The discussion of this alternative was omitted for simplicity.

where c is the speed of sound in the medium and $H(\vec{r}, t)$ is the amount of energy deposited in the medium per unit volume and unit time, and is called the heating function. $p(\vec{r}, t)$ is the optoacoustic pressure field.

Since the propagation of light can be assumed instantaneous at biomedical scales, the heating function is separable as $H(\vec{r}, t) = H_r(\vec{r}) H_t(t)$, where $H_r(\vec{r})$ is described as in Eq. (2.1) and $H_t(t)$ represents the temporal profile of the laser pulse. In the case of tissue-like media, if the duration of the laser pulse is of the order of a few nanoseconds, the heating can be assumed instantaneous and thus $H_t(t) \approx \delta(t)$, where $\delta(t)$ represents the Dirac-delta. The propagation of acoustic waves in tissue-like media (i.e., the solutions to Eq. (2.2)) can be therefore described either in terms of the time-domain Green's function of the wave equation, or in terms of the frequency-domain superposition of harmonic waves.

Let us assume that an object Ω is an optoacoustic source. We are interested in the optoacoustic pressure field generated by Ω at point $\vec{r}$ and given time t after excitation, as shown in Fig. 2a. The solution of the wave equation for object Ω can be computed by assuming that each point $\vec{r}'$ in the object is an emitter of optoacoustic waves, given by a Green's function of the form [5]:

$$G(\vec{r}, \vec{r}', t) = \frac{\delta\left(t - \frac{|\vec{r} - \vec{r}'|}{c}\right)}{4\pi |\vec{r} - \vec{r}'|}. \tag{2.3}$$

Eq. (2.3) represents the elementary wave generated at $\vec{r}'$ at $t = 0$, propagating outwards in a spherical shell of decaying amplitude. We can then write the solution to Eq. (2.2) at a given point in space $\vec{r}$ as:

$$p(\vec{r}, t) = \frac{\Gamma}{4\pi c^2} \frac{\partial}{\partial t} \left[\int_{\Omega} H_r(\vec{r}') \frac{\delta\left(t - \frac{|\vec{r} - \vec{r}'|}{c}\right)}{|\vec{r} - \vec{r}'|} d\vec{r}' \right], \tag{2.4}$$

where the integral spans the whole object. Eq. (2.4) is the optoacoustic statement of Huygens' Principle, since it describes the wave at a measurement point $\vec{r}$ as a superposition of elementary waves generated at points $\vec{r}'$ on the source. It is important to note that, since all of the terms inside the brackets result in a compact, positive-defined function of time, the derivation over time implies that optoacoustic waves of closed sources are in general bipolar [5].

16

2.1.4 Optoacoustic wave propagation in the frequency-domain

The frequency-domain description of optoacoustic propagation is practical to describe the diffractive nature of optoacoustic fields and some phenomena that occur during wave propagation (explained in the subsequent Section). The frequency-domain description of follows by decomposing the optoacoustic pressure field in its harmonic components. A monochromatic acoustic wave of angular frequency ω, propagating in a homogeneous medium, can be expressed as a summation over all possible wave directions $\vec{k}$ [30]:

$$p_\omega(\vec{r}, t) = \frac{1}{2\pi} \iiint\limits_{-\infty}^{+\infty} \alpha(\vec{k}) \, e^{i(\vec{k}\cdot\vec{r} - \omega t)} d\vec{k} \,, \qquad (2.5)$$

where $\vec{k}$ is the three-dimensional propagation vector such that $|\vec{k}| = 2\pi/\lambda$, with λ the acoustic wavelength and $\alpha(\vec{k})$ are the coefficients of the summation. In a similar manner to Eq. (2.4), the solution of the wave equation on the frequency domain for $p_\omega(\vec{r})$ (the Helmohltz equation) can be expressed in terms of Green's functions of the form [30]:

$$\hat{G}(\vec{r}, \vec{r}', k) = \frac{e^{i\vec{k}\cdot(\vec{r}-\vec{r}')}}{4\pi|\vec{r} - \vec{r}'|}. \qquad (2.6)$$

2.1.5 Propagation-related phenomena

There are four main processes that take place when an acoustic wave propagates through tissue: refractions and reflections at boundaries between media, attenuation and diffraction.

a) Refractions and reflections

Acoustic refractions and reflections take place at the interface between two media with different acoustical properties. Both phenomena are due to the conservation of wave momentum and energy across the interface. Refraction appears when the wave crosses the boundary at an angle, and results in a change of the direction of the wave after the interface. Reflection on the other hand, takes place for all incident angles and results in the appearance of a reflected wave in the first medium.
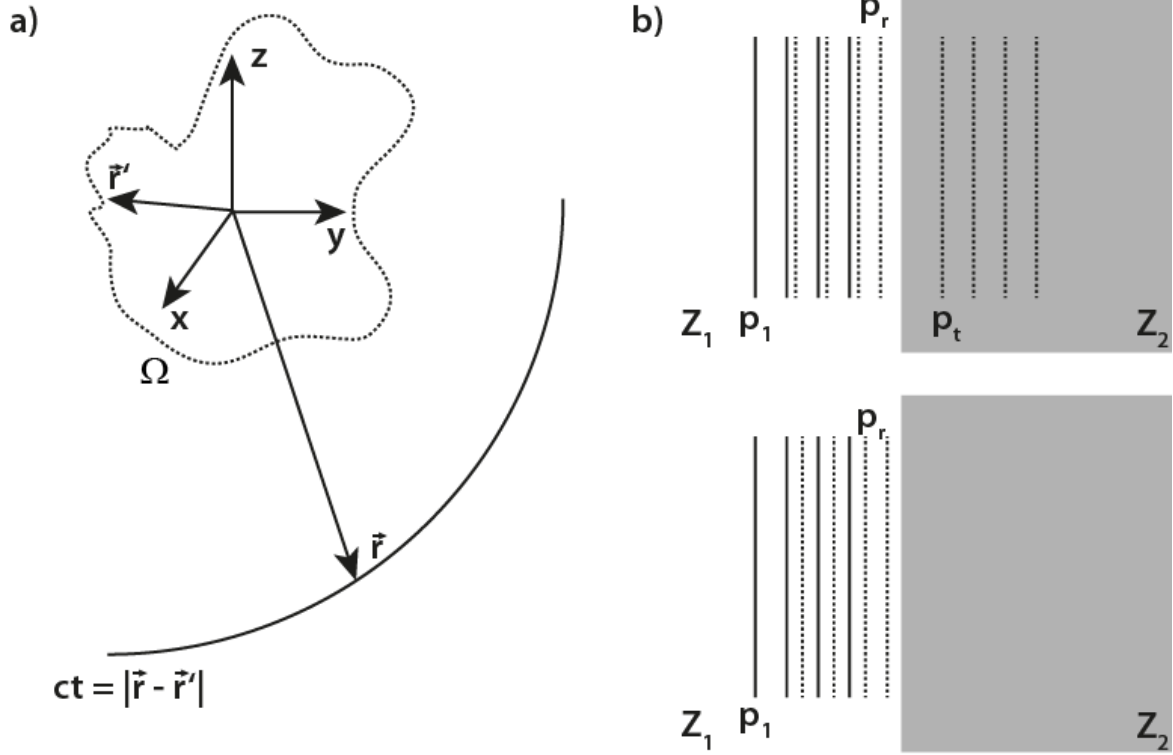
Figure 2 *a)* Coordinate definition for the forward computation of an optoacoustic field. The object Ω is represented by the dotted line. Points of the object are located at $\vec{r}'$ and the optoacoustic field at $\vec{r}$ is calculated by Eq. (2.4). *t* represents the time of flight from $\vec{r}'$ to $\vec{r}$. *b)* Illustration of the reflection and transmission processes between two media of different acoustic impedances. When the acoustic mismatch is low, part of the incident wave is reflected and another part is transmitted (top). When the acoustic mismatch is high, almost no wave is transmitted from one medium to the next (bottom).

Refraction and reflection are related to the acoustic impedances of the media, defined as $Z = \rho c$, where ρ represents the density of the medium and c the speed of sound. Z is measured in Rayls (Pa·s·m^{-1}) and is in the order of 10^6 Rayl for water and tissue. Fig. 2b shows the particular case of reflection for a normal incidence angle, where there is no refraction of the wave. The transmission and reflection coefficients as the wave crosses from medium 1 to medium 2 are thus defined as [31]:

$$T_a = \frac{2Z_2}{Z_1 + Z_2} \tag{2.7}$$

and:

$$R_a = \frac{Z_2 - Z_1}{Z_1 + Z_2}. \tag{2.8}$$

For an incident wave p_1, the amplitude of the reflected acoustic wave is $p_r = R_a p_1$ and the amplitude of the transmitted wave is $p_r = T_a p_1$, where it holds that $p_1 = p_r + p_r$. If the difference between the impedances is large, the relative amplitude of the wave transmitted to the second medium is very low. Due to the high acoustic mismatch between

18

tissue ($Z = 1.5$ MRayl) and air ($Z = 416$ Rayl), optoacoustic measurements have to be performed with the aid of a coupling medium between the tissue and the sensor; otherwise the acoustic waves would remain confined inside the tissue.

In biological tissue there are three major loci of acoustic mismatch: the boundaries between the skin and the outside of the body, between soft tissue and bone, and between the lungs and the surrounding tissue. For other boundaries, reflected acoustic waves are much weaker than the incident wave and the angle of refraction is negligible. For example, the highest acoustic mismatch between any two types of tissue (excluding bone), takes place between fat ($Z = 1.327$ MRayl) and muscle ($Z = 1.679$ MRayl), which results in $R_a = 0.11$ [31], or 89% of transmitted amplitude.

Echographic ultrasound imaging is based on the measurement of reflected waves inside the tissue. In this modality, the problem of weak reflections is circumvented by optimizing the amplitude, frequency and shape of the signal sent into the sample [31]. Additionally, visualization relies less on boundary detection and more on the texture variations between types of tissue (speckle), which is due to the different densities of sub-resolution scatterers.

Optoacoustic imaging, however, is based on the visualization of optical contrast, which is typically much higher than the amplitude difference between the incident and the reflected wave. Therefore, refractions and reflections can be typically neglected, except in the presence of very strong acoustic mismatch [32]. For this reason, throughout the course of this work, media with homogeneous acoustical properties are assumed, unless stated otherwise.

b) Attenuation

Another process that affects optoacoustic waves during propagation is attenuation, which is due to viscous losses in the medium. Attenuation is generally dependent on the frequency of the wave and the acoustic and thermodynamical properties of the medium [31]. In optoacoustic applications below frequencies of 20 to 30 MHz, diffusive optical losses limit the imaging depth to a higher degree than acoustical losses, [7]. Furthermore, at macroscopic scales, the signal distortion due to attenuation in the tissue is generally less important than the distortion due to the transducer properties [7]. Therefore, throughout the present work, acoustical attenuation in the tissue was considered negligible.
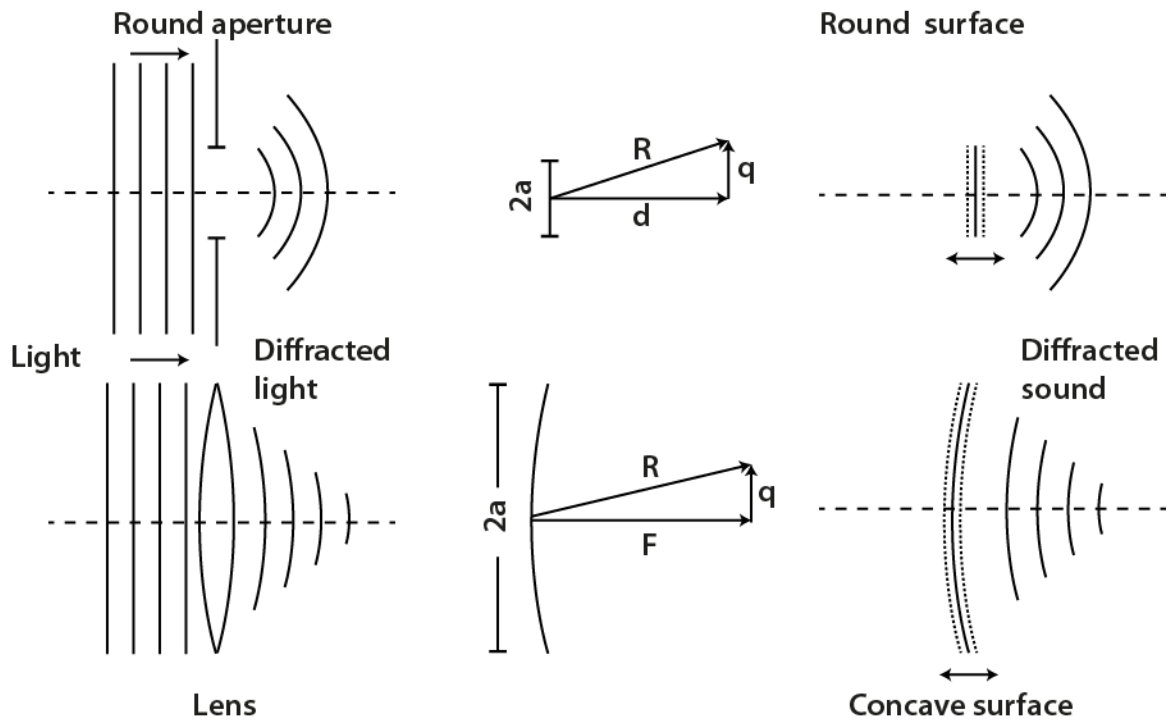
Figure 3: Equivalent diffractive systems in optics and acoustics. *Top row:* the diffraction of a plane wave of light by a round aperture (left) is equivalent to the diffracted acoustic field emitted by a vibrating round ultrasound transducer (right). *Bottom row:* the diffraction of light by a convergent round lens (left) is equivalent to the diffracted acoustic field emitted by an spherically focused (or concave) transducer (right). Revolution symmetry around the dashed axis is implied in all cases. See text for details.

c) Diffraction

Finally, wave propagation is also affected by diffraction, which is due to the mutual interference of the propagating wavefronts originating at neighboring points of the source or the detector [31, 33]. Diffraction has been studied in great detail in the context of optics, where it is described as the interaction between light and objects such as slits, apertures or lenses. In the context of optoacoustics, diffraction is important due to the finite extension of both optoacoustic sources and ultrasound detectors. The diffractive properties of ultrasound sensors are described in section 2.3.4 and investigated in Chapter 3. In the following paragraphs, the general similarities of acoustic and optical diffraction are described qualitatively.

The analogy between optical and acoustic diffraction is illustrated in Fig. 3 for two particular cases. The top row shows a plane wave of light with wavelength λ_o being diffracted by a circular aperture of radius a, compared with a circular surface of the same radius vibrating back and forth with a wavelength λ_a. Similarly, the bottom row shows a plane wave of light being focused by a convergent lens, compared to a vibrating concave surface. Optically, it is assumed that light is a plane wave propagating into the aperture (or the lens) and the diffracted waves propagate afterwards [33]. Acoustically, it is assumed that the surface vibrates as a whole and emits plane waves only onto the right-half medium

[31]. However, both processes are equivalent with respect to wave propagation, and result thus in analogous phenomena that are described formally with the same mathematical expressions.

Diffraction is studied typically in two regimes. The far field regime is reached at a distance R to the diffractive object $R \gg a^2/\lambda$, i.e., for long wavelengths with respect to the aperture size or conversely for points located far from the diffractive object. Conversely the near-field is located at $R \ll a^2/\lambda$. Due to the very different wavelengths and propagation speed of the waves, the main difference between optical and acoustical diffraction is therefore the distance at which the near-field and far-field regimes may be considered.

In practical terms, the optical diffraction pattern of an object is visualized as the light intensity distribution on a screen placed along the path of the diffracted wave. Such a pattern is proportional to the square of the wave amplitude (i.e., the irradiance). On the other hand, the relatively low frequencies of acoustic waves with respect to light make it possible to measure the wave amplitude and phase simultaneously. Therefore, the acoustic diffraction pattern of an object is typically described in terms of the wave amplitude (i.e., the pressure).

For example, let us consider the far-field diffraction for a circular aperture (or surface). We are interested in the diffraction pattern at points located at a distance R from the center of the aperture. The points are assumed to lie in a plane located at a distance d from the aperture and at a radial distance q from the median axis (see Fig. 3). The amplitude of the acoustic diffraction pattern at a distance $R \gg a^2/\lambda$ is described by [27]:

$$p(R,k) = \frac{A}{R}\frac{J_1(kaq/R)}{kaq/R}. \tag{2.9}$$

where $k = 2\pi/\lambda$. J_1 represents a first order Bessel-function, A represents a constant dependent on the amplitude of vibration, the properties of the medium and the size of the aperture, and $p(R,k)$ has units of pressure.

Conversely, the optical diffraction pattern under the same conditions is expressed as [33]:

$$I(R,k) = \frac{B}{R^2}\left[\frac{J_1(kaq/R)}{kaq/R}\right]^2. \tag{2.10}$$

where in this case B depends on the intensity of the electromagnetic field at the aperture and the size of the aperture. The units of $I(R,k)$ are of energy per unit area and

time. While the exact measured quantities differ in the case of optics with respect to acoustics, the functional dependence of the diffraction patterns with respect to the wavelength, distance and aperture size are equivalent. Moreover, the relation between Eqs. (2.9) and (2.10) is also equivalent in the case of the lens and concave surface when the points R lie in a plane located at the center of curvature F, i.e., at the focal plane of either the optical lens or the vibrating surface.

In conclusion, diffraction arises naturally in optoacoustics as a consequence of the propagation of acoustic waves. Diffractive effects and their implications to optoacoustic imaging were therefore investigated in this work, as they ultimately define the properties of optoacoustic sources and detectors [31]. This dissertation may be thus considered a study of the time-domain diffraction of broadband optoacoustic waves, with applications to image reconstruction. Diffraction is further explored when defining sensor properties in section 2.3.5 and experimentally in Chapter 3.

Having an overview of the different physical effects that may affect the propagation of an optoacoustic wave, we proceed to outline several important characteristics of optoacoustic sources both in the time and frequency domain.

2.2   Optoacoustic sources

Under the conditions of uniform illumination and constant light fluence within the object, Eq. (2.4) can be solved exactly both in the frequency and the time domain for some simple source geometries [5]. These geometries include the sphere, the infinite cylinder and the infinite semi-space. While such conditions and sources are indeed highly idealized, the analytical solutions provide nevertheless useful insights into the nature and characteristics of optoacoustic signals and their spectra.

In particular, the analytical solution for the uniformly illuminated sphere sheds light upon several of the most important features of optoacoustic signals, such as the mutual interdependence of size, emission frequencies and signal amplitude. More importantly, this analytical solution has been shown to accurately describe the experimentally measured optoacoustic signals generated by uniformly illuminated absorbing spheres [5]. The solutions provide therefore a realistic model to study the characteristics of optoacoustic signals.

2.2.1 Time-domain characteristics

Let us assume an absorbing sphere of radius a and absorption coefficient μ_a, uniformly illuminated by a laser beam which results in fluence Φ. The acoustic properties of
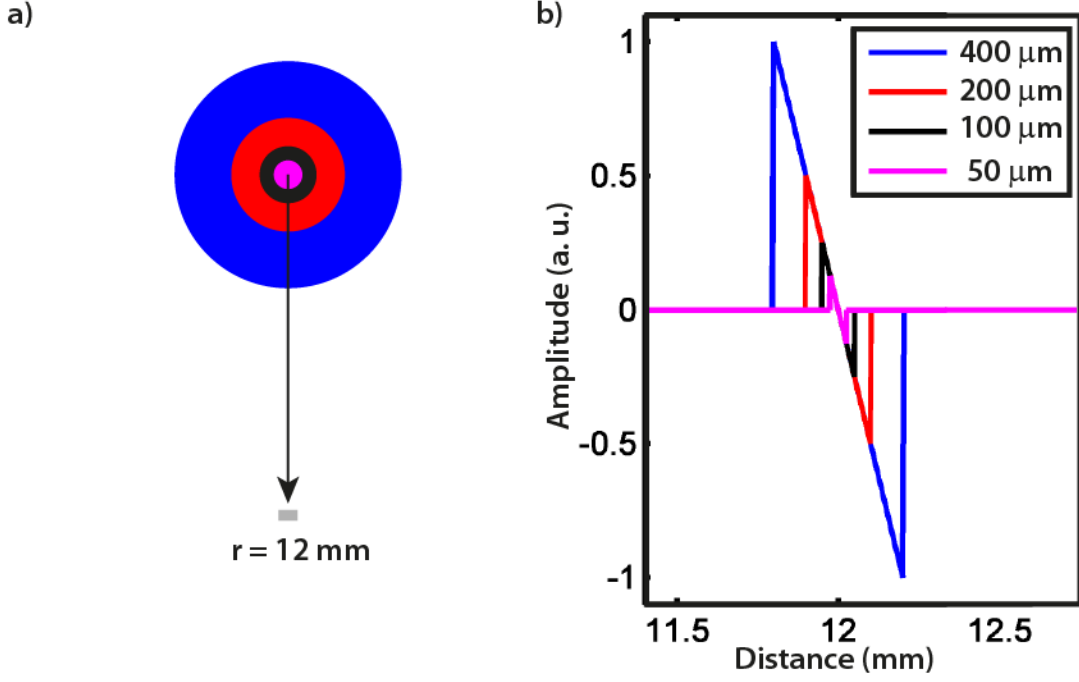
Figure 4: *a)* Relative location of the spheres and the point where the optoacoustic signal is calculated. *b)* Optoacoustic signals of the four microspheres at 12 mm, as per Eq. (2.8).

the sphere are assumed to be the same as those of the surrounding medium (water), so that there are no reflections of the optoacoustic wave at the sphere boundaries. The time-domain solution of Eq. (2.4) under these conditions yields the time-dependent optoacoustic field at a point r from the center of the sphere [5]:

$$p(r,t) = \frac{a\mu_a\Gamma\Phi}{2r}(1 - \hat{t})\Theta_{0,2}(\hat{t}) \ , \tag{2.11}$$

where $\hat{t}$ is a dimensionless retarded time expressed as:

$$\hat{t} = \frac{c}{a}\left(t - \frac{r - a}{c}\right) \ , \tag{2.12}$$

and $\Theta_{0,2}(\hat{t})$ is a boxcar function such that $\Theta_{0,2}(\hat{t}) = 1$ if $\hat{t} \in [0,2]$ and 0 otherwise. From Eq. (2.11), two important features of the optoacoustic signal can be observed. First, the amplitude of the signal is directly proportional to the size of the object, which is to be expected owing to the volume integral in Eq. (2.4). Second, the signal amplitude decays linearly with distance due to the spherical spreading of the optoacoustic wave.

Fig. 4 shows the signals resulting from Eq. (2.11) for several spheres of different radii, at a distance of $r = 12$ mm (from their centers). The speed of sound was set to $c = 1500$ m/s and the factor $\mu_a\Gamma\Phi/2 = 1$, as in this section we are interested only on the signal properties as a function of the object size.

We observe signal durations of $2a$ and the linearly dependent amplitude on the size. From these features, two consequences that are valid for all optoacoustic sources can be extracted. First, small objects emit characteristically weaker signals than larger objects, which may present a challenge in terms of resolving small absorbers close to larger absorbing structures. Second, small objects emit short signals, which require the use of high-frequency sensors in order to resolve them. The size and shape of the sources determine thus the spectrum of the optoacoustic signal, which leads us to the next section.

2.2.2 Frequency-domain characteristics

The emission frequency spectrum of absorbing spheres under uniform illumination can be found either from an analytical derivation or, more conveniently, by calculating the Fourier-transform of Eq. (2.11). The result is a somewhat complex expression [5], but interestingly it can be expressed as a function of a dimensionless frequency $\hat{q}$ defined as $\hat{q} = 2\pi f a/c$. As a consequence, it can be shown that the spectra for spheres of different sizes have always the same shape: a peak frequency at $\hat{q} \sim 2.5$ followed by harmonics of decaying amplitude. The peak frequency in physical units (Hz) is therefore determined by the size of the sphere.

Figs. 5a, 5b, 5d and 5e show the emission spectra for four absorbing spheres of diameters 400 μm, 200 μm, 100 μm and 50 μm respectively. The spectra are represented between 0 and 20 MHz and normalized to the amplitude at the peak frequency f_c of the largest sphere. As the spheres become smaller, there is a net shift of the spectra to higher frequencies and the amplitude at the peak frequency becomes lower.

Fig. 5c shows the dependence of the peak frequency with the size, which is approximately $f_c \sim 0.8c/2a$. It is worth noting that the peak frequency is therefore lower than the frequency corresponding to a wavelength $2a$. As a result, to assume that $f_c = c/2a$ is an overestimation of the optoacoustic peak frequency. This is of importance when assessing the sizes of absorbers present on a sample based on the measured optoacoustic spectrum.

Fig. 5f shows the dependency of the bandwidth B_w with the sphere size. The bandwidth is defined as the full-width at half-maximum (FWHM) around f_c. The figure shows that objects of small sizes emit not only signals at high frequencies but also with a broad spectrum. It can be also seen that the relative bandwidth, defined as $b_{wr} = B_w/f_c$, is independent of the sphere size, or $b_{wr} \sim 140\%$ for all sizes.
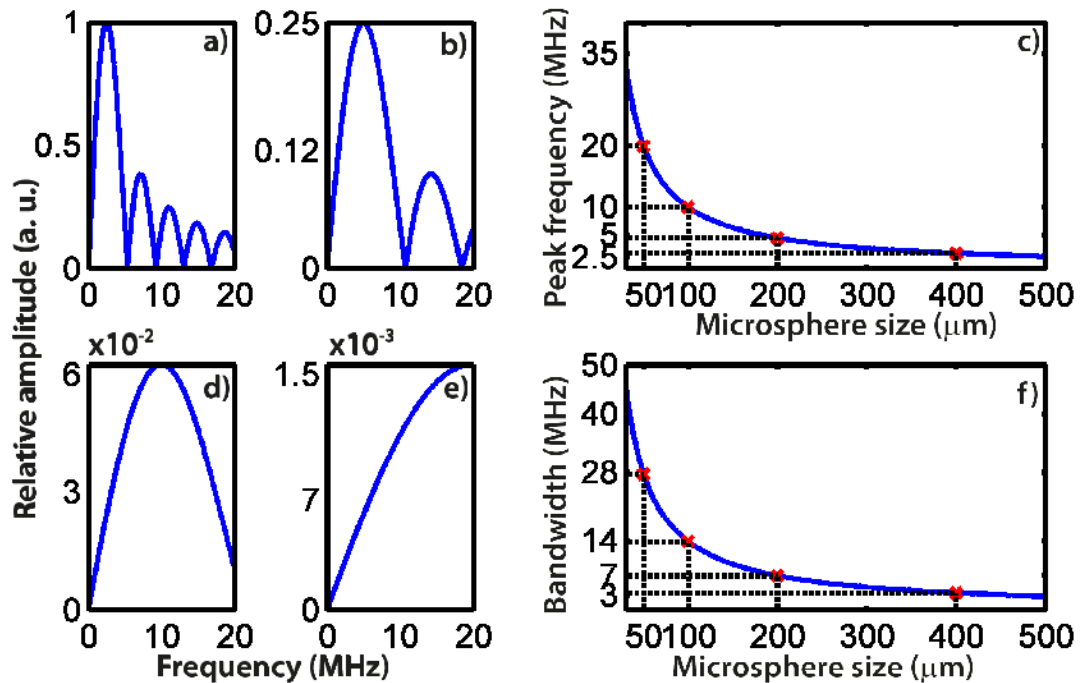
Figure 5: Size dependence of the frequency spectra of optoacoustic signals of absorbing spheres. *a)-b), d)-e)*, spectra of absorbing spheres with diameters 400, 200, 100 and 50 μm respectively. *c)* Peak emission frequency vs. object size. *f)* Emission bandwidth vs. object size. See text for details.

In conclusion, the amplitude of optoacoustic waves scales linearly with the size of the source and their spectra are broadband, with peak emission frequency and bandwidth inversely proportional to the source size. As a consequence, due to the continuum of absorber sizes within tissue, optoacoustic imaging is an inherently wideband modality, especially when compared with echographic ultrasound. This fact has consequences on the understanding of the optoacoustic measurement process and the relevant sensor properties, which are described in the following section and are the subject of Chapter 3.

2.3   Optoacoustic detection

There are several physical processes that can be exploited to measure a propagating ultrasonic wave [9], such as light interference and piezoelectricity. In the context of ultrasonic biomedical imaging in general and optoacoustics in particular, the most commonly used ultrasound sensors are piezoelectric transducers[*]. In this section, the piezoelectric effect is presented, followed by a general discussion on the properties of several piezoelectric materials. Afterwards, a description of the general characteristics of ultrasound sensors is provided.

---

[*] Throughout this work, the terms transducer, sensor and detector are used interchangeably. The term hydrophone is however reserved for calibrated, broadband ultrasound sensors used for the characterization of optoacoustic sources and ultrasound transducers, rather than for imaging applications.

2.3.1 The piezoelectric effect and relevant sensor materials

The direct piezoelectric effect arises in some nonmetallic materials as a deformation of their shape produces a net electric field inside the material [34]. The electric field originates a voltage difference that is proportional to the deformation of the material and that can be easily measured. Conversely, a voltage difference applied to a piezoelectric material results in a change of its shape that is proportional to the voltage, which is called reverse piezoelectric effect. The reverse piezoelectric effect is used for acoustic wave generation in conventional echographic ultrasound, whereas the direct piezoelectric effect is used for the measurement of acoustic waves both in ultrasound and optoacoustics.

There exist a large number of piezoelectric materials used for an equivalent variety of purposes. For ultrasonic applications, the materials can be divided into three major categories: ceramics, polymers, and piezo-composite materials, which consist on piezoelectric ceramics inside an electrically isolating polymer matrix [31].

Ceramics, of which Lead Zirconate Titanate (or PZT) is the most commonly used, offer in general a very good sensitivity but relatively narrow bandwidths, due to their stiffness [35]. They have densities of about 7.8 Kg/m^3 and a speed of sound of 4400 m/s, very different from those of water (1 Kg/m^3 and approximately 1500 m/s), which result in strong acoustic mismatch and therefore highly resonating modes of vibration. Therefore they need to be fitted with acoustic matching layers, which further reduce their attainable bandwidth. PZT-based transducers are widespread and relatively cheap, so that they prove versatile sensors for proof-of-principle studies [36] and have been successfully employed in first-generation optoacoustic setups [14].

Polyvinylidene Fluoride (or PVDF) is the most common of piezoelectric polymers. It exhibits acoustical properties close to those of water, with a density of 1.8 Kg/m^3 and speed of sound 2200 m/s. As a consequence, PVDF sensors do not need acoustic matching layers to operate in water and can be tuned to have a very wide frequency response. PVDF sensors are thus typically used as hydrophones for the characterization of the acoustic field generated by ultrasound transducers [35] and, in the context of optoacoustics, for the characterization of optoacoustic sources (cf. Chapter 3).

Piezo-composites combine the desirable characteristics of both PZT and PVDF. The polymer matrix (typically epoxy) provides some flexibility to the material, which results in an easier production of different sensor shapes in comparison to pure ceramics. Their bulk acoustic properties are strongly dependent on the ceramic-to-matrix ratio, but are in general closer to that of water, with densities of e.g. 4.8 Kg/m^3 and speed of sound 3780 m/s

26

[31]. On the other hand, the PZT component provides good sensitivity. Piezo-composite sensors can be also tuned to wider bandwidths than PZT-only transducers of similar geometry [31, 35] due to their better matching to water.

The exact details on design and construction of ultrasound sensors based on these materials are beyond the scope of the present work. Herein, a more phenomenological description of the transducer properties is used, based on their effect on optoacoustic signals rather than in terms of its components and design. This approach is justified because ultrasound transducers can be accurately described as linear systems. As such, the transducer effect on any optoacoustic signal can be deduced in terms of the sensor impulse response, without considering each transducer component individually [26, 31]. Furthermore, the impulse response can be obtained experimentally with minimal information on the underlying design parameters and provides all the transducer characteristics needed for imaging applications.

2.3.2 Definition of transducer characteristics

It has been shown that detection of an ultrasound wave can be described as a linear process occurring in two steps [26]: a spatially-dependent process, determined by the shape of the transducer, and a spatially independent one, determined by piezoelectric transduction. First, the wavefront of the propagating optoacoustic field may reach different points on the detector's surface at different time instants. As a result, the duration of the measured signal is longer than the duration of the original wave. This effect is modeled by the spatial impulse response (SIR) of the sensor and depends on its shape and the location where the signal is generated [26]. In the second step, the signal distorted by the SIR excites the piezoelectric material, which acts as a band-pass filter around its resonant frequency. This effect is modeled by the electrical impulse response (EIR) of the transducer and depends on the piezoelectric material characteristics, the acoustic matching layers and the electric channel behind the sensor [27].

The response of the transducer to any signal can be therefore described as a convolution, in time, of the signal waveform, the SIR and the EIR. This approach is demonstrated in Chapter 3 whereas a conceptual description of the EIR and the SIR independently is provided in the following.

2.3.3 The Electrical Impulse Response

The EIR describes the response of the sensor to an impulse excitation (i.e., a source with a constant frequency spectrum of infinite bandwidth), and is independent of the source location. It results from the properties of the piezoelectric material and the electronics
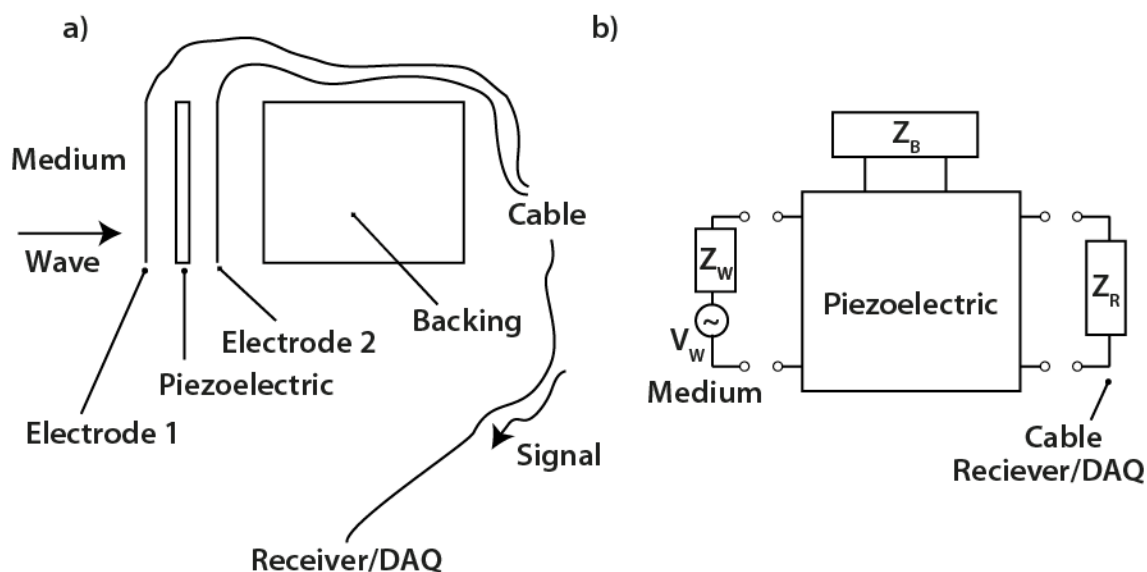
Figure 6: *a)* Schematic of a single-element piezoelectric transducer. *b)* Equivalent electromechanical circuit, based on the KLM model. See text for details

behind it. Some insight can be gained into the characteristics of the EIR by studying a simplified model of the detector and the corresponding electrical circuit.

Fig. 6a shows a sketch of a single-element ultrasound sensor: the piezoelectric element of thickness *d*, the electrodes, the acoustic backing, the cabling and the data acquisition system. For simplicity we have assumed that there is no acoustic matching layer, so that the medium to the left of the active element is water. The electrodes are considered infinitely thin, which is a valid assumption for most sensors; as a result, their effect on the acoustic wave can be neglected. We deal therefore with two acoustic interfaces: one between the medium and the piezoelectric element and another one between the latter and the acoustic backing. The backing provides acoustic matching at the other end of the piezoelectric and its thickness and material can be adjusted for damping the vibrations of the piezoelectric.

The arrangement shown in Fig. 6a can be described by a three-port network such as the Krimholtz, Leedom and Matthaei model, or KLM, where two ports describe the acoustic interfaces and the third port is comprised by the electrodes [34]. The KLM model is widely used for transducer design, as it provides a thorough description of the interdependence of the acoustic and electrical parameters.

Fig. 6b shows the electrical network describing the ultrasound transducer of Fig. 6a. The piezoelectric element is connected to the backing and the receiver electronics, represented as loads in terms of their electrical impedances Z_B and Z_R respectively, and to the medium which is represented as a voltage source V_W in series with an impedance Z_W.

28

The piezoelectric element has a speed of sound c_{pz} and can be understood as a resonator with a first harmonic given by the natural vibration frequency $f_r = c_{pz}/2d$. By tuning the receiver circuit and backing to operate at the transducer resonance, sensitivity at f_r is optimized at the expense of bandwidth. This can be achieved with the use of a highly mismatched backing, which enhances resonance. On the other hand, by using a matched absorbing backing, the piezoelectric is tuned far from resonance and a broader bandwidth can be achieved at the expense of reduced peak sensitivity [34].

As discussed in 2.2.2, optoacoustics is an inherently broadband imaging modality, and therefore wideband transducers are desirable. On the other hand, as the amplitude of optoacoustic sources scales with their size, transducers with extremely large bandwidths but low sensitivity are not practical. Therefore, a balance between the two has to be found.

In terms of characterization, the EIR can be obtained by exciting the transducer with a broadband source with known spectrum, which is subsequently corrected from the measured signal to yield the EIR. This method is further discussed in Chapter 3.

2.3.4   The Spatial Impulse Response

When the optoacoustic signal is detected by a single-element sensor of finite size, different points $\vec{r}_d$ on the surface S of the detector will intercept the optoacoustic field $p(\vec{r}_d, t)$ at different times. This is expressed mathematically as a spatial averaging of the optoacoustic field over the surface of the detector:

$$p_d(t) = \int_S p(\vec{r}_d, t)\, dS\,, \qquad (2.11)$$

The effect of the sensor surface on the propagating optoacoustic wave can be better understood by substituting Eq. (2.11) into Eq. (2.4) and rearranging the terms:

$$p_d(t) = \frac{\Gamma}{4\pi c^2}\frac{\partial}{\partial t}\left\{\int_\Omega H_r(\vec{r}')\left[\int_S \frac{\delta\left(t - \frac{|\vec{r}_d - \vec{r}'|}{c}\right)}{|\vec{r}_d - \vec{r}'|}\, d\vec{r}_d\right] d\vec{r}'\right\}. \qquad (2.12)$$

Eq. (2.14) describes the optoacoustic detection process as a sum of the optoacoustic signals arriving from different points $\vec{r}'$ of the object Ω, weighted and delayed by a factor (shown in square brackets) dependent on the relative geometry of sensor and source. Thus, for a point emitter located at $\vec{r}$, (see Fig. 7a) the detector yields a temporal response only dependent on its geometry:
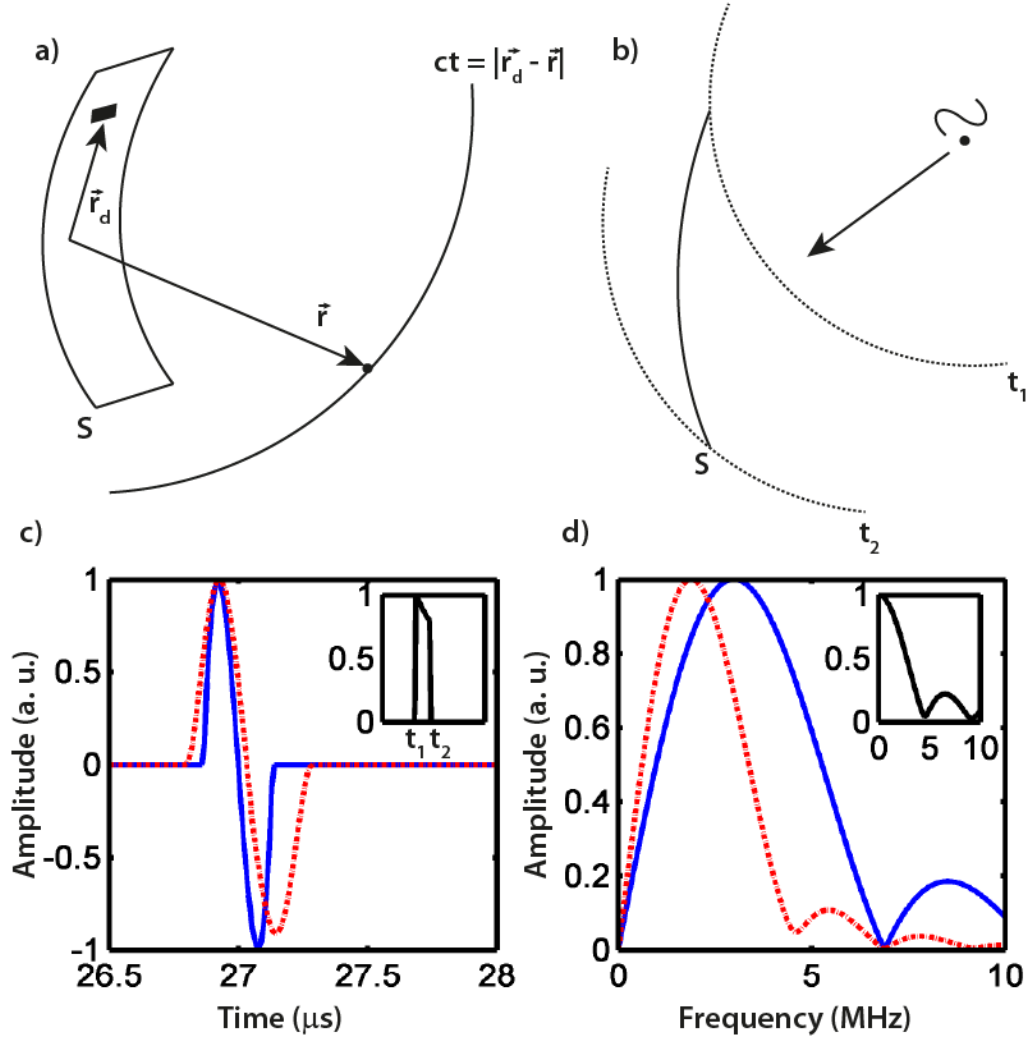
Figure 7 *a)* Geometry for the SIR definition. *b)* Illustration of the time broadening of ultrasound signals due to the surface of the transducers. t_1 represents the shortest time-of-flight between the surface of the sensor and source, and marks the starting time of the SIR and therefore the measured signal. t_2 represents the longest time-of-flight from the source to the sensor's surface and the time instant where the SIR ends. *c)* Simulated optoacoustic signal (blue/solid) and the distorted signal (red/dashed) that results after convolution with the SIR at a point out of focus. Inset: SIR used for convolution. *d)* Frequency spectra of the simulated signal (blue/solid) and of the signal convolved with the SIR (red/dashed). Inset: spectrum of the SIR. See text for details.

$$h(\vec{r}, t) = \int_S \frac{\delta\left(t - \frac{|\vec{r}_d - \vec{r}|}{c}\right)}{|\vec{r}_d - \vec{r}|} d\vec{r}_d \; . \tag{2.13}$$

Except for a constant scaling factor, Eq. (2.13) is known as the spatial impulse response (SIR) of the sensor, and is equivalent to a spatially-averaged Green's function of the optoacoustic field. It can be shown [26] that the SIR distortion on any propagating ultrasound wave can be modeled as a linear process. Such distortion can be thus represented as a temporal convolution of the waveform and the SIR.

Fig. 7b shows a side view of 7a, to illustrate the example of the distortion of an optoacoustic wave produced by the SIR of a sensor, assuming a flat EIR. The effect of the SIR

on the signal is shown in Fig. 7c. The effects on the signal spectrum are depicted in Fig. 7d. The signal is given by the analytical solution for a paraboloidal absorber [21] of 400 μm in diameter. The SIR (Eq. 2.13) is calculated with the software package FIELD II [37] for a cylindrically focused transducer. We can observe the general features of SIR distortion: the optoacoustic signal is no longer antisymmetric and it is stretched, changing notably its frequency spectrum as well. The SIR represents thus a spatially dependent low-pass filter on the optoacoustic signal.

Recalling the Green's function for the frequency-domain, shown in Eq. (2.6), the SIR definition may be rewritten for a monochromatic wave of angular frequency ω as [27]:

$$\hat{h}_\omega(\vec{r}) = \int_S \frac{e^{i\vec{k}\cdot(\vec{r}_d - \vec{r})}}{|\vec{r}_d - \vec{r}|} d\vec{r}_d \ . \tag{2.14}$$

From Eq. (2.14) the diffractive formulation of the acoustic field can be obtained by assuming that the detector behaves like a piston, i.e., that the acoustic waves displace the sensor only in a direction normal to *S.* This approximation is valid at MHz frequencies and for the materials and shapes of almost all ultrasound transducers used for nondestructive testing and ultrasound imaging [27]. Under the piston approximation, Eq. (2.14) is called the Rayleigh-Sommerfeld integral. It is also worth noting that, due to the reciprocity theorem, both Eqs. (2.13) and (2.14) describe not only how the acoustic wave intercepts the surface *S*, but also the wave that would be emitted by *S* if all its points were excited in phase. From the Rayleigh-Sommerfeld equation, the far-field and near-field regimes of diffraction can be obtained.

For some optoacoustic imaging applications, detection in the far-field can be assumed and the spatial properties of the transducer response do not distort the optoacoustic waves strongly. However, in some imaging scenarios it is desirable to use focused transducers located close to the object, as this optimizes signal-to-noise ratio and resolution. Conversely, operation at high acoustic frequencies with elements much smaller than the corresponding wavelength may not be possible, due to current limitations in transducer fabrication techniques. In both cases, the transducer may be considered to operate in the near-field and the distortions on the signal due to its spatial response may not be negligible.

In principle, the SIR of a sensor can be determined through Eqs. (2.13) or (2.14), either numerically or analytically. Experimentally, however, an direct determination of the SIR independently of the EIR is evidently impossible. Furthermore, the SIR represents the

response of the sensor's surface to an impulse excitation, i.e. to a source with infinite bandwidth. As a result, the EIR effectively determines the frequency band of the SIR which is relevant for the sensor spatial properties. For this reason, the SIR of a transducer is often described in terms of the sensitivity field at the central frequency of the sensor [31].

2.3.5 Sensitivity fields

The sensitivity field of a transducer represents the spatial variation in measured signal amplitude that is due only to the sensor characteristics and the position of the source with respect to the sensor. Due to the diffractive nature of acoustic waves, flat unfocused transducers are sensitive to signals originating mainly "in front" of them, as long as the sources are in the near field. Conversely, focused sensors are sensitive mainly to signals originating within a region around the geometrical focal point, which is called the focal zone. The dimensions of the focal zone are in general given by the transducer shape and the wave frequency.

In order to illustrate this important concept, the sensitivity field for a spherically focused transducer was calculated as per Eq. (2.16) with the method described in [27]*. The sensor was defined to have a focal distance of $F = 12$ mm and a diameter of $D = 12$ mm, as shown in Fig. 8a. Two fields were calculated, at 10 and 5 MHz, and they are shown in Figs. 8b and 8c respectively. The sensitivity fields exhibit a diffraction pattern similar to that of a convex optical lens, which have basically the same shape for both frequencies, except for a scaling factor.

The size of the focal zone along the y axis determines beam width at the relevant frequency, whereas the size along the x direction determines the depth of field. Fig. 8d shows the contour plot of the sensitivity field at 5 MHz, with the delimitation of the focal zone. Fig. 8e shows the cut of the fields along the y axis for both transducers, and Fig. 8f shows the cut along the x axis, clearly showing the frequency dependence of the size of the focal zone.

From the laws of diffraction, the beam-width can be expressed as:

$$\delta \approx \frac{Fc}{Df} = \lambda \frac{F}{D}, \tag{2.15}$$

and the length of the focal zone is $\zeta \sim 7\delta(F/D)^2$ [31]. This results in $\delta \approx 300$ μm at 5 MHz, and $\delta \approx 150$ μm at 10 MHz, which coincide approximately with the values in the simulation.

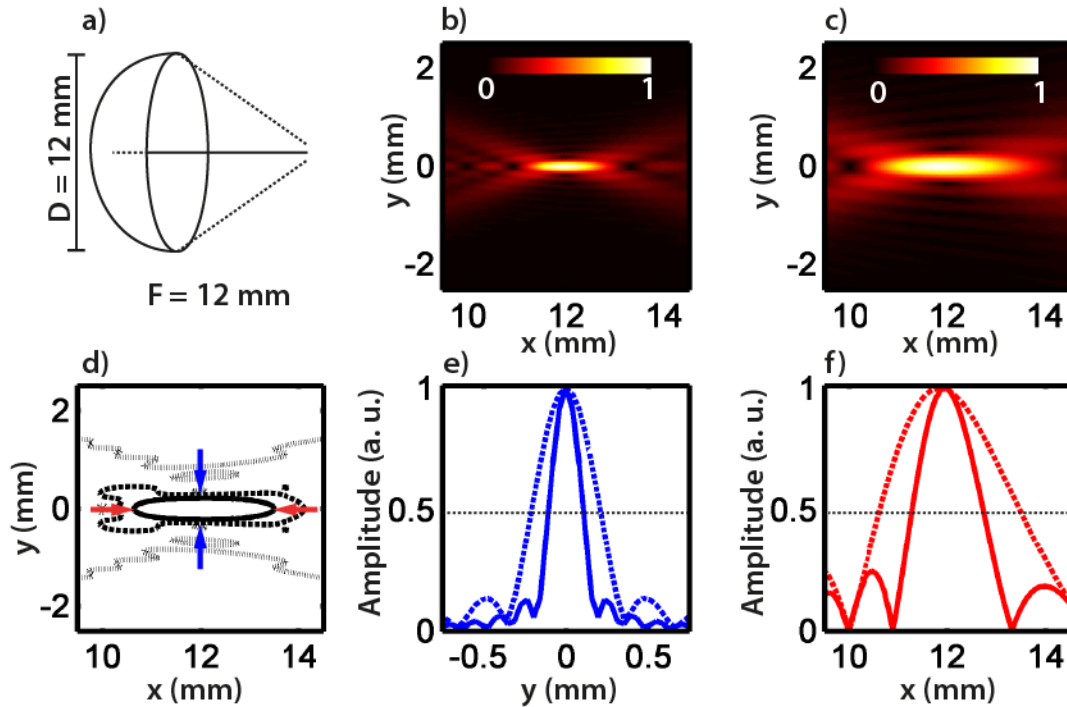* More details on the computation method can be found in Chapter 3.

Figure 8: *a)* Sketch of the transducer used for the illustration of the sensitivity fields.. The sensor is a concave (spherically focused) transducers with the dimensions specified. *b)* Numerically calculated sensitivity field at 10 MHz. *c)* Numerically calculated sensitivity field at 5 MHz. *d)* Contour lines of the 5 MHz sensitivity field at 0.5, 0.25 and 0.05 amplitude. The blue arrows delimit the beam width, the red arrows the length of the focal zone. *e)* Cut through the sensitivity field at the focus along *y* for both fields (5 MHz dashed, 10 MHz solid). *f)* Cut through the sensitivity field at the focus along *x* for both fields (5 MHz dashed, 10 MHz solid).

While useful as a rough estimate of the sensor properties, the sensitivity field at the central frequency is however a rather incomplete description of the sensor distortion of optoacoustic waves, as it completely ignores the phase and the broadband features of optoacoustic signals. This is further explored in Chapters 3 and 4.

2.3.6   Common transducer shapes

In order to understand the rationale behind the different detection geometries employed in optoacoustics, which are described in the next section, it is first necessary to have an overview of the most common transducer shapes. The SIRs and sensitivity fields resulting from the geometry of the sensor's surface determine the imaging performance and the range of applications of an optoacoustic setup with a set illumination. Although there exists a large variety of transducer shapes, the most common are: flat round, cylindrically focused and spherically focused sensor surfaces. All three transducer geometries were employed in the course of this work and are described briefly in the following.

a)   Flat round transducers

This shape is mostly used in calibrated hydrophones, with diameters ranging from 1 mm (Fig. 9a) down to 85 μm. The small size is a desirable characteristic intended to

minimize SIR distortions on the measurement of an acoustic field, as can be understood by examining the sensitivity field of a flat round sensor at two different frequencies (Figs. 9b and 9c). It is observed that, while the sensors are completely unfocused, the diffractive propagation of the acoustic waves produces a "natural focusing" of the acoustic field, with a local maximum at a distance from the sensor surface $z_R = a^2/\lambda = a^2 f/c$, where a is the sensor radius. In order to measure an acoustic field in the far-field regime of the sensor, either the distance between source and sensor them has to be greater than z_R or the sensor ought to have a small diameter. Since acoustic attenuation may also distort the propagating wave, it is thus necessary to minimize the distance between source and sensor and only a small sensor diameter can ensure (ideally) minimal SIR distortion.

Sensors of relatively large diameter (>1 mm) and low frequencies (<5 MHz) are used in non-destructive testing of materials, where a large penetration of the acoustic wave is desirable. In optoacoustics, they can be mounted in a translation stage to emulate a sensor array (cf. Chapter 3) and several of them in parallel have been used in some system prototypes that emphasize acquisition and display in real-time rather than image quality [38, 39].

b) Cylindrically focused transducers

As a first approximation, this sensor shape (Fig. 9d) enhances the amplitude of signals measured within a plane perpendicular to the focusing direction (Fig. 9e and 9f). However, diffraction effects result in a focal plane whose thickness is given by Eq. (2.15). In the axial direction, the length of the focal zone is also dependent on the frequency of the acoustic wave, in a manner similar to that of a spherically focused transducer (as shown in Fig. 8).

The contour of the sensor surface can be a flat stripe or a round surface. Focusing can then be achieved by two different methods. Bending the detection surface, as shown by the PVDF sensor in Fig. 9d (golden), is possible only with polymer and piezo-composite sensors, as ceramics are usually too brittle to allow reshape after fabrication. Alternatively an acoustic lens can be used, as shown by the PZT sensor in Fig. 9d (black surface). Acoustic lenses are made from a material with different acoustic properties than the propagating medium and the sensor surface. In practical terms, the materials for acoustic lenses are highly absorbing and provide an additional acoustic interface between medium and sensor, which in the case of polymer and piezo-composite surfaces is detrimental to the acoustic matching of the materials to water. For these reasons, pre-formed polymers and piezo-
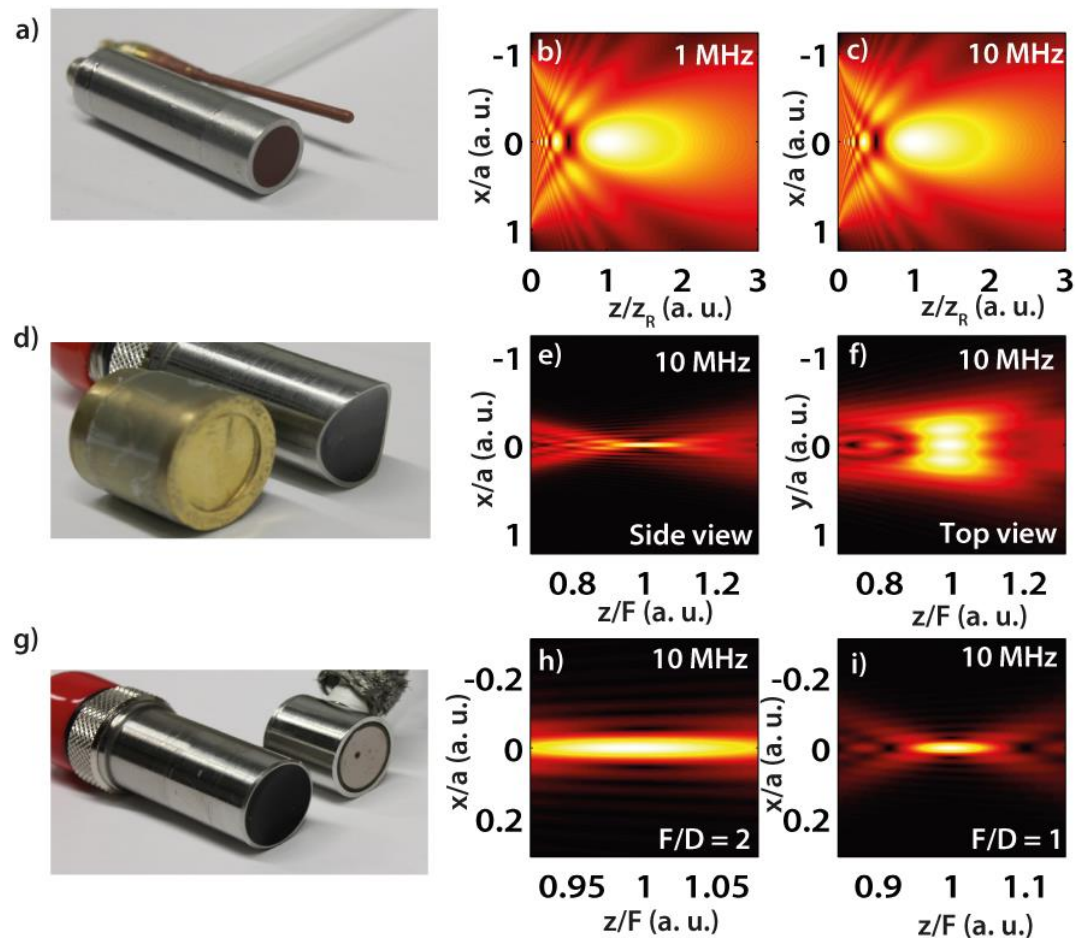
Figure 9: *a)* Two round, flat transducers: a Ø1mm PVDF hydrophone (right) and a Ø6mm PZT transducer (left). *b)* and *c)* sensitivity fields of a Ø13mm round flat transducer at the indicated frequencies. The vertical axis represents the lateral distance *x* normalized by the transducer radius *a*. The horizontal axis represents the axial distance to the transducer surface in terms of the near-field distance. The sensitivity field maximum finds itself thus at 2.8 mm for a 1 MHz frequency and at 28.3 mm for a 10 MHz frequency. *d)* Two cylindrically focused transducers: a Ø13mm, F = 25.4 mm round PZT transducer (right) and a PVDF sensor shaped as a bent stripe (left) with dimensions 1 mm x 13 mm, F = 40 mm. *e)* Side view of the sensitivity field of a round, cylindrically focused transducer (Ø13mm, F = 25.4 mm) at 10 MHz. *f)* Top view of the former. In both field depictions, the horizontal axis is normalized to the focal distance F and the vertical axis is normalized to the transducer radius *a*. *g)* Two round, spherically focused transducers: a Ø12mm, F = 12 mm, piezo-composite sensor (right) and a Ø13mm, F = 25.4 mm, PZT transducer (left). *h)* Sensitivity field of a Ø13mm, F = 25.4 mm, round spherically focused transducer at 10 MHz. *i)* Sensitivity field of a Ø13mm, F = 13 mm, round spherically focused transducer at 10 MHz. In both field depictions, the horizontal axis is normalized to the focal distance F and the vertical axis is normalized to the transducer radius *a*.

composite materials are preferred over PZT in second-generation optoacoustic systems that use cylindrically focused sensors or arrays thereof [11].

c) Spherically focused transducers

These sensors have a concave shape (Fig. 9g) that enhances sensitivity within a given region centered on the geometrical focal spot. As discussed in section 2.3.5 and shown in Fig. 8, the size of the focal zone is determined by diffraction laws, with the relevant parameters being the acoustic wavelength and the ratio of focal distance *F* to diameter *D*

(Eq. 2.15). The dependence of the focal zone characteristics as a function of the acoustic wavelength (or frequency) was illustrated in Fig. 8. Conversely, Figs. 9h and 9i show examples of the sensitivity fields for sensors of different F/D parameters (also called f-number) at the same frequency. These simulations further illustrate the tradeoff between lateral resolution and axial depth-of-field inherent to spherically focused transducers. These sensors are typically used in raster-scanning setups, as they provide good lateral resolution with a limited depth-of-field.

2.3.7 Review of optoacoustic imaging systems

In this section, the state-of-the-art in optoacoustic imaging systems is provided, to give the reader an overview of the most common image acquisition paradigms and modalities. The review is by no means exhaustive and it is rather intended to illuminate the various parameters to be considered in the design an optoacoustic system, such as the sensors' characteristics, their placement with respect to the sample (which we refer to as "measurement geometry") and the arrangement of the illumination. A more detailed overview of the different modalities can be found in the literature [8, 9, 40].

A common criterion to classify the range of optoacoustic imaging systems is the scale at which they operate: from whole-body, macroscopic imagers of small animals [11] (with a resolution >150 μm) down to microscopy of, e.g., subcutaneous vasculature (resolution <50 μm) [18]. An alternative classification can be done in terms of the measurement geometry: tomographic systems surround the sample with sensors, either by mechanically translating a sensor or by the use of transducer arrays, whereas scanned systems consist typically of a single, spherically focused sensor scanned in the two directions perpendicular to the sensor axis. On occasion, tomographic geometries are directly associated with macroscopic imaging modalities and scanned systems are considered as purely microscopic. However, there exist several examples in the literature where scanned systems have been operated at macroscopic scales [41, 42], and tomographic systems are under development for resolutions <100 μm, which rather qualifies as mesoscopic [43]. Therefore, the systems are described here in terms of the measurement geometries, as it represents a more general criterion than scale (or resolution).

a) Two-dimensional tomography

Early systems for two-dimensional optoacoustic tomography consisted of a single, cylindrically focused transducer which was rotated around the sample [13] (or viceversa [14]). The imaging plane is delimited by the focusing properties of the sensor. Translation along the axis perpendicular to the imaging plane is capable of producing a stack of images

that enable quasi three-dimensional visualization[44]. By the use of selective-plane illumination, whereby the laser beam is processed to a sheet of light coplanar with the focal plane of the transducer, sources can be considered to be generated within a limited region of the sample, which resulted in a more accurate delimitation of the imaging plane [22].

Second-generation systems have used an array of ultrasound sensors to avoid movement of either the sensor or the sample [11]. This in turn has accelerated the rate at which images can be acquired, opening the possibility of multispectral imaging within a reasonable timeframe [12] and the visualization of fast physiological processes [11]. Some systems also employ a "limited-view", i.e. less than a full ring of sensors (typically 180° or 240°) to allow a faster placement of the sample [11].

Both first- and second-generation systems were mainly developed for pre-clinical applications, i.e. the imaging of small animals. In the lower spectrum of acoustic frequencies (1 to 7 MHz), two-dimensional tomographic systems have achieved resolutions in the order of 200 μm in-plane and 800 μm in the vertical direction, in samples such as adult mice [45]. Therein, the sensors are typically focused at a distance between 40 mm up to 50 mm, and the radius of curvature of the tomographic surface corresponds to the focal distance. In the higher end of the spectrum (7 to 20 MHz), there have been reports of systems with mesoscopic imaging capabilities, with in-plane resolutions of 40 μm and 150 μm vertical resolution, in samples such as zebrafish [14] and baby mice [44]. In these cases, the radius of curvature of the detection surface and the focal distance of the sensors are typically at 25 mm or less.

While these systems have offered an excellent performance in applications such as functional imaging of the mouse brain [13] and pharmacokinetics [10], their capability as truly three-dimensional imagers through image stacking is contested. This is because the actual thickness of the imaging plane is fundamentally undefined for objects highly scattering to light, owing to the diffractive properties of the acoustic focusing and the inherently wideband spectrum of the optoacoustic signals (cf. Eq. 2.15). For this reason, several three-dimensional imaging systems have been developed.

b) Three-dimensional tomography

These systems aim to surround the sample spatially with a high number of sensors (in the order of several thousands). However, parallel acquisition of more than 1024 sensors results in high hardware expenses, and these systems either use a relatively low number of sensors ($<10^3$) or make use of a sensor array that is scanned (rotated) around the sample to

effectively form an enclosing surface, serializing the acquisition at each scanning (rotation) step.

In our group, a three-dimensional optoacoustic system with 256 sensors placed on the surface of an incomplete sphere has recently been reported to exhibit an isotropic resolution 800 μm at 4 MHz central frequency [46, 47]. In this case, the illumination is driven through the equator of the sphere (where no sensors are located) with the use of optical fibre-bundles. However, due to the relatively big size of the individual sensors (squares of 4 mm by 4 mm) and the relatively low curvature radius of the sphere (50 mm), diffraction effects limit the effective imaging volume to a cube of ~10 mm on the side.

An alternative includes using a sensor array in the shape of a sphere sector placed vertically, which is subsequently rotated to generate a sphere open only at the caps [15, 48]. These systems have been demonstrated for angiographic mammography applications [49] and whole-body small-animal imaging [15], with excellent contrast and isotropic resolutions in the order of 150 μm. The sensors operate typically at 4 MHz and have a size of 2 mm by 2 mm, and are placed at 50 mm of the center of rotation.

c) Scanned systems

In these systems, the sensors are raster-scanned in a plane outside the sample and do not offer a tomographic view, but rather a depth-resolved on-face view of the sample. There exist two major measurement paradigms in such systems: purely optical detection through interferometry and scanning of a piezoelectric, spherically focused sensor.

The purely optical systems consist of an interferometer, which is made of parallel transparent plates through which the illumination to generate the optoacoustic waves is passed onto the sample [50]. A second laser beam interrogates the optoacoustic field at the plates, one point at a time. By raster-scanning the interrogation beam, a virtual array of several thousand point-like (40 μm in diameter) sensors is generated over a surface ~1 cm on the side. The bandwidth of these sensors goes from several kHz up to tens of MHz. This system has been used for the imaging of angiogenesis in mouse models [51] and unborn mice embryos [52], with resolutions of 50 μm up to 5 mm deep in-tissue. The size of the interferometer plates defines the maximum scanning range and hence defines the angle subtended by the detection surface for a given depth (cf. Chapter 5), which results in a depth-dependent lateral resolution [50].

The piezoelectric systems typically make use of spherically focused sensors to define the lateral resolution via acoustic diffraction. Large area scans of internal organs have been

made at frequencies as low as 5 MHz for depths of up to 5 mm (up to 3 cm in phantoms)[42]. At high-frequencies (typically 50 MHz), dark-field-like illumination has made it possible to achieve resolutions in the order of 10 μm, at the expense of a very limited penetration depth, typically sufficient to image subcutaneous vasculature [18]. In Chapter 4, reconstruction methods that aim to expand the imaging depth of this imaging modalities are discussed.

2.4 Reconstruction algorithms in optoacoustic imaging

The aim of optoacoustic image reconstruction is to provide a visualization of the absorber distribution within the tissue. In practical terms, as was discussed in sections 2.1.1 and 2.1.2, optoacoustic sources generate signals proportional to the product of their absorption with the local optical fluence, which in turn determine the initial pressure amplitude as per $p_0(\vec{r}') = \Gamma\mu_a(\vec{r}')\Phi(\vec{r}')$. Therefore, the different image reconstruction algorithms used in optoacoustic imaging are developed to provide a solution to the following problem: given a set of optoacoustic signals $p(\vec{r}_i, t)$ measured at sensor positions $\vec{r}_i$, what was the initial pressure distribution $p_0(\vec{r}')$ in the object?

There exist two main categories of image reconstruction methods in optoacoustic imaging: analytical and algebraic algorithms, which are discussed in detail in sections 2.4.1 and 2.4.2 respectively. A brief overview of the two is given here as an introduction.

Briefly, analytical algorithms express the solution to the optoacoustic inverse problem as approximate formulas related to the spherical Radon transform. These algorithms can be either applied in the time or the frequency domain. Throughout this work, from all of the analytical methods in the literature, only the Back-projection method in the time-domain was considered [20], as it provides a first approximation to image formation without being computationally demanding. In Chapter 4 it will be shown that delay-and-sum algorithms, which are commonplace in conventional ultrasound [31], are closely related to the back-projection method, and they are therefore only briefly discussed within the context of their application.

On the other hand, algebraic algorithms express the forward problem as a linear operator acting on the sources within the image, which generates the optoacoustic signals. By providing the measured signals, the inverse problem is expressed as a linear system of equations with the initial pressure values as the unknowns. The system can be then solved with direct or iterative methods. In the present work, the Interpolated Model-Matrix Inversion (IMMI) in 2D and 3D were considered [21, 53], as they can be modified to include

the effect of the sensor response to achieve superior imaging performance over analytical methods.

It has to be noted that, since actual optoacoustic imaging takes place in real three-dimensional space, herein the expression "2D" is used in a loose sense. Whenever a "2D detection geometry" is discussed, the two-dimensionality implies that the sensors and the sources can be assumed to lie in the same plane, whereas the propagation of the wave takes always place in 3D. It is important to make such a distinction, because the solutions for the N-dimensional wave equation are in general functions with very different properties, depending N. As such, both the Back-projection and the IMMI methods discussed herein are based on a wave propagation described by the 3D Green's functions presented in section 2.1.3, even when dealing with "2D geometries".

2.4.1 Back-projection

The Back-projection method proposes an analytical solution of the optoacoustic inverse problem by back-propagating the measured signals to the imaging region of interest (ROI), which can be a plane or a volume [9]. The derivation of the solution assumes a ROI perfectly enclosed by the detection surface S, which is typically assumed to be a sphere, an infinite cylinder or an infinite plane for simplicity, but can have in general an arbitrary shape. The final form of the method can be expressed as:

$$p_0(\vec{r}') = \int_\Sigma \left[2p(\vec{r}_i, \bar{t}) - 2\bar{t} \frac{\partial p(\vec{r}_i, \bar{t})}{\partial \bar{t}} \right]\Bigg|_{\bar{t}=|\vec{r}'-\vec{r}_i|} \frac{d\Sigma_i}{\Sigma_i}. \qquad (2.16)$$

where $d\Sigma_i/\Sigma_i$ represents an effective angle weighting:

$$\frac{d\Sigma_i}{\Sigma_i} = \frac{dS_i}{|\vec{r}'-\vec{r}_i|^2} \frac{\hat{n}_i^s \cdot (\vec{r}'-\vec{r}_i)}{|\vec{r}'-\vec{r}_i|}. \qquad (2.17)$$

Algorithmically, Eq. (2.16) can be understood with the aid of Fig. 10a. For each sensor position $\vec{r}_i$ an individual sub-image (or sub-volume) is generated. Pixels (voxels) that are located at a distance $|\vec{r}'-\vec{r}_i|$ of the sensor are assigned a value that is equal to the signal measured at $t = |\vec{r}'-\vec{r}_i|/c$ minus its derivative. The sub-image is then weighted by the factor $d\Sigma_i/\Sigma_i$ which represents the solid angle subtended by the point $\vec{r}'$ at sensor position $\vec{r}_i$. The sub-images for every $\vec{r}_i$ are then added to produce the final image.

The Back-projection method has been extensively used in optoacoustic imaging [13, 14], and its performance has been assessed in a variety of geometries and against algebraic methods. Therefore, several interesting features and drawbacks are worth discussing.

40

First, it should be noted that in general $p(\vec{r_i}, \bar{t}) \ll \bar{t} \, \partial p(\vec{r_i}, \bar{t})/\partial \bar{t}$, and it is therefore a good approximation to reconstruct only with the time-derivative term. Since a derivative with respect to time implies a ramp filter in frequency-domain, Back-projection images typically show enhanced boundaries. As a consequence, low-frequency information in the signal, such as light diffusion, is not translated to the images. Additionally, image artifacts without physical meaning such as negative absorption values may appear, which limits the applicability of the method for quantitative imaging.

Second, since the solution is provided in closed form, there is no direct way of modifying the existing formula to take into account effects such as the response of the transducer or differences in speed of sound propagation within the ROI. In particular, the assumption that each sensor is a point-like detector with an infinite bandwidth results in degraded image quality, as will be explored in the following chapters.

2.4.2 Model-based 2D and 3D

The Interpolated-Model Matrix Inversion (IMMI) method in 2D and 3D has been developed in our group in the recent years as an alternative to analytic methods, with the aim of providing images faithful to the actual distribution of light deposition in tissue. The complete derivation of the model can be found in the works by A. Dima [54] and A. Rosenthal [21] for the 2D case and X.-L Déan-Ben for the 3D case [46]. While the exact calculation of the models is different for the 2D and 3D cases, their general structure and meaning are similar. Therefore, the following description is applicable to both cases, and they are referred to as "the model" in this section. Computationally, however, the hardware requirements are very different due to the size of the datasets involved, as is detailed in Chapters 4 and 5.

The model expresses the optoacoustic signals detected at each sensor position as a linear combination of the elementary absorbers (defined by the voxels) within the ROI, as follows:

$$p = Mu .$$

(2.18)

p is a row-vector representing the elementary optoacoustic signals measured by point-like detectors located at different positions. The signals originate at the voxels within the ROI, whose absorption values are given as the column-vector u.

The complete derivation of the model and its theoretical foundations can be found in the literature. However, in future chapters the IMMI algorithm will be modified and adapted to include the properties of the detector. Since that work is based on the properties and
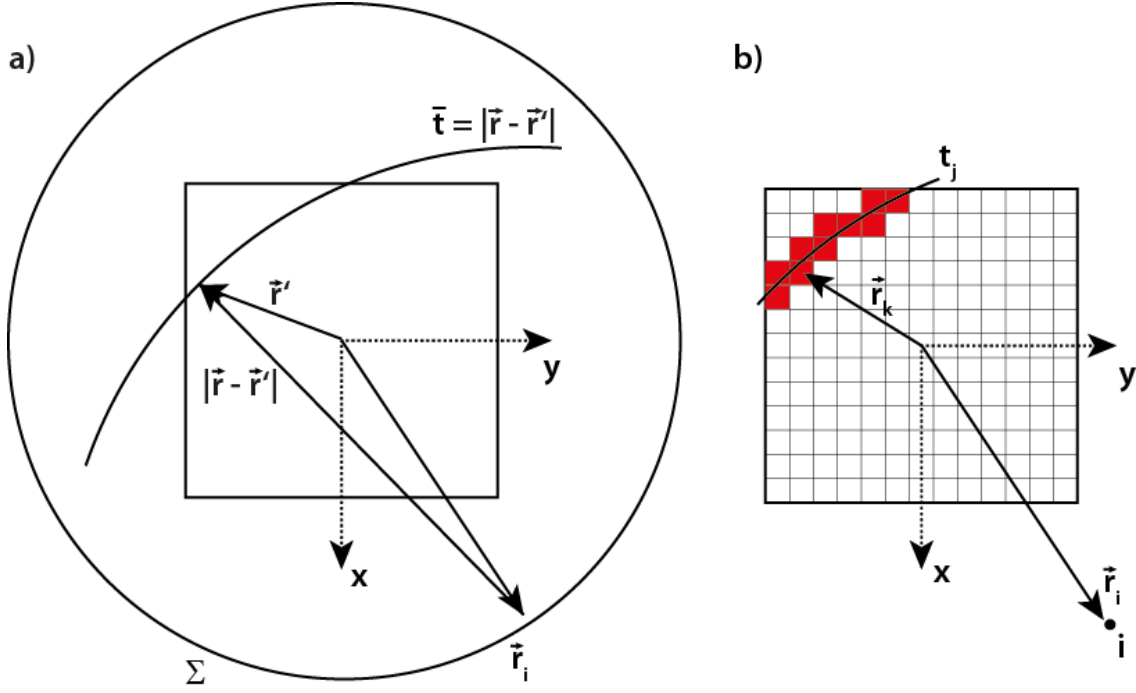
Figure 10: *a)* Geometry for the Back-projection method. *b)* Geometry for model-based methods.

symmetries of the model-matrix *M*, a more detailed overview of its structure is provided in the following.

The model-matrix *M* depends on the relative position between the sensors and the voxels. As a result, it has *N* columns corresponding to the total number of voxels, which we define as *n* by *n* in-plane, (and by n_z out-of-plane in the 3D case). The rows of the model-matrix have a total of $P \cdot T$ entries, where *P* is the number of sensor positions and *T* the number of samples of each signal.

Fig. 10b shows a top-view of the relative arrangement of the ROI and one sensor, to help describe the meaning of the matrix elements. The sensor *i* is located at $\vec{r}_i$ with respect to the center of the ROI. The voxels *k* are located at $\vec{r}_k$ and have an absorption value u_k. With these definitions, $M_{lk}u_k$ is the optoacoustic amplitude generated by voxel *k,* detected at position $\vec{r}_i$ at time *j*, where it holds that $l = j + (i-1) \cdot T$ for $j \in [1,T]$.

A vector $M_{lk}u_k$ can be generated with the amplitudes at different times *j* for one sensor position *i.* Such a vector can be understood as a time-dependent signal $p_{ik}(t)$ and can be expressed as [21]:

$$p_{ik}(t) = M_{lk}u_k \approx u_k \left[m_{lk} \frac{\delta(ct - |\vec{r}_i - \vec{r}_k|)}{|\vec{r}_i - \vec{r}_k|} \right].$$
(2.19)

42

Thus, the matrix elements M_{lk}, shown in brackets, are equal to the Green's function $G(\vec{r}_k, \vec{r}_i; t)$ between the sensor i and the source k, multiplied by a factor m_{lk} that depends on the underlying optoacoustic forward solution[*].

For a sensor i the amplitude of the elementary optoacoustic signal generated by the highlighted voxels in Fig. 10b and measured at a time t_j, can be expressed as:

$$p_i(t_j) = \sum_k M_{lk} u_k , \qquad\qquad (2.20)$$

where the summation takes place over the voxels intersected by the isochrone t_j and $l = j + (i - 1) \cdot T$. It is clear from this definition that $p_i(t_j)$ for all j between 1 and T is a vector representing the signal generated by all the voxels in the ROI, detected at sensor position $\vec{r}_i$. Eq. (2.20) expressed for all sensor positions i and all times j results therefore in Eq. (2.18).

Once the model-matrix has been computed, the image reconstruction is performed with a square error minimization such that:

$$\mathrm{u}_{sol} = \arg\min_u \|p - Mu\|^2. \qquad\qquad (2.21)$$

where $\|\cdot\|^2$ represents the ℓ_2 norm. The inversion can be performed with several methods such as the Moore-Penrose pseudo-inverse or the LSQR algorithm [21]. Herein, the LSQR algorithm was chosen, as it can be easily modified to include regularization procedures. The LSQR method is also less memory-intensive than other alternatives as the Singular Value Decomposition (SVD) or pseudo-inverse methods, since the most computationally demanding operation that it entails is a matrix-vector multiplication [55].

Model-based algorithms show superior performance over analytical techniques with respect to several measures. First, model-based methods do not enhance artificially high-frequencies, as opposed to the Back-projection method, and therefore model-based images can represent accurately slow-varying phenomena such as light diffusion [28]. Second, under optimal measurement conditions, model-based methods provide images without nonphysical artifacts such as negative absorption values [44]. Third and foremost, the characteristics of ultrasound transducers, and other linear phenomena such as acoustic

---

[*] The elements of the matrix are actually elementary optoacoustic signals and therefore bipolar. This fact was omitted for simplicity, but can be assumed to be included in the factor m_{lk} without loss of generality. This representation was chosen to better illustrate the combination of the model with the sensors' SIR in Chapters 4 and 5. The functional form of the matrix elements can be found in the cited literature.

mismatch [53], can be seamlessly implemented in the model, paving the way towards quantification.

Previously however, the characteristics of ultrasound transducers and their response to optoacoustic signals have to be assessed. This will enable us to provide an accurate description of the optoacoustic detection process that can be accounted for during image formation. The characterization and modeling of ultrasound sensors with optoacoustic methods is presented in the next chapter.

3. CHARACTERIZATION OF TRANSDUCERS

3.1 Motivation and objectives

It was discussed in the Introduction that, as a first approximation, most image reconstruction algorithms assume point detectors with infinite bandwidth, which may result in image artifacts and degraded reconstruction accuracy. In order to formulate more realistic reconstruction algorithms, the properties of ultrasound transducers need first to be studied and characterized in terms of their effect on optoacoustic signals. However, the existing calibration and characterization methods for ultrasound transducers are for the most part based on techniques used in conventional ultrasound, which may not be directly applicable to a sensor when used in optoacoustic imaging.

In ultrasound imaging and nondestructive testing, transducer properties are typically characterized with a pulse-echo technique, whereby the same sensor is used for both emission and reception of the acoustic field [27, 31]. Such a methodology is perfectly compatible with actual applications, which are for the most part based on the measurement of acoustic reflections. The pulse-echo technique results in signal amplitudes that are negligible outside the high sensitivity regions of the transducer field-of-view, as well as outside the detector bandwidth. In optoacoustic imaging, however, ultrasound sensors are used as passive detectors and the intrinsic amplitude of optoacoustic signals is determined by the illumination and the object properties. As a result, signals generated in the low sensitivity regions of the sensor field-of-view are typically strong enough to be measured and affect image formation. Furthermore, as discussed in the previous chapter, the amplitude and peak frequency of optoacoustic signals are inversely proportional to the source size. Therefore, signals with lower frequencies than the central frequency may also be detected.

The aim of this chapter is thus to provide an optoacoustic methodology for the characterization of ultrasound transducers. However, the methods proposed herein shall result in descriptions of the sensor properties that can be applied to image reconstruction for enhanced imaging performance. The purpose of the characterization methods is therefore different whether the electrical impulse response (EIR) or the spatial impulse response (SIR) are concerned. For one part, it will be shown that the EIR of the transducer can be measured accurately and with good signal-to-noise ratio (SNR) in most situations. As a result, the measured responses can be readily applied to image reconstruction without degrading the imaging performance. On the other part, an experimental determination of the spatial properties of the sensor with optimal SNR is difficult to achieve, for reasons that

are explored in the following sections. Therefore, in the context of the spatial response the goal is to provide experimentally validated numerical models of the sensor properties.

This chapter is structured in three self-contained parts. First, the measurement of the EIR with optoacoustic methods is discussed, building upon the work by A. Rosenthal et al. [36]. Afterwards, the modeling of the sensitivity fields at single frequencies is presented. Finally, the total impulse response of the transducer, which combines the EIR and SIR for all frequencies, is introduced and its capability to describe de optoacoustic detection process is assessed.

3.2 Characterization of the Electrical Impulse Response

The EIR of a transducer arises from the properties of the piezoelectric, the passive acoustic components (i.e., the matching layers and the backing), the tuning circuits and the electric transmission channel up to and including the acquisition system [27]. Thus, as a linear system, the EIR of the sensor can be obtained as the response to a wideband source, ideally a Dirac-delta in the time domain. One possible method for the EIR characterization is the generation of a short monopolar optoacoustic source, which is referred herein as "direct method", as it yields the EIR directly. An alternative is to excite the transducer with a signal of known frequency spectrum, which is then corrected for. This method is referred to as "indirect". Both methods were cross-validated in [36], yielding equivalent and reproducible results. However, the methods make use of optoacoustic sources generated in agar-ink phantoms, which are fragile and whose optical properties typically degrade after a few days. As a result, every time a transducer is to be characterized, a new set of phantoms has to be built, which is unpractical.

The objectives of this section are: first, to provide and characterize robust sources for the reproducible calibration of ultrasound sensors. Second, to assess the performance and limitations of the indirect method with the source selected. Finally, to present a solution for said limitations and discuss the applicability of the method for the calibration of arbitrary sensors.

3.2.1 The indirect method

The complete derivation of the indirect method can be found in the cited literature [36], but a short overview of the basic principle is provided herein.

The indirect method uses the signal of a point-like absorber as a reference. By substituting $H_r(\vec{r}') = \delta(\vec{r}')$ in the optoacoustic forward solution (Eq. (2.4)), it follows that the signal of a point-like absorber is equivalent to the derivative of a Dirac-delta in the time
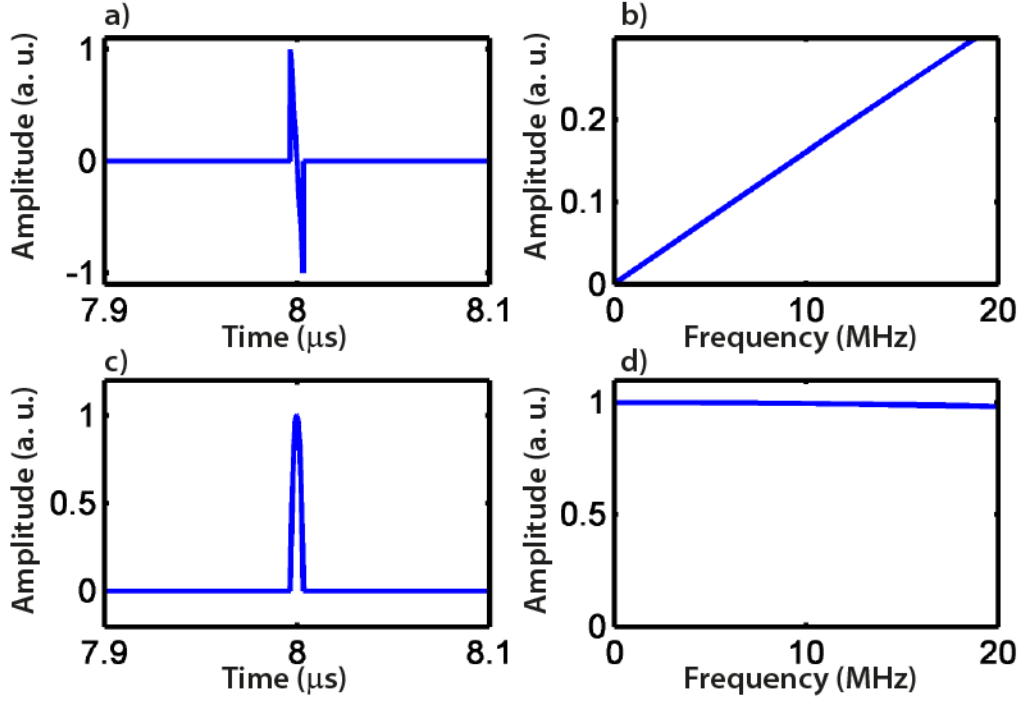
Figure 11: The indirect method for the EIR determination. *a)* Signal of a sphere 10 μm in diameter. *b)* Corresponding frequency spectrum 0 and 20 MHz, normalized to the amplitude at the peak emission frequency (100 MHz). *c)* Integrated signal as per Eq. (3.2). *d)* Corresponding frequency spectrum. See text for details.

domain. If the acoustic wave excites the surface of the sensor simultaneously, the measured signal $s(t)$ can be expressed as:

$$s(t) \approx \frac{\partial i_r(t)}{\partial t},$$

(3.1)

where $i_r(t)$ represents the EIR of the sensor. Thus, in order to correct for the spectrum of the source, the measured signal is numerically integrated over time:

$$i_r(t) = \int_0^t s(t')dt'.$$

(3.2)

The principle is illustrated in Fig. 11. The signal from a small optoacoustic source of 10 μm in diameter is shown in Fig. 11a, after Eq. (2.9). Fig. 11b shows the corresponding frequency spectrum, which can be approximately considered as a straight line for frequencies lower than the peak emission frequency of the source (100 MHz in this case). Fig. 11c shows the resulting signal after integration, which is monopolar. Fig. 11d shows the corresponding frequency spectrum, which is effectively flat within the frequency band shown. From this description it follows that any source whose spectrum can be considered linear up to a given frequency can be used for EIR determination.

The question is therefore how to generate such an optoacoustic source.
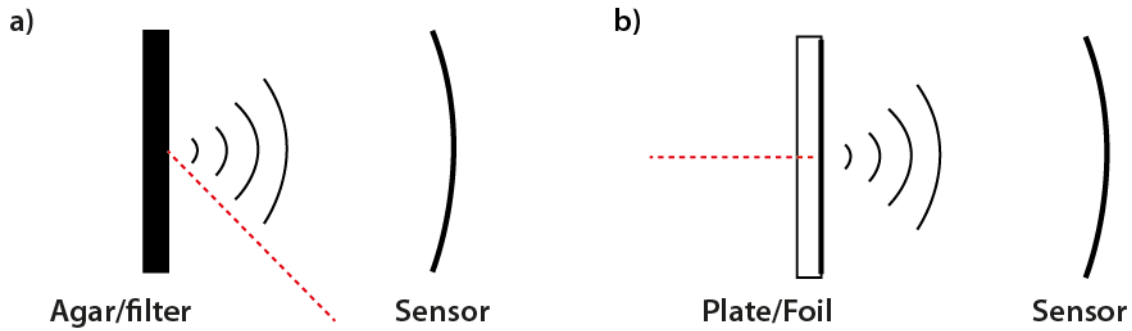
47

Figure 12: *a)* Generation of point-like sources for EIR measurement with thick, highly absorbing targets. *b)* Alternative setup with thin absorbing targets.

3.2.2 Source generation

It was shown in [3] that absorbing microspheres emit with a frequency spectrum that is in principle linear up to relatively high frequencies. However, due to difficulties in achieving completely uniform illumination and to their intrinsically weak signals, it was demonstrated that microspheres do not provide repeatable sources for EIR calibration.

In [3], the source for the indirect method was generated by illuminating the surface of an absorbing agar block, which we refer to as "the target". Fig. 12a shows a sketch of the relative arrangement between target, illumination and detector. For focused transducers, the source was placed at the focal point in order to achieve uniform acoustic excitation on the transducer surface. Laterally, a small source was achieved by limiting the laser beam to a size smaller than the focal width of the transducer. In the direction normal to the target, the high optical absorption of the phantom ensures a very localized absorption, and thus a point-like source.

Herein it is proposed that point-like optoacoustic sources can be generated with targets other than an agar block, by slightly modifying the illumination setup, as shown in Fig. 12b. Specifically, it is proposed that with alternative targets and illumination, sources with small lateral sizes and a broad frequency spectrum can be generated.

A substitute for the agar phantoms must fulfill several criteria. First, it should be as acoustically matched to water as possible, in order to avoid strong reflections at the object/water boundary where the signal is generated. Second, it should be stable enough so that its properties, optical or otherwise, do not change when submersed in water or illuminated with a strong laser beam, and can be therefore reused in several measurement sessions. Third, it should be highly absorbing –black to all effects, in order to provide strong acoustic signals even at low frequencies.

Herein, three candidates where considered: neutral density filters, black plastic foil and a spray-painted PMMA plate. They are discussed in the following section.
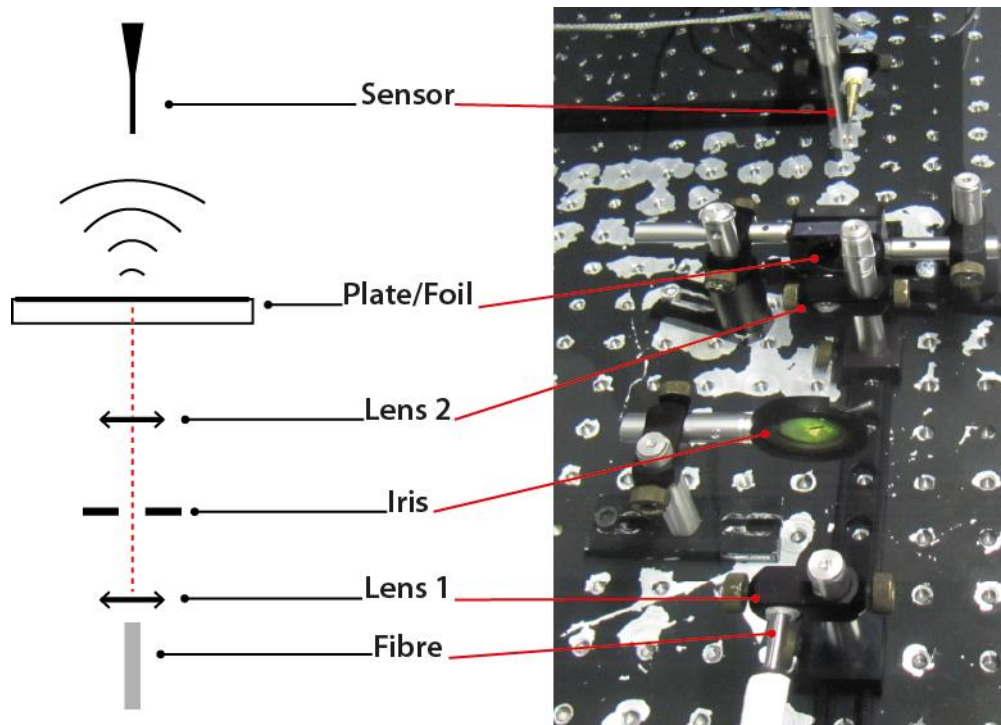
Figure 13: Setup for the characterization of the target candidates for EIR measurements. See text for details.

3.2.3 Experimental techniques

The three candidates and the agar block were used as targets for signal generation and compared to one another. Herein, a description of the targets, the measurement setup and the sensors used for characterization is provided.

A sketch and a picture of the experimental setup can be seen in Fig. 13. The setup consisted on three main parts: the optical bench, the target for signal generation and the detector plus acquisition system. The measurements were taken inside a tank filled with deionized water.

a) Illumination

The excitation was provided by a tunable optical parametric oscillator laser (Opotek Inc., Carlsbad, California), with a pulse width of 6 ns and a repetition rate of 10 Hz. The illumination was coupled through a fiber bundle (CeramOptec GmbH, Bonn, Germany) at a wavelength of 700 nm. Only one of the four bundle arms was used.

A sketch and picture of the underwater optical bench can be seen in Fig. 13. The output of the fiber was coupled to a custom-made semi-convex lens to produce an beam slightly less divergent than at the fiber output. The beam width was limited by an iris aperture and subsequently coupled to a second lens with the same characteristics of the first one, which then focused the light to the target.

b) Targets for signal generation

The neutral density filters (custom cut, NG-9 glass type, Schott AG, Mainz, Germany) were chosen for their low optical transmission coefficient $\tau = 2.5\%$ and acoustical properties close to water (when compared to similar filters): $\rho = 2.45$ Kg/m^3 and $c = 3900$ m/s. They are mechanically resistant and specifically designed to withstand illumination with laser beams.

The black plastic foil (from a garbage bag, Swirl, Melitta Haushaltsprodukte GmbH & Co. KG, Minden, Germany) was chosen for its opacity. Additionally, such foils are manufactured with controlled thickness on the tenths of micrometers, which avoids internal reflections that could corrupt the signal of interest. Their acoustical properties are thus not relevant. The foils resisted the illumination with the laser used in experiments.

The spray-painted PMMA plate (in stock at our institute) was used for the generation of reference acoustic signals in [7]. The signals thus generated were of high amplitude and wideband, but it remained to be tested if they are usable for EIR determination. PMMA has acoustical properties close to water: $\rho = 1.17$ Kg/m^3 and $c = 2800$ m/s, and is a durable material. The paint film was however very sensitive to the laser used for signal generation, being ablated even when the laser output was set to a fraction of its maximum power. To avoid ablation of the paint, a 6 OD neutral density filter was added to the optical bench, between the first lens and the iris.

Finally, the black-agar phantom was fabricated by diluting 1 g of agar powder in 100 mL of pure black India ink. The mixture was heated without letting it boil, poured in a phantom mold and left to harden. The resulting phantom was assumed to have acoustic properties close to those of water and an absorption coefficient of 100 mm^{-1}.

c) Sensor and acquisition system

The sensor was a custom-made PVDF hydrophone, 1 mm in diameter and calibrated by the manufacturer from 1 to 20 MHz (Precision Acoustics, Dorset, United Kingdom). Its frequency response can be assumed flat to within 10% from 1 to 10 MHz. The sensor was mounted on a 3-axis translation system, to find the optimal measurement spot (Thorlabs GmbH, Karlsfeld, Germany).

After all four candidates were tested in terms of their bandwidth, the lateral size and frequency content of the definitive source were measured by a high frequency transducer. The detector was a spherically focused transducer with F = 12 mm and D = 12 mm, specified
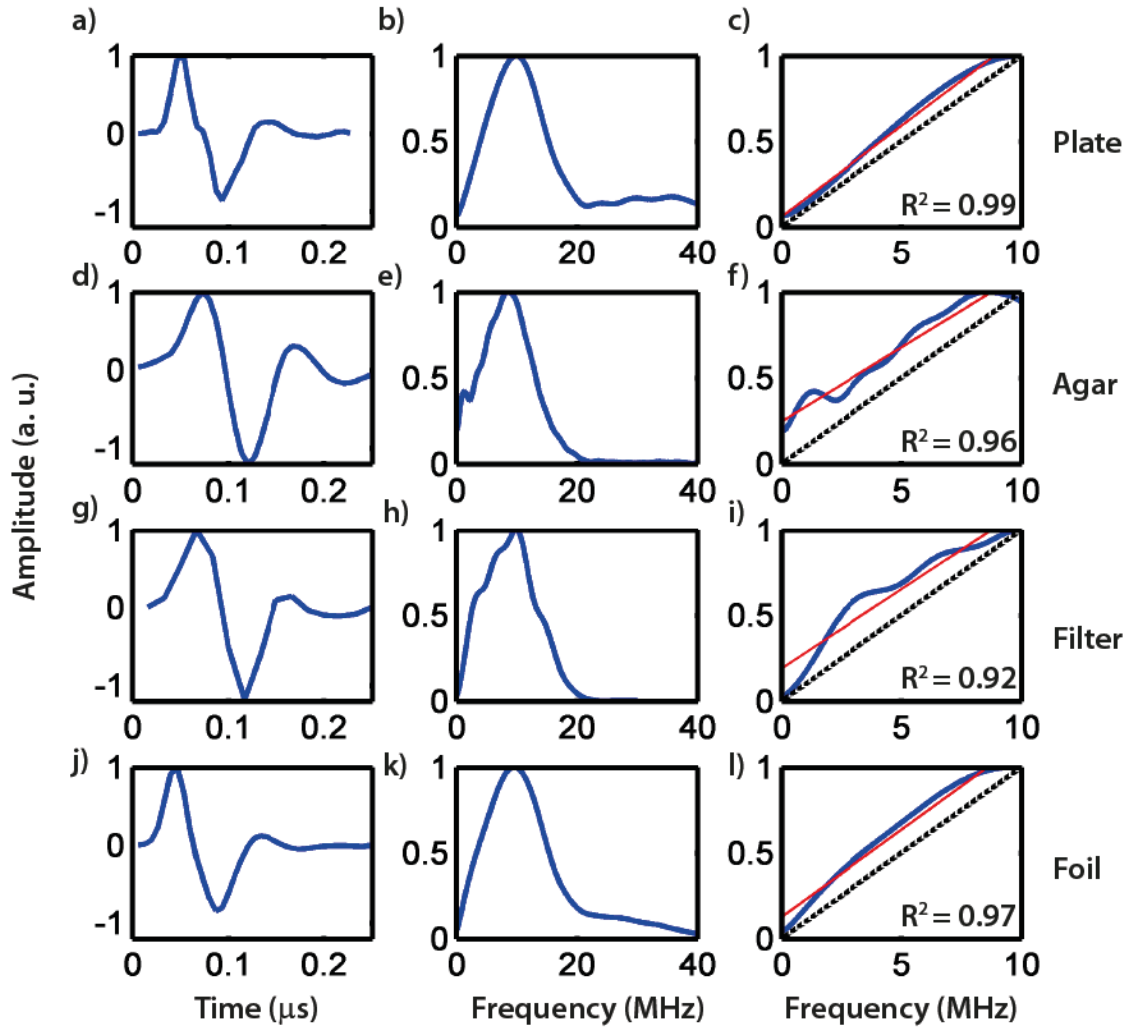
50

Figure 14: Comparison of the signal (*left column*) and spectra (*middle column*) of the sources generated at the different target candidates. The *right column* shows the spectra between 0 and 10 MHz (blue) with the results to a linear fit (red) and the goodness-of-fit R^2. The spectrum of an ideal point source (black dashed) is shown for reference. See text for details.

central frequency of 25 MHz and over 100% pulse-echo -6dB bandwidth (InSensor®, Kvistgaard, Denmark).

The signals were acquired by a 14-bit, 250 MS/s data-acquisition board (Spectrum GmbH, Grosshansdorf, Germany) and high-pass filtered at 50 kHz for low-frequency noise removal. Electronic noise was minimized by averaging the signals for typically 2000 shots.

3.2.4 Results 1: comparison of different sources

The sources generated at the four different targets were measured and the resulting signals and spectra are shown in Fig 14. The results show that all sources emitted a broadband signal with a peak frequency at 10 MHz. Furthermore, the plate source emitted at higher frequencies than 20 MHz. However, due to the limited bandwidth of the detector, it
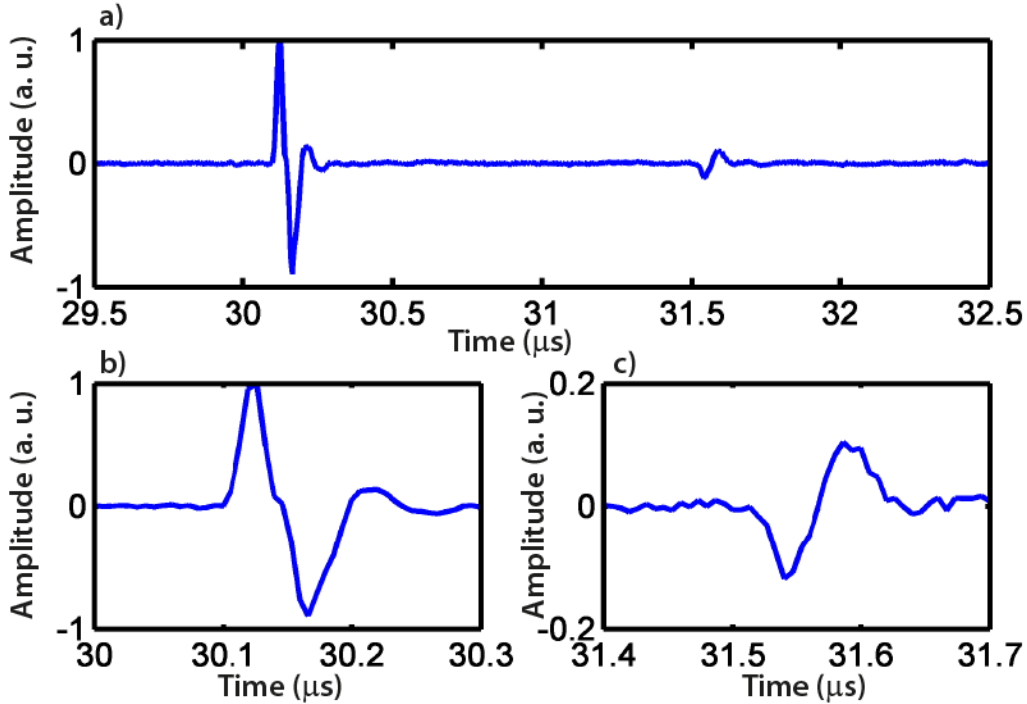
Figure 15: *a)* Raw signal from the source on the PMMA plate as measured with the hydrophone. The high amplitude signal, shown in *b)*, is generated by the source and the weaker signal, detailed in *c)*, corresponds to the reflection at the PMMA/water boundary. Note the inverted polarity of *c)* with respect to *b)*.

could not be determined whether the relatively low amplitude at high frequencies was due to the sensor response or to a property of the signals.

For the determination of the EIR it is necessary that the source spectrum vanishes at 0 MHz and that it is linear up to the peak emission frequency. In order to assess which source fulfilled such conditions, all spectra were fitted to a straight line of the form $A = af + b$ from 0 to 10 MHz. The results are shown in the rightmost column of Fig. 14. The source on the spray-painted PMMA plate (first row) provided the best fit as well as the smallest DC component b, thus approximating a point source optimally.

The source created on the spray-painted PMMA plate was therefore chosen as the source for EIR characterization up to frequencies of 10 MHz.

3.2.5 Results 2: properties of the spray-painted PMMA source[*]

The source was characterized with respect to three measures. First, it was assessed if the acoustic mismatch between PMMA and water may affect the measured signals. Second, the frequency spectrum of the source was analyzed for frequencies higher than 10 MHz with a different sensor. Finally, the lateral size of the source was determined with optoacoustic methods.

---

[*] The results in this section were obtained in cooperation with J. Gâteau.
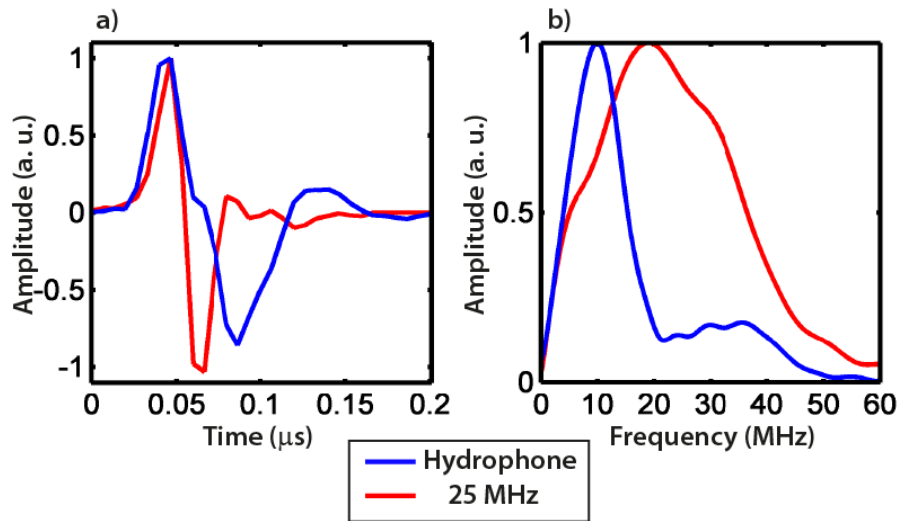
Figure 16: *a)* Signal of the source created at the PMMA plate as measured by the hydrophone (blue) and the 25 MHz transducer (red) normalized to their respective maxima. *b)* Spectra of the measured signals. The hydrophone spectrum peaks at 10 MHz with a 10 MHz bandwidth, whereas the 25 MHz transducer signal peaks at 20 MHz with approximately 30 MHz bandwidth. See text for details.

Due to the acoustic mismatch between PMMA and water, the signal originated at the plate may be reflected inside the plate and measured by the sensor. This may pose a problem if the plate thickness is small compared with the axial resolution of the sensor. However, based on the dimensions of the plate (1.98 mm thick) and the speed of sound in PMMA (2800 m/s), the separation between signal and reflection corresponds to a frequency of 70 kHz. Therefore, the possibility the signal of interest being corrupted by the reflection is ruled out for the majority of the transducers used in optoacustics. An experimental confirmation of this hypothesis is shown in Fig. 15, which depicts the raw signal measured by the hydrophone, showing a clear separation between the signal and the reflection.

In order to characterize the frequency content of the signal above 10 MHz, where the hydrophone response degrades, the plate signal was measured with the 25 MHz transducer. It has to be noted that, since a calibration of the 25 MHz transducer is not available, such a comparison is only meant to provide a qualitative description of the source spectrum. Fig. 16a shows the signal measured by the transducer and the hydrophone and Fig. 16b shows the corresponding frequency spectra. The spectrum measured with the hydrophone had a peak response at 10 MHz, with a -6 dB bandwidth of 10 MHz. The spectrum measured by the transducer had a peak at 20 MHz and a -6 dB bandwidth of 30 MHz. The results demonstrate that the source has a broad frequency spectrum which is distorted by the hydrophone response at high frequencies. However, due to the lack of calibrated reference hydrophones
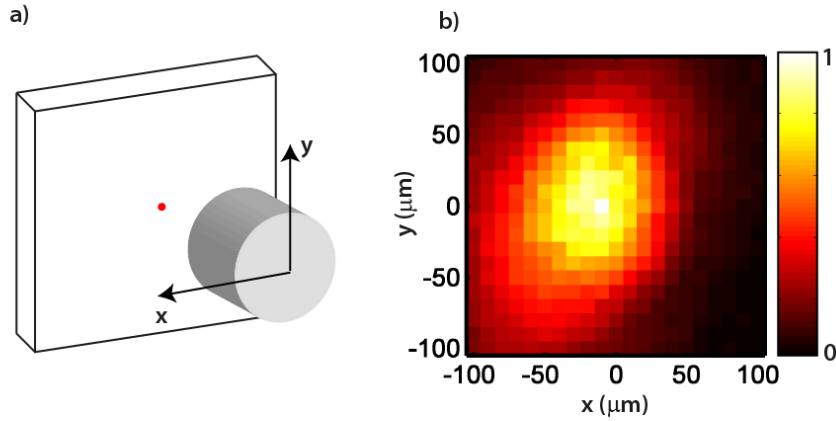
Figure 17: *a)* Sketch of the scanning geometry for the characterization of the source size. *b)* Maximum intensity projection of the resulting scan. The color bar represents a linear amplitude scale. See text for details

above 20 MHz, it could not be decided whether the source is suited for the EIR characterization of transducers with center frequencies above 15 MHz.

Finally, the lateral dimensions of the source were assessed by laterally scanning the 25 MHz transducer as shown in Fig. 17a. The sensor was scanned in a grid of 200 μm by 200 μm centered on the source, with a step size of 10 μm. By representing a maximum amplitude projection (MAP) of the scan from 5 to 45 MHz (Fig. 17b), an image of the source can be obtained. The size of the source can be estimated as the full-width at half-maximum of the MAP.

However, since the transducer has a frequency-dependent lateral resolution δ, given by Eq. (2.15), the actual source diameter a may be overestimated. In order to assess the size of the source independently from the transducer resolution, it was assumed that the measured source size b can be expressed as:

$$b(f) \approx \delta(f) + a = \frac{Fc}{Df} + a. \tag{3.3}$$

Therefore, by computing b for MAPs at different frequencies, a can be found as $a = \lim_{f \to \infty} b$. In practical terms, however, the frequency responses of the transducer and the source are finite. As a result, in the limit of very high frequencies no shape can be recognized in the MAP due to noise. For this reason, the MAPs were calculated for frequencies up to 48 MHz.

Fig. 18 shows four examples of the MAPs at different frequencies. While the change of the spot size from 15 to 25 MHz (Figs. 18a to 18b) is obvious, the images at 35 and 45
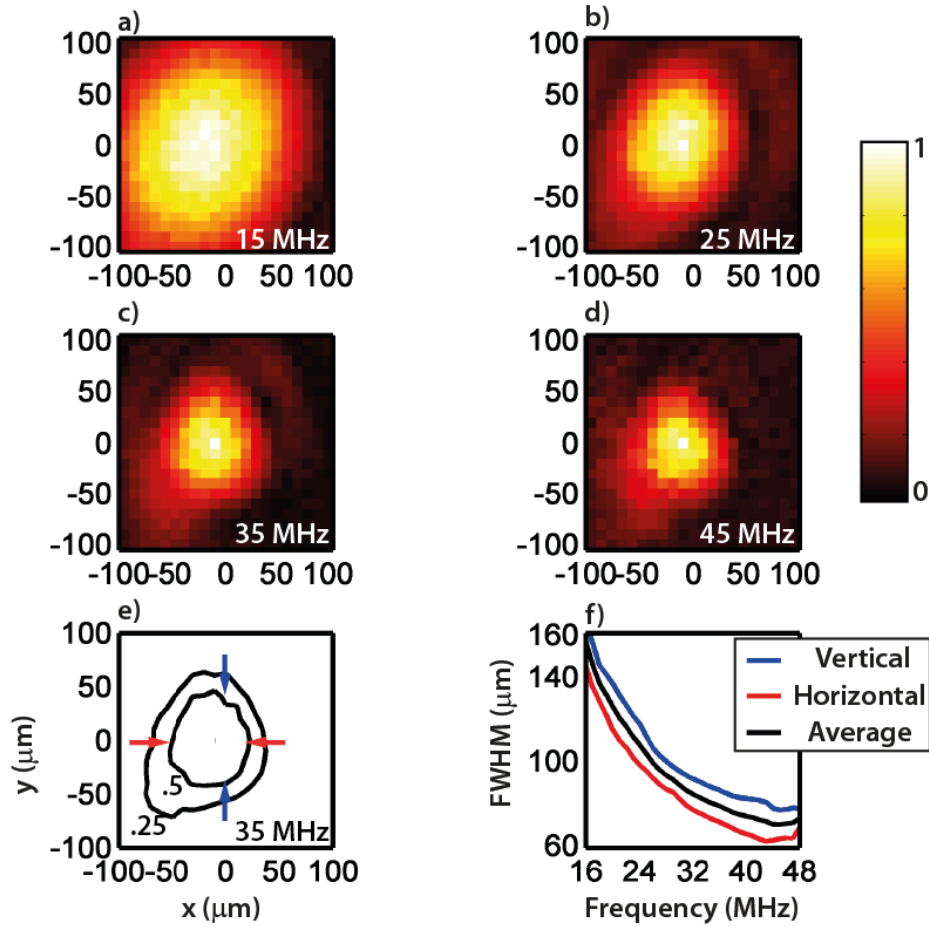
54

Figure 18: *a) –d)* MAPs of the scanned plate source for the frequencies indicated. Each image its normalized to its maximum. *e)* Contours of the MAP at 35 MHz. The blue and red arrows indicate where the FWHMs are measured at each frequency. *f)* FWHM as a function of the frequency. See text for details.

MHz (Figs. 18c to 18d) are almost identical. The rate of change in the MAP shape shows that $b(f)$ indeed reaches an asymptote at high frequencies.

In order to provide an upper limit for a, the FWHM of the spots where calculated for both axis, as shown in Fig. 18e. In Fig. 18f, $b(f)$ is plotted versus the frequency for the FWHMs along the x direction, the y direction and the average of the two. The average reaches a plateau at around 70 μm which, considering that $\delta(48 \text{ MHz}) \approx 31$ μm results in a source size $a \leq 40$ μm.

The source on the spray-painted PMMA plate was therefore assumed a point source for frequencies up to 15 MHz and for focused transducers with a beam width $\delta \geq 2a$. The source was subsequently used for the EIR calibration of different transducers.
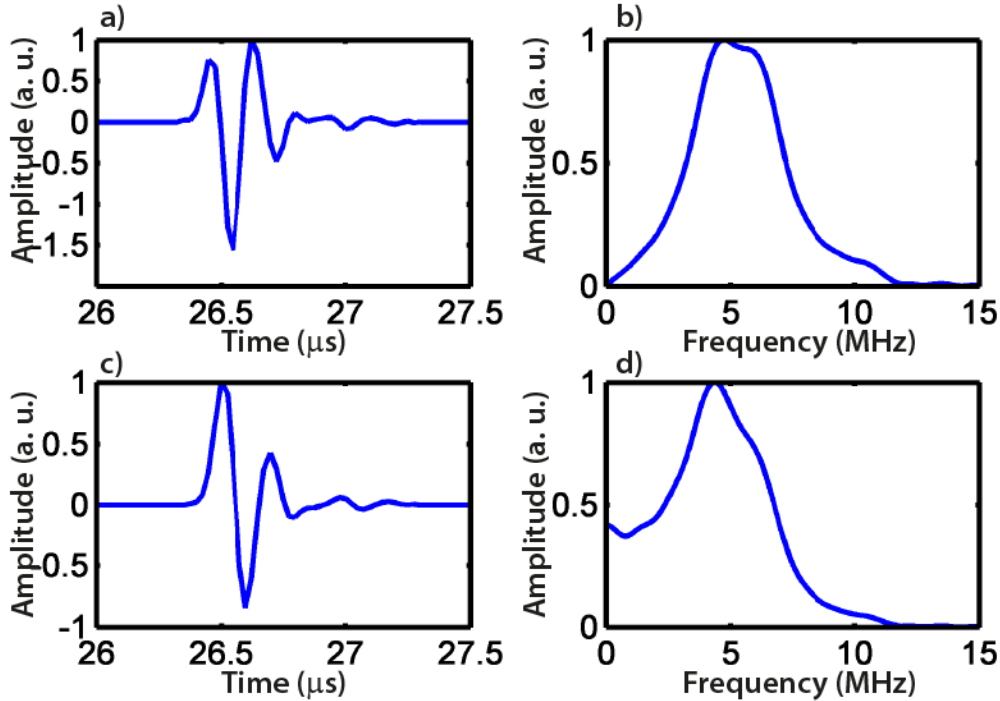
Figure 19: The indirect method for the determination of the EIR applied to a 5 MHz sensor. *a)* Signal from the spray painted plate. *b)* Frequency spectrum of the measured signal. *c)* EIR of the sensor obtained after applying Eq. (3.2) to the measured signal. *d)* Frequency response of the transducer. See text for details.

3.2.6 Results 3: responses of ultrasound transducers*

Several transducers were characterized for different purposes and setups at our institute. Herein, only three relevant examples are provided.

First, the calibration of the 64-element transducer array used in [11, 12] is presented; a more thorough calibration is presented in Section 3.4. The transducer had a specified center frequency of 5 MHz and a pulse-echo bandwidth of 55 %. The signal generated at the PMMA plate as measured by this transducer is shown in Fig. 19a and the corresponding frequency spectrum in Fig. 19b. The results show that, even though the intrinsic source spectrum peaks at 10 MHz, the central frequency of the sensor is still the frequency with the highest amplitude. Fig. 19c shows the EIR of the sensor after the spectrum source has been corrected through integration. Fig. 19d shows the frequency response of the sensor, which has a peak at 4.7 MHz and a -6 dB bandwidth of 93 %.

The values are comparable with the specifications given by the manufacturer. It has to be pointed out that the pulse-echo response provided by the manufacturer is the convolution of the send and receive spectra, which are approximately equal, i.e. $i_{p-e} = i_s * i_r$. The convolution of the impulse response with itself effectively squares the

---

* The measurements herein were performed in collaboration with S. Kellnberger and M. Omar for the characterization of their measurement setups.
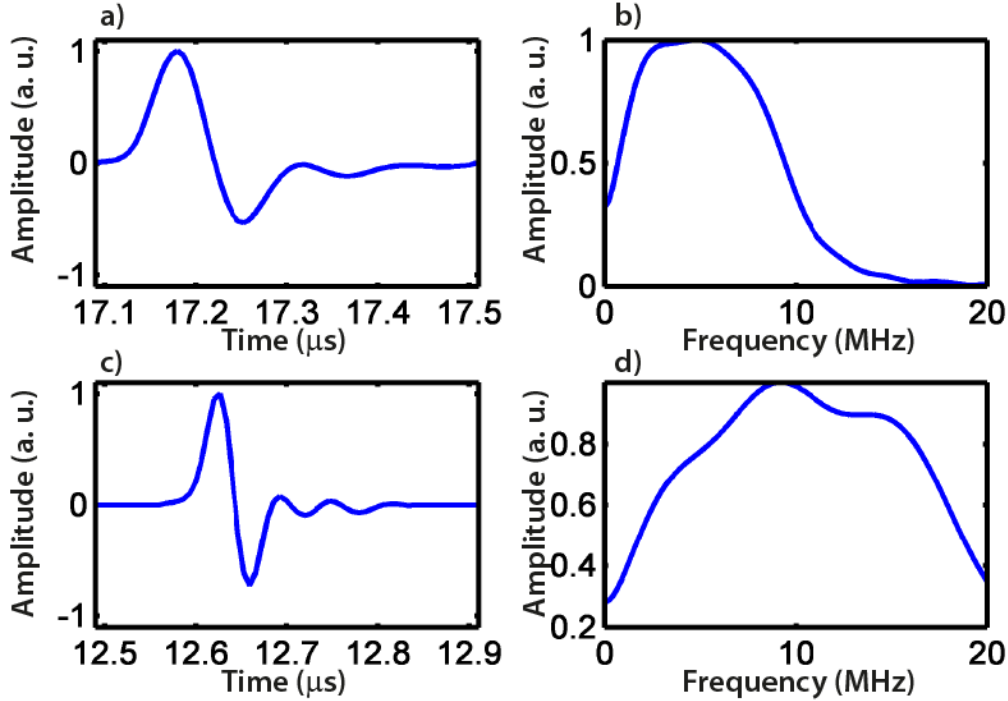
Figure 20: EIRs of ultrasound transducers determined with the indirect method, distorted by geometrical spreading of the wave. *a)* EIR of a 7.5 MHz transducer and *b)* its frequency response. *c)* EIR of a 15 MHz transducer and *d)* its frequency response. See text for details.

frequency response of the transducer. On the other hand, with our technique only the receive spectrum of the sensor is measured, which explains the ~2 factor in the measured optoacoustic bandwidth with respect to the specified by the manufacturer.

The second and third sensors that were characterized have been used previously in optoacoustic measurements at the mesoscopic scale [32, 44]. Both are cylindrically focused transducers. One has a central frequency of 7.5 MHz, with F = 25.4 mm and D = 13 mm (model V320, Panametrics-NDT, Waltam, MA). The other one (model V319, same manufacturer), has a center frequency of 15 MHz, with F = 19 mm and D = 13 mm. The definitive impulse and frequency responses, after the indirect method has been applied, can be seen in Fig. 20. In both cases, there is a clear bias towards lower frequencies, with the supposedly 7.5 and 15 MHz transducers showing 4.5 and 9.2 MHz peak frequencies respectively.

The reason behind this bias can be understood with the help of Fig. 21a, which shows the same configuration as Fig. 12 but seen from the top of the sensor instead of from the side. If the lateral size of a sensor is large enough, a signal originating at the focal point of the transducer needs a non-negligible amount of time to excite the surface of the transducer. For sensors with a relatively small lateral size, the wave can be assumed to excite the whole surface of the transducer simultaneously, as seen in Fig. 21b.
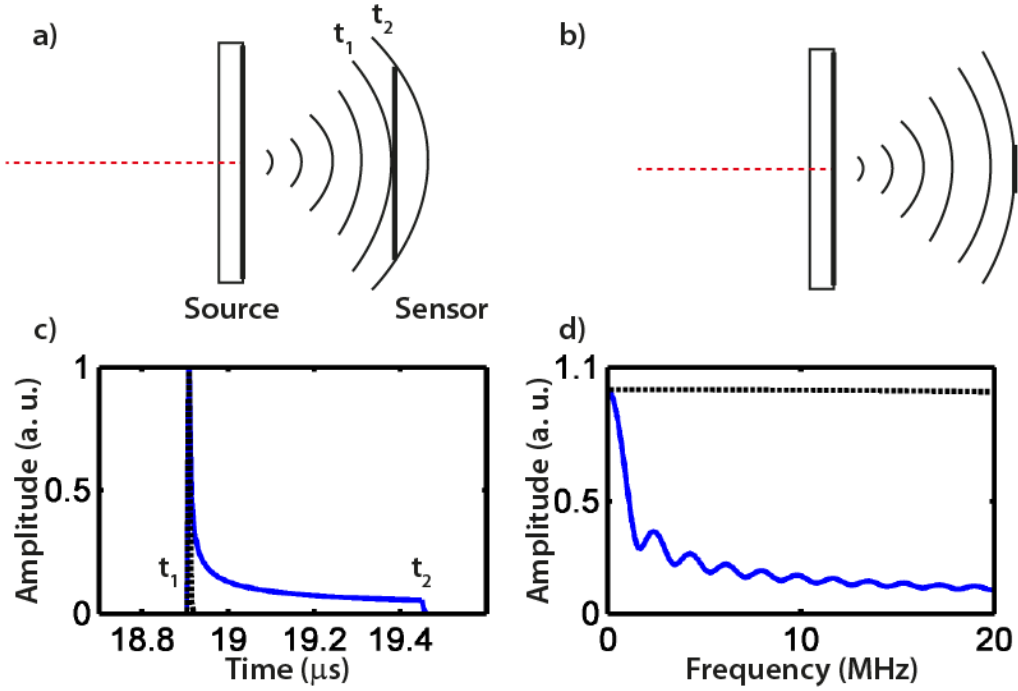
Figure 21: Origin of the measured distortion in the EIR determination. *a)* Acoustic spherical wave measured by a transducer of length D = 13 mm. *b)* Acoustic spherical wave measured by a transducer of length D = 1.88 mm. The sketches show a top view of the geometry presented in Fig. 12. *c)* Geometrical spreading $g_F(t)$ and *d)* corresponding frequency spectra for the 13 mm sensor (blue) and the 1.88 mm sensor (black).

Rigorously, the time interval $\Delta t = t_2 - t_1$ can be expressed as $\Delta t = -F\left(1 - \sqrt{1 + D/2F}\right)$. Therefore, the distortion of the measured signal due to the surface of the detector is only negligible when $f \ll 1/\Delta t$ or $F \gg D$, i.e., if the source is generated in the far field. Such distortion is in fact the definition of the SIR of the transducer, and can be calculated from Eq. (2.13) numerically [26]. For simplicity, we refer to this distortion of a Delta-like pulse due to the surface of the sensor as $g_F(t)$.

Fig. 21c shows $g_F(t)$ for two sensors. Both are cylindrically focused at a distance F = 25.4 mm. One of them has a lateral size of D = 13 mm, while for the other one has D = 1.88 mm. The interval Δt is almost negligible for the smaller sensor, whereas for the larger sensor it has a duration similar to the EIR of the transducers corresponding to Fig. 20.

The spectra corresponding to $g_F(t)$ for both sensor geometries are shown in Fig. 21d. The calculations show that the geometrical distortion of the measured signals significantly degrades the frequency bandwidth that effectively excites the transducer. While a similar analysis was done in the context of Ref. [36], the relatively low frequency of the transducer characterized therein justified the approximation of $\Delta t \sim 0$. For the EIR measurement of arbitrary detectors, however the distortion $g_F(t)$ limits severely the applicability of the indirect method and has to be corrected for.
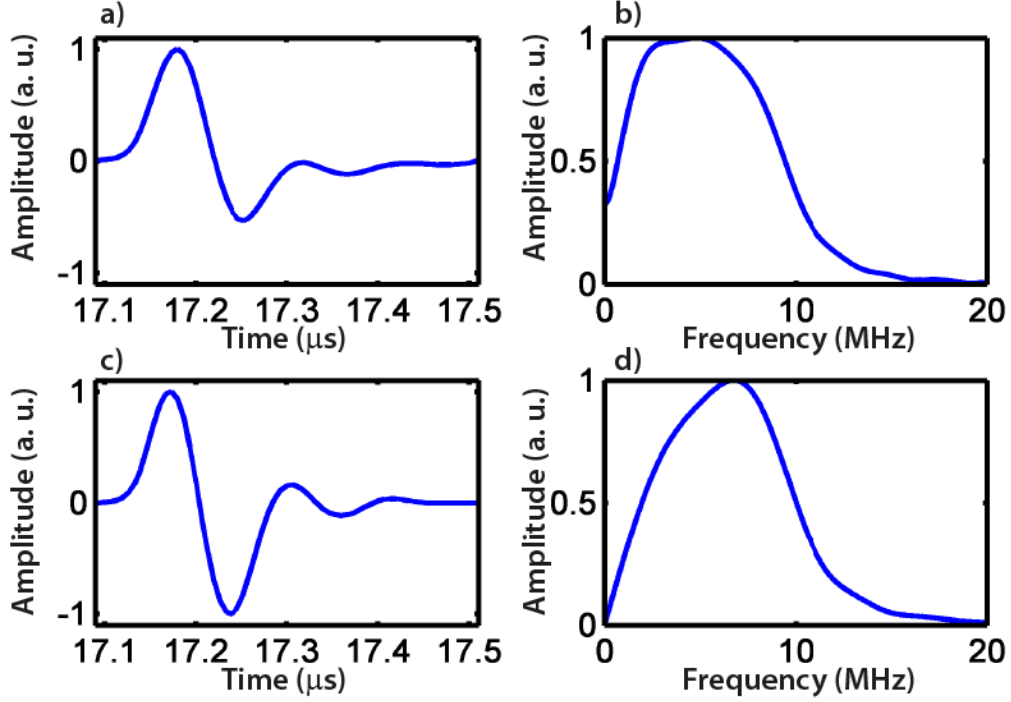
58

Figure 22: EIR of a 7.5 MHz transducer corrected for geometrical spreading as per Eq. (3.4). *a)* EIR before correction. *b)* Frequency response before correction. *c)* EIR after correction. *d)* Frequency response after correction. See text for details.

Herein it is proposed that the measured signal $s(t)$ be corrected with $g_F(t)$ through deconvolution before the integration over time (Eq. 3.3) is applied

$$\hat{s}_{corr}(f) = \frac{\hat{s}(f)}{\hat{g}_F(f)}, \tag{3.4}$$

where $\hat{}(f)$ denotes the frequency dependent Fourier-transform of the quantity in question. The corrected signals are then obtained as the inverse Fourier-transform of $\hat{s}_{corr}(f)$, and the EIR through integration of the signals as per Eq. (3.2).

Fig. 22 shows the result of applying Eq. (3.4) to the 7.5 MHz transducer. After applying the correction for the geometrical spreading, the measured peak frequency is 7 MHz and the -6 dB bandwidth is 100%, which is in better agreement with the expected sensor response than before applying the correction.

Fig. 23 shows the result of applying Eq. (3.4) to the 15 MHz transducer, which yields in a center frequency of 15.1 MHz and a -6 dB bandwidth of 96%, also corresponding to the expected values.

The results show that the correction for the geometrical spreading in combination with the sources created on the spray-painted PMMA plate can be used to accurately determine the EIR of sensors of arbitrary geometry.
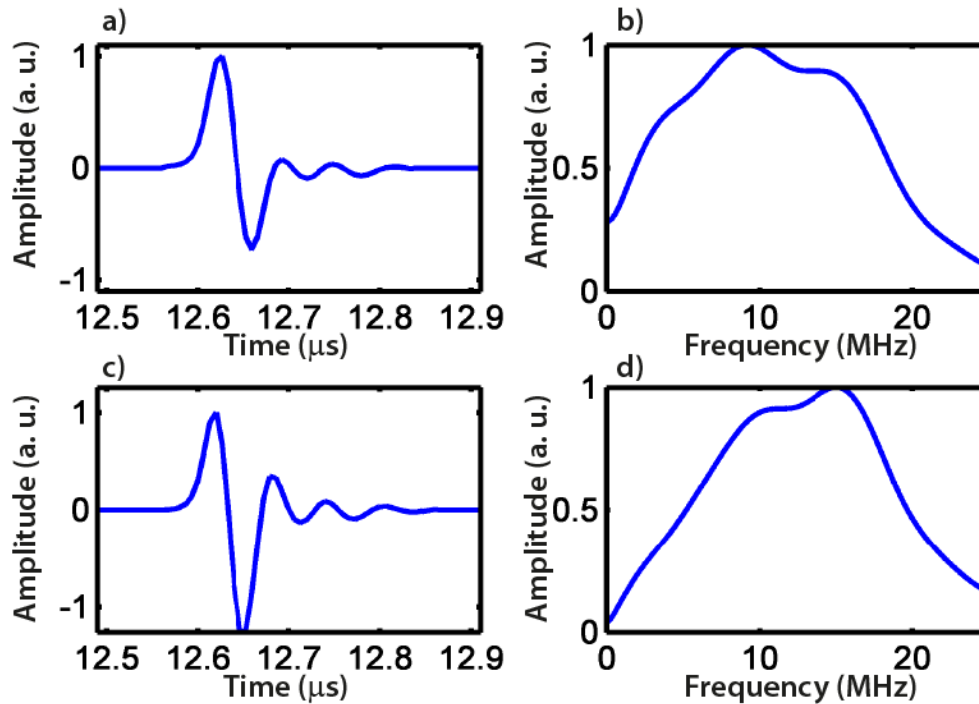
Figure 23: EIR of a 15 MHz transducer corrected for geometrical spreading as per Eq. (3.4). *a)* EIR before correction. *b)* Frequency response before correction. *c)* EIR after correction. *d)* Frequency response after correction. See text for details.

3.2.7 Conclusion

An existing method for the determination of EIRs of arbitrary transducer was optimized and extended to higher frequencies. The method consists in the generation of point-like sources in the surface of an absorbing object. The spectrum of the source is corrected by numerical integration of the measured signal. It was shown that a spray-painted PMMA plate provides a reliable and repeatable target for signal generation. The performance of the method was assessed by measuring the responses of several transducers and comparing them with the specifications of the manufacturer. It was found that the geometry of the detector may distort the measured response if the sensor size is comparable to its focal distance. The distortions were corrected by deconvolving the geometrical response at the measurement point from the measured signal. Overall, the optimized method showed a good performance in the determination of the EIRs of ultrasound transducers, as the measured characteristics were in accordance to the sensor specifications.

The method has some limitations that could be improved in future work:

Regarding the source generation, the illumination could be optimized. Since the output of the fiber bundle is not collimated, the spot size on the target that can be achieved with the present configuration is larger (tens of microns) than would be with microscopy-

grade optics (micron to sub-micron). This limits the performance of the method for spherically focused transducers at acoustic frequencies higher than 30 MHz, since at such frequencies the size of the source becomes comparable to the focal width of the sensor. One alternative would be to work with a free, collimated laser beam that is coupled to a microscope lens. Conversely, a fiber bundle with coupled optics may be designed with this application in mind, but a thorough analysis of the trade-off between the versatility of such an approach and the minimum spot size should be made.

In terms of characterization, the lack of calibrated hydrophones for frequencies higher than 20 MHz limits severely the information that can be obtained about the intrinsic spectrum of very wideband sources. As a result, there is a degree of uncertainty in the exact value for the maximum frequency at which the method is applicable.

The method herein presented may be further improved by the use of a more controlled and thinner paint layer in the manner of [56]. Such targets should result in sources of even higher frequencies and broader bandwidth.

Finally, some interesting consequences for optoacoustic imaging can be extracted from the results presented herein. First, in an optoacoustic context the bandwidth of an ultrasound transducer can be considered to be approximately two-times wider than in ultrasound applications. Second, since the amplitude of an optoacoustic source is directly proportional to its size (cf. Chapter 2), whereas the frequency is *inversely* proportional to the source dimensions, the optoacoustic signals of large objects may be measured with high amplitude, even by transducers with a relatively high center frequency.

3.3   Modeling of sensitivity fields

Having characterized the electrical properties of the transducer, the next important step towards a full model of optoacoustic detection is to provide a description of the spatially dependent sensor properties. In this section, the spatial properties of the transducers are analyzed in terms of their effect on the amplitude of measured signals.

In conventional ultrasound, transducers are used in pulse-echo mode. As discussed previously (3.2.6), this operation principle results in an effective frequency response that is relatively narrowband. For this reason, the spatial characteristics of ultrasound transducers are typically described in terms of the sensitivity field at the central frequency of the sensor. On the other hand, optoacoustics is inherently a broadband modality, owing to the intrinsic signal properties (see Chapter 2) and to the relatively broader frequency response of ultrasound transducers.
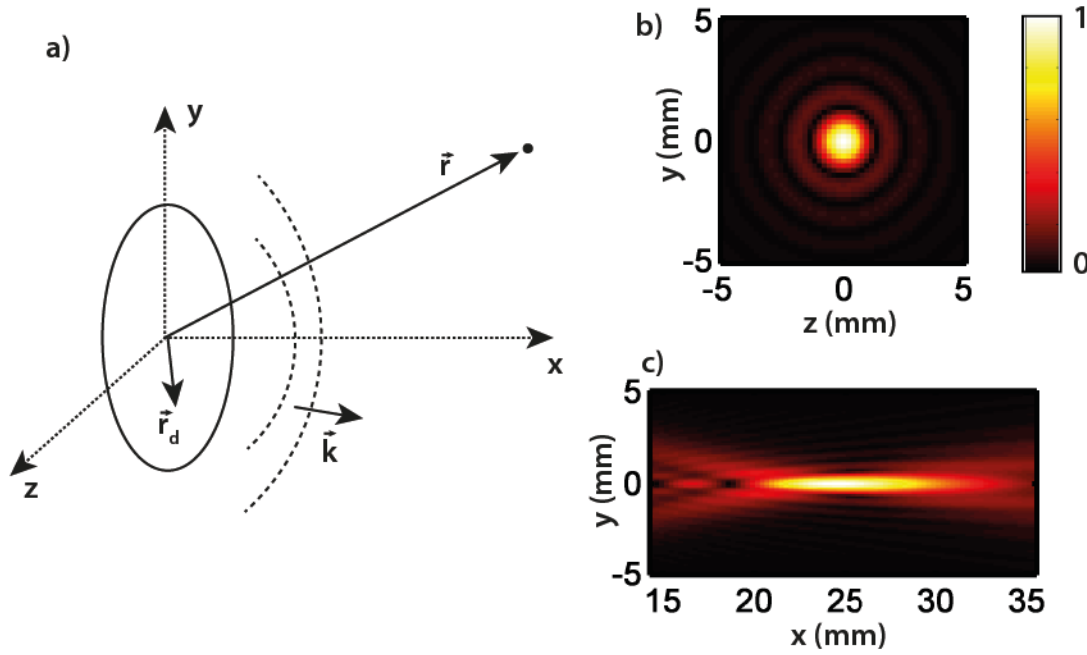
Figure 24: *a)* Geometry for the description of the Multi-Gaussian Beam method. *b)* and *c)* sensitivity fields calculated as per Eq. (3.5) for a spherically focused transducer with $F = 25.4$ mm, $D = 13$ mm and central frequency 5 MHz. The fields were calculated at the focal distance (*b*) and along the transducer axis (*c*). See text for details.

In this section, it is proposed that existing models for the description of single-frequency sensitivity fields of ultrasound sensors may be optimized to take into account the transducer's broadband frequency response. The method proposed herein is based in a numerical approximation to the Rayleigh-Sommerfeld integral [27], known as the Multi-Gaussian Beam method (MGB), which describes the sensitivity field of a sensor at a single frequency. The broadband field of the transducer is computed as a weighted sum of the fields at single frequencies, given in general by the sensor frequency response. The method is validated experimentally for a cylindrically focused transducer with known EIR.

The section is organized as follows: in 3.3.1 the MGB method is briefly described. In 3.3.2 the proposed extension of the MGB method is presented. In 3.3.3 the experimental techniques are described. In 3.3.4 the results of the proposed method and its experimental validation are presented and finally in 3.3.5 a discussion on the limitations of the proposed method is provided.

3.3.1 The Multi-Gaussian beam method at single frequencies

Due to the reciprocity theorem, the description of the acoustic radiation by an ultrasound sensor into a medium is equivalent to the description of the detection of waves originating inside the medium. Therefore, the MGB method is described in terms of acoustic emission. A complete derivation of the method can be found in [27].

Briefly, let us assume that a round ultrasound transducer of radius a is located at the origin and radiates waves into a medium of density ρ and speed of sound c, as shown in Fig. 24a. Under the piston approximation, the surface of the sensor is only displaced along the x direction, defined as the "transducer axis". If the medium is a fluid, said displacement originates waves that propagate mostly along the x direction, i.e. the propagation of the waves can be considered paraxial[*]. Under these assumptions, the radiated field at a single frequency can be described by a sum of complex Gaussian functions of the form [27]

$$p_\omega(x, y, z) = \sum_j^n \frac{A_j e^{ikx}}{1 + iB_j x/x_r} \exp\left[\frac{ikC_j}{2}(y^2 + z^2)\right]. \tag{3.5}$$

A_j and B_j are some complex coefficients, $x_r = ka^2/2$ is called the Rayleigh distance and it holds that:

$$C_j = \frac{iB_j}{x_r + iB_j x}. \tag{3.6}$$

In general terms, A_j and B_j are constants determined through an optimization process, which minimizes the difference between the field described by Eq. (3.5) and the theoretical sensitivity field, which is described by the Rayleigh-Sommerfeld equation [27], Eq. (2.14).

The optimum number of parameters n is typically 10 for round transducers and 15 for square surfaces. The MGB method is in fact very flexible, and focused transducers may be considered by substituting $B_j \rightarrow B_j + x_r/F$. Additionally, rectangular or elliptical transducers are described in terms of Rayleigh distances for y and z which are dependent on the sides or semi axes of the sensor respectively. Thus the exponential factor is redefined as $C_j(y^2 + z^2) \rightarrow \left(C_j^y y^2 + C_j^z z^2\right)$. With such modifications, Eq. (3.5) describes the sensitivity fields of a wide variety of transducers accurately [27, 57]

An example of the sensitivity fields calculated with the MGB method can be found in Figs. 24b and 24c. The sensitivity field for a round spherically focused transducer with $F =$ 25.4 mm and $D =$ 13 mm was calculated at the focal spot (24b) and along its axis (24c) for a frequency of 5 MHz. The calculations were done in a 81x81 grid and took less than a second to perform for $n = 15$ in an average desktop PC.

---

[*] The MGB method is valid for distances greater than one transducer radius for most relevant frequencies in optoacoustics.
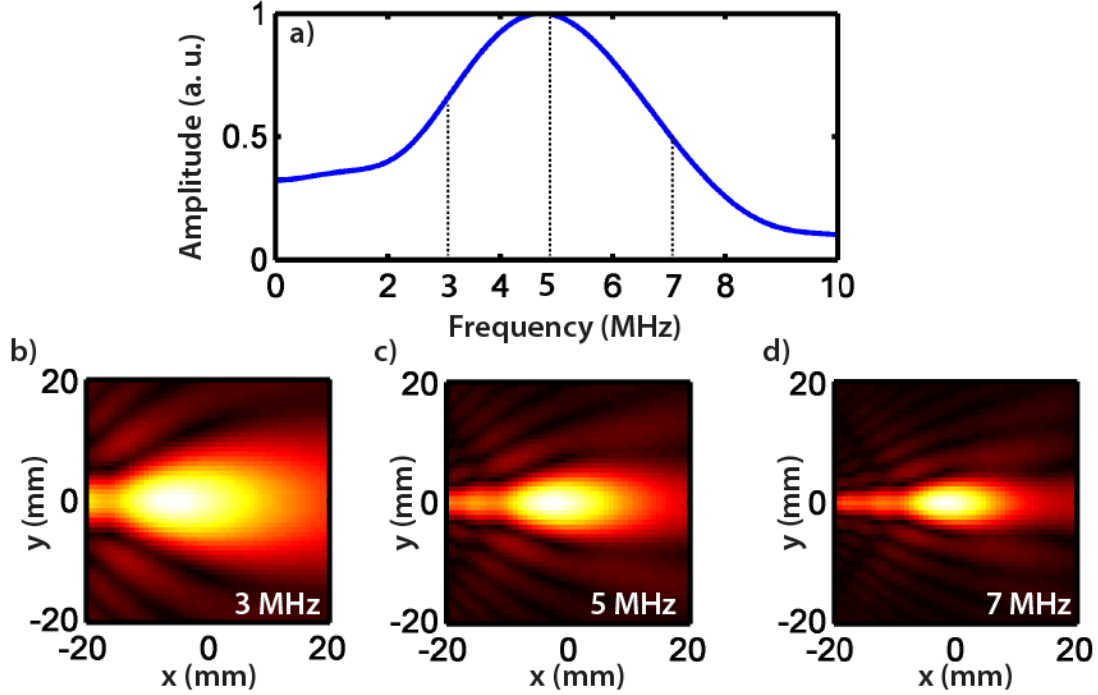
Figure 25: Principle for the calculation of the sensitivity field of a broadband transducer from its frequency response. *a)* Frequency response of an arbitrary transducer. *b)* to *d)* Fields at several frequencies. The individual fields are weighted by the amplitude value of the FR at that frequency and added together.

The MGB method offers a fast alternative to the Rayleigh-Sommerfeld integral for the calculation of sensitivity fields of arbitrary shapes. The method is however limited to paraxial conditions, i.e., it is only valid for points located at $|\vec{r}| > a$ and focused transducers such that $F/D \geq 1$ [27].

3.3.2 The broadband MGB method

Herein it is proposed the sensitivity field of a broadband sensor can be computed from the fields at single frequencies provided that its frequency response $FR(\omega)$ is known. The broadband field is calculated as a weighted sum:

$$p(x, y, z) = \sum_{FR(\omega) \geq 0} FR(\omega)\, p_\omega(x, y, z), \tag{3.7}$$

where the summation takes place over the response of the sensor*. $FR(\omega)$ is obtained as the amplitude of the Fourier-transform of the EIR, which can be determined with the method discussed in Section 3.2. Owing to the computational efficiency of the MGB method, the number of individual fields to be computed and summed can be determined by the frequency resolution of the EIR measurement.

---

* The method described by Eq. (3.7) was developed by the author. While searching for independent confirmation, the more general concept of the SIR was encountered. Thus, the characterization efforts where shifted towards implementing and validating a description of the transducer characteristics based on the SIR in combination with the EIR, which ultimately resulted in the work described in Section 3.4.

The idea of the proposed method is illustrated in Fig. 25. The frequency response of a sensor is measured experimentally (25a). The sensitivity fields at single frequencies are calculated by Eq. (3.5) for several frequencies, of which some are shown (25b to 25d). The fields are weighted by $FR(\omega)$ and summed up to yield a broadband field, as per Eq. (3.7).

3.3.3 Experimental techniques

In order to assess the validity of the proposed method, the sensitivity field of one element of a 64-channel transducer array was measured experimentally and compared with the field calculated with Eq. (3.7).

a) Experimental setup.

The experimental setup consisted of a 64-element ultrasound array, mounted on a three axis translation system for scanning. The sensor was submerged in deionized water, which provides a homogenous medium with tissue-like acoustic properties. The illumination was provided by a pulsed laser and the measured signals are digitized by an analog-to-digital data acquisition system. The scanning and data acquisition were controlled by a computer and synchronized by a trigger signal from the laser. The details of the setup components follow.

The sensor was a custom-made ultrasound array (Imasonic SaS, Voray, France) used for video-rate multi-spectral optoacoustic tomography (MSOT) [11], shown in Fig. 26a. The sensor consists of 64 elements arranged in a semicircular geometry of 40 mm radius. The dimensions of each element are: $D = 15$ mm in elevation (out-of-plane) and $l = 1.88$ mm in the lateral direction (in-plane). Mechanical focusing at $F = 40$ mm results in $F/D = 2.67$, enough for the discrimination of out-of-plane signals without loss of radial sensitivity. The response of the central element was characterized by the method described in Section 3.2; a central frequency of 4.7 MHz and a –6 dB bandwidth of 96% were found. The frequency response of the sensor is shown in Fig. 26b[*].

The array as connected to 8 multichannel analog-to-digital acquisition boards (Model PXI5105, National Instruments, Austin, Texas). The signals were acquired at a rate of 60 MS/s and digitally filtered from 50 kHz to 10 MHz.

---

[*] The EIR was measured as described in Section 3.2. However, the spray-painted plate had not been characterized at the time of the measurement and thus the black-agar phantom was used instead. For the frequency range of the transducer measured herein, however, calibrations performed with the plate or the black-agar phantom were found to be compatible.
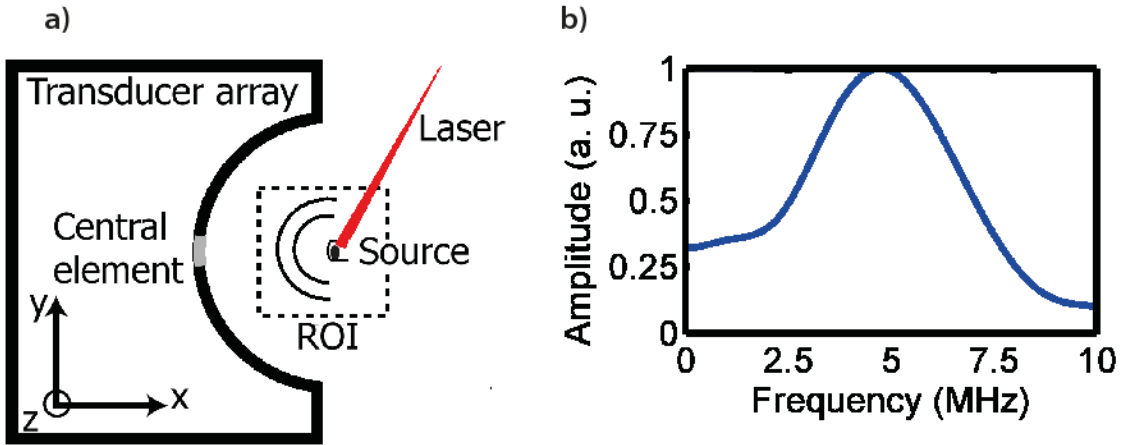
Figure 26 *a)* Sketch of the measurement setup, seen from above the imaging plane *XY*. The transducer array and the dimensions of the region of interest (*40 mm by 40 mm)* are drawn to scale. *b)* Frequency response of the sensor used for the TIR determination. We observe a center frequency of 4.7 MHz and a receive-mode bandwidth of 96% at full-width half-maximum (FWHM).

The multi-axis positioning system consisted of three translation stages for 3D scanning and a rotation stage, for orientation in the horizontal plane (2xMTS50-Z8, NRT150 and PRM1-MZ7, Thorlabs GmbH, Karlsfeld, Germany).

The illumination for signal generation was provided by the 532 nm pump-beam of a tunable optical parametric oscillator laser (Vibrant, Opotek Inc., Carlsbad, California), at a repetition rate of 20 Hz and pulse duration of 8 ns.

b) Measurement of the sensitivity field

The experimental sensitivity field was determined by scanning a sub-resolution absorber in front of the transducer[*]. A black, 50 μm in diameter polyethylene microsphere was used as the optoacoustic source (Cospheric LLC, Santa Barbara, California). In order to achieve uniform illumination, the microsphere was embedded in a light-scattering cylindrical agar phantom (reduced scattering coefficient $\mu'_s = 10\ cm^{-1}$), 5 mm in diameter. The phantom was illuminated with a laser beam of about 3 mm in diameter, and the source can be thus considered a point-like emitter of isotropic, broadband optoacoustic signals [5].

The transducer was scanned in the x-y axes (see Fig. 26a) within a region of 40 mm by 40 mm centered in its focal point. The step size was 800 μm in both directions, resulting in a square grid of 51 pixels on each side. The microsphere and its illumination were left static and the signals at each position were averaged for 50 laser shots and stored for later analysis. The total scanning time was about two hours.

---

[*] The measurements here presented were obtained in collaboration with A. Bühler for the characterization of his sensor.
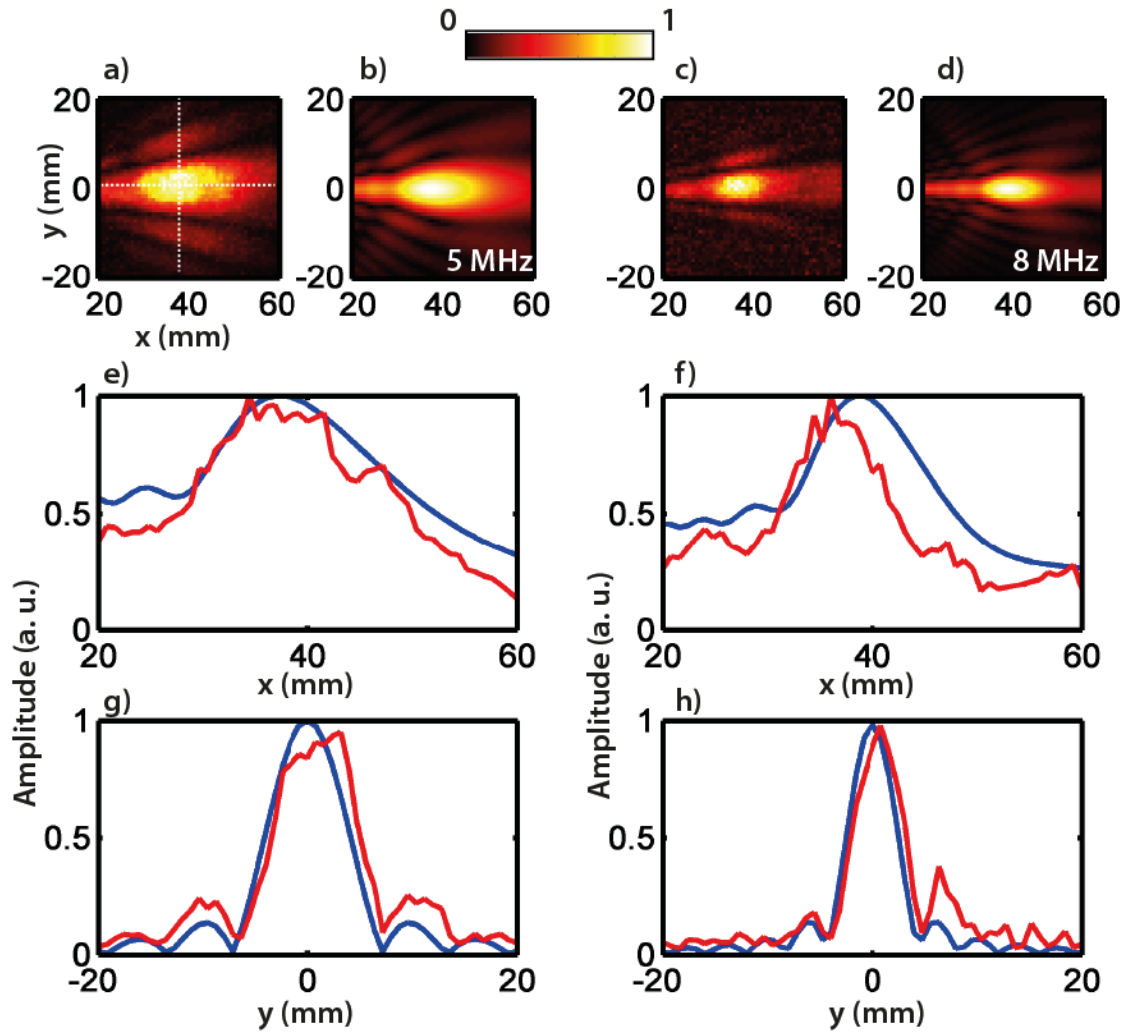
Figure 27: Experimentally measured sensitivity fields at single frequencies with the field predicted by the MGB method. *a)* Experiment and *b)* simulation of the field at 5 MHz. The dotted lines indicate where the profiles along the *x* and *y* axis are taken. The profile along x is shown in *e)* (red: experiment, blue: simulation) the profila along the *y* axis is shown in *g)*. The same description applies for the field measured and calculated at 8 MHz, shown in *c), d)* respectively and the profiles, shown in *f)* and *h)*. See text for details.

The sensitivity field was computed by taking the maximum amplitude of the filtered signals at each scanning point *(x, y)*.

During the experiments, there were small drifts in the location of the agar phantom, which were caused by the transient water flow during the movement of the sensor from one measurement point to the next. The uniformity of the illumination was nevertheless ensured by the scattering agar phantom where the source was contained. However, these drifts resulted in variations in the amount of light absorbed by the source at each sensor position. As a consequence, for any two neighboring measurement points the changes in amplitude were much higher than expected. For this reason, the experimental amplitude map was spatially filtered with a 5x5 pixels median mask.

c) Computation of the broadband sensitivity field

The number of fields to be calculated was determined by analyzing the frequency resolution *df* of the EIR measurement. The acquired signals were $3 \cdot 10^3$ samples long, with a sampling rate of 60 MS/s, thus *df* = 20 kHz. The fields where calculated for the frequency span between 50 kHz and 10 MHz. Therefore, ~500 distinct sensitivity fields were computed in a grid with the same characteristics than the measurement grid. The broadband field was computed as per Eq. (3.7).

3.3.4 Results

First, the performance of the MGB method was assessed by comparing the fields calculated at several frequencies with the experimentally measured ones. The experimental fields were obtained by filtering the signals with a 20 kHz bandpass filter around the frequency of interest. The results are depicted in Fig. 27 for fields at 5 MHz (Figs. 27a, b, e and g) and 8 MHz (Figs. 27c, d, f and h). The discrepancies between the MGB method and the experiment arise when the sensitivity of the sensor is low: either at 8 MHz or at distances away from the focus. Nevertheless the findings showcase the ability of the MGB method to accurately describe single frequency sensitivity fields. The MGB method reproduces the diffractive features of experimental fields such as sidelobes and a slight shift of the maximum sensitivity towards the transducer surface.

The calculated and measured broadband fields are shown in Fig. 28. The experimentally measured field is shown in Fig. 28a and the field calculated with the broadband MGB method is shown in Fig. 28b. In both cases it can be seen that the presence of lower frequencies broadens the focal zone. It is interesting to note that, as several frequencies are combined, the sidelobes smooth out. Figs. 28c and 28d show the profiles of the broadband fields along the transducer axis and at the focus, which show a good match between the predictions of the method proposed herein and the experimental findings.

3.3.5 Conclusion

A method for the modeling of the sensitivity field of broadband ultrasound transducers has been shown. The method consists in computing a weighted average of different sensitivity fields at single frequencies to obtain a broadband field. The weighting factors are extracted from the experimentally measured frequency response of the sensor. The method was shown to accurately describe the experimentally determined sensitivity field of a broadband transducer. The proposed method can therefore provide a noiseless description of the sensitivity field of ultrasound sensors for image formation.
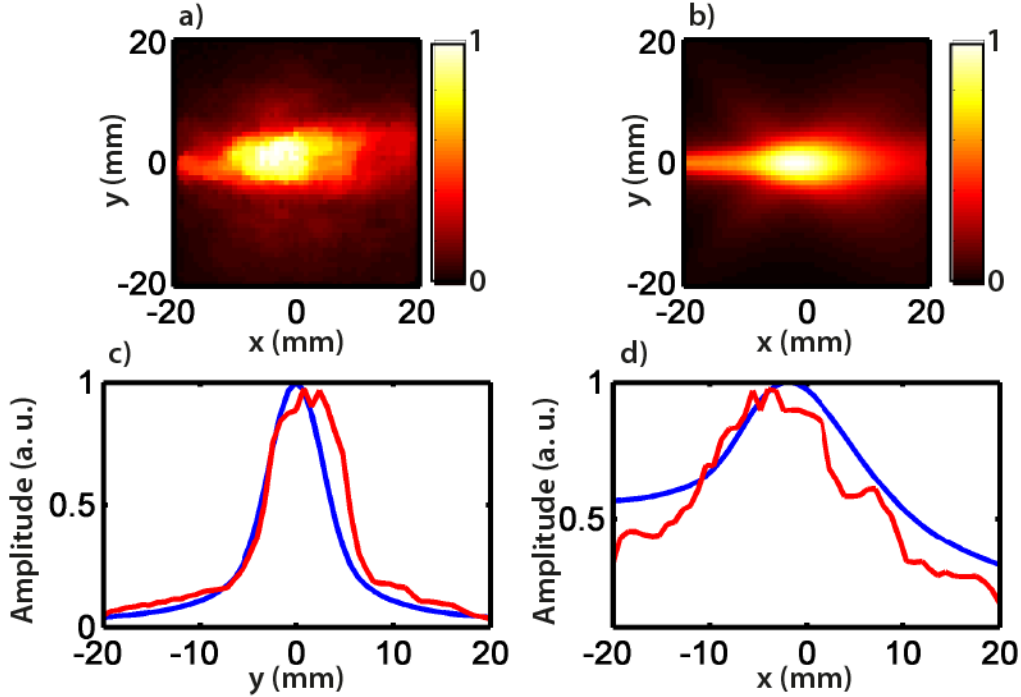
68

Figure 28: Broadband field resulting from *a)* the measurements at the full sensor bandwidth and *b)* the calculation with the extended MGB method. *c)* Profile along the *y* direction at the focus (red: experiment, blue: simulation). *d)* Profile along the *x* direction. See text for details.

The proposed method exhibits however one major limitation with respect to its accurate description of optoacoustic detection. The sensitivity field is indeed a good representation of "where" signals are mainly measured from, and therefore offers useful insights, e.g. when designing an experiment or a setup. However the field description of "how" the signals are measured is very incomplete. A sensitivity field is a measure of the spatial variation in measured signal amplitude, which completely ignores the signal phase and frequency content.

In section 3.2.6 it was shown how the frequency content of a signal may be distorted by the SIR of the detector in absolute terms, i.e., not with respect to signals generated at neighboring points. Therefore an accurate description of the sensor spatial properties shall include the SIR, which describes both the broadband field weighting and the low-pass filtering on propagating optoacoustic waves.

3.4 The Total Impulse Response

In this section, a full description of the optoacoustic detection process is provided. The description is based on the combination of the SIR and the EIR into a global sensor response, referred herein as the TIR. A short review of previous efforts to characterize the TIR either globally or in terms of its components is provided in the following, to best put the method described in its due context.

There are three main approaches to obtain the TIR of an ultrasound transducer: purely experimental measurements, purely theoretical analyses, and hybrid methods that make use of an experimental EIR and a numerical SIR.

The experimental retrieval of the transducer's TIR can be achieved by optoacoustic detection of a sub-resolution emitter, in a similar manner to the sensitivity field measurement of the previous section. The only requirement to retrieve the TIR is that the emission frequency spectrum of the source is known and can be corrected for, as demonstrated for the EIR determination. Such a source is not well suited for scanning measurements since it does not emit isotropically. On the other hand, wideband isotropic sources, such as small absorbing microspheres, emit characteristically weak signals at low frequencies. As a consequence, it is difficult to correct for their emission spectra in a reliable way [36]. Purely experimental methods are therefore well-suited for the TIR determination only within the frequency band where the microsphere signals are strongest [5].

In order to obtain good signal to noise ratio (SNR) in the TIR measurements, it is necessary to use signal averaging since the optoacoustic signals of small sources are weak. If the sources are outside the focal zone, the measured signal amplitude is even lower, and therefore more averages are needed. Signal averaging is however time-consuming, so a trade-off between the number of points in which the TIR is measured and the desired SNR has to be found. As a consequence, in previous works the TIR has been characterized with good SNR only for a few points inside the focal zone [39], [58]. However, strong absorbers placed outside the focal zone can be detected and may produce artifacts in the reconstructed images [24, 59]. TIR characterization with good SNR, in- and outside the focal zone, and a spatial sampling similar to the imaging resolution is therefore important for image formation in optoacoustic imaging.

Alternatively, there exist purely theoretical determinations of the transducer's TIR. Recent work by Rosenthal et al. [24] presented a purely theoretical approach for the determination of the SIR, with good correspondence between theory and experiment. Since the SIR was calculated for every point inside the ROI, even outside the focal zone, the application of the calculated SIR to image reconstruction shows an improvement over standard image reconstruction methods.

Kozhushko et al. [58] discussed the determination of the TIR with the convolution method, where both the EIR and the SIR were described by theoretical models. The predictions of the theory are confirmed by experiments, although within a relatively small region close to the focus of the transducer. Furthermore, such a theoretical approach

requires that the sensor's geometry and the parameters of its piezoelectric-plus-backing (or acoustic stack) are known exactly. However, most transducer design parameters are accessible only to the manufacturer of the transducer, whereas for the end-user, typically only a few specifications of the sensor are known. As a result, the theoretical method for the determination of the TIR is of limited use in terms of transducer calibration.

The hybrid approach, using the measured EIR and the analytical SIR of a sensor, has been recently applied to image reconstruction in [59]. In this case, both responses are implemented in an iterative reconstruction algorithm, improving the images obtained when compared to a point-like sensor model. However, the implementation presented was limited to flat detector geometries under the far field approximation. More importantly, no experimental validation of the TIR was obtained which could suggest favorable performance over purely experimental methods.

To the best of our knowledge, the determination of the TIR of ultrasound sensors in optoacoustics has so far been limited to either theoretical approximations, on descriptions of the EIR and SIR without a validation of the resulting TIR, or has been performed only within the focal zone. With the availability of robust methods for EIR characterization, as the one presented in section 3.2, and the variety of accurate SIR models for arbitrary detector geometries [24, 26], a more standardized and systematic approach to the TIR determination ought to be considered.

Herein it is demonstrated that the TIR of the transducer in and outside its high-sensitivity region can be accurately determined by the hybrid method, and that said accuracy can be validated experimentally. Specifically, it is proposed that the EIR be determined with the method described in section 3.2 and convolved with the numerically calculated SIR as per [26]. Both methods separately have proven to have high fidelity and may be applied to general detector geometries. The procedure is demonstrated using a cylindrically focused transducer and is validated by comparison to a purely experimental characterization of the sensor. In section 3.4.1 we provide the description of the experimental method for the TIR determination. In Section 3.4.2, a description of the hybrid method is presented. Section 3.4.3 describes the experimental setup and the measurements performed. Section 3.4.4 presents the results and validation studies and finally section 3.4.5 discusses the results and their implications to optoacoustic imaging. The contents of this section have been submitted for publication to IEEE T-UFFC [60].

3.4.1 Experimental determination: concept

In order to determine $h_T(\vec{r}, t)$ experimentally, a point-like absorber $H_r(\vec{r}) = \delta(\vec{r})$ can be scanned in the imaging ROI, centered at the focus of the detector ($\vec{r} = 0$). From Eq. (2.2) and Eq. (2.8), and due to the associativity of the convolution with respect to the derivation, the measured signals will be of the form:

$$s_d(\vec{r}, t) = h^{exp}(\vec{r}, t) * \frac{\partial i_r(t)}{\partial t} = \frac{\partial h_T^{exp}(\vec{r}, t)}{\partial t}. \qquad (3.8)$$

Eq. (3.8) is the basis for the experimental determination of the total impulse response of the sensor: an integration of the measured signals over time yields the TIR of the detector $h_T^{exp}(\vec{r}, t)$. The integration process, however, is highly sensitive to the noise at low frequencies, a problem exacerbated outside the focal zone of the transducer.

3.4.2 The hybrid method: concept

Conversely, herein we propose that the TIR of the sensor ought to be determined in and out-side the focal zone with the convolution method described in section I. In particular it is proposed that the components of the TIR are first obtained independently, as follows.

The EIR is obtained at a point $\vec{r}_0$, which may be anywhere inside the ROI, with the method described in section 3.2. If necessary, the deconvolution for correcting the SIR at $\vec{r}_0$ (section 3.2.6) may be applied. After this deconvolution, the EIR represents the response of the sensor which is truly independent of the source position.

On the other hand, the SIR can be calculated either analytically or numerically for every point $\vec{r}$ in the ROI. Finally, the EIR and the SIR at $\vec{r}$ are combined using temporal convolution to yield the TIR of the sensor.

Since the deconvolution operation is defined in the frequency domain, the calculation of the TIR with the method just described is expressed mathematically as:

$$\hat{h}_T^{hyb}(\vec{r}, f) = \frac{\hat{i}_r(\vec{r}_0, f)}{\hat{h}^{sim}(\vec{r}_0, f)} \cdot \hat{h}^{sim}(\vec{r}, f). \qquad (3.9)$$

$\hat{i}_r(\vec{r}_0, f)$, and $\hat{h}^{sim}(\vec{r}, f)$ represent the Fourier-transforms of the measured EIR and the simulated SIR respectively. $\hat{h}_T^{hyb}(\vec{r}, f)$ is therefore the total frequency response of the transducer, from which the TIR can be obtained by performing the inverse Fourier-transform. We refer to $h_T^{hyb}(\vec{r}, t)$ as the hybrid TIR, which describes all of the transducer-related distortions upon a propagating optoacoustic wave.

In practical terms, $\vec{r}_0$ should be a highly sensitive point of the transducer field-of-view, and the SIR at that point should be as broadband as possible. For focused transducers, the obvious choice for $\vec{r}_0$ is therefore the focal point of the transducer, defined here as $\vec{r}_0 = 0$.

3.4.3 Experimental and numerical techniques

The EIR and TIR were determined experimentally as described in sections 3.2 and 3.4.1. The analysis here presented makes use of the same dataset. A few more details are provided with respect to the computation of the TIR and the sensitivity and bandwidth fields (called maps herein).

a) Computation of the numerical SIR

The SIR was calculated with the ultrasound simulation software FIELD II [37]. The program divides the surface of the transducer in small square sub-apertures, and computes the analytical solution to Eq. (2.13) for each of them, summing up the resulting responses coherently to obtain the final SIR.

The simulation was computed in a grid with the same dimensions and number of pixels as the experimental scanning grid. The parameters of the transducer surface were as described in section III a). The time sampling was set to 100 MS/s and the speed of sound in water to 1500 m/s.

b) Computation of the hybrid TIR

To compute $h_T^{hyb}(\vec{r}, t)$, we first resampled the TIR at $\vec{r}_0$ to the sampling rate of the simulated SIR, and then applied Eq. (3.9). In practical terms, the SIR at the focus of the transducer is a Dirac-delta, equivalent to a constant function in the frequency-domain. As a result, Eq. (3.9) simplifies to the product of the Fourier-transforms of the EIR and SIR. Thus, $h_T^{hyb}(\vec{r}, t)$ is readily calculated with a convolution operation between the SIR and the EIR, performed in the time domain.

To validate the proposed method, $h_T^{hyb}(\vec{r}, t)$ was compared with $h_T^{exp}(\vec{r}, t)$. The experimental measurements were however of the form $\partial h_T^{exp}(\vec{r}, t)/\partial t$, and had to be corrected for the microsphere spectrum as discussed in section IIc. Such correction can enhance low-frequency noise, which can distort the spectrum of $h_T^{exp}(\vec{r}, t)$, making the comparison difficult. For this reason, and in order to avoid the spectrum correction of $\partial h_T^{exp}(\vec{r}, t)/\partial t$, a second hybrid TIR, $g_T^{hyb}(\vec{r}, t)$, was calculated.

$g_T^{hyb}(\vec{r}, t)$ makes use of the EIR measurement before it has been integrated as per Eq. (3.2), i.e., it is calculated by convolving the numerical SIR with the measured signal. Like this, $g_T^{hyb}(\vec{r}, t)$ can be compared with the measured signals $\partial h_T^{exp}(\vec{r}, t)/\partial t$ directly.

c) Computation of the amplitude and bandwidth maps

In order to have a global overview of the TIR properties in the scanned region, we computed amplitude and bandwidth maps from all experimental and hybrid TIRs. The amplitude map depicts the spatial dependence of the transducer sensitivity, whereas the bandwidth map shows the spatial variation of the measured signal frequencies.

The bandwidth maps were computed by numerically performing the Fourier transform of the filtered signals and computing an effective bandwidth as per:

$$B_w(x, y) = \sqrt{\frac{\int_0^\infty \left|\hat{h}_T(x, y, f) \, f\right|^2 df}{\int_0^\infty \left|\hat{h}_T(x, y, f)\right|^2 df}}. \qquad (3.10)$$

$\hat{h}_T(x, y, f)$ represents the frequency-dependent Fourier transform of the filtered signals at each scanning position (x, y). Since in Eq. (3.10) each signal is normalized by its total energy, $B_w(x, y)$ represents a global property of the signal, independent of its amplitude. As a consequence, the experimental bandwidth map is less sensitive than the amplitude map to the fluctuations in the illumination. The median mask applied was thus 2x2 pixels instead of 5x5 as in the case of the amplitude map (recall 3.3.3).

3.4.4 Validation of the convolution method

In order to validate the hybrid TIR, $g_T^{hyb}(\vec{r}, t)$ was compared with $\partial h_T^{exp}(\vec{r}, t)/\partial t$, first by making use of their amplitude and bandwidth fields, as shown in Fig. 29. The amplitude maps shows good correspondence of the shape and size of the focal zone, with the discrepancies arising from the illumination fluctuations, as discussed in section 3.3.3. Of greater interest are however the bandwidth maps (Figs. 29b and 29d), which also show very good agreement. We can see how the experimental map becomes noisier as we approach the regions where the SNR is very low. Despite low SNR the sidelobe pattern along the lateral direction is confirmed by the hybrid TIR. This pattern implies good spectral sensitivity even outside the focal zone. As consequence for signal analysis and imaging, strong absorbers in this area cannot be suppressed in the signal through band-pass filtering, as this would also filter out signals coming from absorbers in front of the sensor. Overall, the
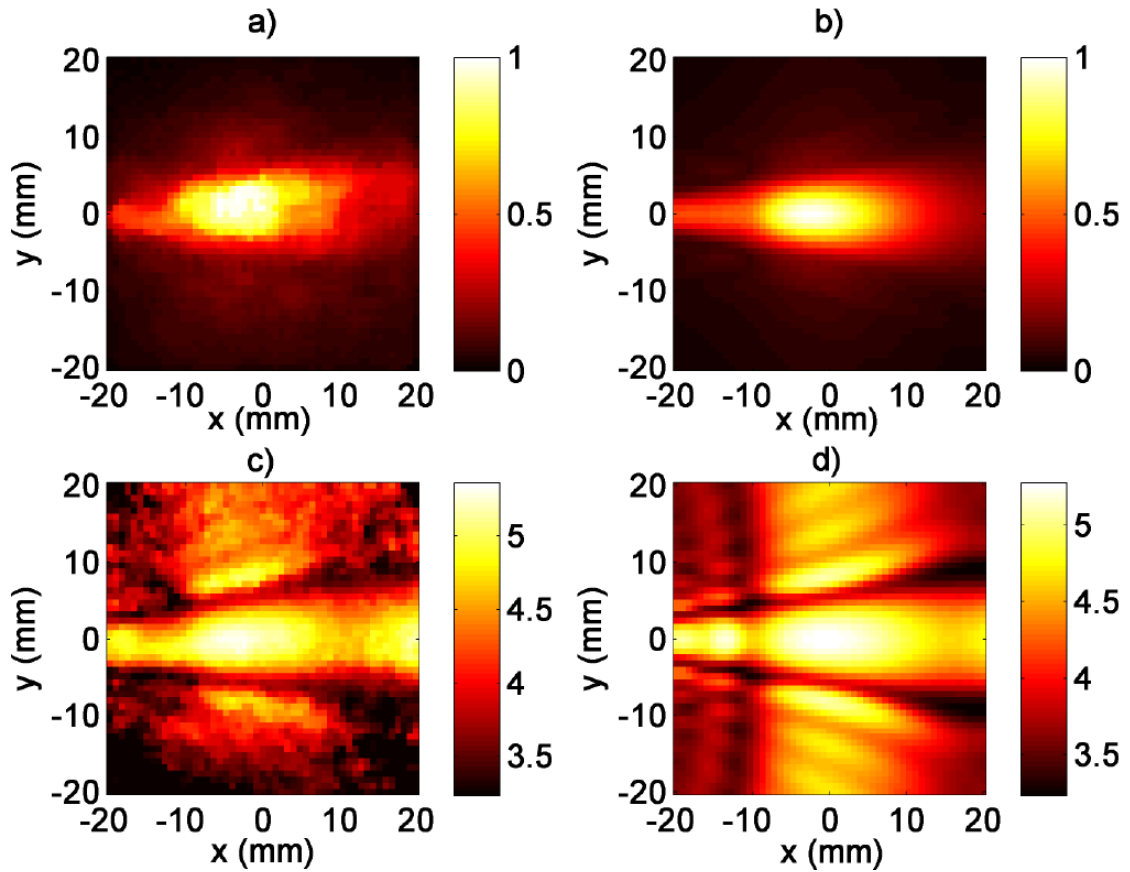
74

Figure 29: Validation of the global properties of the hybrid TIR. The top row shows the amplitude maps of a), the experimental measurement $\partial h_T^{exp}(\vec{r}, t)/\partial t$ and b), $g_T^{hyb}(\vec{r}, t)$. The color bars represent relative amplitude with respect to the maximum. The bottom row shows the corresponding bandwidth maps as obtained from c), the experiment and d), the hybrid TIR. The color bars represent a frequency scale in Megahertz.

results show that the hybrid TIR accurately describes the global properties of the sensor's response to a point source.

Fig. 30 shows the comparison of $g_T^{hyb}(\vec{r}, t)$ with $\partial h_T^{exp}(\vec{r}, t)/\partial t$ at the signal level for three microsphere locations of interest. Fig. 30a and 30b show the signals and spectra when the microsphere was located at the focus. Here, the agreement between the hybrid TIR and the experimental data is very good since the SNR is optimal. Figs. 30c and 30d show the results when the source was at the border of the focal zone, defined as the half-amplitude boundary in the amplitude map. The hybrid TIR and the experiment match, as we observe a slight shift of the spectra to lower frequencies in both cases. Figs. 30e and 30f show the results for a point at the first sidelobe in the bandwidth map, where the amplitude of the sensitivity field is about 15% (–16 dB) of that in focus. The hybrid TIR still reproduces the experimental findings, even though this point is outside the focal zone and its signal has a very low SNR. The results demonstrate that signals originated outside the focal zone are not only measured with lower amplitude, but also that their spectra are distorted in non-trivial manner. The overall good correspondence between the calculated TIR and the experiments
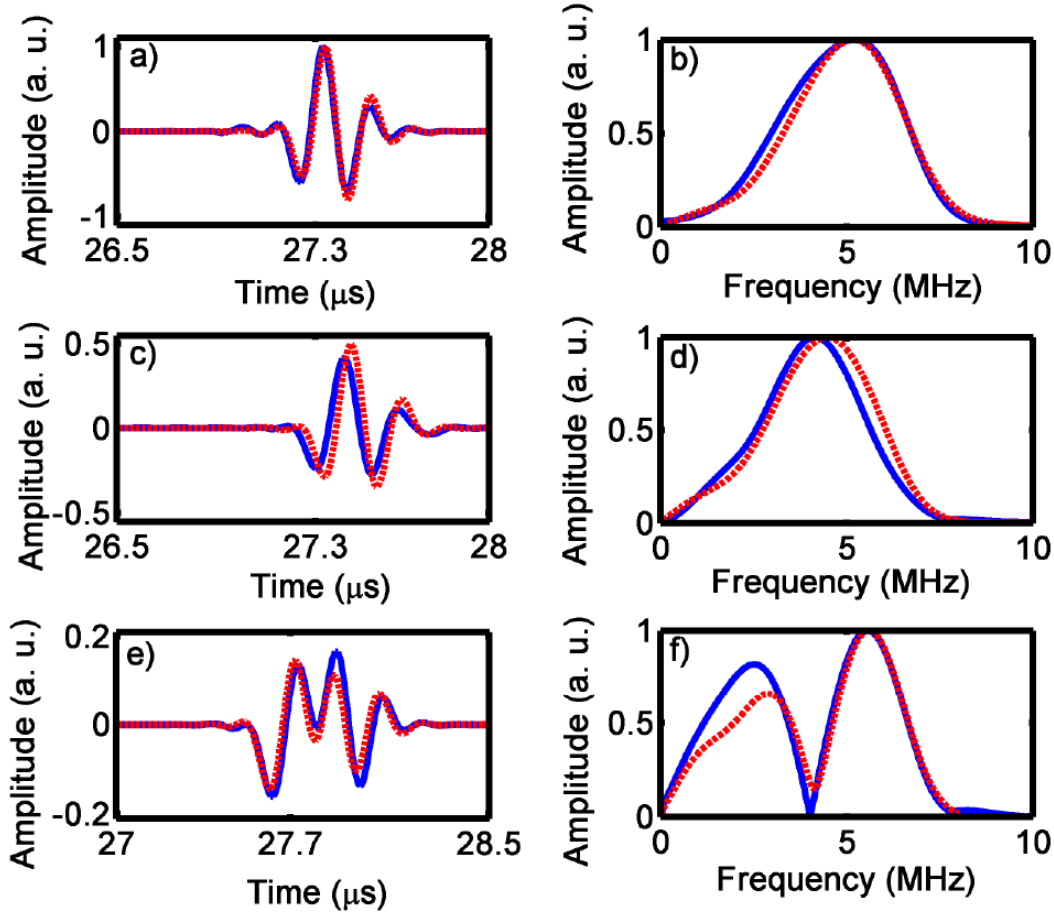
Figure 30: Validation of the hybrid TIR at three representative locations in the measurement grid. The experimental signals (blue/solid) and the ones calculated with the hybrid method (red/dashed) are shown in the left column. Their respective spectra are depicted in the right column. All signals come from points located at *x = 0.0 mm* but different *y* positions. *Top row:* emitter located at the focal point of the transducer, *y = 0 mm*. *Middle row:* point located at *y = 4 mm*, the boundary of the focal zone. *Bottom row:* point located at *y = 8 mm*, one of the sidelobes of the bandwidth map. See text for details.

confirms that the hybrid method provides an accurate description of the response of the sensor to a point source.

The comparison between the amplitude and bandwidth maps of $h_T^{hyb}(\vec{r}, t)$ and $h_T^{exp}(\vec{r}, t)$, which have been corrected for the source contribution, is shown in Fig. 31. Figs 21a and 21c show the amplitude and bandwidth maps of $h_T^{hyb}(\vec{r}, t)$ respectively. The wider field-of-view and smoother appearance of the maps, when compared to the ones obtained for $g_T^{hyb}(\vec{r}, t)$ are due to the presence of the low frequencies in the spectrum of $h_T^{hyb}(\vec{r}, t)$. In comparison, the experimental maps are completely blurred by low-frequency fluctuations. The bandwidth map shows a slightly better match to the hybrid TIR's map than the sensitivity map. This is to be expected since the effective bandwidth is a global property of the signal, and it is therefore more robust against low-frequency fluctuations than the
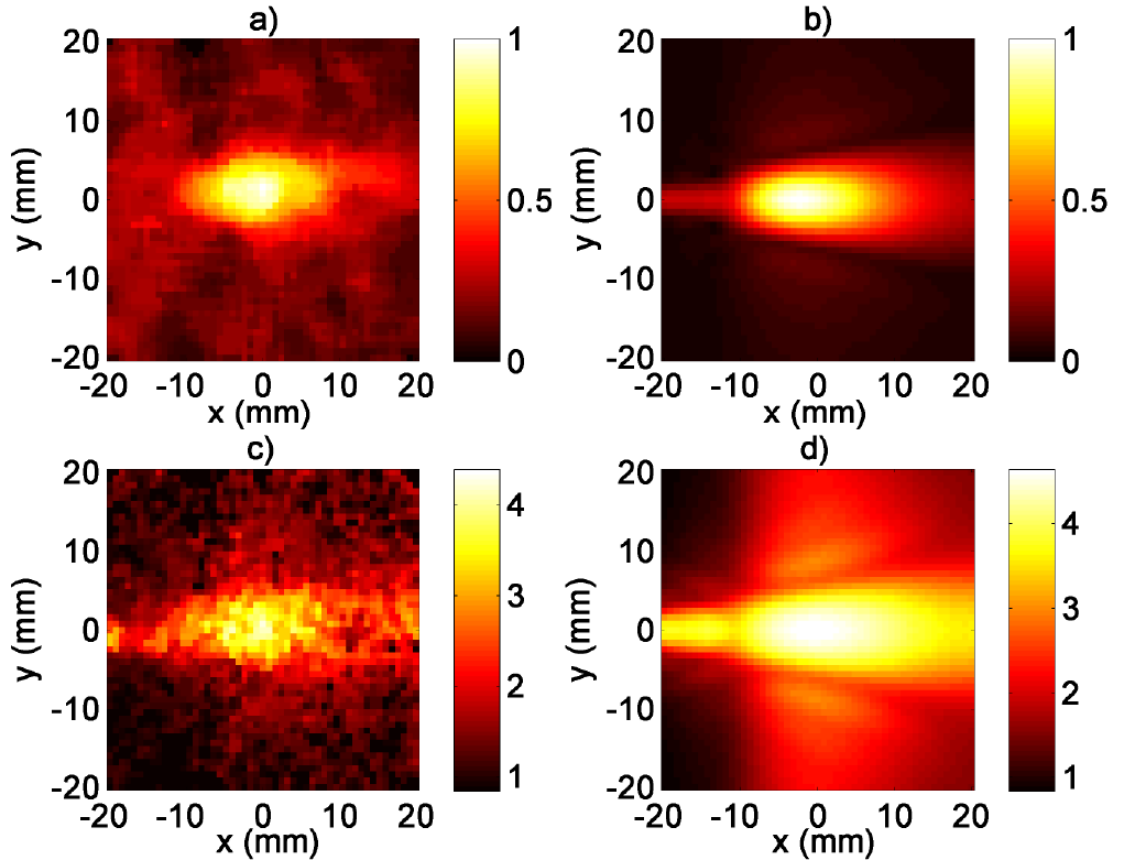
Figure 31: Demonstration of the instability of the experimental TIR upon integration. The top row shows the amplitude maps of the TIRs, as resulting from a), $h_T^{exp}(\vec{r}, t)$, and b), $h_T^{hyb}(\vec{r}, t)$. The color bars represent relative amplitude with respect to the maximum. The bottom row shows the bandwidth map as obtained from c), $h_T^{exp}(\vec{r}, t)$ and d), $h_T^{hyb}(\vec{r}, t)$. The color bars represent a frequency scale in Megahertz.

amplitude. The findings depicted in the figure illustrate the unreliability of the experimental method for obtaining the TIR of the sensor.

Fig. 32 shows the comparison of $h_T^{hyb}(\vec{r}, t)$ and $h_T^{exp}(\vec{r}, t)$ at the signal level. The figure depicts an example of two signals from neighboring points in the measurement grid for the experimental and the hybrid TIR. The points are located along the *y* axis, 0.8 mm apart from each other in the *x* direction. The signals and spectra obtained with $h_T^{hyb}(\vec{r}, t)$ are very similar to the experimental results, especially at frequencies above 2 MHz. Such agreement is to be expected, since the proposed and the experimental TIRs have been shown to match previously. On the other hand, the experiment shows a difference of up to 50 % in spectral amplitude at low frequencies between the neighboring signals. The fluctuations at low frequencies are therefore the origin for the distorted appearance of the experimental fields shown in Fig. 31. The findings showcase the fundamental limitation for the retrieval of the TIR through purely experimental means.
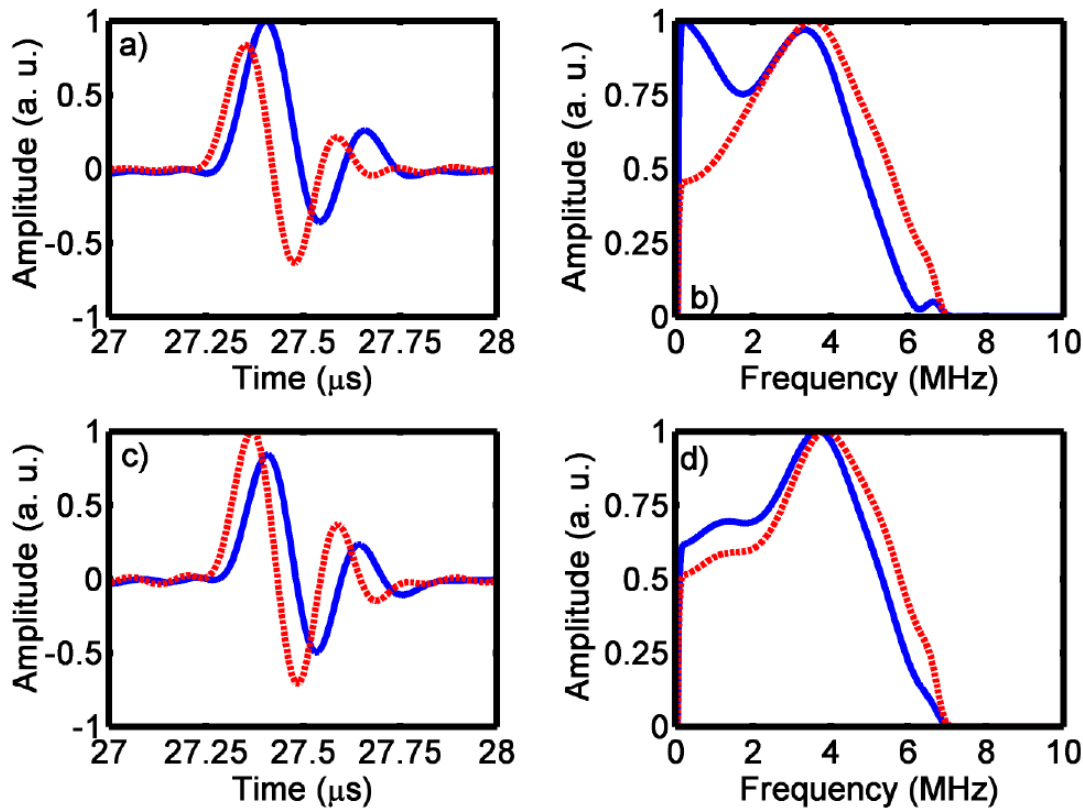
Figure 32: Example of the instability of the experimental TIR upon integration. The top row shows a), the experimental signals and b), their spectra, for contiguous points in the scanning grid. The blue/solid curves correspond to a point located at (x, y) = (-4.0, 0.0) mm; the red/dashed curves, to a point at (x, y) = (-4.8, 0.0) mm. The bottom row shows c) the signals and d) their spectra, as described by the hybrid TIR at the same grid points. See text for details.

3.4.5 Conclusion

The performance of the hybrid method for the determination of the total impulse response of optoacoustic transducers was assessed. The method is based on modeling the optoacoustic measurement process as a linear system. The response of an ultrasound transducer was described in terms of spatially dependent and independent responses. The spatially dependent response, the SIR, was numerically computed for points in- and outside the focal zone of the transducer. The spatially independent response, the EIR, was determined through experiment. The EIR and the SIR were combined through temporal convolution to yield the total, spatially dependent response of the sensor, the hybrid TIR.

The method's performance was assessed by comparing the modeled transducer response to an optoacoustic point source with the experimentally measured one. The spatial variation of signal amplitudes and bandwidths predicted by the hybrid TIR showed good agreement with the measurements. The results confirm that the hybrid TIR accurately

describes the sensor's response to optoacoustic sources located in- and outside the focal zone.

The hybrid TIR offers several advantages over alternative descriptions of the sensor response.

First, owing to the high SNR of the EIR measurement, the hybrid TIR provides an accurate description of the sensor response at low-frequencies. This is in contrast to purely experimental methods, which yield a sensor response that is corrupted by low-frequency noise.

Second, the SIR simulation was based on the exact geometry of the sensor and provided a noiseless description of its spatial properties. Therefore, the hybrid TIR accurately describes the sensor response even outside the focal zone, where the sensitivity is low.

Finally, the TIR provides a unified description of the measured spatial variations in phase, amplitude and frequency spectrum of optoacoustic signals. Therefore, sensor characteristics such as the sensitivity field or the frequency response are but representations of the TIR and can be obtained naturally from it.

The method has some limitations, which are also separable in the two components of the TIR.

For one part, the measurement of the EIR is in principle suited for a very broad span of frequencies (up to 20 MHz), as was discussed in section 3.2. If the EIR characterization at these frequencies was available, the hybrid TIR could be easily calculated. However, the present work deals with the combination of the EIR and the SIR as a general procedure, and the microscopic regime poses challenges of its own that do not relate to the hybrid method. The EIR calibration at high-frequencies lies therefore beyond the scope of this work.

For the other part, the numerical SIR calculated herein would be erroneous if the sensor's response was not uniform along its surface. This effect is called apodization, and the calculation of the SIR can be modified to include it [26]. However, in the case of the sensor discussed herein, the possibility of an apodized surface is ruled out by the experimental validation of the hybrid TIR. Furthermore, the hybrid TIR can be used as a standard against which to test the presence of apodization or fabrication defects on the sensor surface.

In conclusion, the method presented herein enables the determination and calibration of the spatio-temporal response of ultrasound sensors with optoacoustic means. The obtained response represents an important component in the characterization of optoacoustic systems, as it encompasses all of the sensor-related phenomena. More importantly, the hybrid method offers the possibility of using the sensor's response for imaging applications, knowing that it describes the optoacoustic detection process accurately.

4. RECONSTRUCTION ALGORITHMS FOR MICROSCANNING

In the previous chapter, the effect of the transducer properties on optoacoustic signals was assessed and a general framework for their characterization was provided. It was shown that the sensitivity and bandwidth of a detector is in general dependent on the relative position between source and sensor. In most optoacoustic image reconstruction algorithms, however, the assumption is made that the detector behaves as a point-like sensor with infinite bandwidth. The aim of this chapter is to illustrate the degraded imaging performance that results from such assumptions, and develop image reconstruction algorithms that overcome those limitations. This is done within the context of a specific optoacoustic modality: microscanning. However, from the results in this chapter some general principles about optoacoustic image formation with sensor properties may be established.

The chapter starts (Section 4.1) with an introduction to the concept of microscanning, its applications and a description of the image reconstruction problem. In Section 4.2, microscanning with unfocused detectors is investigated and the effects of the sensor spatial properties on the reconstructed images are showcased. Several modifications to standard image reconstruction algorithms, based on approximate descriptions of the sensor properties, are presented and their imaging performance is assessed with experiments. In Section 4.3, microscanning with focused detectors is studied. An algorithm for accurate image reconstruction that takes into account the exact sensor properties is presented and its performance assessed both in simulations and experiment. The results of the chapter are discussed at the end of that Section.

4.1 Introduction to Microscanning

4.1.1 The technique

By microscanning we refer to any optoacoustic imaging modality whereby a sensor is scanned in the two directions of a plane (the scanning directions) at a distance from the sample, as shown in Fig. 33a. The planar configuration is advantageous with respect to a tomographic arrangement for applications where it is not possible to surround the sample with detectors. Thus, microscanning is well-suited for the superficial, high-resolution imaging of organs, extremities and subcutaneous tumors, and has found applications to vasculature imaging [19], functional imaging and hemodynamics [16].
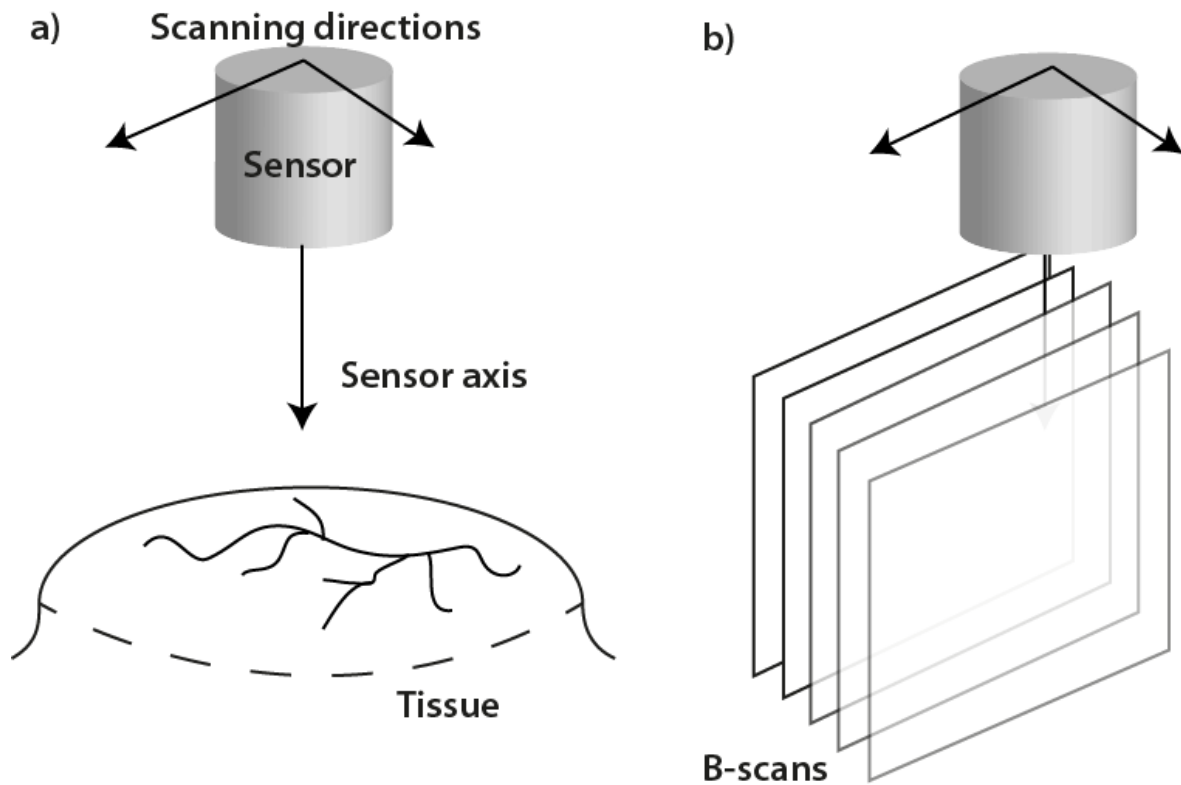
Figure 33: *a)* Concept of microscanning: a sensor is scanned along two perpendicular directions, at a fixed distance from the sample. *b)* Microscanning can be understood as the stacking of line-scans, where each of them provides a depth-resolved view of the sample. See text for details.

Different applications have different requirements with respect to the resolution and the imaging depth. For one part, microscanning setups may achieve submicron resolutions at very shallow penetration depths, which effectively qualifies as optoacoustic microscopy [16]. On the other part, microscanning at several millimeters deep, with resolutions in the tens of microns, may be described as mesoscopic imaging. The present work is aimed towards mesoscopic imaging, but some of the techniques developed herein may find application on optoacoustic microscopy as well. As both imaging regimes are ultimately established by the combination of illumination and detector, a more detailed overview of the different design strategies is now presented.

The illumination may be adjusted to excite either a broad tissue region or a localized area. Bulk illumination generates optoacoustic sources within a volume larger than the imaging resolution. Thus, signals from different scanning positions may be combined numerically to improve image quality or extend the imaging depth up to a few millimeters [50]. This approach is therefore suited for mesoscopic applications. Alternatively, optoacoustic microscopy setups utilize a spatially confined illumination scanned together with the sensor, which may help to achieve optical resolution at the expense of penetration depth [18]. Unless stated otherwise, bulk illumination was assumed throughout the present chapter.

The sensor shape and frequency band are chosen in order to provide the optimal resolution at the required imaging depth. Mesoscopic applications have been investigated with a variety of sensors. Spherically focused transducers have been used at frequencies ranging from 5 MHz, for the imaging of deep seated organs [42, 61], up to 50 MHz, for the visualization of superficial vasculature [18, 41, 62]. Such sensors provide good resolution and sensitivity in the focal zone, but these properties degrade rapidly away from the focus. This potential drawback can be compensated with image reconstruction algorithms, which shall be demonstrated in more detail in section 4.3.

Alternatively, point-like sensors have been generated optically in a Fabry-Perot interferometric configuration, resulting in detectors with relatively flat frequency responses up to 20 MHz. Such a sensor can achieve a resolution of ~70 μm at the tissue surface and imaging depths of a few millimeters. The applications have been mostly to vasculature imaging [19, 50].

Finally, one of the scanning directions may be substituted by an array of detectors to shorten acquisition times, which has been reported up to frequencies of 30 MHz and resolutions of ~70 μm [17]. Due to current limitations in the fabrication technology of transducer arrays at frequencies higher than 30 MHz, such an implementation of microscanning is therefore limited to mesoscopic applications.

For microscopic applications, only spherically focused transducers at frequencies of 50 MHz or higher have been utilized [18, 63]. By providing localized illumination at the focal point of the transducer, optoacoustic microscopy with optical resolution has been achieved. However, as discussed previously, this results in a very limited penetration depth and was not considered in this work.

In the first part of this chapter (Section 4.2), microscanning was investigated at relatively low frequencies (up to 6 MHz), with the aim to develop an understanding of the technique and the challenges related to image reconstruction. In section 4.3, however, the frequency of the transducers was increased to 10 and 25 MHz, as the experiments and reconstruction methods were gradually scaled-down to actual mesoscopic applications.

4.1.2 The image reconstruction problem

Before the image reconstruction problem is stated, it is convenient to define some relevant concepts. When performing microscan measurements, the full 2D scan can be usually divided into a set of parallel linear scans, as illustrated in Fig. 33b. The figure shows that each linear scan provides a depth-resolved sectional view of the sample. This view is

typically referred to as B-scan, for historical reasons[*]. The stacking of several B-scans provides a 2D+time dataset which, after signal processing, may yield a 3D representation of the sample. Which one of the scanning directions is referred to as B-scan is in general a matter of definition for a particular experiment. The image reconstruction algorithms reported in the present chapter were applied to the reconstruction of single B-scans, which were later stacked to form the final image. Thus, the image reconstruction problem for microscanning is stated herein in terms of the image formation problem for B-scans[†].

Let us describe the general problem with a simple model: a set of sources scanned by a point-like detector. Fig. 34a shows a sensor that is scanned along the x direction for N positions, with a scanning step size Δx. Several optoacoustic sources are originated in the region in front of the sensor at different depths. The optoacoustic waves generated by one absorber reach the sensor at time instants t. Due to the different times-of-flight between the source and the sensor at positions 1 and 2, there exists a delay Δt between the measured signals s_1 and s_2, as shown in Fig. 34b. The delay can be easily deduced from the Pythagorean Theorem and is dependent on the angle between sensors 1 and 2 as seen from the absorber. Therefore, when the signals measured at all the scanning steps are stacked to form the B-scan, as shown in Fig. 34c, the signal maxima appear at different depths for each sensor position. Additionally, due to the spherical propagation of the waves, the measured signal amplitudes depend on the sensor position as well. A signal-processing or image reconstruction algorithm shall therefore compensate for such a delay in the signals in order to recover the original position and amplitude of the absorbers, Fig. 34d.

In the previous chapter it was demonstrated that the spatial properties of finite-sized transducers depend non-trivially on the relative position between sensor and source. The spatial impulse response (SIR) of the transducer may alter the features of the B-scan described in Fig. 34c in several ways. First, signals measured in front of the transducer may be measured with higher amplitude than signals measured at other positions, due to the (frequency-dependent) sensitivity field of the sensor. Second, the detected signals may be distorted due to the filtering properties of the SIR. Finally, the times at which the signals are measured may also differ from the spherical spreading assumed in Fig. 34, since the minimum distance between source and sensor depends on the geometry of the detector. As a result, standard image reconstruction algorithms, which typically assume point-like sensors, have to be modified to include the properties of arbitrary detectors.

---

[*] In such a representation, the Brightness in the image is proportional to the signal amplitude, hence B-scan.

[†] For a discussion of microscanning as a full 3D modality, refer to the conclusions in the last section.
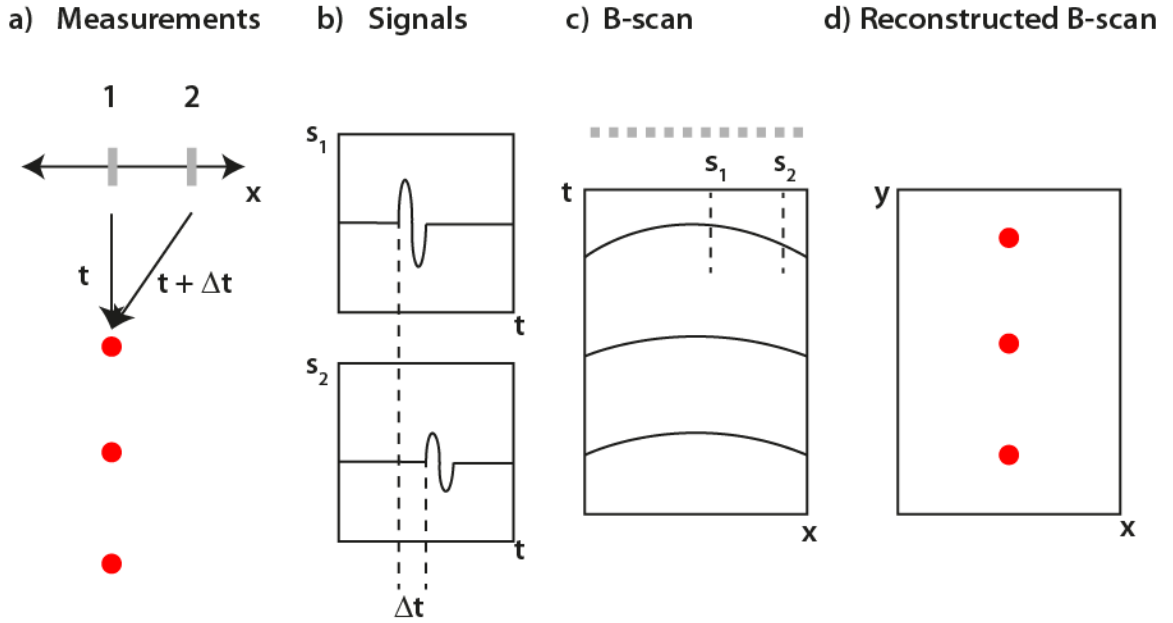
Figure 34: the image formation problem for a B-scan. *a)* Sources scanned by a sensor. *b)* Delayed signals for sensor positions 1 and 2. *c)* The stacking of the signals measured for each sensor position results in a B-scan, where the signals appear delayed with respect to the central position. *d)* B-scan after image reconstruction or signal processing. See text for a detailed description.

At this point, it is relevant to outline under which conditions a sensor may be considered point-like.

Due to the diffractive nature of optoacoustic waves, whether a sensor of diameter a (unfocused) may be considered point-like or finite-sized is dependent on its distance to the source and the wavelength λ of the acoustic wave [31]. This can be quantitatively determined by recalling the definition of the diffraction regimes (cf. Chapter 2). A point located at a distance R from the sensor was considered to be in the far field if $R \gg a^2/\lambda$ and in the near field whenever $R \ll a^2/\lambda$, which results in distinct diffraction patterns. It can be shown that for points located at $R \geq 3a^2/\lambda$, the acoustic waves propagate approximately as spherical waves and the sensor can be thus considered as a point-like detector for that wavelength[*] [27]. $3a^2/\lambda$ is defined as the "near field distance" of the transducer, where λ is given by its central frequency. For optoacoustic applications, which are inherently broadband, we find a more adequate definition $N_F \equiv 3a^2/\lambda_{min}$ where λ_{min} is the lowest wavelength (i.e., corresponding to the highest frequency) in the measured signal spectrum. Therefore, herein it is considered that a sensor is point-like if the sources are generated at distances greater than N_F.

The different behavior of point-like and finite-sized unfocused sensors in microscanning applications is investigated in the following Section.

---

[*] The reciprocity theorem is implied in this discussion.

4.2 Microscanning with unfocused detectors

4.2.1 Motivation

Depending on their size, unfocused detectors exhibit different desirable properties for microscanning applications. For one part, point-like sensors (as defined above) exhibit a wide angle of acceptance for most frequencies. As a result, the signals measured at several sensor positions may be used to reconstruct for the spherical spreading of the optoacoustic wave. Conversely, sensors with large diameters have a limited angle of acceptance but offer good sensitivity for sources originating at relatively narrow detection angles [27]. In this Section, it is investigated whether the limited field-of-view of unfocused sensors may be compensated with signal processing and image reconstruction.

In section 4.2.2 two standard reconstruction algorithms for B-scans are described: synthetic aperture and Back-projection. In section 4.2.3 a description of the experimental setup and the sensors is provided. In section 4.2.4 B-scan reconstructions with the standard methods are presented. In section 4.2.5 the limitations of the standard Back-projection technique are explained in terms of the sensor properties. In sections 4.2.6 and 4.2.7 two distinct modifications of the conventional back-projection algorithm are presented and its performance assessed under the same experimental conditions. Finally, in section 4.2.8 the results of the section reviewed and the suitability of using unfocused transducers for microscanning is discussed.

4.2.2 Synthetic aperture and Back-projection

The synthetic aperture algorithm (SA), also known as delay-and-sum, provides an intuitive solution to the problem of B-scan image formation. An illustration of the method is provided in Fig. 35a (top row). The SA algorithm can be described as follows: for each sensor position i, the depth-dependent delays Δt_{ij} for the neighboring sensors j are computed and their signals are delayed accordingly. Afterwards, the j time-shifted signals are added to the signal of interest i. The reconstructed B-Scan is thus formed by stacking the corrected signals. Since the time-shifts effectively compensate for the phase-difference between the signals at different sensor positions, this process is commonly referred to as a "coherent summation" of the signals [31].

In echographic ultrasound, the sensor positions are typically given by the location of the the elements of a transducer array. In such applications, the SA algorithm is used not only to coherently sum the measured signals in the receive mode, but also to focus the ultrasound wave sent into the tissue at a given depth. By a clever choice of the delay for each sensor, the emission direction can be steered at a given angle or focusing can be adapted to
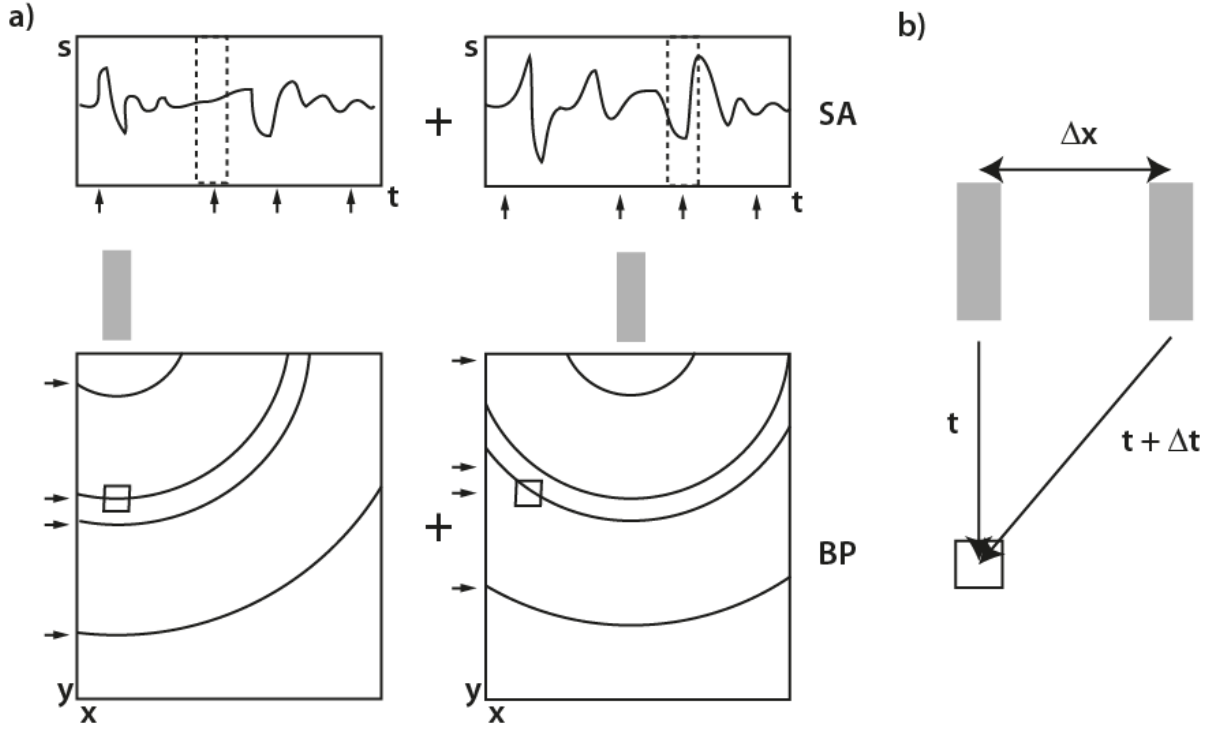
Figure 35: *a)* Equivalence between the Synthetic Aperture (SA) and the standard Back-projection algorithms. The top row represents the SA processing of two signals and the bottom row the intermediate steps of an image reconstruction with the Back-projection algorithm. The dashed-boxes in the top row represent the signal samples that are used to reconstruct the highlighted pixel in the bottom row, and are related by a delay dependent on the pixel position and the distance between the sensors, as shown in *b).*

the distance and resolution desired. These procedures effectively determine the shape of the ultrasound beam and for this reason SA is also sometimes called "beamforming" [31].

The SA processing for each scan line may thus be expressed as

$$s_i(t) = \sum_{j=i-n}^{i+n} w(t,j)s_j\big(t - \Delta t_{ij}\big).$$

(4.1)

where Δt_j represents the time delay for each time instant and each pair of signals *ij*. The summation takes place over $2n$ individual sensor positions; in general $2n$ is at most equal to the total number of signals. $w(t,j)$ represents a weighting function, called "apodization factor" or "window function" and may be used to give more weight to signals *j* that are closer to the signal of interest *i*. From Eq. (4.1) it follows that the SA algorithm improves the signal-to-noise ratio (SNR) of the B-scan by effectively averaging neighboring signals.

Back-projection was described in Chapter 2, but a short reminder is provided herein. The general Back-projection formula (Eq. (2.16)) can be discretized for a scanning geometry and a discrete set of sensor positions. This is achieved by substituting the integral over the detection surface with a summation over individual sensor positions:

$$p_0(\vec{r}) = \sum_{i=1}^{N} \Omega(\vec{r}, i) \left[p(\vec{r_i}, t) - t \frac{\partial p(\vec{r_i}, t)}{\partial t} \right]\Bigg|_{t = |\vec{r} - \vec{r_i}|/c} . \qquad (4.2)$$

where $\vec{r} = (x, y)$ are points on the reconstructed image and the solid-angle weighting factor has been rewritten as $\Omega(\vec{r}, i)$. For each pixel in the image, thus, Eq. (4.2) expresses a delayed sum of the measured signal at time and its derivative, weighted by a factor $\Omega(\vec{r}, i)$.

Herein it is proposed that the SA method is equivalent to the first term of Eq. (4.2). Likewise, the derivative term of Eq. (4.2) can be understood as a SA algorithm applied to $t\, \partial p(\vec{r_i}, t)/\partial t$. In order to explain this assertion, let us analyze the direct term of Back-projection together with the SA method as represented in Fig. 35.

For one part, the top row of Fig. 35a shows the signals for two different sensor positions; the arrows mark different time instants. As described previously, in the SA method the first signal is corrected by the second by computing the time delays between them for each depth and summing up coherently. For the other part, the bottom row of the figure shows the process of image formation with Back-projection: for each sensor position $\vec{r_i}$, pixels located at a distance $|\vec{r} - \vec{r_i}|$ from the sensor are assigned a value $p(\vec{r_i}, |\vec{r} - \vec{r_i}|/c)$ i.e., the signal sample that corresponds to the time-of-flight between sensor and pixel. This is referred to as "back-propagation" of the signal. The sub-images obtained for the back-propagation at each sensor position are then summed up to obtain the final image. Therefore, the value of the highlighted pixel in the bottom row is actually calculated with the signal samples highlighted in the top row. This demonstrates that the Back-projection algorithm and the SA procedure are in principle equivalent. In the results section this assertion will be verified experimentally and therefore, from this point on, all proposed modifications are applied to the Back-projection algorithm.

In practical terms, of course, SA yields corrected signals, which are then stacked to form the reconstructed B-scan. Therefore, the resulting image has a maximum of N pixels along x and a number of pixels T along y, where N represents the total number of scan positions and T the number of samples in the signals. For Back-projection images, the ROI may be defined with a number of pixels determined by the desired resolution. Therefore, images reconstructed with both methods will be identical only if the Back-projection image is calculated in a grid of N by T pixels.

The reconstruction methods described herein have been developed under the assumption that the detector is point-like [20, 31]. In the following sections, it will be shown

that such an approximation may result in the breakdown of the Back-projection method if a different sensor is used. In particular, a flat detector of large area (compared to the imaged object) results in severely distorted images [23, 24]. Several corrections for these artifacts are proposed, and their performance was assessed with experimental measurements. The modifications to Back-projection are discussed after the preliminary results with standard Back-projection have been presented. This heterodox layout was chosen exceptionally to better develop an intuition of the problem faced and the solutions proposed, without having to turn back to the present section for reference.

4.2.3   Materials and methods

a)   Source and excitation

In order to assess the imaging performance of the different reconstruction methods, a simple phantom with a point-like source was built. A graphite rod, 0.3 mm in diameter, was cut to a length of about 0.5 mm and was subsequently encrusted in white plastiline, to provide a surrounding medium scattering to light. The graphite dot was illuminated by the 532 nm pump-beam of a tunable optical parametric oscillator laser (Vibrant, Opotek Inc., Carlsbad, California), at a repetition rate of 20 Hz and pulse duration of 8 ns. This resulted in a strong isotropic source of optoacoustic waves. The source and the illumination were left static for all measurements and only the transducers were scanned.

b)   Detectors and processing

The signals were measured by two sensors of different diameters. The first sensor was an unfocused transducer, 6 mm in diameter, with a center frequency of 2.25 MHz and a -6 dB bandwidth of 120% (model V323, Panametrics-NDT, Waltam, MA). The second sensor was the custom-made PVDF hydrophone used for the plate characterization in the previous chapter. It had 1 mm in diameter and was calibrated by the manufacturer from 1 to 20 MHz (Precision Acoustics, Dorset, United Kingdom). Its frequency response can be assumed flat to within 10% from 1 to 10 MHz. However, in order to compare the measurements under similar conditions, the signals acquired with both sensors were band-pass filtered between 50 kHz and 5 MHz. Within this bandwidth, the near field distances result in $N_{Fh} = 10$ mm for the hydrophone and $N_{F6} = 30$ mm for the 6 mm transducer. The sources where scanned at three different depths d, chosen so that the hydrophone could be considered a point-like sensor whereas the 6 mm sensor cannot, i.e. $N_{Fh} < d < N_{F6}$. The signals were digitized by a DAQ-card at a sampling rate of 100 MS/s (GageScope, Lockport, IL).
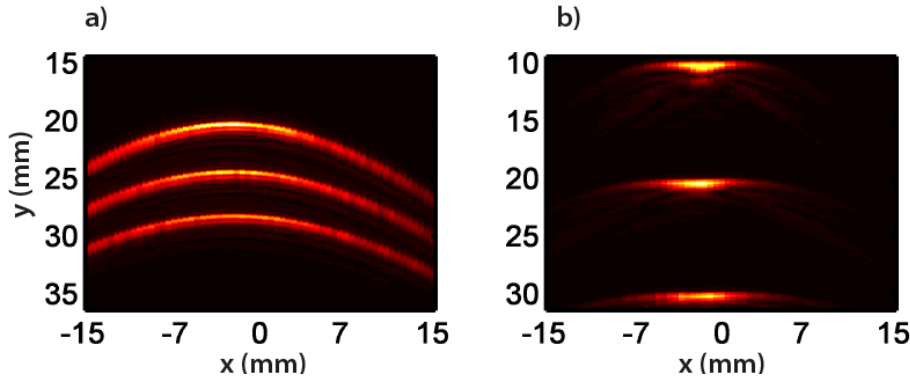
Figure 36: *a)* B-scan of three sources taken with a sensor with 1 mm diameter. *b)* B-scan of three sources taken with a 6 mm transducer. The images are shown in a linear color scale and are normalized to their respective maxima. See text for details.

The sensors were mounted on a 3-axis translation system for positioning (Thorlabs GmbH, Karlsfeld, Germany). The measurements were done by scanning the sensors for 61 positions over a range of 30 mm on the plane where the source was contained. Such a scan was repeated three times for each sensor, each time at a different axial distance from the source. The three scans are always represented in the same image for convenience.

In the previous chapter, it was also argued that the spatial properties of the detector are affected by its electrical impulse response (EIR). Since the EIR represents a global filtering on the measured signal, the EIR was in general corrected before image reconstruction, when available. Such a correction was done with a Wiener filter applied to each signal [64].

c) Image reconstruction

The SA algorithm was implemented as per Eq. (4.1). The Back-projection algorithm was implemented according to Eq. (4.2). In both cases the reconstruction resulted in images with the following size: 30 mm in 61 pixels (columns) along the scan direction *x* and 25 mm in 200 pixels (rows) along the depth *y*. This asymmetric ROI was chosen to make the comparison between SA and Back-projection possible, as discussed in the previous section. Finally, the images are represented as the norm of the Hilbert transform (i.e., envelope) for each processed signal (or image row) [31].

4.2.4 Results with Standard Back-projection and Synthetic Aperture reconstructions

In Fig. 36, the unprocessed B-scans for both detectors are shown. The B-scan of the point-like detector (Fig. 36a) shows the expected spreading of the signals due to the wide angle isotropy of a point-like sensor. The B-scan taken with the 6 mm sensor (Fig. 36b) shows a different behavior due to the limited angle of acceptance of the transducer. The

consequences of these very different behaviors can be observed in the reconstructed images, as shown in the following.

In Fig. 37, the B-scan taken with the 1 mm transducer and the resulting SA and Back-projection reconstructions are shown. Fig. 37a shows the unprocessed B-scan for reference. Figs. 37b and 37c show the SA and Back-projection (direct term) reconstructions respectively. The results demonstrate that SA and Back-projection are essentially the same algorithm, one expressed as signal-processing method (SA) and the other as an image reconstruction procedure (Back-projection).

Fig. 37d shows the Back-projection reconstruction including the derivative term. The image shows better resolved absorbers with respect to the previous images. This is due to the multiplication by t in the derivative term of Eq. (4.2), with results and a ramp-filter in the frequency domain and thus enhanced higher frequencies [21].

Fig. 37e shows the profile of the reconstructions, taken along the depth direction (as shown in Fig. 37c). The profile actually shows all 3 reconstructions, but the SA (blue) and direct Back-projection (red) are completely undistinguishable. There is a 90% difference in the reconstructed amplitudes between the source at 15 mm and the source at 25 mm, due to the actual size of the sensor, which is only approximately point-like.

Fig. 37f shows the profile of the reconstructions along the scanning direction. The full-width at half-maximum (FWHM) of the full Back-projection is ~1 mm, i.e., the diameter of the sensor, as expected from the theory [23]. Overall, the results demonstrate the accuracy of standard Back-projection and SA when reconstructing B-scans with a point-like sensor.

The reconstruction results for the 6 mm transducer are shown in Fig. 38. The unprocessed B-scan is shown in Fig. 38a, and Figs. 38b to 38d show the image reconstructions with SA, direct Back-projection and full Back-projection respectively. The reconstructed images show only a slight improvement of the lateral resolution with respect to the unprocessed B-scan. In particular, it is interesting to note that even the full Back-projection reconstruction (Fig. 38d), which is biased towards higher frequencies, does not improve the lateral resolution notably. Fig. 38e shows the reconstruction profile along the depth (as indicated in Fig. 38c). The source amplitudes reconstructed with SA and direct Back-projection increase with their distance to the transducer, whereas for full Back-projection they decrease. While this effect was already observed for the 1 mm detector, it is actually exacerbated for the 6 mm sensor, which confirms that such a reconstruction artifact
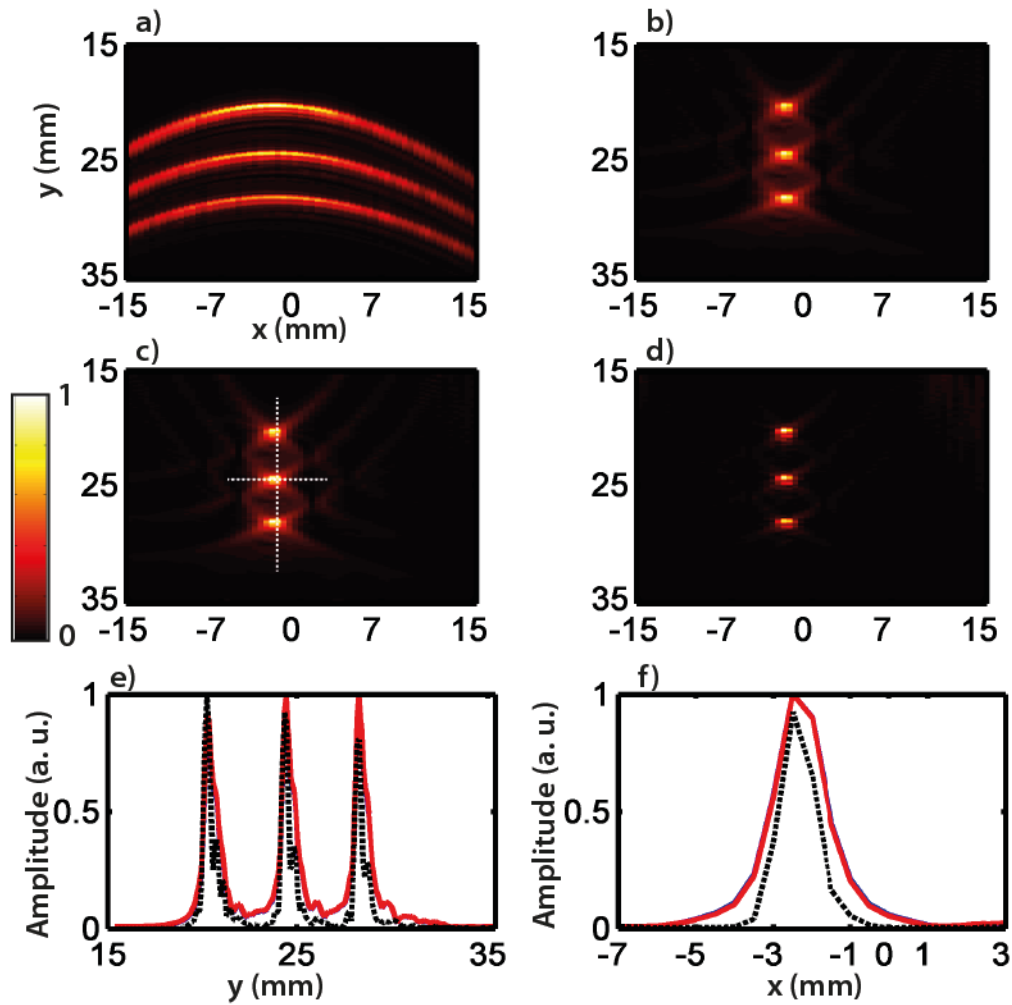
Figure 37: B-scan reconstructions with the 1 mm sensor. *a)* B-scan of the three sources, unprocessed. *b)* SA reconstruction. *c)* Back-projection reconstruction (direct term). *d)* Back-projection reconstruction (direct and derivative terms). *e)* Profile of the reconstructions taken along the vertical direction as shown in *c)*. Black: Back-projection with both terms. Red (and blue, but it is undistinguishable): Back-projection with the direct term (and SA). *f)* Profile along the scan direction, same colors as *e)*.

is dependent on the size of the sensor. Fig. 38f shows the lateral profile for the middle absorber with a FWHM of ~6 mm as opposed to the ~0.5 mm source size.

The results demonstrate the breakdown of the Back-projection method when directly applied to a B-scan, if the sensor is unfocused and its diameter is larger than the source. These results can be understood by analyzing the spatial properties of the sensors and their divergence with respect to a point-like behavior, which is presented in the following section.

4.2.5 Analysis of transducer properties

The TIRs of two round transducers with diameters $D = 1$ mm and $D = 6$ mm were calculated with the method described in the previous chapter [26]. Briefly, a numerical
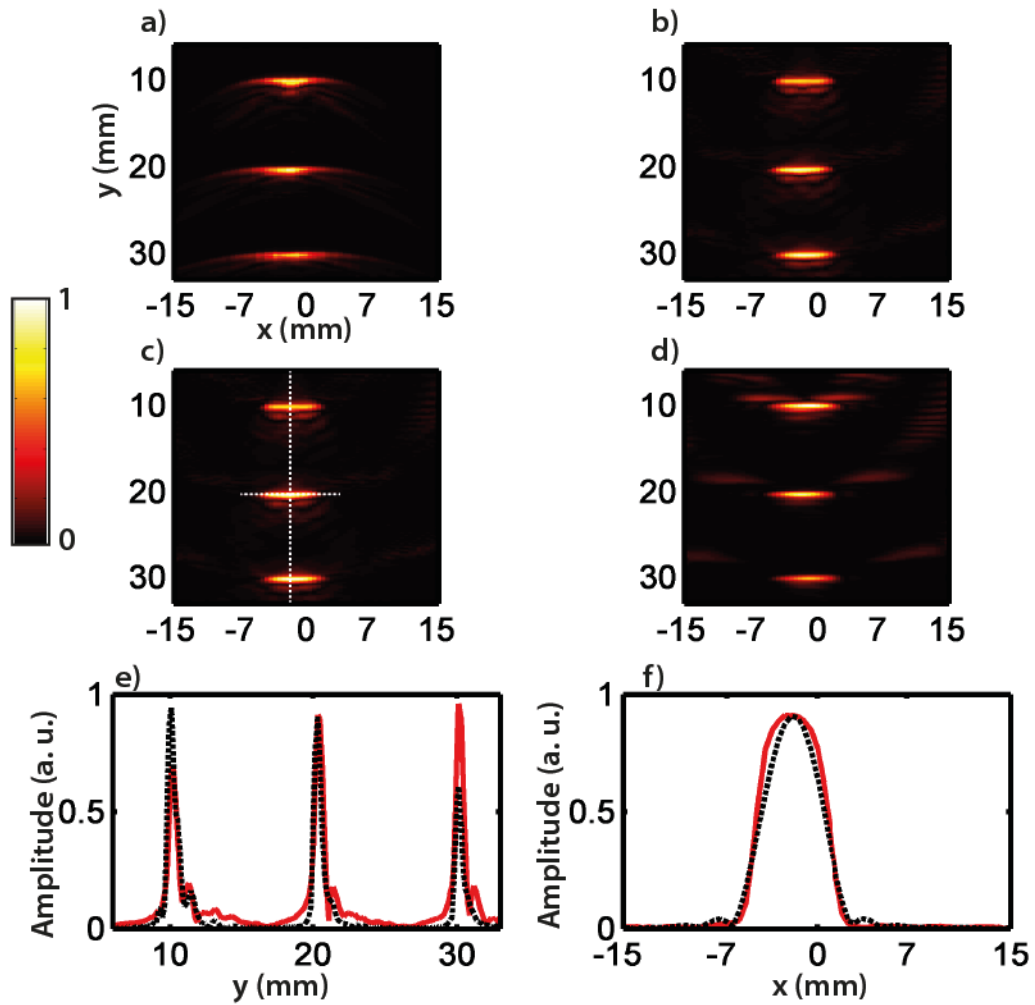
Figure 38: B-scan reconstructions with the 6 mm sensor. *a)* B-scan of the three sources, unprocessed. *b)* SA reconstruction. *c)* Back-projection reconstruction (direct term). *d)* Back-projection reconstruction (direct and derivative terms). *e)* Profile of the reconstructions taken along the vertical direction as shown in *c)*. Black: Back-projection with both terms. Red (and blue, but it is undistinguishable): Back-projection with the direct term (and SA). *f)* Profile along the scan direction, same colors as *e)*.

computation of the SIR of the sensors is convolved with the EIR of the sensor to yield the TIR. This results in a time-dependent function for points in front of the sensor, and said function defines the distortion of optoacoustic signals due to the sensor properties. The first sensor property to be analyzed was the time of arrival of the optoacoustic waves, as a function of the lateral position and depth of the source. We refer herein to this property as the "delay field" of the sensor.

In Fig. 39a, the delay fields for the 1 mm and 6 mm sensors are represented as a contour plot. The black dotted lines represent the contours of the delay field of the 1 mm sensor. That is, for each scanning position, the lines represent the time of arrival of the signal to the sensor. The red lines, on the other hand, represent the delay field of the 6 mm sensor. In this case, the behavior is different from that of a point-like source, and the delay
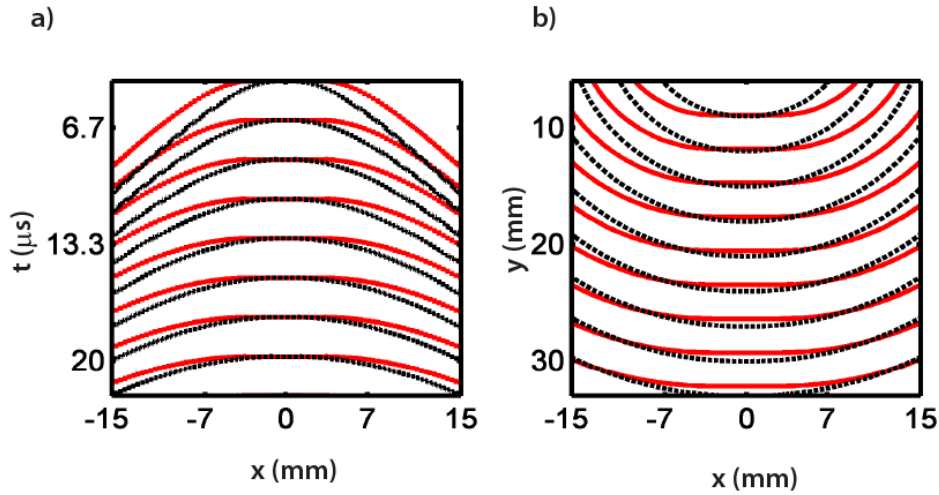
Figure 39: *a)* Contours of the delay fields of the 1 mm sensor (black dashed) and the 6 mm sensor. *b)* Back-propagation isochrones superposed with the ROI for the same sensors.

field shows a constant time of arrival for some scanning positions. The reason is that, whenever the source is at a lateral distance $|x| \leq D/2$ with respect to the transducer axis, the shortest distance between source and sensor (i.e., the signal delay) is constant. The results show that the time-delay assumed by standard Back-projection, based on point-like transducers, does not correspond to the actual signal delay measured by a large flat detector.

As shown previously (Fig. 35), Back-projection operates by back-propagating the signal measured at one sensor position onto the pixels in the ROI that fulfill $t = |\vec{r} - \vec{r_i}|/c$, i.e., onto circles centered on the sensor. Intuitively, the Back-projection algorithm may be modified by back-propagating onto pixels that correspond to the actual sensor's delays. The principle behind such a modification is illustrated in Fig. 39b. The back-propagation isochrones t for a point-like detector (black dashed lines) are superimposed on the imaging ROI. The isochrones t' that would correspond to a sensor with $D = 6$ mm are shown in red. However it can be easily understood that back-propagating the signals onto t' would effectively spread the signal over a wider extent of the ROI than in the case of standard back-propagation.

Let us now analyze the sensitivity and bandwidth fields that result from the TIR of the sensors. Fig. 40a shows the sensitivity field of the 1 mm sensor and Fig. 40b its bandwidth field. The fields are not exactly as isotropic as those of a point-like sensor[*] the approximation did not result in significantly degraded imaging performance. The fields of

---

[*] The fields corresponding to an ideal point-like sensor are not shown as they are somewhat trivial. The sensitivity field is the $1/r$ amplitude decay of spherical waves. The bandwidth field would be a constant function equal to the sampling frequency used in the calculation (i.e., virtually infinite bandwidth for all points in space).
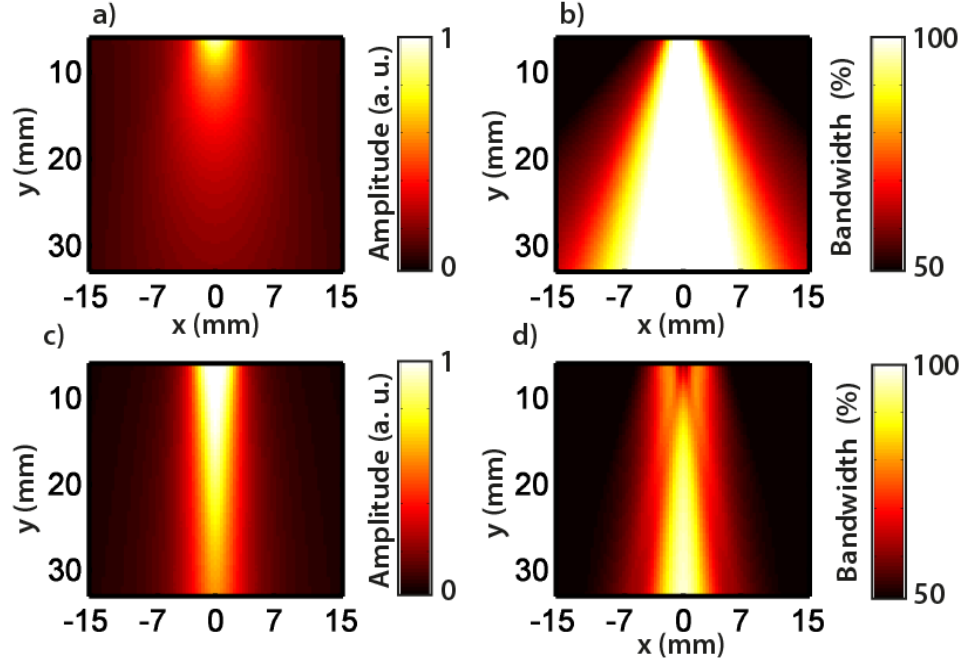
Figure 40: Simulations of the SIR of the sensors. *a)* Sensitivity field of the 1 mm sensor. *b)* Bandwidth field of the 1 mm sensor. *c)* Sensitivity field of the 6 mm sensor. *d)* Bandwidth field of the 6 mm sensor. All fields calculated within the measurement frequency band (50 kHz to 5 MHz).

the 6 mm sensor are shown in Figs. 40c and 40d, and they exhibit a completely different behavior. For one part, the sensitivity field indicates that only sources located in front of the sensor, (i.e., $|x| \leq D/2$) are measured with optimal amplitude. Conversely, the bandwidth field shows that signals from such sources are measured with at least 75% bandwidth with respect to the full bandwidth of the sensor ($\sim$2.7 MHz). We refer in the following to this region of the sensor's field of view as "the main lobe".

These analyses demonstrate that the signals that play a significant role for Back-projection reconstructions are those generated in the main lobe. In the following sections it is assessed whether the Back-projection algorithm may be modified to enhance the lateral resolution by weighting the relative amplitudes of the signals within the main lobe.

4.2.6 Weighted Back-projection

In this section, a modification of standard Back-projection is proposed in order to take into account the sensitivity field of the sensors. In a few words, the approach presented herein consists on applying a weighting mask to the back-propagation sub-images generated for each sensor position. By doing so, the signals back-propagated onto the ROI are limited to the main lobe of the sensor's field-of-view. A more detailed description of the method follows.

The standard Back-projection formula (Eq. (4.2)) expresses each of the sub-images $p_0(\vec{r}, i)$ as the weighted difference between signal and derivative, back-propagated to the ROI:

$$p_0(\vec{r}, i) = \Omega(\vec{r}, i) \left[p(\vec{r}_i, t) - t \frac{\partial p(\vec{r}_i, t)}{\partial t} \right]\Bigg|_{t=|\vec{r}-\vec{r}_i|/c}, \qquad (4.3)$$

where $\Omega(\vec{r}, i)$ can be understood as a weighting mask applied to the to the back-propagation term, which we define as $P[\vec{r}_i, t] = [\, p(\vec{r}_i, t) - t\partial p(\vec{r}_i, t)/\partial t]$. Herein it is proposed to substitute $\Omega(\vec{r}, i)$ by the sensitivity field of the transducer at the sensor position, defined as $\Psi(\vec{r}, i)$. However, since the width of the main lobe is in general inversely proportional to the frequency ([27], cf. Chapter 3), weighting the sub-images with the global sensitivity field would result in a mask that is too wide for the highest frequencies, and too narrow for the lowest frequencies in the signal.

Instead, the $P[\vec{r}_i, t]$ term is first divided into its Fourier components, which are back-propagated individually onto the ROI. Since we deal with discrete quantities, a given signal $s[t]$ may be expressed as the discrete summation over its frequency components [64], i.e. the inverse Discrete Fourier Transform of the signal spectrum $\hat{s}[f]$

$$s[t] = \Re\left\{ \sum_f \hat{s}[f] e^{-i\varphi(f,t)} \right\}, \qquad (4.4)$$

where $\Re\{\cdots\}$ represents the real-part of the quantity between brackets and $\varphi(f, t)$ is the phase of the signal. In this manner, we can back-propagate each frequency component of $P[\vec{r}_i, t]$, and weight it with the sensitivity field at the relevant frequency, $\psi(\vec{r}, f)$:

$$p_0(\vec{r}, i, f) = \psi(\vec{r}, f) \, \Re\{\hat{P}[\vec{r}_i, f] e^{i\varphi(f,t)}\}\Big|_{t=|\vec{r}-\vec{r}_i|/c}, \qquad (4.5)$$

where $\hat{P}[\vec{r}_i, f]$ represents the spectrum of the back-propagation term $P[\vec{r}_i, t]$. The summation takes place for all the frequencies within the band of interest, which we define as the limiting frequencies of the band-pass filter applied to the signals (cf. section 4.2.3 b).

The procedure described is illustrated in Fig. 41 for two frequencies (1 MHz in the top row and 3 MHz in the bottom row)[*] and two sensor positions. In Fig. 41a, the first sensor position is shown. In the top image, the frequency component f_1 is back-propagated from sensor position i and the resulting sub-image is multiplied pixel by pixel by the sensitivity field at that frequency. In the bottom image, the same is done for a frequency $f_2 > f_1$.

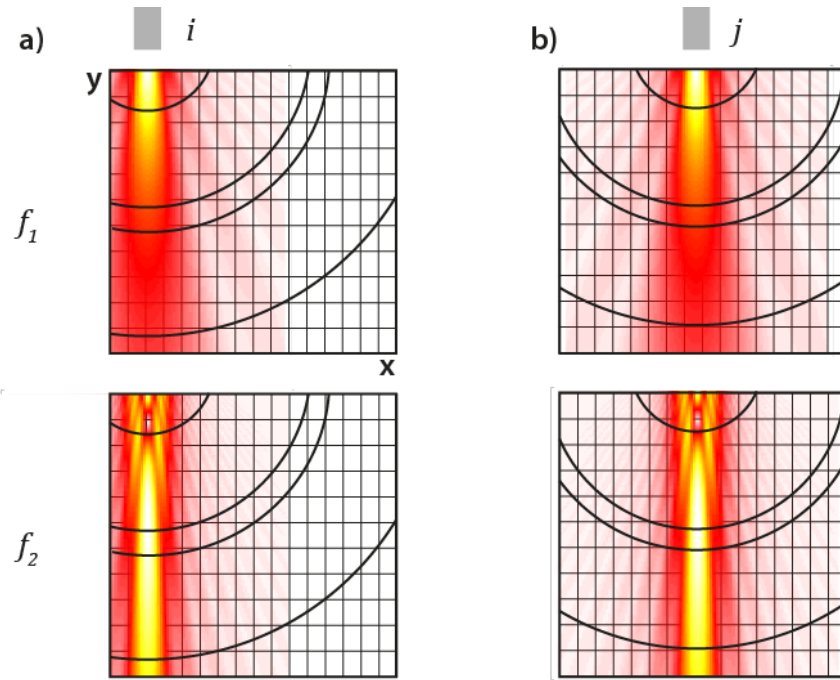[*] As computed with the Multi-Gaussian Beam method, see Chapter 3.

Figure 41: Concept of the weighted Back-projection algorithm. *a)* For sensor position *i*, the frequency components of the signals are back-propagated individually (two are shown: $f_1 = 1$ MHz, $f_2 = 3$ MHz). The sensitivity fields for those frequencies are applied to the ROI as a weighing mask, by multiplying the back-propagated value with the field amplitude at that pixel. The same is repeated for each sensor position *j* (shown in *b)* for the middle scanning position). All sub-images thus obtained are summed to form the final image.

Likewise, Fig. 41b shows the procedure for sensor position *j* and the same frequencies. After back-propagation and weighting, the sub images for every sensor position and frequency are summed to yield the final image.

The result of applying this modified Back-projection to the measured B-scans is shown in Fig. 42. The standard Back-projection reconstruction is shown in Fig. 42a for reference. Fig. 42b shows the weighted Back-projection image, where almost no difference can be noticed with respect to the standard case. In the profile along the depth (Fig. 42c) it can be seen that the axial resolution is improved with respect to standard Back-projection, whereas along the scanning direction (Fig. 42d) the resolution is marginally degraded.

The results in this section show that masking the back-propagated terms does not improve resolution along the scan direction for a flat round detector. The mask applied does not change the pixel values inside the main lobe significantly and thus no improvement is obtained from this procedure. It might be tempting to propose a mask that is either wider or narrower than the main lobe. However, it can be easily understood that a narrower mask effectively limits the number of signals used to reconstruct one pixel, which is equivalent to assume a sensor with an angle of acceptance even more limited. On the other part, a wider
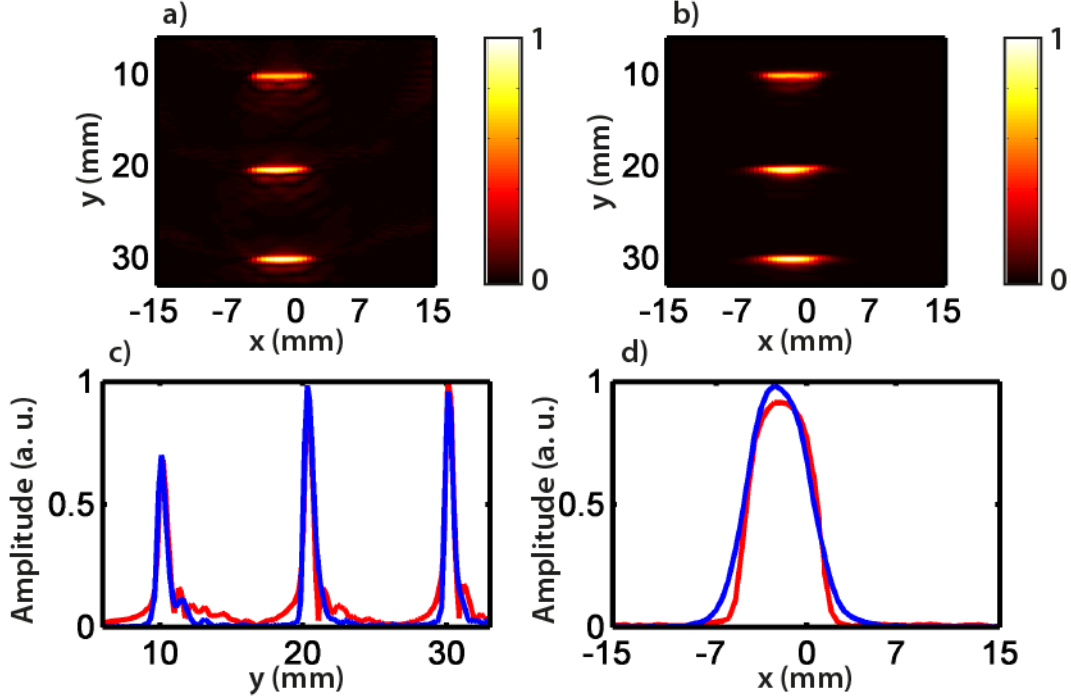
Figure 42: B-scan reconstructions with the weighted Back-projection method. *a)* Standard Back-projection reconstruction. *b)* Weighted back-projection reconstruction *c)* Profile of the reconstructions taken along the vertical direction at $x = 0$ mm. Blue: weighted Back-projection. Red: standard Back-projection. *d)* Profile of the middle absorber, same colors as *c)*. See text for a detailed discussion.

mask would result in a reconstruction inside the main lobe approximately equal to standard Back-projection, i.e., no mask applied.

The failure of the proposed method is understandable in terms of the delay field of the sensor, as discussed in the previous section. The width of the reconstructed object arises from the indistinguishable times of arrival of the signals. Thus, such an effect may not be corrected by a masking of the reconstructed image, as this does not change the constant detection times within the main lobe.

4.2.7 Point Spread Function-corrected Back-projection

In this section, it is proposed that the resolution of the B-scan along the lateral direction may be improved with a Point-Spread-Function (PSF) deconvolution approach.

The principle behind the proposed algorithm follows from the analogy between optical and acoustical diffraction presented in Chapter 2. Therein, it was argued that some optical systems have an acoustic counterpart, which results in similar diffraction patterns for both systems. The diffraction pattern of an optical system is however closely related (if not completely identical in some cases) to the resolving power of the system, i.e., the image of a point source produced by the system — its PSF [33]. Herein, the PSF of the system at a given depth y is defined as the profile of the sensitivity field at y.
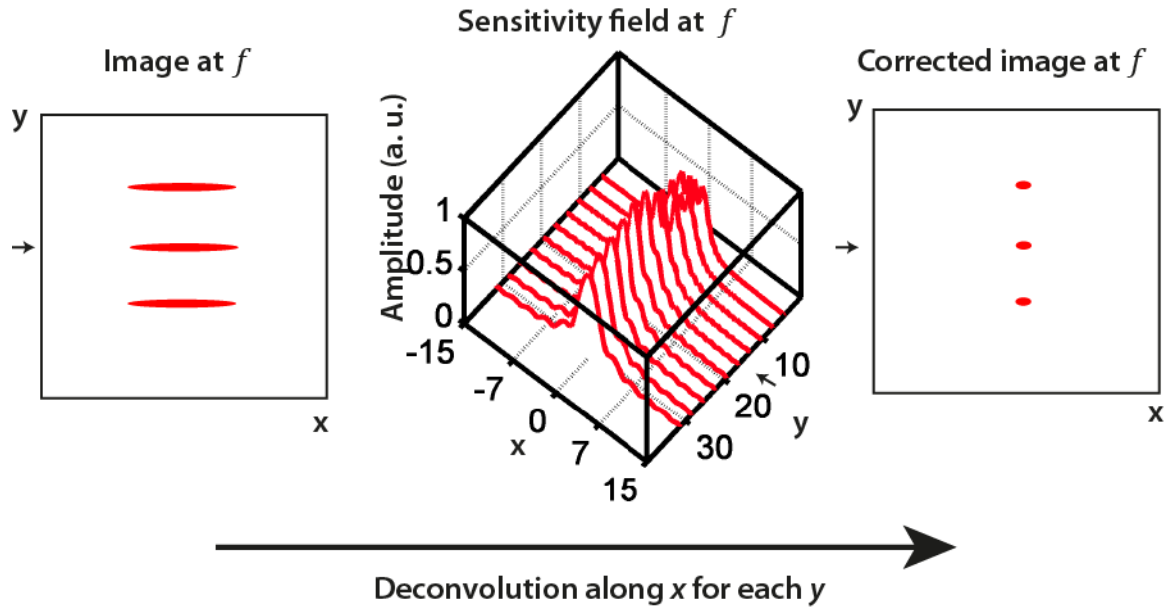
Figure 43: Concept of the PSF-corrected Back-projection algorithm. The full Back-projection algorithm is applied for each frequency component of the signals. The sensitivity field for that frequency (shown here for 3 MHz) is understood as set of PSFs at each row y in the B-scan. The rows of the single-frequency image are then deconvolved with these PSFs resulting in a corrected image for that frequency. The images for each frequency are then summed to generate the final image.

The image formation method proposed herein is illustrated in Fig. 43. The starting point of the method is the decomposition in single frequencies of the back-propagation term $P[\vec{r}_i, t]$, as presented in the previous section (Eq. (4.4)). For each frequency component of $P[\vec{r}_i, t]$, one image is reconstructed with the Back-projection algorithm. Afterwards, the rows in the image are deconvolved along x with a PSF that is dependent on the depth, using the Wiener-deconvolution algorithm [65]. The resulting corrected images for single frequencies are then added to form the final image.

The result of applying the proposed method to the experimental measurements is presented in Fig. 44. The image obtained with standard Back-projection is presented in Fig. 44a as a reference. Fig. 44b shows the B-scan reconstructed with the proposed method. The results show the deconvolution approach does improve the resolution of the image along the scanning direction when compared with standard Back-projection. The images of the three absorbers are similar, but they are reconstructed with different amplitudes. This can be observed in more detail in Fig. 44c, where the profiles of the standard and proposed reconstructions along y are shown in blue and red respectively. Since the proposed method only operates along the scanning direction, the true amplitude of the absorbers along the transducer axis cannot be recovered. Fig. 44d shows the profile of the reconstructions along the scanning direction x. The absorber size resulting from the proposed reconstruction
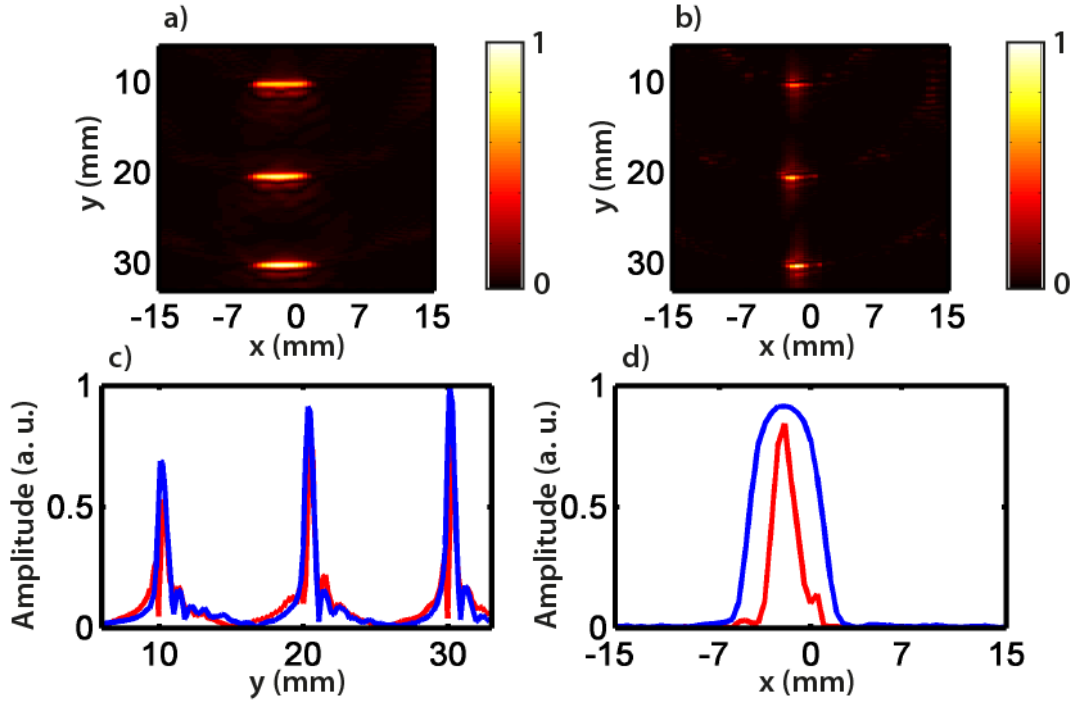
Figure 44: B-scan reconstructions with the PSF-corrected Back-projection method. *a)* Standard Back-projection reconstruction. *b)* PSF-corrected Back-projection reconstruction *c)* Profile of the reconstructions taken along the vertical direction at $x = 0$ mm. Red: PSF-corrected Back-projection. Blue: standard Back-projection. *d)* Profile of the middle absorber, same colors as *c)*. See text for a detailed discussion.

method is approximately 1 mm, in accordance with the results obtained with the small-diameter sensor. The findings demonstrate that the proposed deconvolution method can improve the resolution of B-scan images with a detector of diameter larger than the source.

In realistic situations, however, absorbers with different sizes may be present in the sample. In order to assess the performance of the proposed deconvolution method in the presence of larger objects, the B-scan of an absorber with 2 mm in diameter, located at three different depths, was simulated. The simulation was based on the exact optoacoustic forward solution for a spherical absorber (cf. Chapter 2, Eqs. (2.4) and (2.11)). The effect of the transducer's SIR was taken into account by numerically integrating the signals over the surface of the detector (cf. Chapter 2, Eq. (2.13)).

The results of applying standard Back-projection to the simulated signals are shown in Fig. 45a. The image shows depth dependent reconstructed amplitude that enhances objects closest to the sensor as well as absorber diameters of approximately 5 mm. The amplitude bias towards the surface of the transducer is in contrast to the reconstructions of smaller objects. This is to be expected due to the shape of the sensitivity fields at different frequencies, in which the main lobe has a maximum at a depth inversely proportional to the frequency (see e.g., Fig. 41 where the sensitivity fields for 1 and 3 MHz are shown).
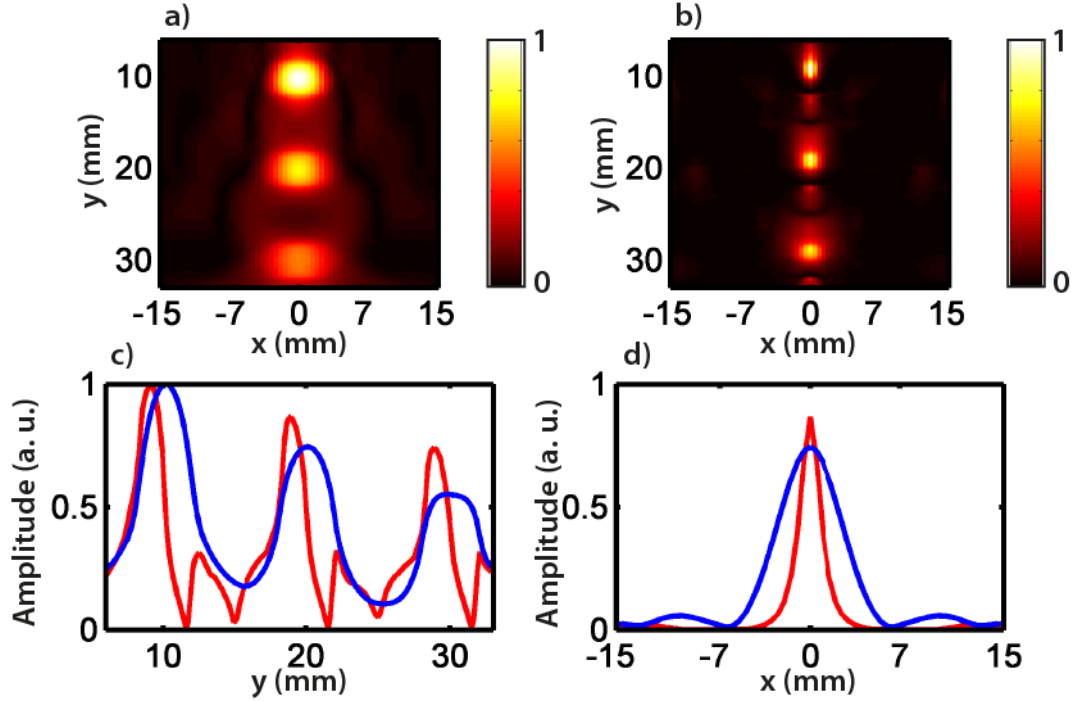
100

Figure 45: B-scan reconstructions with the PSF-corrected Back-projection method of a numerical phantom with three absorbers 2 mm in diameter . *a)* Standard Back-projection reconstruction. *b)* PSF-corrected Back-projection reconstruction *c)* Profile of the reconstructions taken along the vertical direction at $x = 0$ mm. Red: PSF-corrected Back-projection. Blue: standard Back-projection. *d)* Profile of the middle absorber, same colors as *c)*. See text for a detailed discussion.

Fig. 45b shows the B-scan reconstructed with the proposed deconvolution method. The figure shows that the proposed method improves the resolution of the reconstructed image along the scanning direction. However, the reconstructed absorber size and amplitude are depth-dependent, which represents a drawback for the method. Fig. 45c shows the profiles of the standard (blue) and proposed reconstructions (red) along *y*. While the resolution along the transducer axis is improved by the proposed method, there are some image artifacts related to the deconvolution process such as the peaks close to the absorbers. In Fig. 45d, the profile along the scanning direction for the absorber located at 20 mm from the sensor is shown for the standard and the proposed reconstructions (blue and red respectively). The FWHM obtained with standard Back-projection is ∼5 mm whereas in the case of the proposed method is approximately 1 mm, which is erroneous in both cases as the real absorber diameter was defined as 2 mm. Thus, the proposed reconstruction method may result in an underestimation of the absorber size when the source is located near the sensor. As a result, the PSF-corrected Back-projection method is not consistent for all absorber sizes and its application is therefore limited to the particular case of small absorbers.

4.2.8 Conclusion

In the previous sections, the standard Back-projection algorithm was applied to the reconstruction of B-scans obtained with flat unfocused detectors, resulting in poor resolution along the scanning direction. This effect is due to the SIR of the transducer: signals measured with optimal sensitivity and bandwidth are mainly generated in front of the sensor. However, such signals are mostly indistinguishable from one another, be it in terms of their amplitude, their bandwidth or their measurement time. Therefore, it can be argued that the number of distinct signals effectively available for image reconstruction is very limited.

Several modifications of standard Back-projection that make use of the spatial properties of the sensor were proposed, with the aim to compensate for the limited resolution of the sensor. Weighted Back-projection was based on the masking of the back-propagated signals with the sensor sensitivity field. Conversely, PSF-corrected Back-propagation was applied as a post-processing step for the images obtained at single frequencies, whereby the PSF was defined based on the properties of the sensor. The proposed methods produced generally inconsistent results, such as image artifacts, over- or underestimated absorber sizes and erroneous absorber amplitudes. The reason behind the failure of the different reconstruction methods can be attributed to their implicit description of the ultrasound detection process. The weighted and PSF-corrected Back-projection methods assume that the effect of the transducer on the measured signals can be described in terms of the frequency-dependent sensitivity fields. Such a description is indeed valid with respect to the measured frequency spectrum and signal amplitude as a function of the absorber location. However, sensitivity fields describe the SIR effects only in terms of amplitude weighting and thus fail to properly account for the phase distortion due to the SIR. Therefore, an accurate image reconstruction algorithm shall include the SIR of the sensor both in terms of its amplitude per frequency and its phase. This approach presented in the next Section, 4.3.

From the findings in this section several conclusions with respect to the utilization of flat unfocused detectors for microscanning may be established. It has to be reminded that microscanning ought to work at mesoscopic scales, i.e. at optoacoustic frequencies of about 25 MHz. Additionally, it was discussed that a flat transducer may be considered point-like or finite-sized depending on its near field distance N_F. Therefore, an unfocused sensor working at mesoscopic frequencies may be considered point-like if its size is much smaller than 60 μm or if it is placed far from the sample. On one part, such sensor sizes are at the boundary of what is nowadays technically possible in ultrasound transducer fabrication. On the other

part, placing the sensor far from the sample is in general disadvantageous, as a long propagation path through tissue-like media strongly attenuates high acoustic frequencies [7, 31].

In the light of the results in this section, if follows that unfocused transducers do not fulfill the requirements for microscanning in mesoscopic applications. In the next section, microscanning with spherically focused sensors is investigated.

4.3   Microscanning with focused detectors

4.3.1 Motivation

At their focal point, spherically focused detectors generally exhibit good lateral resolution and better sensitivity than an unfocused detector of comparable size and central frequency [27]. As a result, sources located out of the focus yield distinct signals for neighboring scanning positions, which can be exploited during image formation for improved imaging performance.

Standard image reconstruction with focused detectors is based on delay-and-sum techniques, mainly the Synthetic Aperture method described in previous sections. The spatial properties of the sensor are taken into account by approximating the focal spot of the detector as a point-like sensor, in which is called the Virtual Detector approximation (VD) [66]. Such an approximation represents an accurate description of the measured signal delays, but fails to acknowledge other sensor properties, such as the sensitivity field or the low-pass filtering properties of the SIR. Herein, a method to take into account all of the signal distortions due to the SIR of focused detectors during image reconstruction is presented. The proposed method makes use of the model-based reconstruction described in Chapter 2, the Interpolated Model-Matrix Inversion (IMMI), for the description of optoacoustic signal generation and propagation [21, 53]. The properties of the detector are taken into account by convolving the SIR with the model-matrix in a manner similar to the one proposed by Rosenthal et al. [24]. The implementation of the method presented herein, however, differs in some crucial aspects with respect to [24] and will be consequently detailed in following sections. The performance of the proposed method was assessed with simulations and experiments in simple phantoms and biological tissue.

In section 4.3.2 a definition of coordinates, sensor properties and relevant concepts for microscanning with focused detectors is provided. In section 4.3.3 the standard image reconstruction method for such sensors, the Virtual Detector method, is presented. In section 4.3.4 the IMMI method including the SIR of the detector is presented. In section 4.3.5 a description of the measurement setup and the sensors used is provided. In section 4.3.6

the results of the simulation study and experiments are presented. Finally, in section 4.3.7 the performance of the proposed method and its applications to optoacoustic imaging at the mesoscopic scale are discussed. The results of this Section can be also found in Ref. [67].

4.3.2 Principles and definitions

Optoacoustic microscanning with spherically focused transducers may be used to obtain a 3D image of the sample in two different ways, depicted in Fig. 46. One alternative is to simply scan the sensor along the two scanning directions, generating one image by time-windowing the signals originated within a given interval of the focus. Afterwards, the imaging plane may be translated to a different depth by moving the sensor closer to or further away from the sample. A new image may be performed as described above, and the full 3D dataset is then rendered by stacking the images measured at each depth. This procedure is shown schematically in Fig. 46a.

If the scanning steps along x and y are small enough, each image has a minimum resolution δ dependent on the sensor characteristics and the optoacoustic frequency f (cf. section 2.3.5)

$$\delta \approx \frac{Fc}{Df} = \lambda \frac{F}{D}, \qquad\qquad (4.6)$$

where F is the focal length of the sensor, D its diameter and c the speed of sound in the medium. Since optoacoustic sources are inherently broadband, the resolution of the image may be adapted to a desired source size by filtering the measured signals within a given frequency band. Ultimately, it is the interplay between the sensor frequency response and the object's spectrum which will determine the frequency band that may be used for image formation, and hence the image resolution. In the previous chapter (section 3.2.5), a single 2D scan was used to assess the lateral size of the optoacoustic source used for EIR characterization, showing a clear example of the relationship between resolution and frequency. Along the sensor axis, on the other hand, the resolution is determined by the wavelength of the maximum frequency within the sensor's bandwidth [31]. This resolution defines the minimum distance at which the 2D images may be taken.

The second method for the generation of a 3D representation of the sample relies on the B-scan approach discussed throughout this chapter. The stacking of several B-scans can be used to yield a 2D+time dataset and, through image reconstruction, a 3D rendering of the sample. In Fig. 46b, a single B-scan is shown in relation to the stacking of 2D scans described in the previous paragraph. If the degradation in axial and lateral resolution can be correctly
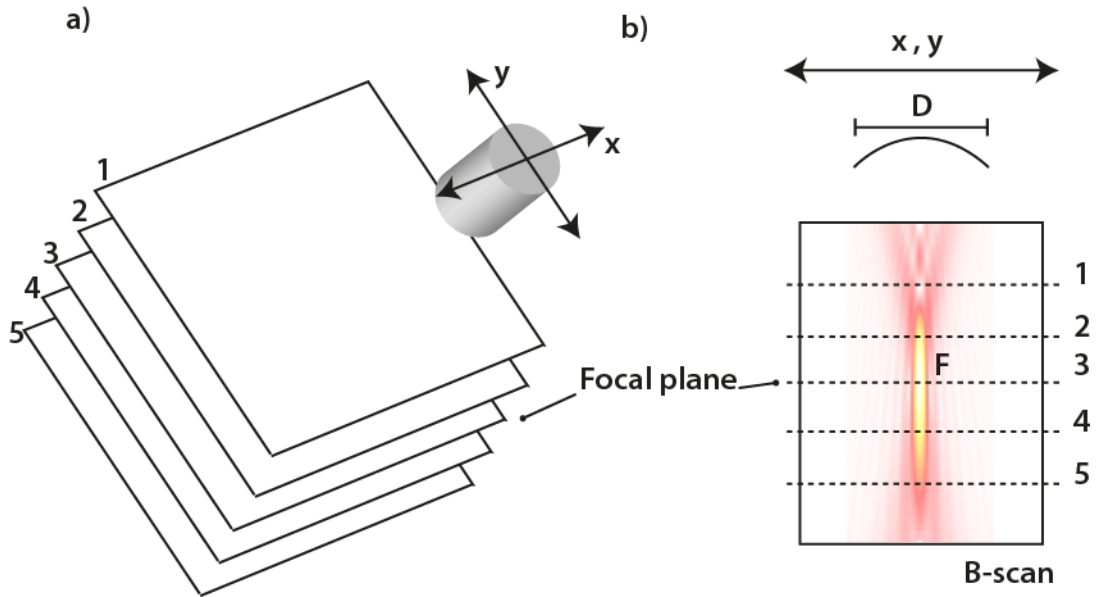
Figure 46: Microscanning with spherically focused detectors: two methods for obtaining a 3D dataset. *a)* Several microscans are performed at different distances from the sample, producing one image at the focal plane of the sensor for each vertical position. The 3D dataset is rendered by stacking the images. *b)* One single microscan is performed and the images at several planes are obtained by reconstructing and stacking the individual B-scans, as described at the beginning of the chapter. Due to the properties of the sensor (of focal length F and diameter D), resolution and sensitivity degrade for planes parallel to the focal plane. This shall be taken into account during B-scan reconstruction for optimal performance. See text for more details.

compensated for during image reconstruction, the B-scan approach is in principle capable of producing a 3D dataset with equivalent resolution to the stacking method. As a result, the imaging performance of a microscanning system may greatly benefit from the B-scan method as the measurement time is significantly reduced. In the next section, the standard algorithm for B-scan image formation is presented.

4.3.3 The Virtual Detector method

Now that the reader is familiar with the B-scans of small sources taken with point-like and unfocused sensors, the B-scan measured with a spherically focused transducer can be best demonstrated with an experiment. The source was an absorbing microsphere, 100 μm in diameter, and the sensor a spherically focused transducer with $F = 25.4$ mm, $D = 13$ mm and 10 MHz center frequency*. In Fig. 47a, the geometry of the measurement is illustrated, and Figs. 47b to 47d show the B-scans taken when the source is located closer to the transducer, at the focus and deeper than the focus, respectively. Several features of the B-scan may be pointed out. For one part, the time of arrival of the signals when the source is further away than the focus is similar to the expected from a point-like transducer: the signal arrives at a later time when the source is located off-axis. This is in contrast to the source located closer to the focus, in which the signals off-axis actually reach the transducer

---

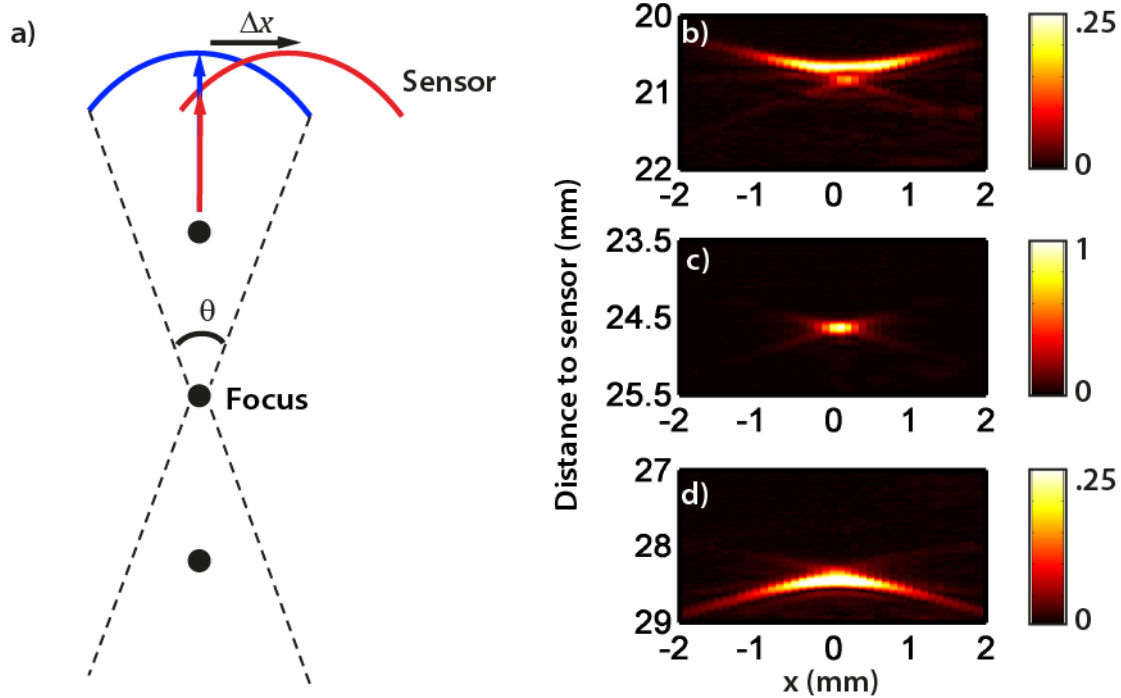* The full details of the experimental setup can be found in section 4.3.5.

Figure 47: Experimental basis for the Virtual Detector approximation. *a)* Three absorbers are imaged by a spherically focused sensor scanned along a line. The sensor has an angle of aperture *θ*. The arrows mark the shortest distances between the source and the sensor at the two scanning positions. *b)* B-scan of the source located closer to the sensor. *c)* B-scan of the source located at the focus. *d)* B-scan of the source located deeper than the focus. See text for a detailed discussion and the characteristics of the detector.

surface at an earlier time. Such effect can be understood with the help of Fig. 47a, where the shortest distance between source and sensor is marked by arrows for two scanning positions[*]. The resolution and sensitivity variation with depth can be also observed, as the source in focus is measured with optimal amplitude and resolution while the sources out of the focus are not.

The time-shift between signals measured with the source located on-axis and off-axis forms the basis of the Virtual Detector (VD) method. VD is based on the assumption that the optoacoustic waves are measured by a point detector located at the focus of the actual sensor [66, 68]. Thus, the image formation problem for the half-spaces to either side of the focus is similar to the one described for point-like detectors at the beginning of the chapter. The VD method may be thus expressed in a similar manner to the SA or Back-projection algorithms for each half-space, with three modifications. First, as observed in Fig. 47, the time shifts should be applied in opposite directions, whether the signal to correct (or pixel to reconstruct) is at a distance shallower or deeper than the focus. Second, it is assumed that the point-like detector at the focus has an angle of acceptance that is $= arc\ sin(D/2F)$, so

---

[*] It is actually slightly more subtle: the arrows mark the shortest distance regardless of the depth. However, at distances deeper than the focus, the sources enter the far-field regime and the detector is seen as a point.
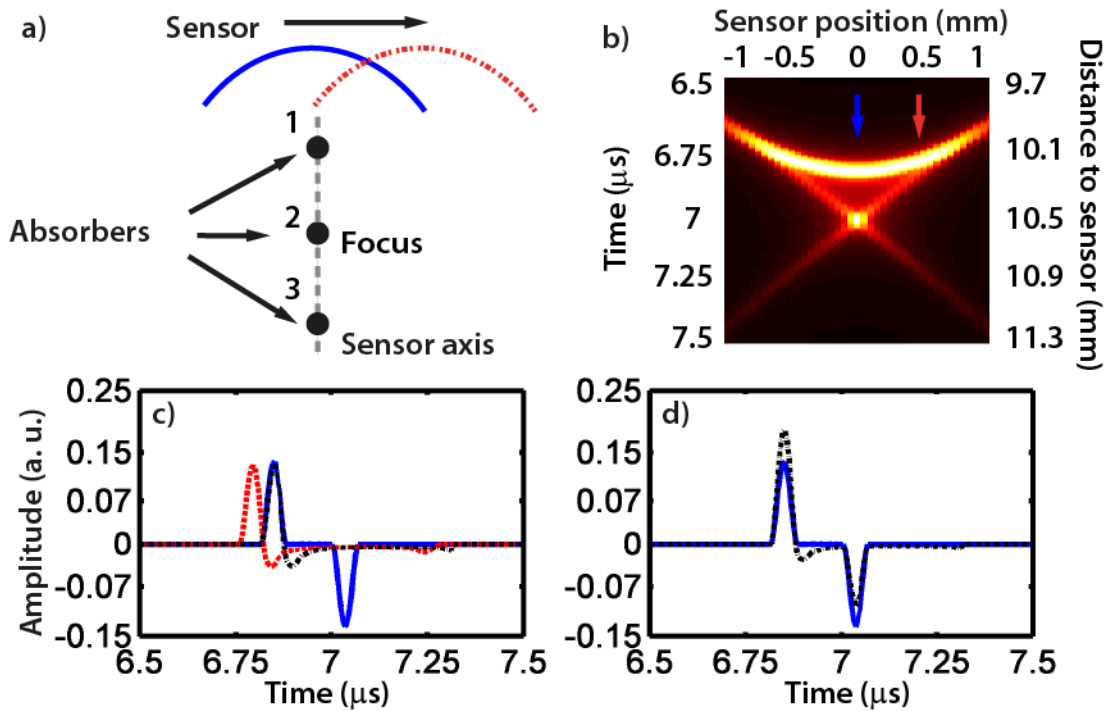
Figure 48: Operation of the VD method at the signal level. *a)* Geometry for the simulated B-Scan with a sensor of focal distance *F = D = 12 mm*. *b)* Result of the B-scan for absorber 1. The color scale is linear, and the image is normalized to its maximum. *c), d)* Virtual detector processing of two simulated signals for absorber 1, taken at the locations marked in b). The amplitude of the signals is normalized to the signal amplitude of the absorber at focus. c) The signal of interest is on-axis (blue/solid), and is to be corrected with the aid of signals acquired at other sensor positions, of which one of them is shown (red/dotted). The time-shift on the off-axis signal is corrected for, as per the VD method, generating the delayed auxiliary signal (black/dashed). d) The delayed auxiliary signal is added to the signal of interest (blue/solid), resulting in the VD-processed signal (black/dashed).

that no signals outside this angle are used in image formation. As a result, sources located near the focus are reconstructed with fewer signals than sources located away from the focus. In order to maintain a SNR as uniform as possible throughout the corrected image, each pixel is weighted with the number of signals it has been corrected with, which constitutes the third and last modification of VD with respect to standard delay-and-sum.

In order to illustrate the concept and operation of the VD method, the B-scan of a small absorber imaged with a spherically focused sensor was simulated. The sensor had a focal length F = 12 mm and diameter D = 12 mm. The absorber was a sphere with a paraboloidal absorption profile and diameter 100 μm, located at 10.7 from the sensor (on-axis) and was assumed to be uniformly illuminated. A lateral scan (off-axis) was performed with a width of 2 mm and a step size of 50 μm. The acoustic fields at each point in space were calculated using an analytical solution, which is a generalization of the solution provided in [21]. The analytical signals were then numerically integrated over the surface of the transducer, in order to take into account its geometry. The speed of sound was set to 1490 m/s and the time resolution to 170 MS/s.

Fig. 48b shows the simulated B-scan for reference, where the signals for two sensor positions are highlighted with arrows. Figs. 48c and 48d illustrate the VD operation at the signal level for those positions. The figure shows that the VD method is indeed a valid description for the time shift on the optoacoustic signal that is due to the surface of the detector. VD can therefore be applied for coherent summation, enhancing the amplitude of the signal of interest. It can be noted, however, that the slowly-varying, negative part of the signal remains for the most part unchanged by VD. In following sections, it will be shown that the failure to correct for this signal distortion severely limits the performance of the VD in terms of accurate B-scan reconstructions. For this reason, a reconstruction algorithm that includes a more accurate description of the detection process was developed and is discussed in the following section.

4.3.4 Model-based image reconstruction for focused detectors

It was discussed in Chapter 2 that model-based algorithms, mainly the Interpolated Model-Matrix Inversion (IMMI) developed in our group, offer several advantages over standard reconstruction techniques such as Back-projection. For one part, IMMI has been shown to yield images without nonphysical artifacts such as negative absorption values or artificially enhanced boundaries [21, 44]. More importantly for the discussion herein, IMMI can be adapted to account for processes that may take place in actual experiments, such as varying illumination patterns [28] or tomographic detection geometries that do not fully enclose the object [55]. In particular, Rosenthal et al. [24] showed recently that the spatial properties of a finite-sized sensor can be combined with the model-matrix and demonstrated enhanced imaging performance in a tomographic configuration as a result.

Despite the advantages of IMMI reconstruction algorithms over standard techniques, they have so far been limited to tomographic detection geometries in which either point-like or flat detectors are assumed. In this section, an IMMI algorithm for spherically focused transducers in a microscanning geometry is developed. The proposed algorithm is based on the combination of IMMI with the SIR of the detector through temporal convolution similar to [24]. The implementation of the SIR of the sensor differs with respect to [24] in one crucial aspect: instead of the semi-analytical solution proposed therein, the exact solution of the SIR for spherically focused transducers was used [69]. Due to the mathematical properties of the SIR in the vicinity of the focus, the combination of the model and SIR proved a non-trivial task.

In the following paragraphs, the proposed reconstruction algorithm is described. Afterwards the possible errors due to an incorrect calculation of the SIR are explained and
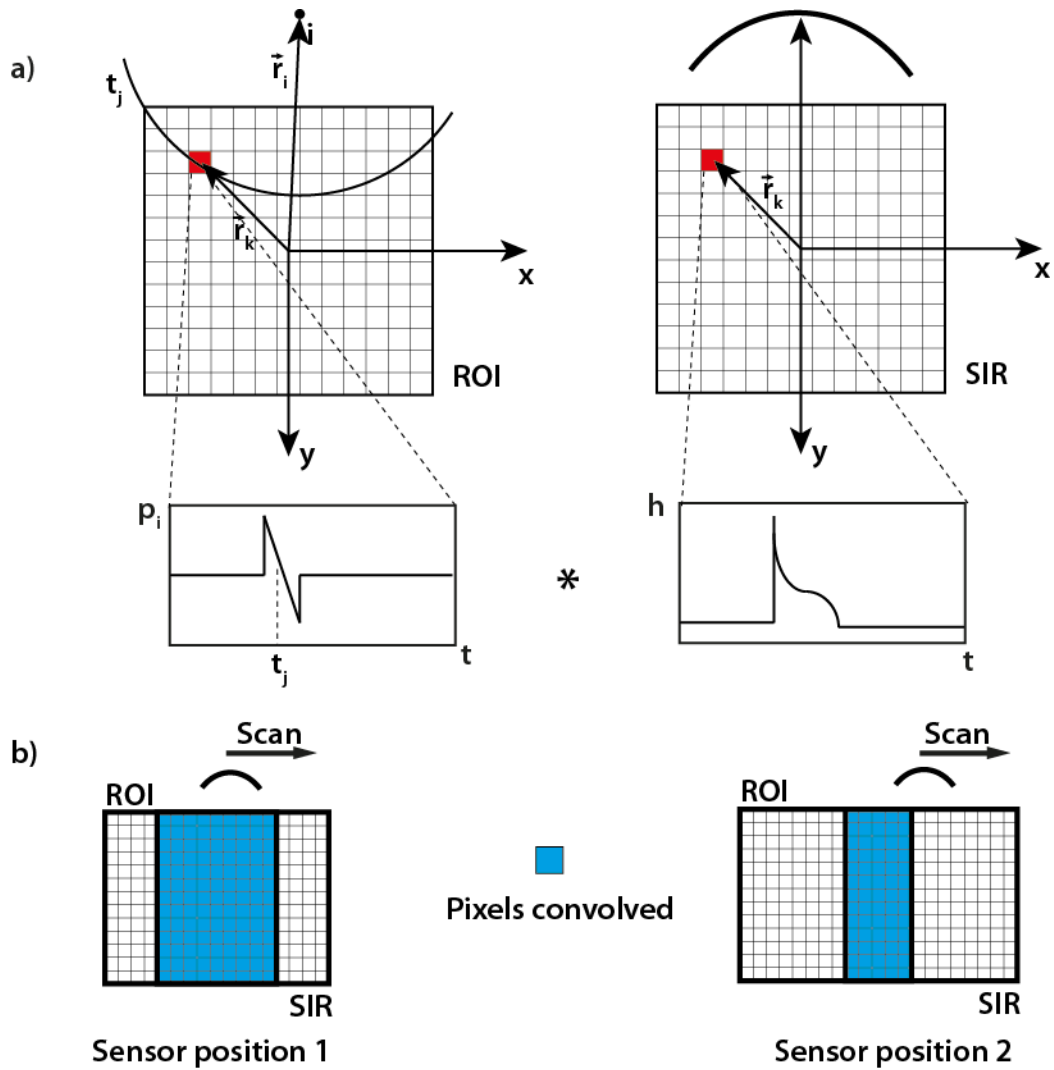
Figure 49: Model-based algorithm (IMMI) including the SIR of a sensor. *a)* The elements of the model-matrix can be understood as optoacoustic signals generated by elementary absorbers within the ROI, i.e., the pixels. On the other hand, the SIR expresses the distortion of an impulse-signal due to the surface of the sensor. The proposed model-matrix is generated by convolving the signal and the SIR at each pixel in the ROI, for all sensor positions. *b)* In general, the SIR is calculated only once within the same grid as the ROI, and for each scanning position only the pixels that overlap are convolved.

the proposed solution is presented. Finally, the reconstruction method with the final model is briefly discussed.

a) Combination of the Model-matrix and the SIR

Let us start the discussion with a reminder of the IMMI description of the optoacoustic problem, with the aid of Fig. 49a. IMMI expresses the optoacoustic signals p measured at sensor positions $\vec{r}_i$ as a linear combination of the elementary optoacoustic signals from absorbers within the discretized region of interest (ROI). The absorbers are located at positions $\vec{r}_k$ and have an absorption z_k. The linear combination is expressed in matrix form as
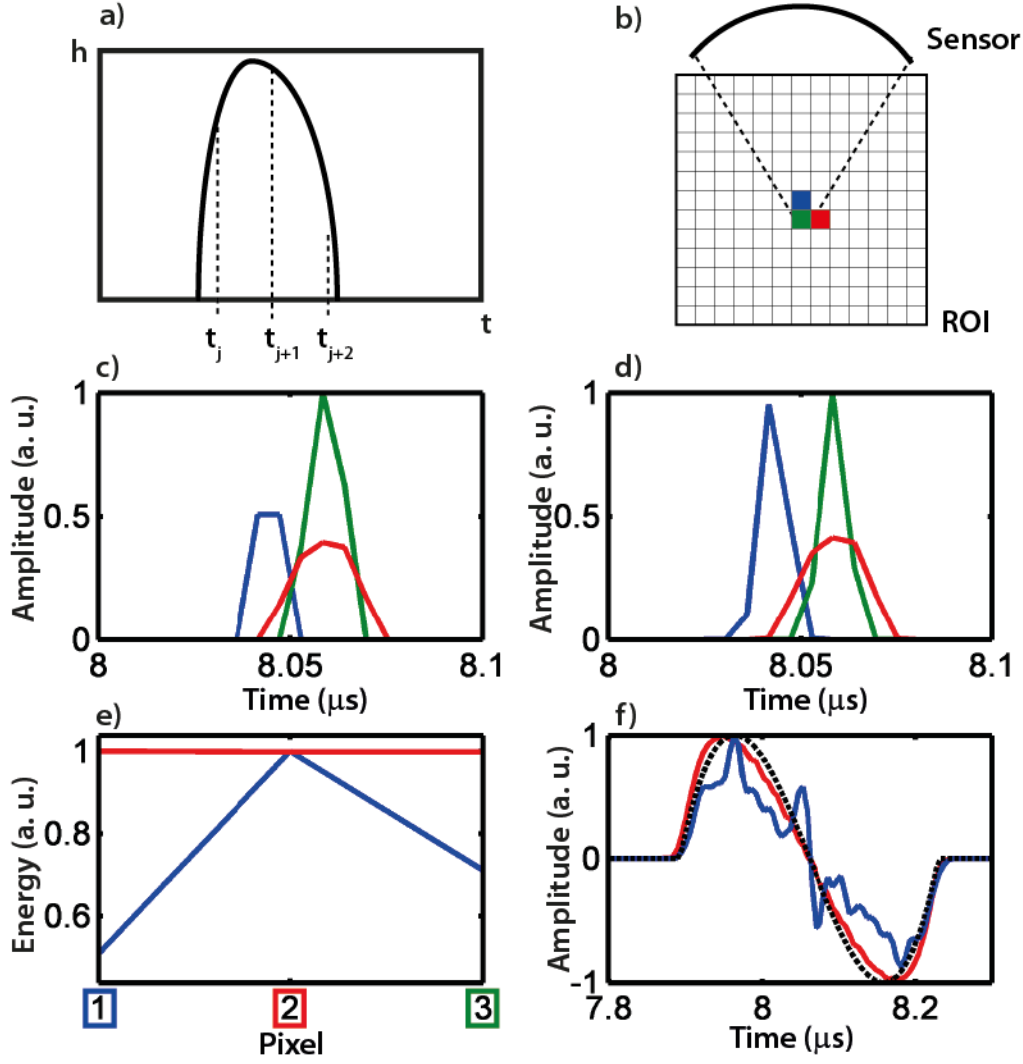
Figure 50: The problem with the SIR discretization in the vicinity of the focus. *a)* Example of the SIR at one pixel close to the focus. Such function *h* has to be discretized to the model-matrix time instants for that pixel. *b)* Geometry of the sensor and the ROI for reference in the next sub figures. *c)* SIRs at the pixels, computed with the sampling rate and at the time instants of the model-matrix. Note the strong variations in amplitude along the sensor axis and along the scanning directions. The latter are expected, as they are due to the strong focusing of the sensor. The variations along the axis, however, arise from an inefficient sampling of the SIR. *d)* SIRs at the pixels, computed with the proposed oversampling/downsampling scheme. *e)* Energies of the SIRs *h* shown in *c)* (blue) and *d)* (red). The energy is defined as $E = \int h^2(t)dt$. *f)* Forward signal resulting from a model with an incorrectly discretized SIR (blue) and a correctly discretized one (red) compared with the analytical solution (black-dashed).

$$p = Mz ,$$

(4.7)

where *M* is the point-like model matrix.

On the other hand, it has been shown in Chapter 3, that the optoacoustic signal of a small absorber located at $\vec{r}_k$ measured by a finite-sized transducer may be expressed as a convolution of the signal with the SIR of the sensor $h(\vec{r}_i, \vec{r}_k, t)$

$$s_d(\vec{r}, t) = h(\vec{r}_i, \vec{r}_k, t) * p(\vec{r}_i - \vec{r}_k, t) .$$

(4.8)

From these definitions, it follows that the SIR of the detector may be included in the model matrix M by convolving the signals p_{ik} for each pixel and each sensor position with the corresponding SIR $h(\vec{r}_i, \vec{r}_k, t)$, which yields a finite-sized model-matrix H.

The steps of the proposed algorithm may be then described as follows:

1. Compute the model matrix M for the point-like case for the ROI and scan parameters desired.

2. Compute $h(\vec{r}_i, \vec{r}_k, t)$ for the central scanning position for every pixel inside the ROI.

3. For each sensor position, find the pixels to be convolved as per Fig. 49b, apply Eq. (4.8) to them and repeat for the whole scan[*].

b) Correct computation of the SIR in the vicinity of the focus

The SIR is a mathematical singularity at the focal point, which results in fast variations of the SIR amplitude for points close to the focus [69]. These variations take place at scales typically much smaller than the temporal and spatial resolutions of IMMI and the SIR may be discretized incorrectly even though an analytical solution is provided (Fig. 50).

As a consequence, significant image artifacts may arise if the SIR is not represented correctly near the focus. The problem was solved here in two steps. First, the SIR was calculated with a time sampling rate two orders of magnitude higher than the IMMI sampling, to yield smoothly varying amplitudes. Afterwards, the SIR was downsampled in several steps to the IMMI sampling while keeping its energy constant at each pixel. This was achieved by the use of Finite Impulse Response filters at each downsampling step [64]. The procedure is a time-intensive operation but ensures the correct convolution of the model and the SIR for every point in the ROI. The procedure is illustrated in Figs. 50b to 50f.

c) Image reconstruction

Once the complete model matrix has been built, the image is reconstructed with iterative inversion. In the context of microscanning, there is a so-called limited-view situation due to the linear scanning geometry and the limited angle of acceptance of the sensor. Limited-view is a non-negligible issue in IMMI when the angle covered by the sensors is ≤180°, as the inversion problem becomes ill-conditioned [55]. In the case discussed herein, the effective detection angle is given by the angle of acceptance of the

---

[*] In Chapter 5, the possibility of using sensors located far away from the imaging ROI is demonstrated.

sensor, i.e. 60°. Therefore, we used a regularized matrix inversion. Specifically, the truncation of the LSQR method discussed in [55] was chosen, as it yielded the optimal reconstruction of numerical phantoms.

4.3.5 Experimental techniques*

The performance of the different reconstruction methods (VD and IMMI incorporating the SIR) was assessed for experimental measurements of increasing complexity. First, a description of the measurement setup is provided, and afterwards the different experiments are briefly described.

In all experiments, the excitation was provided by a tunable optical parametric oscillator laser (Opotek Inc., Carlsbad, California), with a pulse width of 6 ns and a repetition rate of 10 Hz. The illumination was coupled through a fiber bundle (CeramOptec GmbH, Bonn, Germany) at a wavelength of 740 nm and it was left static throughout the experiments. The signals were acquired by a 14-bit, 250 MS/s data-acquisition board (Spectrum GmbH, Grosshansdorf, Germany) and band-pass filtered from 50 kHz to 40 MHz for noise removal. The sensor was mounted on a 3-axis translation system (Thorlabs GmbH, Karlsfeld, Germany).

a) Measurement 1: single source

The purpose of this measurement was to showcase the operation of the VD and IMMI methods experimentally, but under less demanding conditions than an actual biological experiment. The source was therefore a single absorbing microsphere, 100 μm in diameter. The sensor was a spherically focused transducer with $F = 25.4$ mm, $D = 13$ mm and 10 MHz center frequency with over 100% bandwidth (model V311, Panametrics-NDT, Waltam, MA). In the results section, this sensor is referred to as "the 10 MHz transducer". Three B-scans with the sensor located at approximately 21, 25 and 29 mm from the source were taken, each with a 100 μm scanning step size over a length of 10 mm (although they are represented within the central 4 mm). In this case, each of the signals was averaged for 100 laser shots for optimal SNR. The total measurement time was approximately 1 hour.

b) Measurement 2: multiple sources in a plane

As an intermediate step from B-scans to full microscanning images, a simple phantom was measured to assess the performance of the transducer later used for biological measurements. The sample was a scattering agar phantom of cylindrical shape.

---

* Measurements taken in collaboration with J. Gâteau.

On its top surface, 100 and 50 μm black microspheres were deposited. The phantom was measured by a spherically focused transducer with $F = 12$ mm and $D = 12$ mm, specified central frequency of 25 MHz and over 100% pulse-echo -6dB bandwidth (InSensor®, Kvistgaard, Denmark). This sensor is referred to as "the 25 MHz transducer". The measurements were only taken with the microspheres lying in the focal plane. A 2D scan was performed in a region 4 mm by 3 mm with a step size of 100 μm in both directions. The scan is represented as the maximum amplitude projection (MAP) along the transducer axis, 300 μm around the focal point. The total measurement time was approximately 30 minutes.

c) Measurement 3: stacking of reconstructions

From the previous scan, one isolated microsphere was selected and a finer scan was performed around it with the 25 MHz sensor. Afterwards, the sensor was moved away from the microsphere, perpendicularly to the scanning plane. Two more scans were thus performed, at 0.25 and 0.5 mm from the original scanning position. The purpose of this measurement was twofold: first, to showcase the performance of the different reconstruction methods in a more complex environment than in the first experiment; and second, to demonstrate the formation of a 3D dataset from a stack of B-scans. Each B-scan had a length of 0.5 mm and was comprised of 51 scanning positions. 31 B-scans were obtained over a length of 0.3 mm at each depth. The step size was 10 μm in each direction. The 31 B-scans were reconstructed with the VD method and the proposed IMMI method. The resulting reconstructions at each depth were stacked together and are represented as the MAP taken within 300 μm of the expected source position. The total measurement time was approximately 1 hour.

d) Measurement 4: imaging of real tissue

Finally, the head vasculature of a 9 days-old mouse was measured ex vivo without removing the scalp. The mouse was 9 days old, shaved CD1® specimen, (Charles River Laboratories, Research Models and Services, Germany GmbH). It was euthanized with an intraperitoneal overdose of ketamine/Xylacin. The measurements were performed with the 25 MHz sensor. Each B-scan had a length of 4 mm and was comprised of 81 scanning positions. 141 B-scans were obtained over a length of 7 mm. The step size was 50 μm in both directions. Each individual signal was averaged for 5 laser shots. The 141 B-Scans were reconstructed with the VD method and the proposed IMMI method. The resulting reconstructions were stacked together and are represented as the MAP taken between 10.5 and 13.5 mm along the sensor axis. The total measurement time was approximately 5 hours.
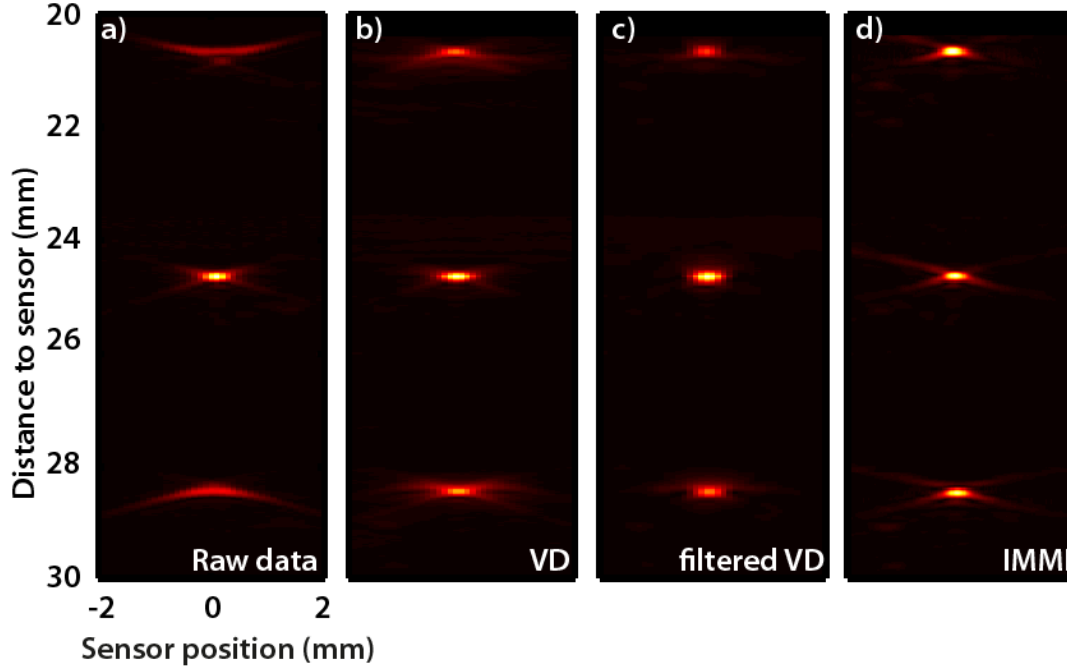
Figure 51: Experimental B-scan with the 10 MHz sensor ($F = 25.4$ mm and $D = 13$ mm), and reconstruction methods. The detector is scanned along the top of the image. The images are represented in a linear color scale and normalized to their respective maxima. See text for the simulation details. *a)* Simulated B-scan before any reconstruction is applied. *b)* Reconstruction with the VD method. *c)* Reconstruction with the filtered VD method. *d)* Reconstruction with IMMI.

4.3.6 Results

a) Measurement 1: single source

The experimental B-scan of a 100 μm microsphere, performed with the 10 MHz sensor and reconstructed with VD and the proposed IMMI method is shown in Fig. 51. The raw data (Fig. 51a) is the same as already presented in Fig. 47, but it is shown here with the source at the three positions in the same image for convenience. The figure shows the relative amplitude of the sources as well as the SIR distortion of the wavefronts inherent to a spherically focused sensor. In Fig. 51b, the reconstruction with the VD method is shown. The reconstructed amplitude of the out-of-focus absorbers is lower than at the focus, since the low-frequency components of the signals remain partially spread around the real location of the absorbers and do not contribute to the reconstructed amplitude. The results demonstrate the inability of the VD method to accurately recover the absorber amplitude and shape when the source is out of focus.

Fig. 51c shows the result of VD after applying a 5 to 20 MHz band-pass filter on the signals, in order to improve the lateral resolution (Eq. 4.6). While the lateral size of all absorbers has indeed been improved, the reconstructed amplitude is still lower than expected. These results show that, even with signal filtering, the VD method cannot provide an accurate image reconstruction.
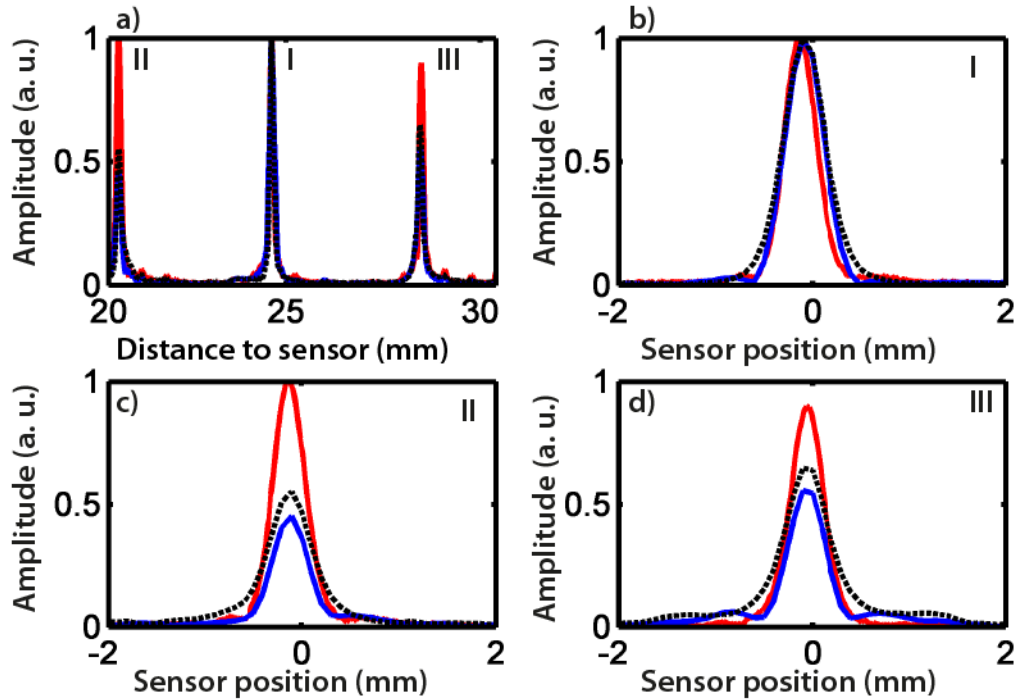
114

Figure 52: Profiles along the reconstructions shown in Fig. 51. *a)* Profile along the depth for the middle of the reconstructions. *b)* to *d)* profiles along the scanning direction for the sources located at different depths as shown in *a)*. Blue: VD reconstruction. Black-dashed: filtered VD. Red: IMMI.

Fig. 51d shows the performance of the generalization to IMMI developed in this work. The results show that by including the SIR of the transducer, IMMI is able to recover the amplitude of the absorbers more accurately. At the same time it yields uniform lateral dimensions, and therefore resolution, along the sensor axis, without the need for signal filtering. It is important to stress that neither in this case nor in the following the signals reconstructed with IMMI were treated with a filter other than the high-pass at 0.05 MHz for the removal of parasitic signals and signal offset.

The reconstructed source absorption and size can be analyzed more closely with the aid of Fig. 52, where the axial and transversal profiles of the reconstructed B-scans are shown. Fig. 52a shows that the amplitudes reconstructed with IMMI are uniform to within 5% of the maximum. Figs. 52b to 52d show the reconstructed profiles taken along the scanning direction for all three absorbers. The FWHM of the filtered VD reconstructions at the focus is 475 μm and similar for the absorbers out of focus. The FWHM of the IMMI reconstructions, however, is ~400 μm for all three absorbers which, taking into account the intrinsic resolution of the sensor, results in an estimated object size of ~100 μm, as expected. The results show that the proposed IMMI method provides accurate and well-resolved reconstructions of experimental B-scans in simple phantoms.

As the 25 MHz transducer has a tighter focus than the previous sensor, it is worth to illustrate the effect of a tighter focus on the B-scan of a point absorber and the reconstructed
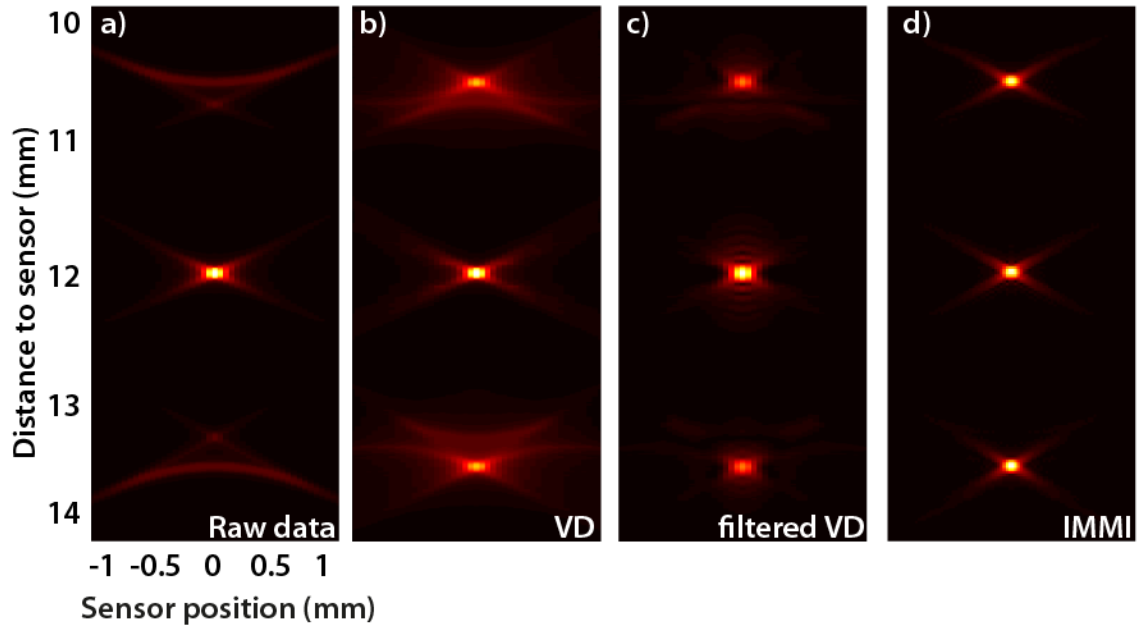
Figure 53: Simulation of a B-scan with a spherically focused detector ($F = D = 12$ mm),, and reconstruction methods. The detector is scanned along the top of the image. The images are represented in a linear color scale and normalized to their respective maxima. See text for the simulation details. *a)* Simulated B-scan before any reconstruction is applied. *b)* Reconstruction with the VD method. *c)* Reconstruction with the filtered VD method. *d)* Reconstruction with IMMI.

images. For that, the B-scan of a 100 µm absorber measured with a sensor of $F = D =12$ mm (i.e., the geometry of the 25 MHz sensor) was simulated for three absorbers located along the axis. The unreconstructed B-scan is depicted in Fig. 53a. The figure shows that the amplitudes of the out-of-focus signals are 25% of the amplitude in focus, even though the sources are located only 1 mm away from it. This is in contrast to the 10 MHz transducer, where the sources were measured with 25% amplitude at 4 mm from the focus. The results demonstrate the trade-off to be made between lateral resolution at the focus and axial sensitivity when working when focused sensors.

In Fig. 53b, the unfiltered VD reconstruction is shown. In this case, the effect of the transducer surface is also more significant than for the 10 MHz transducer: the low frequencies in the signals pose a serious limitation to the attainment of a uniform lateral resolution along the transducer axis. Of course, a good resolution may be partially restored by the use of signal filtering, as shown in Fig. 53c (high-pass filter at 4 MHz). However, the amplitude of the absorbers is not correctly recovered. The reconstruction for the proposed IMMI method is shown in Fig. 53d. In this case, the sources are reconstructed with uniform amplitude and resolution along the axis. The FWHMs correspond to the expected object size in all three cases, 100 µm[*].

---

[*] The reconstruction profiles are qualitatively similar to the ones shown in Fig. 52; therefore they do not add to the discussion and were omitted.
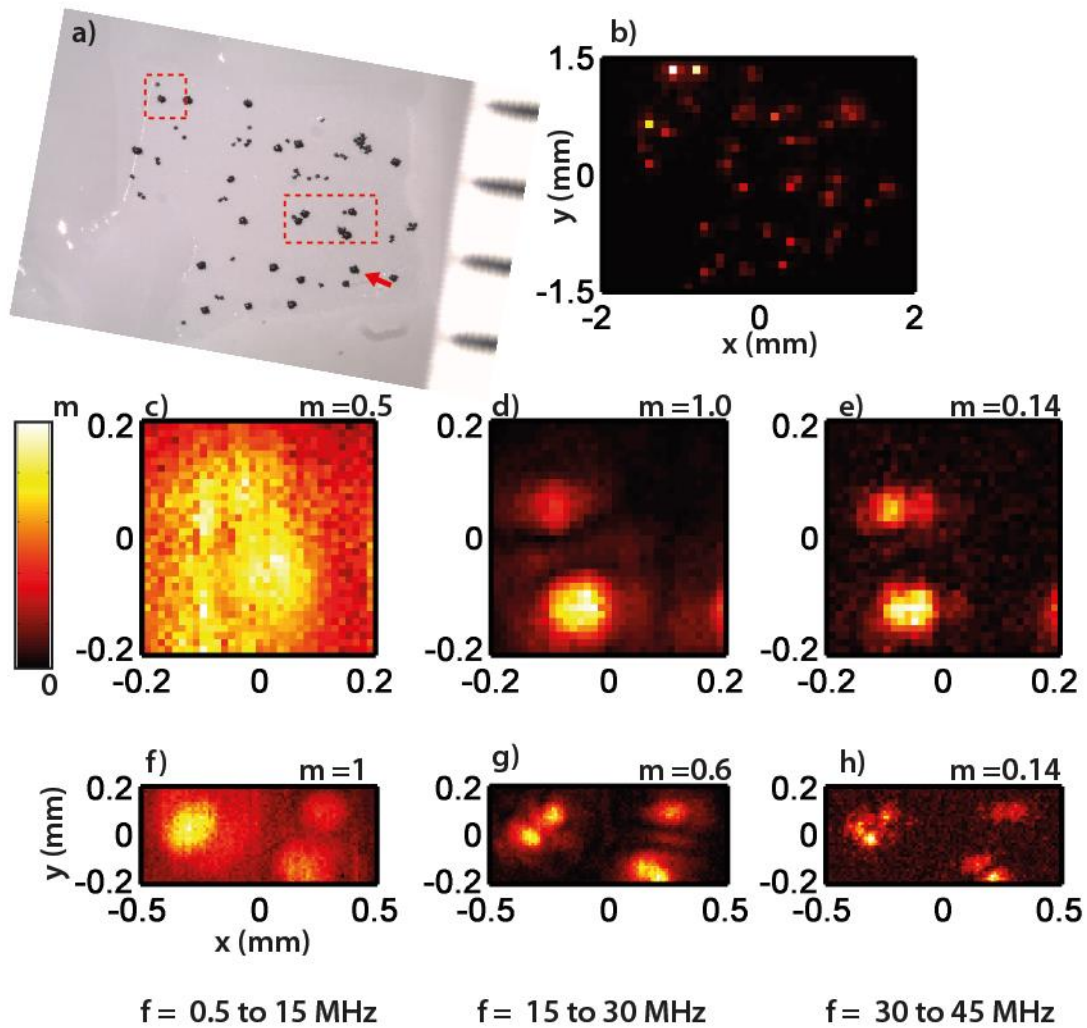
116

Figure 54: 2D scan of a 100 and 50 m microspheres lying on a plane. *a)* Photograph of the phantom with delineated regions where a finer scan was performed. *b)* Coarse scan of the full phantom. *c)* to *e)* finer scan of the square region. Each image results from filtering the signals with a band-pass filter which frequencies are shown in the bottom of the column. Each image its normalized to its maximum *m*. *f)* to *h)* Same for the rectangular region. See text for a detailed discussion.

b) Measurement 2: multiple sources on a plane.

A photograph of the multiple-microsphere phantom is shown in Fig. 54a and the coarse 2D scan of the full phantom is shown in Fig. 54b, where some of the structures can be recognized. The microsphere marked with an arrow was chosen for Measurement 3. The areas marked in red correspond to the finer scans shown in the bottom rows. For each row, the columns show the same scan filtered within different frequency bands, normalized to its maximum *m*. The figure shows several results worth noting.

Fig. 54c shows that the definition sensor resolution as $\delta = Fc/Df$ must be interpreted carefully in an optoacoustic context. Indeed, from such definition one would expect a resolution in focus of 100 μm as corresponds to the 15 MHz in the frequency band and therefore well-resolved sources. This is however not the case for the image shown. It

can be therefore concluded that the resolution is ultimately determined by the lowest frequencies in the source spectrum. If no image reconstruction is applied, the only way of improving the resolution is thus by high-pass filtering the signals, as shown in Figs. 54d and 54e.

Figs. 54f to 54h show that the lowest frequencies in the phantom are measured with higher amplitude that the higher frequencies (as shown by the *m* values). Since the phantom is only comprised of 100 and 50 μm sources, it can be understood that the low frequencies arise from the mutual interference of the individual microsphere optoacoustic waves and as a result, the whole phantom emits as a bulk for those frequencies. Additionally, it has to be noted that the frequency range from 0.5 to 15 MHz lies (for the most part) outside the optimal bandwidth of the detector. This finding shows that low frequencies compared to the central frequency of the detector may be measured with high amplitude if they are generated by objects that are absorbing or large enough (in this case, the bulk of the phantom), i.e. if they emit optoacoustic waves with high amplitude.

c) Measurement 3: stacking of reconstructions

From the phantom shown in Fig. 54a, the microsphere selected with an arrow was chosen and three 2D scans were performed with the source located at three different distances from the sensor. The scans along the *x* direction were chosen as the B-scans to reconstruct with filtered VD and IMMI. The reconstructed images were stacked and the resulting 3D datasets are represented as MAPs along the transducer axis in Fig. 55.

Figs. 55a to 55c show the filtered measurement data and the reconstructions when the microsphere is in focus. In that case, it can be observed that the IMMI method improves the resolution along the scanning direction when compared with the VD method. VD however only results in better contrast of the image, which is to be expected since VD does not modify signals at the focus significantly. From these findings it can be concluded that the IMMI method provides superior imaging performance over signal filtering or the VD method in the vicinity of the focus for noisy signals.

Figs. 55d to 55f show the measurement data and reconstructions with the source located at 0.25 mm from the previous location. In the case of the measured data, no object may be recognized. The filtered VD method (Fig. 55e) results in improved resolution and amplitude over the raw data, but results in a reconstructed object shape different from that in focus. Conversely, the reconstruction with IMMI (Fig. 55f) is similar to the reconstruction
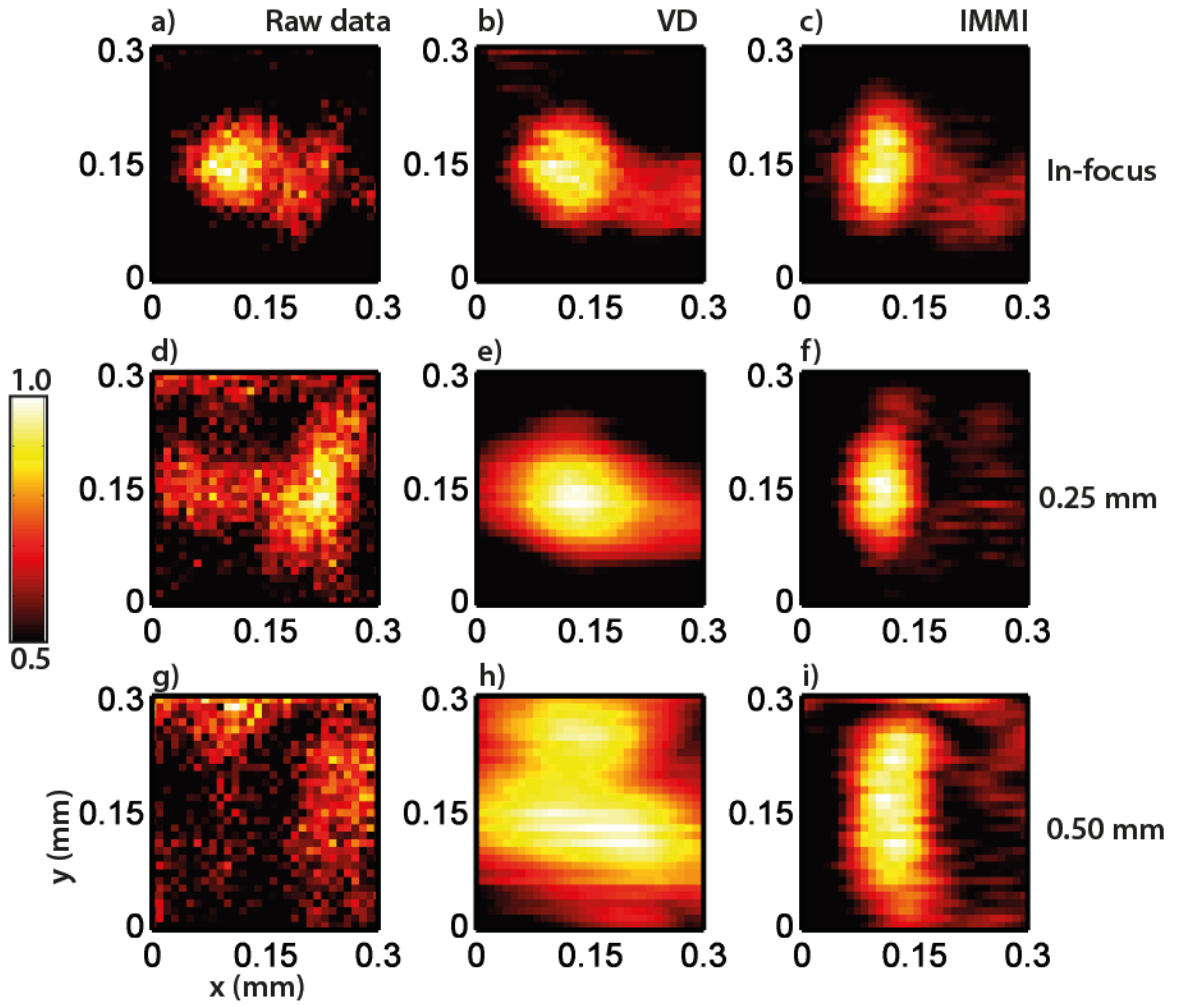
Figure 55: Microscanning of a microsphere at different distances from the sensor focus, reconstructed with the methods indicated. The reconstructions were applied to the scans at along the *x* direction. The left column represents the MAP of the filtered signals. The middle column represents the reconstructions with the filtered VD method. The rightmost column represents the reconstructions with the proposed IMMI method. See text for details.

in focus, which implies constant lateral resolution within 0.5 mm of the focus (0.25 μm to either side), as expected from the simulations.

Figs. 55g to 55i show the measurement data and reconstructions with the source located at 0.5 mm from the first position. As expected, the measured data shows no resemblance to the expected object, but more importantly, the reconstruction filtered VD (Fig. 55h) provides little improvement in this case. This is in contrast to the IMMI reconstruction, in which the resolution along the scan direction *x* is kept constant when compared with the previous reconstructions. However, since the correction is only applied to one of the scanning directions, the reconstructed object shape is distorted. The results show that, despite this limitation, IMMI provides better imaging performance than the standard VD method for greater depths. Moreover, the IMMI method results in superior
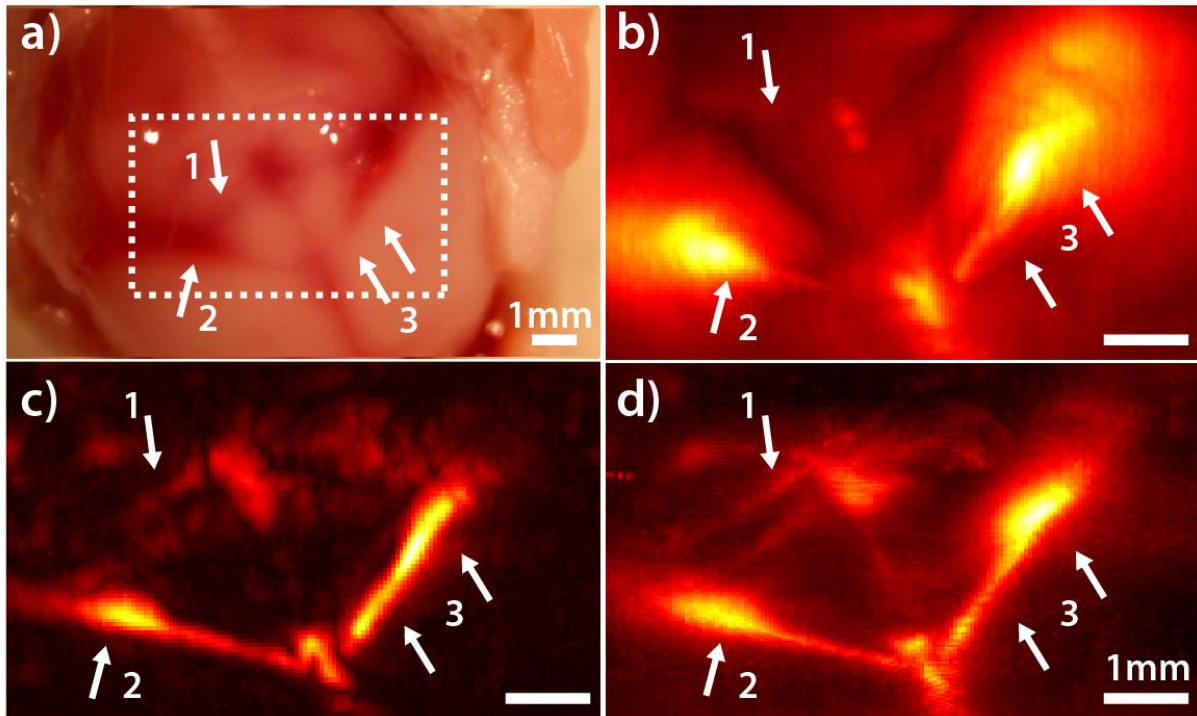
Figure 56: Performance of the different reconstruction methods for an *ex-vivo* biological measurement. The head vasculature of a 9 days-old mouse was measured. The reconstruction images are normalized to their respective maxima and represented in a linear color scale. *a)* Picture of the imaged region after the experiment, with the scalp removed. One of the ears is visible to the right of the picture, with the snout outside of the lower part of the image and the body above. *b)* VD reconstruction. *c)* filtered-VD reconstruction. *d)* Reconstruction with IMMI. See text for further details.

performance even with very noisy data, in spite of the signal-averaging properties inherent to delay-and-sum algorithms such as VD.

d) Measurement 4: imaging of real tissue

Fig. 56a shows a photograph of the sample after optoacoustic imaging, with the scalp removed to reveal the head vasculature. Fig. 56b shows the reconstruction results of the VD method without additional signal filtering. Some blood vessels cannot be resolved (hint 1) and the shape of others does not match with the validation photograph (hints 2 and 3). This shows the failure of the unfiltered VD method to yield an image of the sample.

Fig. 56c shows the VD method after an extra high-pass filter at 5 MHz was applied on the signals. Significant improvement in reconstruction quality is observed owing to the filtering procedure. Now different structures can be recognized and matched to the validation image in Fig. 56a (e. g., hints 1 and 2). However, there are some inconsistencies of the VD reconstruction with respect to the validation photograph. Indeed, as seen in Fig. 56a, vessel 3 broadens and acquires a darker tone towards the ear, which should result in higher reconstructed amplitude in that region. In Fig. 56c, however, the reconstructed width and amplitude of the vessel remain relatively constant throughout its length.

Fig. 56d shows the image obtained with IMMI. The proposed method yields a more accurate image than both VD reconstructions as the features of the blood vessels are more consistent with the validation photograph than in the VD cases. IMMI is able to correctly reconstruct the change in shape of vessel 3, and resolves the vessels in 1 more clearly. The reconstructed size of vessel 2 is slightly larger than the filtered VD reconstruction shows, which is expected from the validation image. The results show the overall superior performance of the proposed method over standard techniques in biological samples.

4.3.7 Conclusion

An image reconstruction method for scanning optoacoustics with spherically focused sensors has been presented. It is based on the model-based optoacoustic reconstruction algorithm IMMI for which the spatio-temporal response of the sensor was included. The reconstruction was applied to simulated and measured B-scans of point sources, and to the stacking of experimental B-scans of a biological sample. The IMMI reconstructions of the numerical and experimental data yielded uniform amplitude and lateral resolution along the sensor axis, in contrast to the standard image reconstruction method. As a result, in the biological application, the IMMI reconstructions of the experimental data were more consistent with the validation image than standard methods. The method proposed herein provides accurate images for scanning optoacoustics and can be readily applied to anatomical, functional and multi-spectral imaging at meso- and microscopic scales.

There are several aspects in which both microscanning with focused detectors and the IMMI method described herein may be modified for improved performance. In the following paragraphs, changes to the current hardware and reconstruction method are discussed. Afterwards, the fundamental limits of the technique as a full 3D modality are analyzed.

a) Practical considerations

Currently, a microscan experiment such as the *ex vivo* measurement shown in the previous section takes approximately 5 hours to complete. Even the measurements of simple phantoms, like the 2D microsphere sample of Fig. 54, are time-consuming and laborious. Due to the small dimensions of the focal spot of the sensor and the long time it takes to obtain one single B-scan, the initial alignment and the choice of the scanning parameters usually take as long as the definitive measurement itself. As a result, *in vivo* studies in this system are not feasible and the applicability of the technique is thus limited.

There are two main bottlenecks in the current implementation, which may be alleviated for improved performance and acquisition times. First, the pulse repetition rate of the laser is 10 Hz. With the use of kHz repetition rate lasers, for example, acquisition times could be reduced at least tenfold[*]. Second, the translation stages are part of a setup intended for proof-of-principle studies in a variety of geometries, and were thus chosen for their versatility and carrying capacity, not for their speed or submicron accuracy. Thus, a setup specifically designed for microscanning and the choice of faster and more accurate stages should result in improved overall performance. Additionally, substituting the single element sensor by a multi-element array should result in shorter acquisition times as well. Ultrasound arrays, however, open the door to different measurement strategies, which are discussed in the next chapter.

With respect to the proposed IMMI method, the current implementation combines a 2D propagation model with a 3D SIR. In a full 3D implementation, the complete 2D set of signals could be used during image formation and the scanned volume would be reconstructed simultaneously. This should result in isotropically enhanced resolution, and not mainly along the scanning direction, as seen in Fig. 55. There are two main reasons why this approach was not pursued on the present work. First, as discussed in the previous paragraph, the current microscanning implementation is not practical and has not gone beyond the proof-of-principle stage as a consequence. Therefore, the efforts were shifted towards a more practical modality for 3D imaging, as presented in the next chapter. The second reason relates to the planar acquisition geometry inherent to microscanning and is discussed in more detail in the following.

b) Fundamental limits

A planar measurement geometry is indeed practical for the imaging of murine anatomical regions with restricted access (e.g. joints or the neck area), and for superficial and microscopic applications. However, in terms of the efficient acquisition of signals from the object, planar scanning is far from the performance of a geometry that partially or totally surrounds the object (i.e., a tomographic geometry).

This was discussed in the context of the model-matrix inversion but it is a limitation more fundamental than just numerical. The reason is that microscanning with focused detectors may be understood as a particular case of tomography with a very limited-angle of view, i.e., the angle of acceptance of the sensor, θ. In the case of the 25 MHz transducer, $\theta = 60°$, which is far from being considered tomographic in the traditional sense. While a

---

[*] See dissertation by R. Ma for an implementation of scanning microscopy along these lines.

broader angle of acceptance can be obtained only by a tighter focusing of the sensor ($F/D <$ 1), this in turn results in degraded axial sensitivity, limits the penetration depth and thus the 3D performance of the technique.

The use of transducer arrays, however, allows for certain flexibility in the choice of the focusing parameters and the arrangement with respect to the sample. This takes us to the final chapter, outlining image formation with ultrasound arrays in a 3D tomographic geometry, and the corresponding reconstruction algorithms that take into account sensor properties.

5. RECONSTRUCTION ALGORITHMS FOR NON - CIRCULAR TOMOGRAPHIC GEOMETRIES

In the previous chapter, it was demonstrated that making use of the transducer properties during image reconstruction results in improved image quality and resolution in a microscan geometry. However, it was also argued that this geometry was somewhat limited in terms of 3D imaging. In the present chapter, the knowledge of transducer properties and the image formation methods are adapted to the reconstruction of volumetric images in a truly 3D imaging geometry*.

In contrast to the previous chapter, the work reported herein deals with a tomographic measurement geometry that encloses the object. In optoacoustics, tomography has been traditionally applied to the imaging of biological tissue at macroscopic scales, i.e., for whole-body anatomical imaging of small animals. In combination with multi-spectral techniques, it has resulted in a variety of applications, such as functional imaging of the brain [13], time-resolved imaging of physiological processes such as kidney perfusion [11] and the imaging of exogenous contrast agents coupled to biomarkers of disease development [10, 12]. By the use of confined a illumination and high-frequency (>10 MHz) transducers, some results towards the imaging at mesoscopic scales have been also demonstrated [14, 32]. Tomography is therefore a powerful approach to image formation in optoacoustics, as it can provide well-resolved images at depths of up to a few centimeters.

Traditionally, optoacoustic tomography in 3D has been performed by the stacking of 2D cross-sectional images, each 2D image being acquired by surrounding the sample with detectors cylindrically focused to the imaging plane. Only in recent years has optoacoustic tomography been genuinely demonstrated in 3D with good performance [15, 49], where the sensors have been arranged on the surface of a sphere. However, rotationally- (or spherically-) symmetric tomography may exhibit degraded lateral resolution and contrast for sources away from the center of rotation. This effect is due to the sub-optimal spatial sampling of points in the periphery of the ROI [30]. As a result, the system achieves optimal performance only in a region close to the center of rotation, which effectively constraints the characteristics and dimensions of the samples that can be investigated with a given setup.

It has been demonstrated that the loss of resolution and sensitivity may be exacerbated in part by the spatial properties of the detector and in part by the failure to acknowledge them during image formation. Rosenthal et al. [24] have shown in a 2D proof-

---

* At the time of writing, the results in this chapter are under consideration for publication to Medical Physics.

of-principle study that the loss of resolution can be compensated by taking into account the shape of the detector in the image reconstruction procedure. However, in actual biological measurements, the signal-to-noise ratio (SNR) for objects away from the focus may not be sufficient to restore image quality by computational means alone.

In order to circumvent the limitations of conventional tomographic arrangements, Jérôme Gâteau, post-doc in our group, and the author have proposed a solution based both on a different measurement geometry and the use of a realistic image reconstruction algorithm[*]. The aim of this chapter is to present a description of the reconstruction algorithm and showcase its performance with respect to standard reconstruction algorithms in simulations and experiment. A brief description and motivation of the non-conventional measurement geometry is provided for reference.

The chapter starts (Section 5.1) with a short background on conventional optoacoustic tomography and its proposed nonconventional counterpart. In Section 5.2, the proposed reconstruction algorithm is described in detail. In Section 5.3, the experimental and numerical techniques used to test the performance of the method are provided. In Section 5.4 the results of simulation and experiments are shown, and finally in Section 5.5 the results of the chapter are discussed. The novel measurement geometry is, at the time of writing, in press at Med. Phys. [43], and the proposed reconstruction algorithm is under consideration for publication in the same journal.

5.1   Conventional vs. nonconventional optoacoustic tomography

In this section, the characteristics of conventional tomography and its limitations are briefly described; a detailed discussion of the concepts outlined herein can be found in the literature [23, 24]. Afterwards, the proposed geometry is described and the relevant parameters are given.

Let us introduce tomography with a simplified case of a circular detection geometry. Fig. 1a shows an schematic of the geometry: the region of interest (ROI), that contains the sample, is measured by sensors located at different positions along a circle of radius R_0. The individual sensor positions are referred throughout this chapter as projections. Whether the sensor is actually translated from one position to the next or is part of a circular array of identical sensors makes no different for the present discussion. Additionally, the phenomena described herein are equally applicable to the case of sensors cylindrically focused onto the plane, and to the case of an array with symmetry along the z axis.

---

[*] At the time of writing, the development of the measurement geometry, by J. Gâteau, and the work on the corresponding image reconstruction algorithms, by the author, are still work in progress.

In the particular case of point-like sensors[*], each source in the ROI is measured isotropically: the measured amplitude for each projection depends only on the source distance to the sensor. In the general case of a sensor with a finite lateral size d (focused or not), it can be understood from the results of previous chapters that this will not be the case. Due to the finite size of the sensor, sources located outside the main lobe of its sensitivity field will be measured with less amplitude than sources located in front of the detector. This is depicted in Fig. 57a as the -6 dB contour of the sensitivity field of a focused or finite-sized transducer. It can be observed that the fields corresponding to different projections will overlap only on a region whose radius is approximately determined by the width of the main lobe. As a result, sources outside the overlapping region (marked in red in Fig. 57a) will be reconstructed inaccurately unless the sensor properties are taken into account during image formation. However, the SNR of those sources may not be sufficient for an accurate reconstruction, depending on the robustness of the algorithm.

The concept of the nonconventional geometry is shown in Fig. 57b. The proposition is that, by linearly scanning the sensor at each angular position, the sensitivity fields overlap with one another in a larger region and signals generated at every point in the ROI are efficiently measured. An additional advantage of the scan+rotation geometry is its flexibility. By adjusting the number of scanning positions at each angle and the distance between them, the scanned area can be chosen to fully cover of the object under study. Thus, the application at hand defines the scan parameters, instead of the opposite. For the case presented in this work, the details on the scanning parameters can be found in Section 5.3.

Let us now discuss the measurement geometry in the 3D case. As discussed previously, one of the most common implementations of 3D imaging in a tomographic environment makes use of sensors cylindrically focused to the ROI, as shown in Fig. 57c. The volumetric image is generated by scanning the sensors vertically and stacking of the 2D images taken on each plane. As discussed in the previous chapter, the fixed focus F and diameter D of the sensor results in a resolution along the scan direction (the z axis in this chapter) which is dependent on the frequency f as $\delta \approx Fc/Df = \lambda F/D$ where c is the speed of sound in the medium and λ the wavelength for that frequency. However, this resolution is only attained at the focal point of the sensor and, together with the sensitivity, degrades rapidly away from it.

---

[*] The definition of point-like sensor within this context is equivalent to the one discussed in Chapter 4, section 4.1.2.
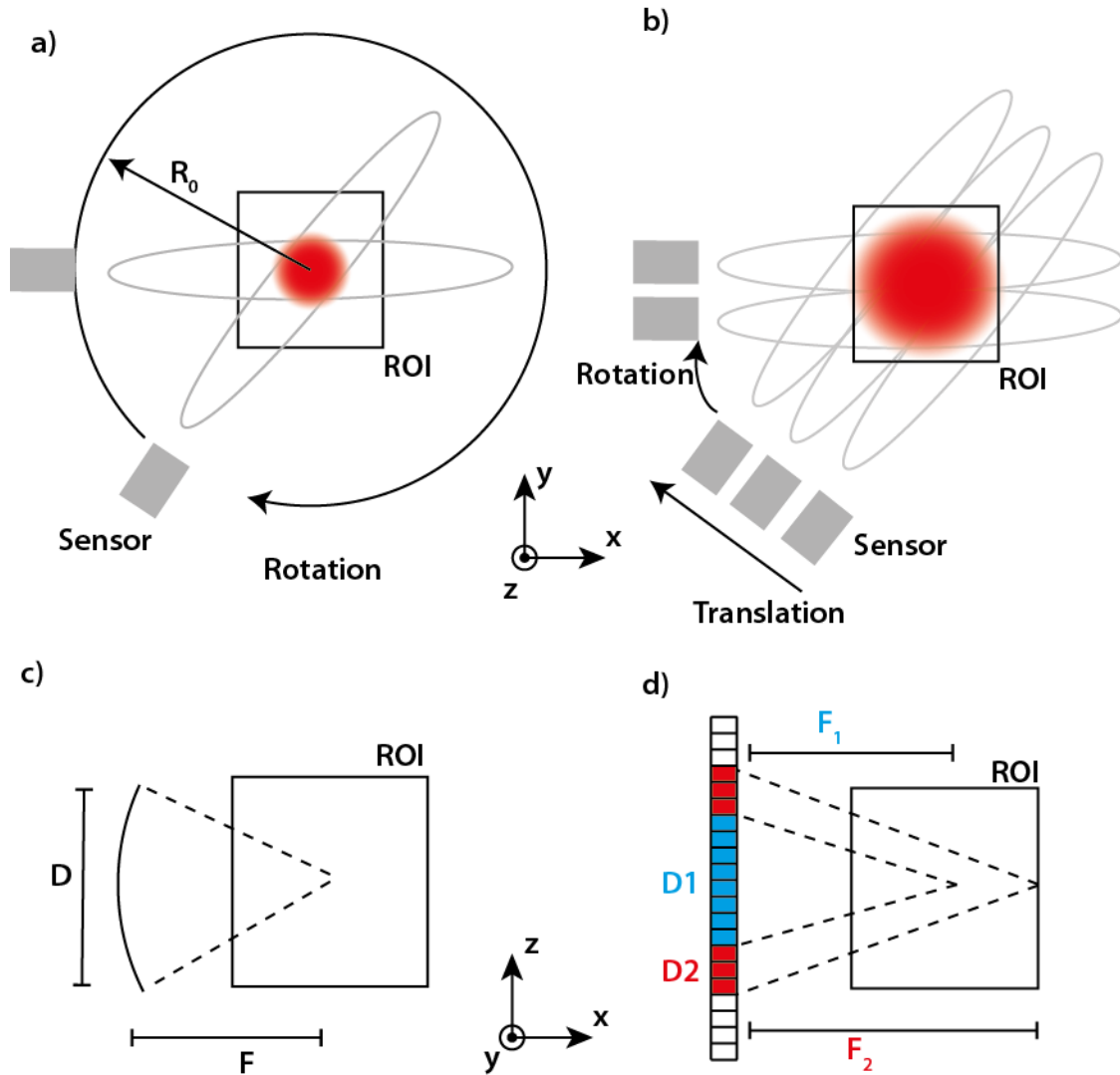
Figure 57: *a)* Conventional tomography with a finite sized sensor. The sensitivity field, represented as the -6 dB contour, overlaps in a region in general smaller than the ROI. *b)* Proposed nonconventional tomography: the sensor is scanned laterally at each angular position. By adjusting the spacing and number of scanning positions, the overlapping region can be adapted to the size of the ROI. *c)* Lateral view of the ROI with a focused transducer. *d)* Lateral view of the ROI with an ultrasound array. The colored array elements are used to attain the desired resolution at the corresponding distance. See text for details.

In the work presented herein, a linear transducer array was used instead, as shown in Fig. 57d. The main advantage of using a linear array as opposed to a focused detector is the possibility of attaining a uniform vertical resolution without the need to mechanically scan the sensor. A uniform resolution δ is achieved by reconstructing the image with the sufficient number of array elements, which is explained in the following.

The vertical resolution achieved by the array can be described in analogy to the focused sensor (see Fig. 57d): in the case of the array, F represents the distance from the middle of the array to the point being imaged. D is determined by the number of sensors used to reconstruct and the distance between the individual array elements d_e, which sets an upper limit for D, which we define as $D_{max} = N_{elem} \cdot d_e$. Thus, the vertical resolution for

128

any two points in the ROI will be equal if $F_1/D_1 = F_2/D_2$. However, for an arbitrarily large D the maximum resolution achievable by this technique is limited to $\delta = \lambda/2$ [31] and therefore no resolution is gained if $F/D < 0.5$. This implies that, by placing the array at a distance $F_1 \leq D_{max}/2$ from the ROI, the full array can be used during image formation[*]. In the work presented herein, the full array was used in the reconstructions, thus ensuring a constant vertical resolution throughout the ROI.

In spite of the clear advantages of the proposed non-conventional geometry over standard tomography, it will be shown that the use of reconstruction algorithms based on a point-like approximation may still result in degraded imaging performance. In order to optimally reconstruct a volumetric image of the object, an advanced imaging algorithm was developed and is discussed in the following.

5.2 Model-based image reconstruction in 3D with sensor properties

In this section, the proposed reconstruction method is described. The algorithm is based on the 3D Interpolated Model-Matrix Inversion (IMMI) presented in Chapter 2. A brief overview is provided to set the basis of the modifications implemented in the following sections. However, since the modifications are based on the structure of the model-matrix, and not on the underlying semi-analytical solution to the optoacoustic forward problem, what follows is a qualitative exposition of the IMMI algorithm. For a more detailed review, refer to Chapter 2 and the cited literature.

The IMMI algorithm expresses the optoacoustic signals detected at each sensor position as a linear combination of the elementary absorbers within the ROI

$$p = Mu.$$ (5.1)

where p is a vector representing the signals for every sensor position and u represents the absorption of the elementary sources within the ROI. M is the model matrix, that describes the generation and propagation of the optoacoustic signal from every absorber to every sensor position.

In Chapter 2 (section 2.4.2) $p_{ik}(t)$ was defined as the wave generated by the source u_k and measured at sensor position $\vec{r}_i$, as can be seen in Fig. 58a

$$p_{ik}(t) \propto u_k \left[\frac{\delta(ct - |\vec{r}_i - \vec{r}_k|)}{|\vec{r}_i - \vec{r}_k|} \right].$$ (5.2)

---

[*] Due to the tomographic geometry in the plane, points at distances further than F_1 for one array position will be located closer for the opposite array position.

The term in brackets is the Green's function between source and sensor and corresponds to the elements in the model matrix, whereas u_k is the absorption of the elementary source k *.

In the following, the combination of the model-matrix with the sensor properties is explained. Afterwards, the details on the computation of the matrix are described.

5.2.1 Model-based in 3D with transducer characteristics

The implementation of the transducer properties presented herein is different than the convolution method of the previous chapter. The reason is that the convolution method requires an explicit analytical solution for the SIR, which does not exist for the geometry of the array elements in this work (cylindrically focused detectors). The proposed method is based on the computation of the SIR with the model-matrix itself, as follows.

Let us recall the definition of the SIR of a detector i at a point $\vec{r}_k$

$$h_i(\vec{r}_k, t) = \int_S \frac{\delta(ct - |\vec{r}_s - \vec{r}_k|)}{|\vec{r}_s - \vec{r}_k|} dS \ , \tag{5.3}$$

where $\vec{r}_s$ spans the surface S of the detector. Eq. (5.3) can be discretized dividing the surface of the detector into point-like sensors, and the integral in Eq. (5.3) can be thus performed numerically. From Eq. (5.2) and the discretization of Eq. (5.3), it follows that the model-matrix for a sensor of finite size can be computed by summing up model-matrices for point detectors. Such matrices are calculated for point-like sensors located on the surface of the finite-sized sensor.

Fig. 58b shows a top-view of the relative arrangement of the ROI and one finite-sized sensor of surface S to illustrate this concept. The center of the finite-sized sensor i is located at $\vec{r}_i$ with respect to the center of the ROI. Its surface is comprised of elementary sub-sensors s located at $\vec{r}_s$. The signal generated at voxel k and measured by sensor i is defined as $p_{ik}^{finite}(t)$. By applying Eq. (5.3), such signal can be synthetized from the signals measured by the sub-sensors s, $p_{sk}^{point}(t)$, which have the form of Eq. (5.2). Thus, $p_{ik}^{finite}(t)$ can be calculated in the following manner

$$p_{ik}^{finite}(t) = \sum_{s \epsilon S} p_{sk}^{point}(t) \Delta S = u_k \sum_{s \epsilon S} \left[\frac{\delta(ct - |\vec{r}_s - \vec{r}_k|)}{|\vec{r}_s - \vec{r}_k|} \right] \Delta S \tag{5.4}$$

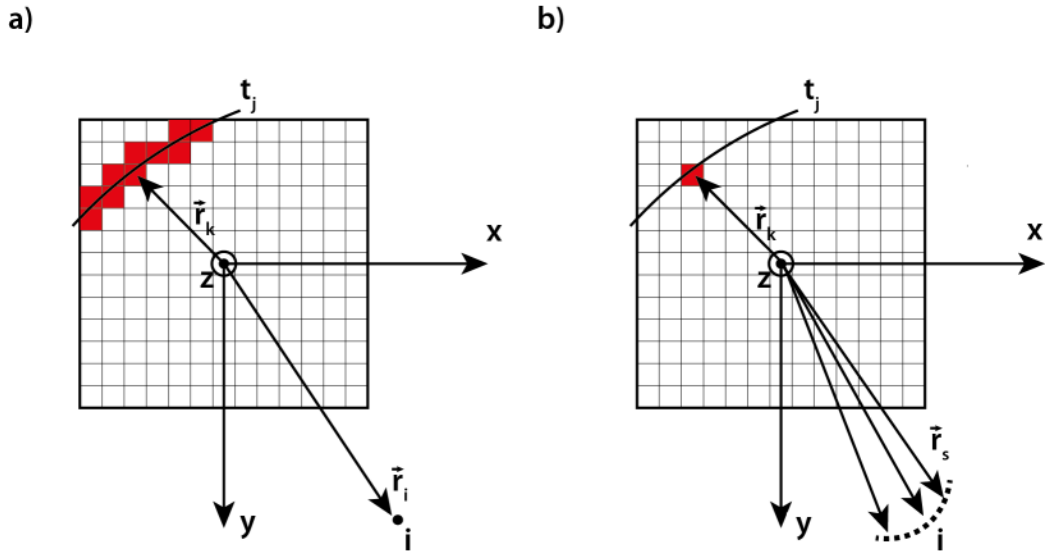* The multiplicative factor m_{lk} has been omitted for simplicity.

Figure 58 *a)* Schematic of the discrete ROI and one point-like sensor to illustrate the structure of the model-matrix elements. *b)* Schematic of the discrete ROI and one finite-sized sensor to illustrate the principle of matrix summation for the SIR implementation into the model-matrix. See text for details.

Eq. (5.4) shows that a discrete computation of the SIR can be done by summing elements of the model-matrix, which are shown in brackets.

In terms of SIR calculation, the spacing δs between the sensors is typically chosen such that it can be considered infinitesimally small compared with a given wavelength, i.e. $\delta s \leq \lambda/10$. λ typically represents the wavelength at the central frequency of the sensor. However, for the implementation in the model-matrix, it was found in a simulation study that a spacing close to the voxel size is usually enough for an accurate representation of the SIR on the measurement geometry. Therefore for the present study, the spacing was chosen as $\delta s = \lambda/4$. The exact quantities used for the calculation of the matrix are provided in section 5.3.3.

In conclusion, the SIR of a finite-sized sensor can be included in the IMMI algorithm following these steps:

1. For each sensor position of the actual scan *i,* the sensor surface is divided into point-like sensors *s* spaced by δs.
2. For each of the sensors *s,* the corresponding model-matrix $M[s]$ is computed.
3. A new model-matrix for the sensor *i* is computed, by summing up the matrix elements of $M[s]$ for all *s* corresponding to the same voxel *k*.

The details of the matrix computation and inversion are provided in the following Section.

5.3   Experimental and numerical techinques

The performance of the proposed IMMI method was assessed in simulations and experiment. Since the parameters of the measurement geometry and the model-matrix are determined by the sample measured, a description of the measured samples and the experimental setup is provided first (sections 5.3.1 and 5.3.2). In section 5.3.3 the computation of the model matrix is detailed. In section 5.3.4 the computation of the theoretical signals for the simulation study is briefly discussed. Finally, the Back-projection algorithm in 3D used for comparison is described in section 5.3.5.

5.3.1 Samples and experimental setup

a) Sample 1: absorbing microspheres

A phantom was built that consisted on three absorbing polyethylene microspheres (Cospheric LLC, Santa Barbara, California), 50 μm in diameter. The microspheres were placed 1 cm below the surface of a transparent agar block, and the phantom was positioned so that the three microspheres lay approximately on the *x-y* plane, defined as the middle of the array.

b) Sample 2: knotted suture

In this case, the phantom consisted of a suture thread, 300 μm in diameter (RESORBA Wundversorgung GmbH & Co. KG, Nürnberg, Germany), tied to a loose knot and inserted in a scattering agar matrix. Such a phantom provides a complex structure with high amplitude signals.

c) Sample 3: mouse paw

The biological sample was the hind left paw of a mouse, measured *ex vivo*[*]. The sample was chosen for two reasons. First, its recognizable features and vascularization offered an interesting and challenging imaging environment. Second, the mouse paw fits a relatively small ROI, such that the corresponding model-matrix was of a manageable size for this proof-of-principle study.

d) Detector and acquisition system

The detector used in this study was a medical ultrasound linear array of 128 elements (Acuson L7 probe, Siemens AG, Erlangen, Germany). The array was placed vertically as shown in Fig. 59a. Each of the elements was focused in the rotation plane at a

---

[*] A CD1 (r) specimen, Charles River Laboratories, Research Models and Services, Germany GmbH. The mouse was euthanized with an intraperitoneal overdose of ketamine/Xylacin.

distance of $F = 19$ mm (which was determined experimentally) and had lateral dimensions of $d = 4$ mm in-plane and $L = 300$ μm out-of-plane. The electrical impulse response of the transducer was characterized as described in Chapter 3, yielding a central frequency of 5 MHz and over 100% -6dB bandwidth. For this reason, the computation of the model matrix, the discretization of the ROI and the choice of the scanning parameters were done considering the wavelength at 5 MHz, $\lambda = 300$ μm.

Unless stated otherwise, the signals were averaged over 10 laser shots and acquired in parallel for all 128 elements by 8 custom-made acquisition boards, with 16 channels each, 12-bit resolution (over a 16 mV range) and a sampling rate of 40 MS/s (Falkenstein Mikroelektronik, Baldham, Germany). Before image reconstruction, the signals were corrected with the experimentally determined electrical impulse response with a Weiner deconvolution procedure [65]. Afterwards, a band-pass filter from 50 kHz to 9 MHz was applied to for noise removal and to delimit the reconstruction bandwidth.

e) Illumination

The excitation was provided by a tunable optical parametric oscillator laser (Opotek Inc., Carlsbad, California), with a pulse width of 6 ns and a repetition rate of 10 Hz. The illumination was coupled through a four-arm fiber bundle (CeramOptec GmbH, Bonn, Germany) at a wavelength of 760 nm.

f) Sensor movement

The array was mounted on a positioning system with three linear translation stages and one rotational stage (Thorlabs GmbH, Karlsfeld, Germany). The movement of the stages, the laser excitation and the data acquisition were synchronized by a trigger signal from the laser.

The transducer, illumination and the mouse were held inside deionized water in order to achieve optimal acoustic coupling. The water temperature was maintained at room temperature (19°), which resulted in a speed of sound of 1475 m/s. This value was used for both for image reconstruction and simulations.

The measurement time was 20 minutes for each sample.

5.3.2 Measurement parameters

For the proof-of-principle presented herein, the dimensions of the ROI were set to: 6 mm by 6 mm in the *x-y* plane and 13 mm along the vertical direction *z*. These parameters where chosen to fully enclose the samples described previously. The discretization of the
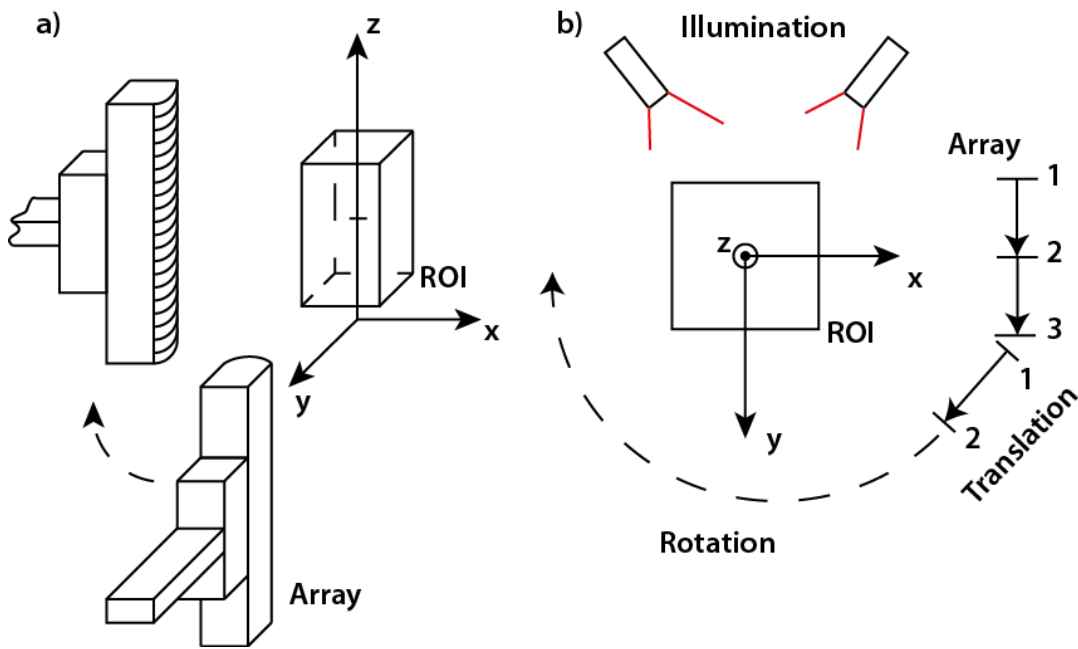
Figure 59: *a)* Perspective view of the relative position of the ROI and the array. Note that the elements of the array are positioned vertically, resulting effectively in a cylindrical detection geometry. (The illumination was omitted from this graph for simplicity) *b)* Top-view of the relative position of the ROI, the illumination and the array positions. At each rotation angle, the transducer array is translated linearly.

ROI into voxels is discussed later in this section, where the parameters of the model-matrix used for image reconstruction are explained.

The ROI was scanned using the 128-element transducer array, whose elements were positioned parallel to the z axis, as was shown in Fig. 59a. Fig. 59b shows a top-view of the measurement geometry with respect to the ROI. The sensor was arranged tomographically around the ROI at 72 angular positions, spanning 180°. Within each angle, the sensor was scanned linearly, alternating between 2 and 3 positions per angle. The spacing between linear positions was set to $2\lambda F/d = 2.7$ mm, where the quantities are as defined in 5.3.1. The total translation span was therefore 6.75 mm and the scan spacing corresponds to the sensor's beam-width, defined as the full-width at half-maximum (FWHM) of the sensor's sensitivity field at 5 MHz. With such a spacing value, the 3-2 overlapping pattern of the scan ensures a thorough sampling of the ROI.

5.3.3 Computation of the model-matrix

The model-matrix was calculated for the ROI and the measurement geometry described in the previous section.

a) Discretization of the ROI

We recall that the dimensions of the ROI where 6 mm x 6 mm in-plane and 13 mm out-of-plane. Since the detection geometry is tomographic in the *x-y* plane and linear along

the z-direction, the maximum resolutions achievable in each direction are a priori different [23]. The ROI was discretized based on this constraint. Furthermore, the discretization was done in fractions of the wavelength at 5 MHz, in order to fulfill the Shannon criterion in terms of spatial sampling [31]. Specifically, the resolution in-plane was set to $\delta xy = \lambda/4 = 75$ μm, corresponding to half the Shannon frequency, which resulted in $n = 81$ voxels in the x and y directions.

The voxel size out-of-plane was based on the maximum resolution that can be achieved through beamforming, as explained in Fig. 57d. A constant $F/D = 0.5$ out-of-plane was chosen so that $\delta = \delta z = \lambda/2 = 150$ μm. δz and the height of the ROI, 13 mm, determine the number of voxels in the z-direction, $n_z = 88$.

b) Discretization of the sensors

The discretization of the sensors was done based on $\delta s = \lambda/4 = 75$ μm. Given the dimensions of each sensor in the array (0.3 mm by 4 mm), this resulted in 4 point-like detectors along the vertical direction and 53 in-plane, for a total of 212 sub-sensors per individual projection. From this point on, the discussion of the matrix computation is done based on the final matrices that result from summing the matrices for the sub-sensors.

c) Dimensions of the matrix

The dimensions of the model matrix are determined by the ROI discretization and the measurement geometry, as described previously: 72 angles with a 3-2 scanning pattern, for a total of $N_\varphi = 180$ detection positions. Vertically, the transducer has $N_e = 128$ elements. This results in a total of $P = 23,040$ distinct sensor positions to be computed. Each of the signals is discretized in a time T.

While N and P are determined by the ROI and the measurement geometry, the exact value that T can take is constrained by N, P and the dimensions of the ROI. In order to fully enclose the ROI, the model must sample the time-of-flight from the closest distance between any sensor position and any voxel, up to the furthest. The sampling interval, defined as δt, should fulfill the Shannon criterion, and thus be chosen as a fraction of the time it takes for the optoacoustic wave to traverse one voxel [21]. As a result, $\delta t = \delta xy/2c \sim 50.85$ ns and T = 784 time samples per sensor position.

With these parameters, the model-matrix would have approximately 18 million rows and 0.6 million columns. Such a number of matrix elements is equivalent to 0.6 TB of data, even considering that the matrix is sparse. The processing and storing of such a matrix is
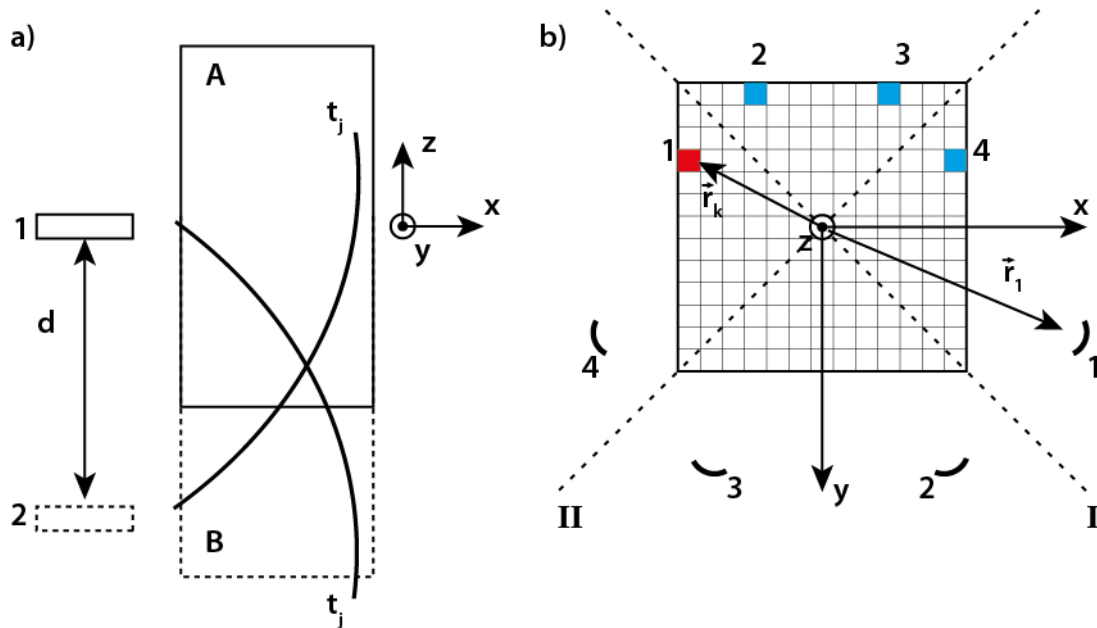
Figure 60 *a)* Illustration of the vertical symmetry of the measurement geometry and hence the model-matrix. *b)* Illustration of the in-plane symmetries of the measurement geometry with respect to the ROI. See text for details

indeed possible with a cluster or a Teraflop-capable supercomputer, but such computational power was not readily available to our group. Therefore, in order to reduce the size of the matrix to be computed, we exploited the symmetries of the measurement geometry.

d) Symmetries in the ROI and the matrix

We consider two groups of symmetries separately: out-of-plane translations[*] and in-plane reflections.

Fig. 60a illustrates the principle behind the out-of-plane translational symmetry of the scan. The ROI, labeled A, is shown on a side view with respect to the position of two sensors of the array. Sensor 1 is closest to the *x-y* plane and sensor 2 is at a distance *d* from sensor 1. Let us assume that A is extended symmetrically along the vertical direction, as shown by the dotted line, resulting in the auxiliary volume labeled B, wherein A is contained.

Let us also assume that a matrix is calculated for the ROI B. Thus, the values for such a matrix at a given time t_j (i.e., for the voxels located at a distance ct_j), would be the same for both sensors 1 and 2. Thus, the matrix would have stored exactly the same values at two different locations: the sub-matrix for the voxels within A that are detected by sensor 2, can

---

[*] The general concept of vertical symmetry for 3D model-based reconstructions was conceived by Andreas Bühler. The more general implementation of the method, discussed here, was done by the author.

be obtained by the sub-matrix of voxels within B that are detected by sensor 1. The only operation needed is a reordering of the matrix elements.

In this manner, a matrix M_A calculated for each element of the array in the ROI A, and a matrix M_B calculated only for sensor 1 in the ROI B, contain both all the information needed to reconstruct the volume A.

The benefit of this approach can be understood by computing the total number of elements for both matrices, defined as N_{TA} and N_{TB} for M_A and M_B respectively. If all other parameters of the matrices are equal, the ratio between N_{TA} and N_{TB} results in:

$$\frac{N_{TA}}{N_{TB}} = \frac{N_e \cdot N_\varphi \cdot T \cdot n^2 \cdot n_{zA}}{1 \cdot N_\varphi \cdot T \cdot n^2 \cdot n_{zB}} = \frac{N_e \cdot n_{zA}}{n_{zB}}. \tag{5.5}$$

Given the resolution along the vertical direction δz and the height of ROI A, n_{zA} is given and n_{zB} is thus determined by the distance d between sensor 1 and sensor 2. In order to reconstruct the volume A with an F-number of 0.5 at every voxel, all 128 elements of the array have to be used in the reconstruction, which in turns determines d. The result is an extended ROI B of 57.6 mm in height and $n_{zB} = 385$ voxels. With these values and Eq. (5.5) it follows that, by exploiting the vertical symmetry of the measurement geometry, M_B is 29 times smaller than M_A would be, or $\sim$21 GB. The load times and RAM memory requirements for computing and inverting such a matrix are still very demanding. The size of the actual matrix to be computed was further reduced by making use of the in-plane symmetries of the measurement geometry.

Fig. 60b shows a top view of the ROI with the in-plane sensor positions. Since the measurement geometry is not circular, two contiguous sensor positions are not related by a rotation around the z axis. However, the measurement geometry was chosen to be symmetric with respect to four of the eight symmetries of a square: the null symmetry, two reflections and a 90° rotation.

In Fig. 60b, the sensor positions symmetric to sensor 1 are shown and labeled 2 to 4. Sensor 1 yields: sensor 2 under reflection with respect to the I axis; sensor 3 under a clock-wise 90° rotation around the z axis; and sensor 4 under reflection with respect to the x axis. If similar symmetries are applied to voxel k, it is evident than the sub-matrices for sensors 1 to 4 are the same for every k, except for a reordering of the voxel indexes.

Therefore, by computing the model-matrix for the first ¼ of the sensor positions, the other $3N_\varphi/4$ individual projections can be found transforming the voxel indexes

n	n_z	P	T	Sub-sensors	δs
81	88	45	784	4 x 53	75 μm
δxy	δz	ROI B width	ROI B height	ROI A width	ROI A height
75 μm	150 μm	6 mm	56.7 mm	6 mm	13 mm

Table 1: Parameters for the final model-matrix and the imaging ROI.

accordingly. The application of the in-plane symmetries just described further reduces the size of the calculated matrix to ~10 GB[*].

e) Final parameters of the model-matrix

The final matrix was computed with the parameters shown in Table 4.1. The computation was performed on a workstation with 16 X5650 Intel Xeon cores, at 2.67 GHz each, running in parallel. The algorithm was programmed and executed in MATLAB (. The total computing time was about 35 hours, at 45 minutes per projection. The matrix was stored and used for both the simulation study and the reconstruction of the experimental data.

In order to demonstrate the effect of including the SIR in the model, a second matrix with the same parameters was computed. This matrix, however, was calculated only for one sensor per projection, i.e., is the model-matrix corresponding to point-like sensors.

The inversion of the matrix was performed with an unregularized LSQR algorithm. The optimal inversion parameters were assessed by reconstructing the signals from a numerical phantom and comparing with the expected image. The minimization of the reconstruction error was achieved after 6 iterations. Due to the re-indexing of the matrix associated to the symmetries, the time needed to compute one iteration of the reconstruction is about 5 hours.

5.3.4 Calculation of theoretical signals

In order to avoid the inverse crime, whereby the forward signals are computed with the same model that is used for inversion, the theoretical signals for the simulation study were calculated analytically.

---

[*] As a result of the transducer response and its location with respect to the ROI, the number of nonzero matrix elements is different for each projection. Therefore, the matrix computed with both sets of symmetries is not half the size of the matrix computed with only the vertical symmetries.
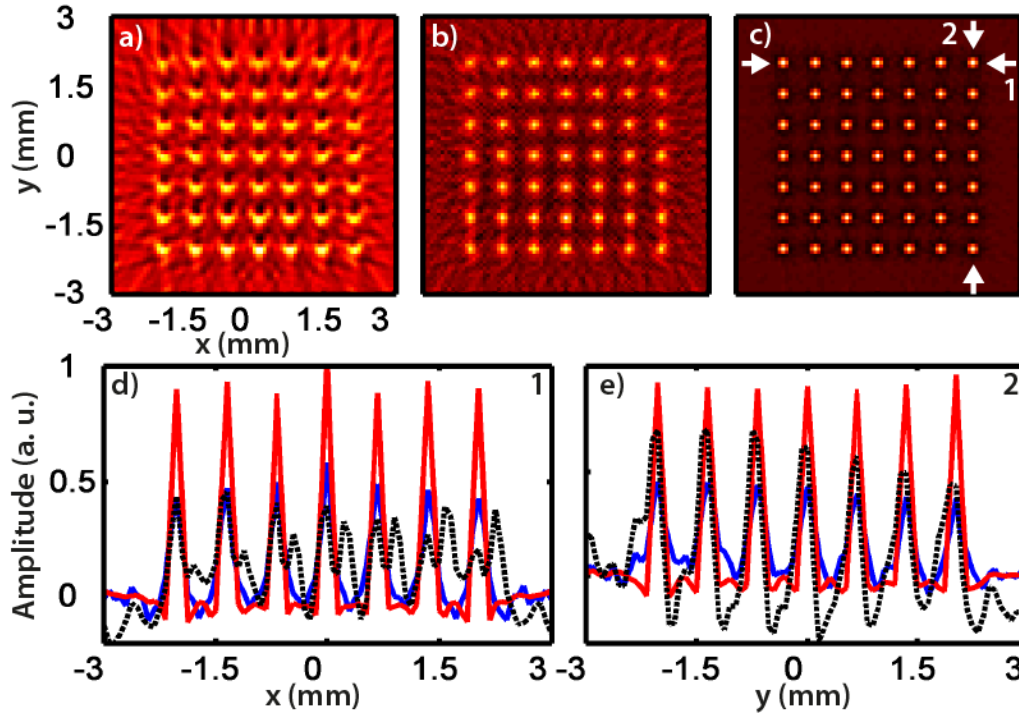
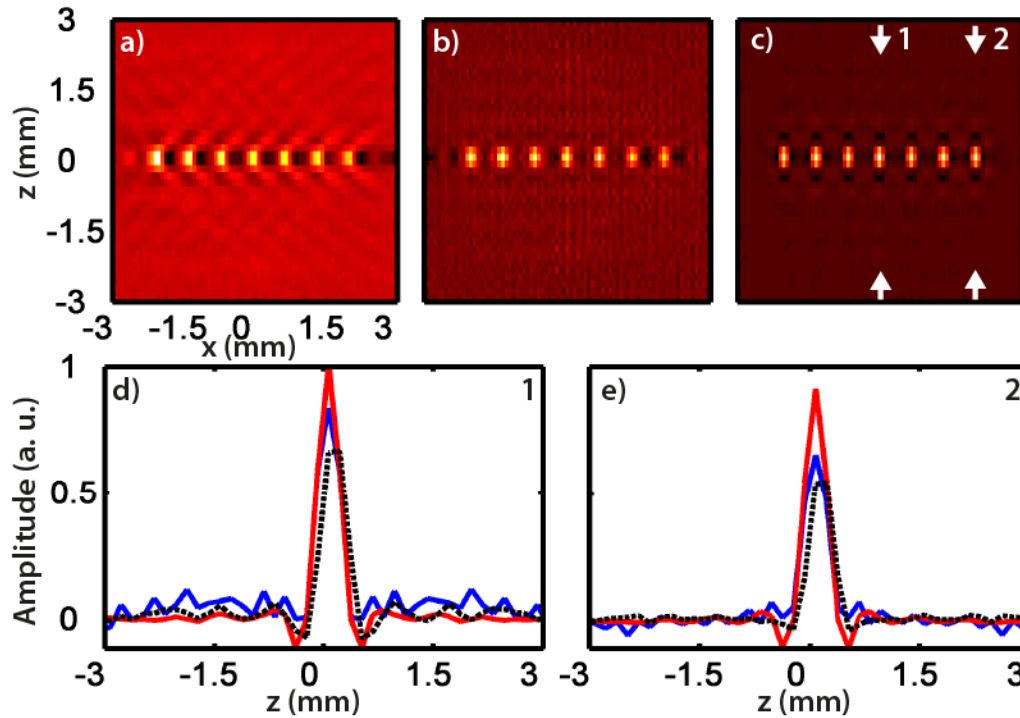**Figure 61:** Reconstructions of a plane full of point absorbers. *a)* Back-projection. *b)* Point-like IMMI. *c)* Proposed finite-sized IMMI. *d)* Profiles through the absorber row marked with 1 in *c)*. Black-dashed: Back-projection. Blue: point-like IMMI. Red: Proposed finite-sized IMMI. *e)* Profiles through the absorber column marked with 2 in *c)*. Colors as in *d)*. See text for discussion.

The sources were a grid of 7 by 7 spherical absorbers with a paraboloidal absorption profile, generalized to 3D from [21]. They were placed on the median plane of the ROI and had diameter of $3\delta xy = 225$ μm.

The effect of the transducer SIR on the forward signals was taken into account by dividing the sensor surface into points and summing up each individual signal. The distance between the elemental sensors was taken as $\lambda/10$, which represents a finer spacing than in the model implementation. This resulted in 10 x 134 sub-sensors for every projection. The signals were calculated for every projection.

5.3.5 Back-projection reconstructions

In order to assess the performance of the proposed model against conventional reconstruction methods, the simulated and experimentally measured signals were processed with the Back-projection method as discussed in Chapter 2.

The parameters of the ROI were the same as for the model-matrix. The sensors were assumed to be point-like, located at the center of the actual sensors. The reconstruction of the whole volume took approximately 4 minutes on an average desktop PC.

Figure 62: Reconstructions of a plane full of point absorbers, side view. *a)* Back-projection. *b)* Point-like IMMI. *c)* Proposed finite-sized IMMI. *d)* Profiles through the absorber row marked with 1 in *c)*. Black-dashed: Back-projection. Blue: point-like IMMI. Red: Proposed finite-sized IMMI. *e)* Profiles through the absorber column marked with 2 in *c)*. Colors as in *d)*. See text for discussion.

5.4   Results

5.4.1 Simulation results

The reconstruction results of the numerical phantom are shown in Figs. 61 and 62. Fig. 61 shows the results in the median plane of the ROI and Fig. 62 shows the same results from a side-view of the ROI, in order to illustrate the in-plane and out-of-plane performance of the reconstruction algorithms.

a) In-plane

Fig. 61a shows the reconstruction of the numerical phantom that was obtained with the full Back-projection method as a cut through the median plane of the ROI. The results show that the objects are reconstructed in a square grid, as expected, but the reconstructed amplitudes show a gradient towards the positive *y* direction (the sensor positions surround the ROI as shown in Fig. 59). Additionally, the reconstruction shows the presence of negative values, which degrades the contrast in the image. The results shows the failure of conventional Back-projection to achieve a uniform reconstruction in the plane.

The results for the point-like model-matrix are shown in Fig. 61b. The figure shows an slight improvement with respect to Back-projection, in the form of better contrast. However, the variation in reconstructed amplitudes along the *y* axis can still be observed

(for a clearer view refer to Fig. 61e). We may conclude that such an effect is due to the sensitivity field of the sensor, which is not completely uniform along the transducer axis.

On the other hand, the reconstruction with the model-matrix including the sensor properties, shown in Fig. 61c, exhibits not only improved contrast but also a uniform reconstructed amplitude throughout the plane. The results demonstrate the importance of taking into account the sensor properties during image reconstruction.

Fig. 61d shows the profiles of the reconstructions for the three different methods, taken along the x axes for the furthermost row of absorbers. The figure shows a twofold increase of the reconstructed amplitude with the finite-sized model as opposed to Back-projection or the point-like model. Additionally, the object sizes reconstructed with the proposed method correspond to the expected object size: the full-width at half-maximum (FWHM) is approximately 3 voxels for each source. The results show the improved in-plane resolution that results from the inclusion of the transducer properties in the image reconstruction process.

Fig. 61e shows the profile taken along the row of absorbers located near the right edge of the ROI. Both of the reconstruction methods based on point-like detectors fail to compensate for the gradient in amplitudes that result from the properties of the sensor. The reconstructed amplitudes with the proposed model, on the other hand, are approximately constant. From these results, it can be concluded that the combination of the nonconventional geometry with an accurate image formation algorithm achieves an accurate and uniform reconstruction on the planes of the ROI.

b) Out-of-plane

The same reconstructed volume is shown as a cut through $x = 0$ in Fig. 62, where the sensor is located left to the image. Like in the previous figure, Figs. 62a to 62c show the results for the Back-projection, point-like model and finite-sized model respectively. The Back-projection reconstruction (Fig. 62a) shows the same artifacts as for the in-plane case, namely the gradient in amplitudes and low contrast. Additionally, the shape of the objects is slightly distorted, as can be noted by the ripples above and below the median plane of the ROI.

The image reconstructed with the point-like model is shown in Fig. 62b. In this case, the contrast in the image is better than in the Back-projection case, but the absorber amplitudes are not reconstructed uniformly and the shapes are also slightly distorted. Fig.
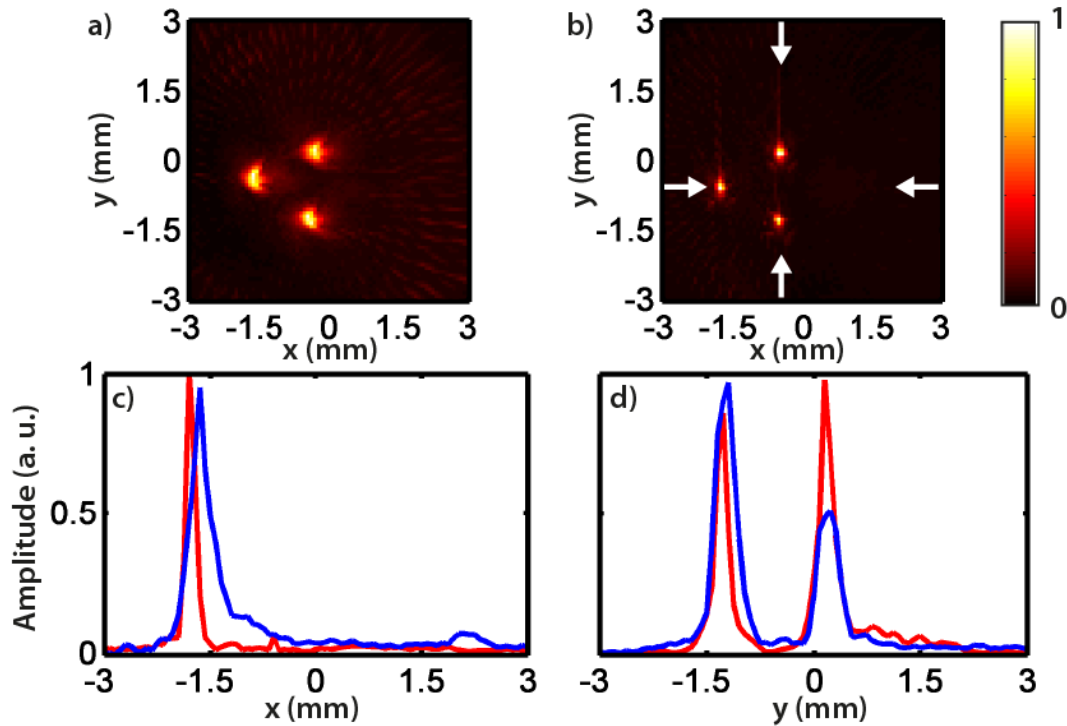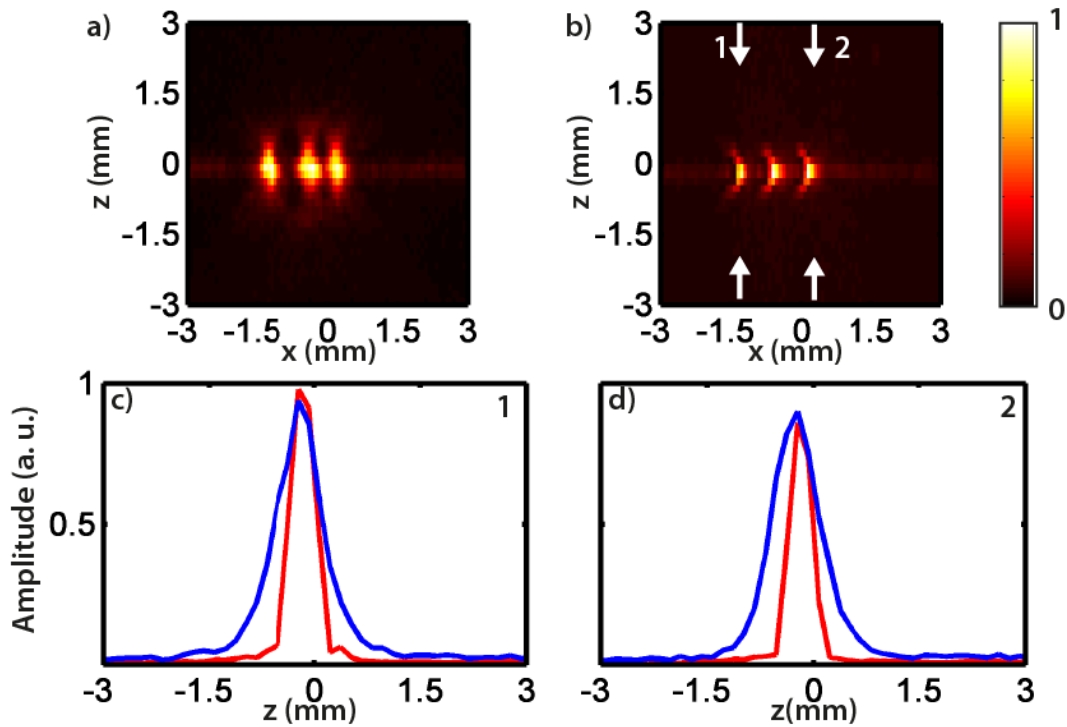
Figure 63 Reconstructions of an experimental phantom with three microspheres. *a)* Back-projection. *b)* Proposed finite-sized IMMI. *c)* Horizontal profiles through the line marked in *b)*. Blue: Back-projection. Red: Proposed finite-sized IMMI. *d)* Vertical profiles through the line marked in *b)*. Colors as in *c)*. See text for discussion.

62c shows the results for the finite-sized model, which results in uniform reconstructed amplitude and shape for all absorbers and optimal contrast of the image.

The profiles of the middle and furthermost absorbers are shown in Figs. 62d and 62e to illustrate the vertical resolution attained by the different reconstruction methods. The profiles show that all three methods achieve a similar resolution along the vertical direction. This is to be expected since array elements can be considered almost point-like along *z* and therefore the Back-projection or the point-like model are valid approximations in this respect.

Overall, the results demonstrate that the proposed algorithm provides accurate volumetric images of numerical phantoms. This is in contrast to standard techniques, such as Back-projection or IMMI for point-like detectors, which exhibit degraded contrast and resolution.

5.4.2 Experimental results 1: small absorbers

Since the absorbers were placed approximately on the median plane of the ROI, the analysis of the results is done along the lines of the previous section: first, the reconstruction in the median plane is presented and afterwards the out-of-plane behavior is analyzed. Having showcased the importance of taking into account the properties of the

sensor in the reconstruction procedure, from this point on the performance of the proposed method was assessed only against standard Back-projection.

a) In-plane

The images obtained with Back-projection and the proposed method are shown in Fig. 63. The results show the maximum amplitude projection (MAP) taken along the z axis and the corresponding profiles.

In Fig. 63a, the Back-projection image is shown. The reconstructed amplitude of the spheres is similar since they are located close to the center of the ROI. However, they are not well resolved. In contrast, the image obtained with the proposed method (Fig. 63b) shows three sources resolved as precisely as the discretization of the ROI allows. The resolutions of the reconstructions can be better investigated with the profiles taken through the absorbers. In Fig. 63c, the profile along the middle absorber for both reconstructions is depicted. The results demonstrate a twofold increase in the resolution of the proposed method with respect to Back-projection, as expected from the simulations. This finding can be also observed in Fig. 63d, where the profile along y for the two microspheres in the middle of the images is shown. The difference in amplitude is due to the fact that, in the Back-projection image, the two absorbers do not lie along the same line.

These results demonstrate experimentally the improvement of in-plane resolution achieved by the proposed method over a standard reconstruction method.

b) Out of plane

The same volumetric images are shown in Fig. 64 as a MAP taken along the y axis. Fig. 64a shows the Back-projection reconstruction, with object shapes that are distorted due to the limited view of the detection geometry along the vertical axis. In contrast, the reconstruction with the proposed method (Fig. 64b) shows absorbers more localized in the median plane although with slightly distorted shapes.

The profiles for two of the absorbers are shown in Figs. 64c and 64d. In both cases, the FWHM of the reconstructed Back-projection is approximately 600 μm whereas in the case of the proposed method the FWHMs are ~300 μm. Considering that the voxel size along the vertical direction is 150 μm, we may conclude that the performance of the proposed model is at the limit attainable in a noisy measurement. The findings in this section demonstrate that the proposed method is able to achieve uniform resolution both in-plane and out of the plane, up to the discretization of the ROI.

Figure 64: Reconstructions of an experimental phantom with three microspheres, side view. *a)* Back-projection. *b)* Proposed finite-sized IMMI. *c)* Vertical profiles through the line marked 1 in *b)*. Blue: Back-projection. Red: Proposed finite-sized IMMI. *d)* Vertical profiles through the line marked 2 in *b)*. Colors as in *c)*. See text for discussion.

5.4.3 Experimental results 2: complex source

The reconstructions of the knotted suture are shown in Fig. 65. The top half of the image shows the MAPs taken along each of the image axes for the Back-projection reconstructions. The lower half of the image, on the other hand, shows the projections for the image obtained by the proposed method.

The Back-projection reconstructions show a clear shape of the object with good contrast, owing to the use of a MAP, which eliminates the negative values from the image. However, the boundaries of the knot are blurry, which degrades the contrast where the suture overlaps (see e.g. Fig. 65a, top, or Fig. 65c, bottom-left).

On the other hand, the IMMI reconstructions show a better contrast with respect to the background and a less blurry image. In particular, it is worth noting that the points where the suture overlaps are in general better resolved than in the Back-projection images (see, e.g. Fig. 65d top or Fig. 65f bottom-left). Additionally, the reconstructed amplitude is more uniform throughout the extension of the object. The main differences arise for sections of the knot mainly along a vertical direction, when compared with sections mainly lying in a plane, and are thus originated by the directivity of the source.
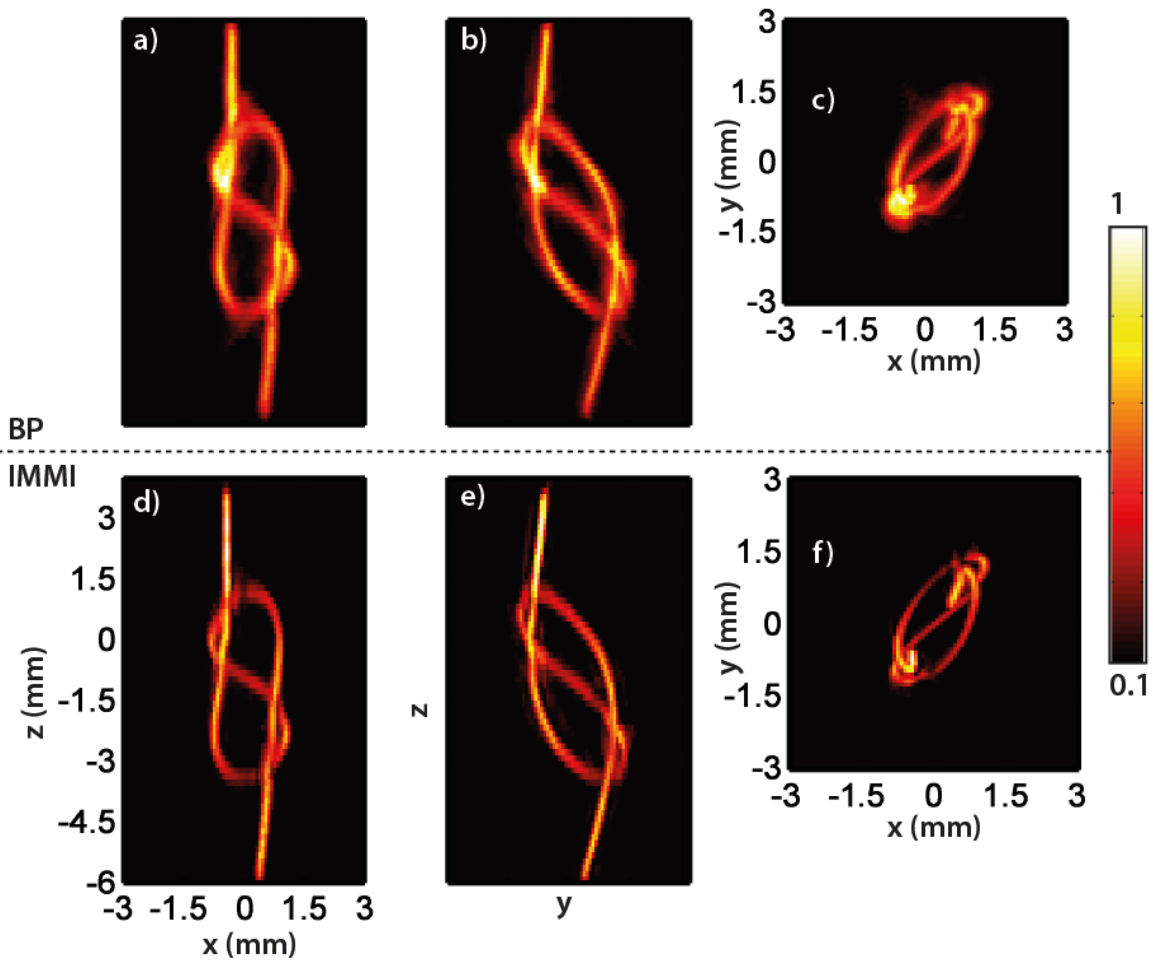
Figure 65: Reconstructions of an experimental phantom with a knotted 300 µm suture. All figures represent the MAP of the volumetric image through one of the axis. They are normalized to their respective maxima and represented in a linear color scale. *a)* to *c)* Back-projection reconstructions. *d)* to *f)* reconstructions with the proposed finite-sized IMMI method. See text for discussion.

The results demonstrate the ability of the proposed method to resolve complex structures and to tell apart objects close to each other.

5.4.4 Experimental results 3: real tissue

The reconstructions of the biological sample are shown in Fig. 66. Like in the previous figure, the top half of the image shows the Back-projection reconstructions and the lower half the images obtained with the proposed method. In this case, the MAPs are taken along the *x* and *y* axis to represent the side views of the sample. However, taking the MAP along the *z* axis would project the approximately 12 mm length of the sample into one plane, which is devoid of meaning. Instead, two MAPs taken within a 1.5 mm region at two different distances from the fingertips are presented.
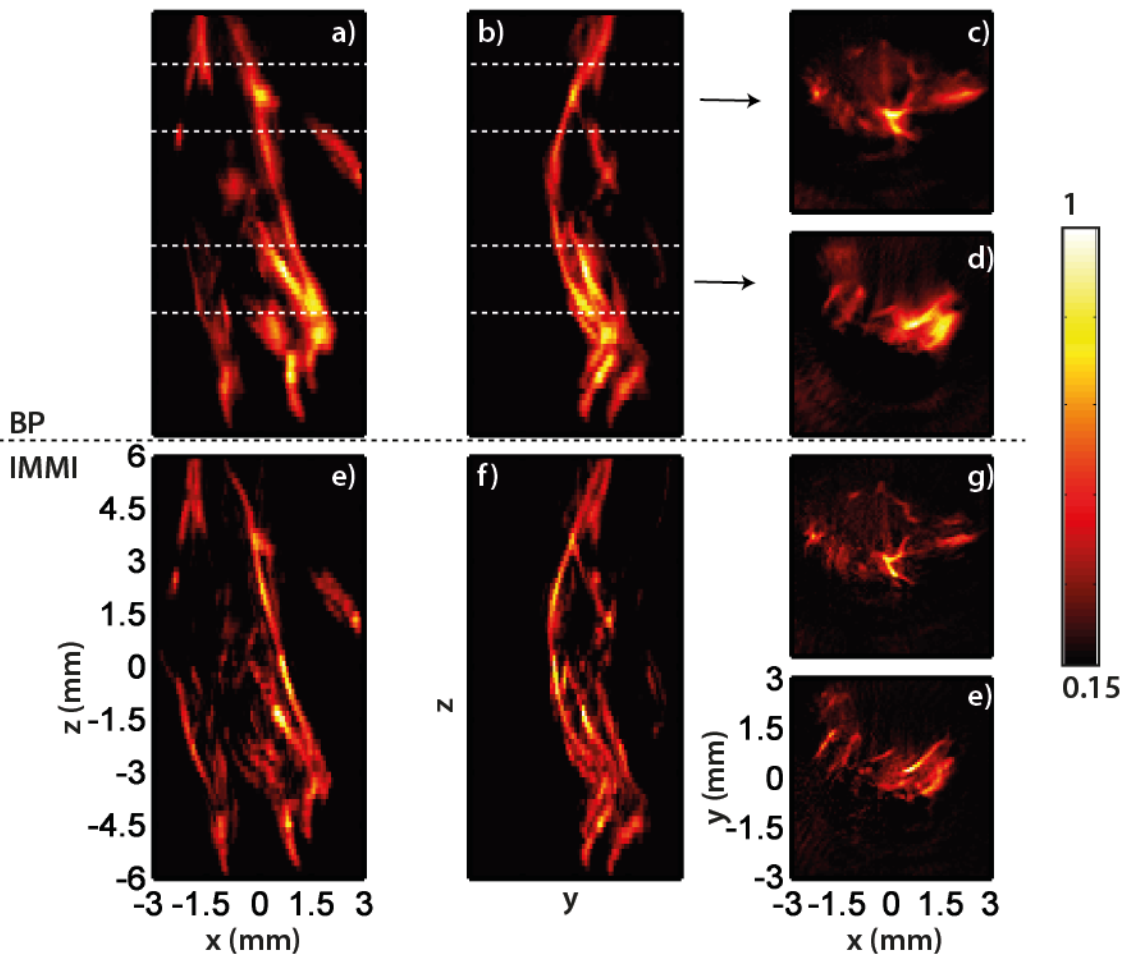
Figure 66. Reconstructions of the hind paw of a mouse. All figures represent the MAP of the volumetric image through one of the axis. The figures on the rightmost column represent the MAPs along the *z* axis within the dotted region in *b). a)* to *d)* Back-projection reconstructions. *e)* to *h)* reconstructions with the proposed finite-sized IMMI method. See text for discussion.

In general, the Back-projection images show a clear shape of the paw and the vasculature therein. However, there are some spots where the contrast is poor or some structural information has been lost. This can be seen, for example, when comparing Figs. 66a and 66e along the $x = -1.5$ mm line, where a group of (presumably) vessels is lost from the back-projection image. The improved resolution of the images resulting from the proposed method can be analyzed when observing Figs. 66d and 66e in particular (and the corresponding segments in the other projections). The figures show a better separation of the structures that stem from the fingertips in the case of the proposed method.

Overall, the results show the superior resolution and imaging performance achieved by the proposed method when compared with standard techniques. This was achieved by

146

including the characteristics of the sensor on an accurate model for the propagation and measurement of optoacoustic signals.

5.5 Conclusion and Outlook

In this chapter, an accurate three-dimensional image reconstruction algorithm for a nonconventional tomographic geometry was proposed. The method was based on an algebraic image reconstruction procedure, IMMI, that was modified to include the spatio-temporal properties of an ultrasound transducer. This was done through numerical integration of the model over the surface of the sensor. The method also made use of a symmetry-based computation strategy that greatly reduced the calculation times and size of the model-matrices, enabling us to reconstruct images with 75 μm resolution using a dataset with over 20,000 distinct projections.

The performance of the method was assessed in comparison with standard reconstruction techniques, such as Back-projection and IMMI for a point detector. This was done by reconstructing volumetric images of numerical phantoms and in experiment. The results obtained with point sources showcased the ability of the proposed method to reconstruct with isotropic amplitude and resolution in the ROI, both in simulations and in experiment. This was in contrast to standard methods which showed poor contrast and resolution in comparison. The results with a complex phantom demonstrated the superior performance of the proposed method when reconstructing a truly three-dimensional structure, yielding in less blurred images and better contrast than the Back-projection method. Finally, the performance was assessed in an *ex vivo* measurement of the hind paw of a mouse. The proposed image reconstruction method was able to form an image with improved resolution and contrast than a standard technique. The method presented herein may be thus applied to the imaging of biological data in 3D imaging scenarios.

The proposed method has two drawbacks that should be overcome in order for the technique to reach its full potential. First, the method is computationally very intensive. With the use of the symmetries and the optimization of the ROI dimensions to fit the objects imaged the technique was made feasible. However, achieving an isotropic pixel size and resolution in the order of $\sim$40 μm, while feasible with the hardware and nonconventional geometry presented herein, is still a very challenging goal with the present implementation of the proposed method. Possible solutions to this drawback include a shift towards Graphics Processing Unit (GPU)-based computations or further parallelization of the algorithm.

The second caveat has to do with the image reconstruction procedure. At the moment, image reconstruction takes place with an unregularized iterative algorithm that has been optimized and yields consistent results and, as has been shown, good imaging performance. However, it has been shown that measurement geometries that do not fully enclose the object may result in degraded performance. For the case presented herein, the cylindrical symmetry of the measurement geometry leaves two open spaces below and above the object. With the utilization of an ultrasound array and thanks to the tomographic geometry in the plane, the effective solid angle covered by the sensor can be considered 180° (for the F/D = 0.5 used herein), which is more than would be achievable by a focused sensor. However, even taking into account the SIR of the sensor during image formation, which partially compensates for the missing projections, this is still far from the 360° of a completely spherical detection. Thus, regularization procedures tailored to the cylindrical detection geometry should result in an optimal imaging performance.

6.   CONCLUSION AND OUTLOOK

In the present work, the development of optoacoustic image reconstruction algorithms that take into account the properties of ultrasound detectors was reported. The proposed algorithms were based on the combination of optoacoustic propagation models with accurate, experimentally validated descriptions of the sensor properties. The performance of the proposed methods was assessed both in simulations and experiment, showing improved image quality over standard reconstruction techniques, which typically ignore the properties of real sensors. Moreover, the proposed methods were successfully applied to the imaging of mouse anatomy *ex vivo,* which, to the best of the author's knowledge, represents the first application of realistic sensor models to optoacoustic image formation in biological tissue*.

In order to develop the proposed algorithms, the properties of ultrasound sensors were first characterized in terms of their spatially dependent and independent properties. The spatially independent properties were described in terms of the electrical impulse response (EIR), which acts as a band-pass filter on the measured optoacoustic signals. The characterization of the EIR was performed by exciting the sensor with a source of known spectrum and compensating for it. The spatially dependent properties of the sensor were first characterized in terms of the frequency-dependent sensitivity fields, which describe the variation in measured signal amplitude as a function of the sensor geometry and source location. However, such a description did not account for the phase and frequency distortion of measured optoacoustic signals. Such a distortion, termed spatial impulse response (SIR), effectively acts as a spatially-dependent low-pass filter on the measured signal. Therefore, a global response of the sensor, the total impulse response (TIR), was obtained as a temporal convolution of the EIR and the SIR. It was experimentally demonstrated that the TIR describes all of the sensor-related distortions upon a measured optoacoustic signal. This description resulted in several insights: first, it was shown that the sensitivity field of a sensor is a particular feature of the TIR. Second, it was demonstrated that the sensor spatial properties are a complex function of the acoustic frequency and the source location and are optimally described by a broad-band, time-domain entity such as the TIR.

The knowledge of the sensor properties was applied to the development of image reconstruction algorithms for two different detection geometries: microscanning and nonconventional tomography in 3D.

---

* Before the official submission of this dissertation, Wang et al. presented an implementation of a three-dimensional model-based reconstruction method incorporating sensor properties.

In the microscanning geometry, algorithms based on the frequency-dependent sensitivity field of a transducer were developed as a first approximation to the image formation problem. Due to the underlying incomplete description of the sensor properties, these algorithms failed to reliably improve imaging performance over conventional techniques. Instead, an algorithm based on the combination of the SIR with the optoacoustic propagation model IMMI was adapted to the particulars of microscanning. The performance of the proposed method was assessed by simple phantoms and a complex biological sample. By including the SIR in the reconstruction process, the properties of the sensor for all acoustic frequencies were taken into account during image formation. As a result, the proposed method was able to provide well-resolved images without the need to adapt the resolution of the sensor by signal filtering, which typically results in degraded accuracy of the images reconstructed with standard techniques. However, due to the limited view of the sensors, the microscanning concept proved lacking in terms of 3D imaging.

A nonconventional tomographic geometry in 3D was developed, with the aim to overcome some limitations of conventional geometries and provide a methodology towards mesoscopic applications. Within this context, the SIR was taken into account summing up IMMI matrices for point-like sensors located on the surface of the actual sensor. Due to the computational demands of 3D propagation and detection models, new strategies for the calculation of IMMI matrices had to be developed. These were based on the symmetries of the measurement geometry and resulted in manageable matrices and feasible computation times. The performance of the method was assessed in simulations and experiment, both in simple phantoms and biological tissue. The combination of nonconventional geometry and the proposed reconstruction method consistently resulted in images with improved resolution and contrast with respect to the ones obtained with standard techniques.

Overall, the present work provides image reconstruction algorithms that are consistent with the realities of the optoacoustic imaging, namely the broadband nature of optoacoustic signals and sensors and the diffractive features of ultrasound detection.

Finally, several non-trivial conclusions and consequences with respect to optoacoustic imaging may be extracted from the present work.

The first finding has to do with the frequency response of ultrasound sensors and can be concluded from two observations. For one part, it was demonstrated in Chapter 3 that an ultrasound sensor used for optoacoustics has an effective bandwidth which is two times broader than when used in conventional pulse-echo mode. For the other part, the interdependence of size, amplitude and acoustic frequency of optoacoustic sources means

that large objects (and collections of small objects) emit characteristically strong signals at low frequencies. As a result, optoacoustic signals with a frequency content much lower than the central frequency of the transducer may be measured. This was demonstrated in Chapter 4, as the low-frequency (<10 MHz) components of optoacoustic signals were measured with high amplitude by a high-frequency sensor (25 MHz). The results demonstrate that low acoustic frequencies may influence non-trivially the image formation process, even when imaging at high-frequencies, i.e., at meso- and microscopic scales. Therefore, image reconstruction algorithms as the IMMI algorithm proposed in Chapter 4 need to be used to discriminate between the low-frequencies inherent to a large source and the low-frequencies that arise from a small collection of absorbers.

The second finding is derived from the previous discussion and relates to the assessment of the properties of a sensor. The maximum resolution theoretically achievable by a focused sensor can be determined by the highest frequency on the frequency response of the sensor. In practical terms, however, the actual resolution in a given application is determined by the optoacoustic signal in the manner discussed in the previous paragraph. Therefore, when deciding upon the optimal sensor for a given application, the study of its inherent resolution should be done for several frequencies or, ideally, with a full model of propagation and detection that includes the (known or expected) properties of the sensor, such as IMMI including the SIR.

The third finding is related to image formation in optoacoustics. The results in this work have demonstrated the need to take into account the full sensor properties during image formation in order to compensate for sensor-related distortions. Even in a measurement geometry like the one presented in Chapter 5, which was specifically designed to minimize such distortions, accurate image reconstruction methods provide qualitatively better images than conventional reconstruction techniques. Therefore, herein it is proposed that image formation taking into account the sensor properties should be standard practice for image formation in optoacoustics.

The fourth finding relates to the previous one and deals with the design of next-generation optoacoustic setups. Accurate reconstruction algorithms with sensor properties effectively minimize the effect of the sensor characteristics on the final image. The algorithms achieve this by compensating for the sensor distortions independently of the source location and frequency spectrum. As a result, the design of a new optoacoustic setup does not have to be constrained to traditional designs, which are either based on single-

frequency descriptions of the sensor properties[*] or try to minimize the sensor size to attain point-like behavior[†]. By mutually adapting the setup parameters and the reconstruction method, the cost, performance and versatility of the setup may be significantly optimized.

In conclusion, the knowledge of ultrasound sensor characteristics in optoacoustics, and the use of that knowledge in realistic image formation algorithms results in improved image quality in existing systems and can provide new design principles for future setups. In following years the optimization of the proposed algorithms through parallelization and GPU-based computation will allow for real-time, three-dimensional accurate optoacoustic image formation.

---

[*] For example, the use of focused sensors to define the imaging plane in a tomographic setup, as seen above, may result in an ill-defined imaging plane due to the low acoustic frequencies inherent to optoacoustic signals.

[†] This multiplies the number of sensors needed for an efficient reconstruction, with added cost and complexity.

BIBLIOGRAPHY

1. Croft, W.J., *Under the microscope : a brief history of microscopy*. Series in popular science2006, Hackensack, NJ: World Scientific. xiii, 138 p.
2. Soubret, A. and V. Ntziachristos, *Optical Imaging and Tomography*, in *Textbook of in vivo Imaging in Vertebrates*2007, John Wiley & Sons, Ltd. p. 149-181.
3. Ntziachristos, V., *Going deeper than microscopy: the optical imaging frontier in biology.* Nat Methods, 2010. **7**(8): p. 603-14.
4. Weissleder, R. and M.J. Pittet, *Imaging in the era of molecular oncology.* Nature, 2008. **452**(7187): p. 580-9.
5. Diebold, G.J., T. Sun, and M.I. Khan, *Photoacoustic monopole radiation in one, two, and three dimensions.* Phys Rev Lett, 1991. **67**(24): p. 3384-3387.
6. Wang, L.V. and H.-i. Wu, *Biomedical optics : principles and imaging*2007, Hoboken, N.J.: Wiley-Interscience. xiv, 362 p.
7. Dean-Ben, X.L., D. Razansky, and V. Ntziachristos, *The effects of acoustic attenuation in optoacoustic signals.* Phys Med Biol, 2011. **56**(18): p. 6129-48.
8. Ntziachristos, V. and D. Razansky, *Molecular Imaging by Means of Multispectral Optoacoustic Tomography (MSOT).* Chemical Reviews, 2010. **110**(5): p. 2783-2794.
9. Wang, L.V., *Photoacoustic imaging and spectroscopy*. Optical science and engineering2009, Boca Raton: CRC. xx, 499 p.
10. Taruttis, A., et al., *Fast multispectral optoacoustic tomography (MSOT) for dynamic imaging of pharmacokinetics and biodistribution in multiple organs.* Plos One, 2012. **7**(1): p. e30491.
11. Buehler, A., et al., *Video rate optoacoustic tomography of mouse kidney perfusion.* Opt Lett, 2010. **35**(14): p. 2475-2477.
12. Taruttis, A., et al., *Real-time imaging of cardiovascular dynamics and circulating gold nanorods with multispectral optoacoustic tomography.* Optics Express, 2010. **18**(19): p. 19592-19602.
13. Wang, X.D., et al., *Noninvasive laser-induced photoacoustic tomography for structural and functional in vivo imaging of the brain.* Nature Biotechnology, 2003. **21**(7): p. 803-806.
14. Ma, R., et al., *Multispectral optoacoustic tomography (MSOT) scanner for whole-body small animal imaging.* Opt Express, 2009. **17**(24): p. 21414-26.
15. Brecht, H.P., et al., *Whole-body three-dimensional optoacoustic tomography system for small animals.* Journal of Biomedical Optics, 2009. **14**(6).
16. Zhang, H.F., et al., *Functional photoacoustic microscopy for high-resolution and noninvasive in vivo imaging.* Nature Biotechnology, 2006. **24**(7): p. 848-851.
17. Song, L., et al., *Fast 3-D dark-field reflection-mode photoacoustic microscopy in vivo with a 30-MHz ultrasound linear array.* J Biomed Opt, 2008. **13**(5): p. 054028.
18. Maslov, K., et al., *Optical-resolution photoacoustic microscopy for in vivo imaging of single capillaries.* Opt Lett, 2008. **33**(9): p. 929-31.
19. Zhang, E.Z., et al., *In vivo high-resolution 3D photoacoustic imaging of superficial vascular anatomy.* Physics in Medicine and Biology, 2009. **54**(4): p. 1035-1046.
20. Xu, M. and L.V. Wang, *Universal back-projection algorithm for photoacoustic computed tomography.* Phys Rev E Stat Nonlin Soft Matter Phys, 2005. **71**(1 Pt 2): p. 016706.
21. Rosenthal, A., D. Razansky, and V. Ntziachristos, *Fast semi-analytical model-based acoustic inversion for quantitative optoacoustic tomography.* IEEE Trans Med Imaging, 2010. **29**(6): p. 1275-85.
22. Razansky, D., C. Vinegoni, and V. Ntziachristos, *Imaging of mesoscopic-scale organisms using selective-plane optoacoustic tomography.* Phys Med Biol, 2009. **54**(9): p. 2769-77.

23.   Xu, M. and L.V. Wang, *Analytic explanation of spatial resolution related to bandwidth and detector aperture size in thermoacoustic or photoacoustic reconstruction.* Phys Rev E Stat Nonlin Soft Matter Phys, 2003. **67**(5 Pt 2): p. 056605.

24.   Rosenthal, A., V. Ntziachristos, and D. Razansky, *Model-based optoacoustic inversion with arbitrary-shape detectors.* Med Phys, 2011. **38**(7): p. 4285-4295.

25.   Wang, K., et al., *An Imaging Model Incorporating Ultrasonic Transducer Properties for Three-Dimensional Optoacoustic Tomography.* Ieee Transactions on Medical Imaging, 2011. **30**(2): p. 203-214.

26.   Jensen, J.A. and N.B. Svendsen, *Calculation of pressure fields from arbitrarily shaped, apodized, and excited ultrasound transducers.* IEEE Trans Ultrason Ferroelectr Freq Control, 1992. **39**(2): p. 262-7.

27.   Schmerr, L.W. and S.-J. Song, *Ultrasonic nondestructive evaluation systems : models and measurements*2007, New York: Springer. xv, 602 p.

28.   Jetzfellner, T., et al., *Optoacoustic tomography with varying illumination and non-uniform detection patterns.* J Opt Soc Am A Opt Image Sci Vis, 2010. **27**(11): p. 2488-95.

29.   Fan, Y., et al., *Development of a laser photothermoacoustic frequency-swept system for subsurface imaging: theory and experiment.* J Acoust Soc Am, 2004. **116**(6): p. 3523-33.

30.   Kak, A.C.S., Malcolm, *Principles of Computerized Tomographic Imaging*1988: IEEE Press.

31.   Szabo, T.L., *Diagnostic ultrasound imaging : inside out.* Academic Press series in biomedical engineering2004, Amsterdam ; Boston: Elsevier Academic Press. xxii, 549 p.

32.   Dean-Ben, X.L., et al., *Statistical approach for optoacoustic image reconstruction in the presence of strong acoustic heterogeneities.* IEEE Trans Med Imaging, 2011. **30**(2): p. 401-8.

33.   Hecht, E., *Optics.* 4th ed2002, Reading, Mass.: Addison-Wesley. vi, 698 p.

34.   Arnau, A., *Piezoelectric transducers and applications.* 2nd ed2008, New York: Springer. xxvi, 532 p.

35.   Shung, K.K. and M. Zipparo, *Ultrasonic transducers and arrays.* Ieee Engineering in Medicine and Biology Magazine, 1996. **15**(6): p. 20-30.

36.   Rosenthal, A., V. Ntziachristos, and D. Razansky, *Optoacoustic methods for frequency calibration of ultrasonic sensors.* IEEE Trans Ultrason Ferroelectr Freq Control, 2011. **58**(2): p. 316-26.

37.   Baek, D., J.A. Jensen, and M. Willatzen, *Modeling transducer impulse responses for predicting calibrated pressure pulses with the ultrasound simulation program Field II.* J Acoust Soc Am, 2010. **127**(5): p. 2825-35.

38.   Ephrat, P., et al., *Four-dimensional photoacoustic imaging of moving targets.* Opt Express, 2008. **16**(26): p. 21570-81.

39.   Roumeliotis, M., et al., *Development and characterization of an omnidirectional photoacoustic point source for calibration of a staring 3D photoacoustic imaging system.* Opt Express, 2009. **17**(17): p. 15228-38.

40.   Xu, M. and L.V. Wang, *Photoacoustic imaging in biomedicine.* Review of Scientific Instruments, 2006. **77**(4): p. 041101-22.

41.   Maslov, K., G. Stoica, and L.V. Wang, *In vivo dark-field reflection-mode photoacoustic microscopy.* Opt Lett, 2005. **30**(6): p. 625-7.

42.   Song, K.H. and L.V. Wang, *Deep reflection-mode photoacoustic imaging of biological tissue.* Journal of Biomedical Optics, 2007. **12**(6).

43.   Gateau, J., et al., *Three-dimensional opto-acoustic tomography using a conventional ultrasound linear detector array.* Medical Physics, in press.

44.   Jetzfellner, T., et al., *Interpolated model-matrix optoacoustic tomography of the mouse brain.* Applied Physics Letters, 2011. **98**(16).

154

45. Buehler, A., et al., *High resolution tumor targeting in living mice by means of multispectral optoacoustic tomography.* EJNMMI Res, 2012. **2**: p. 14.

46. Dean Ben, X., et al., *Accurate model-based reconstruction algorithm for three-dimensional optoacoustic tomography.* IEEE Trans Med Imaging, 2012.

47. Buehler, A., et al., *Three-dimensional optoacoustic tomography at video rate.* Opt Express, 2012. **20**(20): p. 22712-9.

48. Wang, K., et al., *Investigation of iterative image reconstruction in three-dimensional optoacoustic tomography.* Phys Med Biol, 2012. **57**(17): p. 5399-423.

49. Kruger, R.A., et al., *Photoacoustic angiography of the breast.* Medical Physics, 2010. **37**(11): p. 6096-6100.

50. Zhang, E., J. Laufer, and P. Beard, *Backward-mode multiwavelength photoacoustic scanner using a planar Fabry-Perot polymer film ultrasound sensor for high-resolution three-dimensional imaging of biological tissues.* Applied Optics, 2008. **47**(4): p. 561-577.

51. Laufer, J., et al., *In vivo preclinical photoacoustic imaging of tumor vasculature development and therapy.* J Biomed Opt, 2012. **17**(5): p. 056016.

52. Laufer, J., et al., *In vivo photoacoustic imaging of mouse embryos.* J Biomed Opt, 2012. **17**(6): p. 061220.

53. Dean Ben, X., V. Ntziachristos, and D. Razansky, *Acceleration of optoacoustic model-based reconstruction using angular image discretization.* IEEE Trans Med Imaging, 2012.

54. Dima, A., *A New Model-Based Image Reconstruction Algorithm for Photoacoustic Tomography*, in *Chair for Biological Imaging*2009, Technische Universität München: München.

55. Buehler, A., et al., *Model-based optoacoustic inversions with incomplete projection data.* Med Phys, 2011. **38**(3): p. 1694-704.

56. Hou, Y., et al., *An Integrated Optoacoustic Transducer Combining Etalon And Black PDMS Structures.* Ieee Transactions on Ultrasonics Ferroelectrics and Frequency Control, 2008. **55**(12): p. 2719-2725.

57. Kim, H.J., L.W. Schmerr, and A. Sedov, *Generation of the basis sets for multi-Gaussian ultrasonic beam models - An overview.* Journal of the Acoustical Society of America, 2006. **119**(4): p. 1971-1978.

58. Kozhushko, V., et al., *Focused array transducer for two-dimensional optoacoustic tomography.* J Acoust Soc Am, 2004. **116**(3): p. 1498-506.

59. Wang, K., et al., *An imaging model incorporating ultrasonic transducer properties for three-dimensional optoacoustic tomography.* IEEE Trans Med Imaging, 2011. **30**(2): p. 203-14.

60. Araque Caballero, M.Á., et al., *Optoacoustic determination of spatio-temporal responses of ultrasound sensors.* Submitted, 2012.

61. Song, K.H. and L.V. Wang, *Noninvasive photoacoustic imaging of the thoracic cavity and the kidney in small and large animals.* Medical Physics, 2008. **35**(10): p. 4524-4529.

62. Zhang, C., K. Maslov, and L.V. Wang, *Subwavelength-resolution label-free photoacoustic microscopy of optical absorption in vivo.* Opt Lett, 2010. **35**(19): p. 3195-7.

63. Hu, S., K. Maslov, and L.H.V. Wang, *Noninvasive label-free imaging of microhemodynamics by optical-resolution photoacoustic microscopy.* Optics Express, 2009. **17**(9): p. 7688-7693.

64. Lathi, B.P., *Linear systems and signals*. 2nd ed2005, New York: Oxford University Press. xvi, 975 p.

65. Gonzalez, R.C., R.E. Woods, and S.L. Eddins, *Digital Image processing using MATLAB*2004, Upper Saddle River, NJ: Pearson/Prentice Hall. xiv, 609 p.

66. Li, M.L., et al., *Improved in vivo photoacoustic microscopy based on a virtual-detector concept.* Opt Lett, 2006. **31**(4): p. 474-6.

67. Araque Caballero, M.Á., et al., *Model-based optoacoustic imaging using focused detector scanning.* Opt. Lett., 2012. **37**(19): p. 4080-4082.
68. Frazier, C.H. and W.D. O'Brien, *Synthetic aperture techniques with a virtual source element.* Ieee Transactions on Ultrasonics Ferroelectrics and Frequency Control, 1998. **45**(1): p. 196-207.
69. Arditi, M., F.S. Foster, and J.W. Hunt, *Transient fields of concave annular arrays.* Ultrasonic Imaging, 1981. **3**(1): p. 37-61.

List of Publications

Model-based optoacoustic imaging with Focused detector scanning, Araque Caballero, M. Á.; Rosenthal, A.; Gateau, J. ; Razansky, D.; Ntziachristos, V. (Optics Letters, Vol. 37, Issue 19, pp. 4080-4082 (2012)). The results presented in this publication are part of Chapter 4.

Optoacoustic characterization of spatio-temporal responses of ultrasound sensors, Araque Caballero, M. Á.; Rosenthal, A.; Bühler, A. ; Razansky, D.; Ntziachristos, V. (under review in IEEE Trans. Ultrasound Ferroelectrics Frequency Control, as of December 2012). The theory, results, materials and methods of this publication are part of Chapter 3.

Volumetric model-based optoacoustic imaging incorporating sensor properties, Araque Caballero, M. Á.; Gateau, J.; Déan-Ben, X-L.; and Ntziachristos, V. (under review in Medical Physics, as of December 2012). This publication represents the definitive results of the preliminary work presented in Chapter 5.

Versatile and high-resolution optoacoustic volume three-dimensional imaging using a conventional linear array ultrasound probe. Gateau, J.; Araque Caballero, M. Á.; Déan-Ben, X-L.; Ntziachristos, V. (Medical Physics **40**, 013302 (2013))

Spatial characterization of the response of a silica optical fiber to wideband ultrasound, Rosenthal, A.; Araque Caballero, M. Á.; Kellnberger, S.; Razansky, D.; Ntziachristos, V. (Optics Letters, Vol. 37, Issue 15, pp. 3174-3176 (2012))

Interpolated model-matrix optoacoustic tomography of the mouse brain, Jetzfellner, T. ; Rosenthal, A. ; Englmeier, K.-H. ; Dima, A. ; Angel Araque Caballero, M. ; Razansky, D. ; Ntziachristos, V. Appl. Phys. Lett. 98 (16):163701 (2011)

Acknowledgements